DESIGN, MODELING AND MOTION PLANNING OF UNDERACTUATED SPHERICAL ROBOTS

セイエド, アミル, タフリシ

DESIGN, MODELING AND MOTION PLANNING OF UNDERACTUATED SPHERICAL ROBOTS

by

Seyed Amir Tafrishi

Supervisor: Motoji Yamamoto

DOCTOR OF PHILOSOPHY

Department: Mechanical Engineering

at

KYUSHU UNIVERSITY

KYUSHU
UNIVERSITY

I dedicate this dissertation to my dearest academic advisor and father-in-law, Professor Esmaeil Esmaeilzadeh, who passed away during my P.hD. studies.

Table of Contents

List of Tables . . . . . **vii**

List of Figures . . . . . **viii**

Abstract . . . . . **xiii**

Acknowledgements . . . . . **xv**

Chapter 1 Introduction **1**

1.1 Motivation 1

1.2 Spherical Mobile Robots 3
1.2.1 Torque-reaction 4
1.2.2 Mass-imbalance 4
1.2.3 Conservation of Angular Momentum 5

1.3 Inverse Dynamics in Underactuated Systems 5

1.4 Non-holonomic Path Planning of a Spin-rolling Sphere 7

1.5 Contributions 9

1.6 Dissertation Outline 11

Chapter 2 Design and Analytical Studies on Novel Fluid Actuated Spherical Mobile Robot **13**

2.1 Introduction 13

2.2 Robot Feature and Rigid Body Model 14
2.2.1 Structure and Components of Rolling Robot 14
2.2.2 Rigid Body Dynamics 15

2.3 Internal Driving Unit 20
2.3.1 Linear Actuator 20
2.3.2 Motion Generation 23

2.4 Simulation Studies 27
2.4.1 Performance of the Internal Driving Unit (IDU) 27
2.4.2 Motion Patterns in Forward Locomotion 33

2.5 Parametric Evaluations on Developed System 37
2.5.1 Mass Ratio Evaluation 37

2.5.2 Cost of Transport 40

2.6 Inverse Dynamics-Based Motion Control 42

2.7 Simulation Results of Feed-Forward Control 45

Chapter 3 Sensor Design for Tracking the Rolling Robot's Rotating Core in the Pipe by Inertial Measurement Unit 51

3.1 Introduction 51

3.2 Experimental Setup 52

3.3 Sensor Fusion 54
3.3.1 Models of the Sensor Signals 55
3.3.2 Filter Structure 56

3.4 Results and Discussion 60

Chapter 4 Singularity in the Inverse Dynamics of the Underactuated Robots 66

4.1 Introduction 66

4.2 Modified Dynamic Model of the Rolling System 67
4.2.1 Rotating Mass Kinematics with a Combined Wave 67
4.2.2 Nonlinear Dynamics 69
4.2.3 Dynamic Model of Underactuated Rolling System 69

4.3 Inverse Dynamics and Singularity Regions of the Rolling System . . . 71

4.4 Simulation Analysis of the Rolling System 79

4.5 Analytical and Simulation Studies for the Planar Manipulator 81
4.5.1 Analytical Study of Minimum Inertial Condition 82
4.5.2 Simulation of the Feed-Forward Control 84

Chapter 5 A Darboux-Frame-Based Approach for Path Planning of Spin-Rolling Sphere on Plane 87

5.1 Introduction 87

5.2 Kinematic Model of a Moving Darboux Frame 88

5.3 Path Planning 94
5.3.1 Problem Statement 95
5.3.2 Geometric Control by Virtual Surface 99

5.4 Motion Planning Algorithm . . . 103
5.4.1 Iterative Tuning Algorithm . . . 103
5.4.2 Global Convergence of Algorithm . . . 111

5.5 Results and Discussion . . . 112

Chapter 6 Conclusion . . . 119

6.1 Summary of Dissertation . . . 119

6.2 Future Works . . . 123
6.2.1 Fluid-Actuated Spherical Robot . . . 123
6.2.2 Underactuated Systems without Inertial-Coupling Singularities 123
6.2.3 Darboux-frame-based Parametrization and Planning Challenges 124

Appendices . . . 126

Appendix A Singularity-Free Model Derivations . . . 127

A.1 Planar n-DoF Underactuated Manipulators . . . 127

A.2 Wave on the Trajectory of the Rotational Joints . . . 128
A.2.1 Kinematics of Small-Amplitude Wave . . . 128
A.2.2 Lagrangian Dynamics of the Manipulator . . . 131

A.3 The Dynamic Model of 4-DoFs Underactuated Manipulator . . . 133

A.4 Design of Small-Amplitude Waves on Rotational Joints . . . 136
A.4.1 Singular-Free Model of the underactuated manipulator . . . 136
A.4.2 Feed-Forward Control for Active Joints . . . 140

A.5 Dynamics of the 4-DoF Manipulator . . . 142

Appendix B Geometric Path Planning . . . 146

B.1 Moving Darboux Frame Preliminaries . . . 146

B.2 Proof of Darboux Frame Kinematics with Sandwiched Virtual Surface 147

B.3 The Curvatures Variation in a Given Direction . . . 150

B.4 Controllability of the Darboux Frame-Based Kinematic Model . . . 152

B.5 Geodesic Torsion Design of the Virtual Surface . . . 155

B.6 Phase I Directional Update . . . 156

B.7 Proof of Closed Set . . . 159

Bibliography **160**

Published Peer-Reviewed Papers **170**

List of Tables

2.1 Nomenclature. 16

2.2 Parameters of the designed IDU. 27

2.3 Setup variables of the robot dynamics. 34

2.4 Parameters of the robot. 45

4.1 Value of parameters for the simulation studies. 79

4.2 Chosen parameters for the analytical studies of a 4-DoFs underactuated manipulator that fails the Strong Inertial Coupling condition. 82

A.1 Singular configurations that have be satisfied due to the inertial coupling [97]. 135

List of Figures

1.1 Example underactuated systems: a) the bird wing [27], b) Pendulum-actuated rolling robot [5, 51, 68], c) Manipulators with passive joints [89] d) Dexterous manipulation with fingertips [32, 35]. . 2

1.2 History of proposed different internal mechanisms for actuating spherical bots with solid shell. 3

2.1 Proposed fluid-actuated spherical robot. 14

2.2 The rolling robot with introduced basic vectors. 15

2.3 Schematic of the fluid actuated mechanism. 20

2.4 The structure of the linear actuator and the connected cylinder. The torque is carried through rotating body to move the joint that is connected to the cylinder rod. 21

2.5 The acting forces on the rotating core at pipe A. In here, $\mathbf{F}_B$, $\mathbf{F}_D$, $\mathbf{F}_W$, $\mathbf{F}_f$ and $\mathbf{F}_d$ are the buoyancy, drag, weight, surface friction, and the dynamic pressure forces, respectively. Also, N and $N+1$ are the connecting ports to provide the liquid circulation with a single fluid actuator. 24

2.6 The fluid pressure and velocity from the cylinder tank to the main pipe with different input torques. 29

2.7 The core locomotion and velocity results with inclusion of the critical input torque T_{cr}. 29

2.8 The IDU simulation results with different piston diameter D_L. 30

2.9 The pressure difference of the main pipe in the transition cycles of the cylinder versus different diameter D_L. Note that the blue graph shows the transition of cylinder tank with bore area A_{CL}^U to the covered plunger area A_{CL}^L. The red graph happens for the opposite process of the green one. Blackline refers to D_L with the reference value in Table 2.2. 31

2.10 The input port pressure of the main pipe, the rotating core position and velocity for various fluids. 33

2.11 The position and velocity of the sphere and the core in the first simulation case. 35

2.12 The location of the core on sphere with respect to the base frame Σ_I in first simulation case. 36

2.13 The position and velocity of the sphere and the core in the second simulation case. 36

2.14 The location of the core on sphere with respect to the base frame Σ_I in second simulation case. 37

2.15 Maximum sphere displacement and velocity for different mass ratio within constant input torque range. 38

2.16 Minimum force for rising core to zenith point of sphere with different mass ratio. 39

2.17 Cost of transport (COT) verses sphere linear velocity, V_o. . . . 41

2.18 Power consumption of motor and circulating fluid for two patterns of sphere motion. 42

2.19 Two-phased motion of the rotating core with using the defined Beta function. 43

2.20 Results of inverse dynamics in simulation of the first case. . . 46

2.21 The core location and velocity respect to base frame in first case. 46

2.22 Results of the inverse dynamics in simulation of the second case. 47

2.23 Core location and velocity respect to base frame in second case. 47

2.24 Example simulation to compute maximum amplitude change $\Delta\dot{\theta}$ for the case that the core states are specified. 48

2.25 a) Velocity fluctuation of carrier state when core states are given, b) Velocity fluctuation of the core when carrier states are given. 49

3.1 Experimental setup and frame transformations. 53

3.2 Schematic and magnetic flux map for the considered tracking carrier sensor. 54

3.3 Structure of the filter in estimating the state vector $\mathbf{x}$ and covariance matrix $\mathbf{P}$. 56

3.4 Experimental results of the proposed filter. a) Obtained results of the IMU for the moving core S_c, b) Obtained results of the IMU for the tracking carrier S_t with the on-board permanent magnet. 61

3.5 Evaluation of the system with external disturbances for the case C and D. 62

3.6 Orientation estimation means errors with different case studies. Case A is the motion tracking with normal angular speeds. Case B is the fast angular speed of the sensors. Case C has an external disturbance from an equally located DC motor. Case D has an external disturbance from a heater gun with the same position as Case C. 63

3.7 Example comparison between the core and tracking carrier IMU sensors when external disturbances are included. Note that the dashed and solid stand for the magnetic fields when there are no external disturbances and there are external disturbances. Also, this is recorded by the DC motor case (case C). 64

4.1 a) A rotating mass with the trajectory of a sine wave (blue color) on a circle with radius r (black dashed line). b) Rolling carrier motion along y axis and frame transformations. 68

4.2 Different mass-rotating systems with passive body/carrier that their inertial matrices $\mathbf{M}(\boldsymbol{q})$ are primarily similar. 69

4.3 Singularity regions in gray color increases as mass-point distance r decreases while the carrier is steady ($\theta = 0$). 73

4.4 Example simulation for passive carrier $\{\theta, \dot{\theta}\}$ and rotating mass-point $\{\gamma, \dot{\gamma}\}$ states by the modified model. 79

4.5 a) Inertia term and output torque results for modified inverse dynamics, b) the true location and velocity of the rotating mass respect to reference frame. 80

4.6 Compared results for a classic (conventional) and modified motion equations in a pendulum system with the inertia tensor I_c. 81

4.7 The minimum inertia verses manipulator configuration for singular-free regions. 82

4.8 The minimum inertia verses manipulator configuration for singular free-regions ($a_2 = 0.011$ case). 83

4.9 Angular displacements of joints for an example simulation. . . 84

4.10 Angular velocities of joints for an example simulation. 85

4.11 Active joints' torque outputs for a desired configuration. . . . 85

5.1 Kinematic model of rotating sphere. Note: ψ is the spin angle between sphere and plane surfaces. 89

5.2 Frame transformations of the spin-rolling sphere on a moving frame Σ_f. Note that n superscript in $\{\boldsymbol{e}_1^n, \boldsymbol{e}_2^n, \boldsymbol{e}_3^n\}$ frame stands for the sphere ($n = o$), the plane ($n = s$) and the virtual surface ($n = v$). 90

5.3 Statement of planning problem while the sphere with contact path of $\mathbf{L}_o$ follows a straight path $\mathbf{L}_s$ on plane. 95

5.4 Limit of minimum distance d that is required to reach desired ψ_f. Note that G_f shows the desired goal angle on plane. . . . 96

5.5 Normalized minimum distance d/R_o for different desired angles where $u_{o,f} \in [0, \pi]$ and $v_{o,f} = 0.01$. 98

5.6 Geometric shape of the used virtual Surface U_V. Note: Green and blue surfaces are for $R_t = 0$ as the sphere and $R_t = R_v$ as the helicoid. 100

5.7 Design of the arc-length-based inputs by using desired virtual surface. Note that schematic is drawn for $u_o = 0$. 100

5.8 R_i determination by incircle of u'_o. 102

5.9 The flowchart of planning algorithm. 104

5.10 Manipulation of the rope-like $\mathbf{L}_o$ curve with the designed virtual surface.Note that following curves are obtained by using formulas in Phase I for ψ_q and δ in Eq. (5.28) and (5.29). . . . 105

5.11 Parametrization of the curve $\mathbf{L}_o$ by cutting planes of $u_{o,f}$ and $v_{o,f}$. 106

5.12 Simulation results of proposed approach for a case study with $\{u_{s,f}, v_{s,f}, u_{o,f}, v_{o,f}, \psi_f\} = \{3, 3.2, -\frac{\pi}{2} - 0.8, 0.8, 0.8\}$ final configuration. 112

5.13 Collected iterations of the given final configuration: 1. The first solution of system ($k = 0$), 2. The first successful results of Phase I, 3. Converging Phase II, 4. The first results before applying Phase III. 113

5.14 Angular velocities of the sphere with the designed arc-length-based based controller. 115

5.15 a) The designed function ω_s in time, b) Smoothed angular velocities of the sphere in two different cases of time scaling T. . 116

5.16 Comparing angular convergence of $\mathbf{\Psi}_f$ at two cases. 117

5.17 The simulation results for having different final spin angles $\psi_f = \{-1.7, 1.3, 2.3\}$. 118

6.1 The limitations of the some well-known driving mechanisms for the rolling robots [5]. 120

6.2 Manipulation with agile fingertips. 125

A.1 General model of the underactuated manipulator. Note that the orange trajectory presents the combined wave trajectory. . 129

A.2 Example mechanism realizations for the wavy displacements of the joints in the cases that $a_k \leq l_k$, a) The trajectory realization with passive mechanical slot. b) The trajectory realization by linear actuator. 130

A.3 4-DoFs underactuated manipulator. 134

A.4 The designed Beta function for the specified passive joints. . . 140

B.1 Two coordinate frames related by φ rotational angle about $\boldsymbol{e}_3$. 146

B.2 Rotating object U_C on the fixed surface U_S with sandwiched virtual surface U_V. Note that n in $\{\boldsymbol{e}_1^n, \boldsymbol{e}_2^n, \boldsymbol{e}_3^n\}$ frame stands for fixed surface (plane) s, virtual surface v and rotating object (sphere) o at each of these compact surfaces. 148

B.3 Sectioned sphere based on the $\mathbf{\Psi}_v$ and $\mathbf{\Psi}_u$ cutting planes for directional updates of ζ_q. Note that $\mathbf{\Psi}_v$ and $\mathbf{\Psi}_u$ are on ϱ_2 and ϱ_3 as an example. 156

Abstract

This dissertation investigates advanced underactuated systems. The underactuated systems have models that their control inputs are fewer than the states (configuration variables). Although this characteristic might be seen as a drawback due to control and application challenges, it has been observed that they are part of nature in the dynamical model of animals and humans including their locomotion. A living example in nature for an underactuated mechanism is the bird's wing that the elastic ligament connection between feathers and skeleton creates a direct control of wing by using wrist and finger motion of the bird. In robotics, underactuated mechanisms can save the actuator's space and power. Also, they can result in optimal and complex motions which is a well-known theoretical challenge in the field of control and robotics. These models can be seen in large numbers of problems. The object manipulation with fingertips (Dexterous manipulation), the rolling robots with rotational mass actuators, certain motions of the legged robots, and even in simple car parking problems are some of these examples.

In this dissertation, our studies are mainly focused on the underactuated rolling systems, however, certain studies aim for broader applications in the field of robotics and control. Part of this study is focused on a novel fluid-actuated rolling spherical robot. The proposed rolling robot works by rotating spherical masses (cores) inside the pipes. In order to push the core, the fluid-actuated mechanism circulates the fluid inside the considered pipe models. After the analytical and performance studies for the underactuated rolling robot, we propose a motion control strategy by using the inverse dynamics of the system.

Next, the fluid-actuated mechanism requires to have a motion tracking of the rotating spherical masses (cores) in pipes. Therefore, a general complementary filter is designed to do the motion tracking of the core by inertial measurement unit under the ferromagnetic effects. Experimental studies take place by comparing the performance of the proposed filter to the well-known QUEST filter. This proposed tracking mechanism with the designed compensatory filter can be used to develop suitable feedback

control strategies for the rolling robot. More importantly, this work shows a new and general observation that using onboard permanent magnets can shield different magnetic disturbances with proper filter design in robots and actuators.

Our studies are continued with a focus on the control problems related to inertial-coupling at underactuated robots. We present a general solution to prevent singularities that exist in the inverse of inertial matrices. The method is applying small-amplitude waves on the rotating mass trajectories. After deriving inverse nonlinear dynamics with combined wave kinematics, we design conditions for the waves parameters to avoid these configuration singularities. Furthermore, the configuration singularities in the mass-rotating rolling systems due to inertial-coupling are presented for the first time. The singular-free model is analyzed for the underactuated rolling systems as well as underactuated planar manipulators.

Finally, a novel geometric-based motion planning is introduced for the spin-rolling sphere with three rotational degrees-of-freedom on a plane. This particular problem has an underactuated model. We use the Darboux Frame kinematics and develop an arc-length-based control strategy. The aim is to create smooth and realizable trajectories for converging the full-configuration of the overall system. Also, the motion of the spin-rolling sphere is planned by following the shortest optimal trajectory on the plane. We illustrate our motion planning strategy in certain simulation studies. This planning approach is intended to be used for the proposed spherical robot but it can be extended to Dexterous manipulation and other mechanics that spin-rolling motion can be realized. This newly proposed geometric planning based on the Darboux Frame can be extended for 2D manifolds with arbitrary surfaces.

Acknowledgements

First and foremost, I would like to especially thank my advisor, Prof. Mikhail Svinin. His advice and continues support during my studies essentially helped me to shape my ideas at the academic level. I can't thank him enough since his academic assist before my Ph.D. studies is the main reason for pursuing my Ph.D. at Kyushu University.

I would like to thank, Prof. Motoji Yamamoto as my Ph.D. supervisor, who gave me insightful comments regarding my research objectives. He supported me in my researches and study.

I would like to sincerely dedicated this work to my advisor, Prof. Esmaeil Esmaeizadeh. His expertise in fluid mechanics offered me the knowledge to solve problems that I've dealt with in this dissertation.

I would like to thank all personnel and professors in Mechanical Engineering Department, Kyushu University for their support in finishing my studies. In particular, I am deeply thankful to Prof. Kenji Tahara and Assoc. Prof. Yasutaka Nakashima for their constructive comments during group meetings and seminars. Also, I would like to thank Mrs. Oiwa Yasura from the Student Affairs Division, Faculty of Engineering for her help in my university procedures.

In the end, I am incredibly grateful to my parents, my wife, and her parents for their unconditional love and emotional support. I can't forget my wife's, Negar, care and attention during the pursuit of this demanding research career. Also, I like to thank my best friends Pedram and Ata who always boosted my morale in every step of my life.

Chapter 1

Introduction

1.1 Motivation

Robots are getting involved in many different tasks from the industry to exploration and rescue activities. However, there is a great level of unsolved problems that are based on mechanism design and theoretical limitations. As an exquisite example, a disastrous heartbroken earthquake and tsunami in March 2011 at Fukushima, Japan, not only showed despite all of the preparations from an advanced country like Japan, humans are still under great threat coming from natural disasters, but also there are challenges in the robotic field for the rescue and investigation. With this inspiration, many researchers are developing different strategies to tackle the technical and theoretical challenges of mobile robots.

A well-known challenge in the control and robotics field is related to cases when the robot has fewer control inputs than the configuration variables of the overall system. This type of system is called an "underactuated system" [69]. The property of this system becomes physically vivid in mechanisms that have passive bodies without any direct control torques. The underactuation can be seen in a fully-actuated system due to damage to the actuator or physical constraints to the robot, robots lose their direct control on certain actuators. However, apart from this point, designing underactuated mechanisms can have interesting advantages. For example, they can save the actuator's space and power besides producing highly complex locomotion. A living example in nature for an underactuated mechanism is the bird's wing [see a-Fig. 1.1] [27]. The wing has an elastic ligament connection between feathers and the skeleton creates a simple control of the complete wing. This happens by using the wrist and finger motion of the bird. Thus, birds with actuating limited joints, they are able to create different maneuvers by the given wing morphology. By focusing on the robotic mechanisms, underactuated models can be seen in broad numbers of problems such as the rolling robots with rotational mass actuators [5] [see b-Fig.

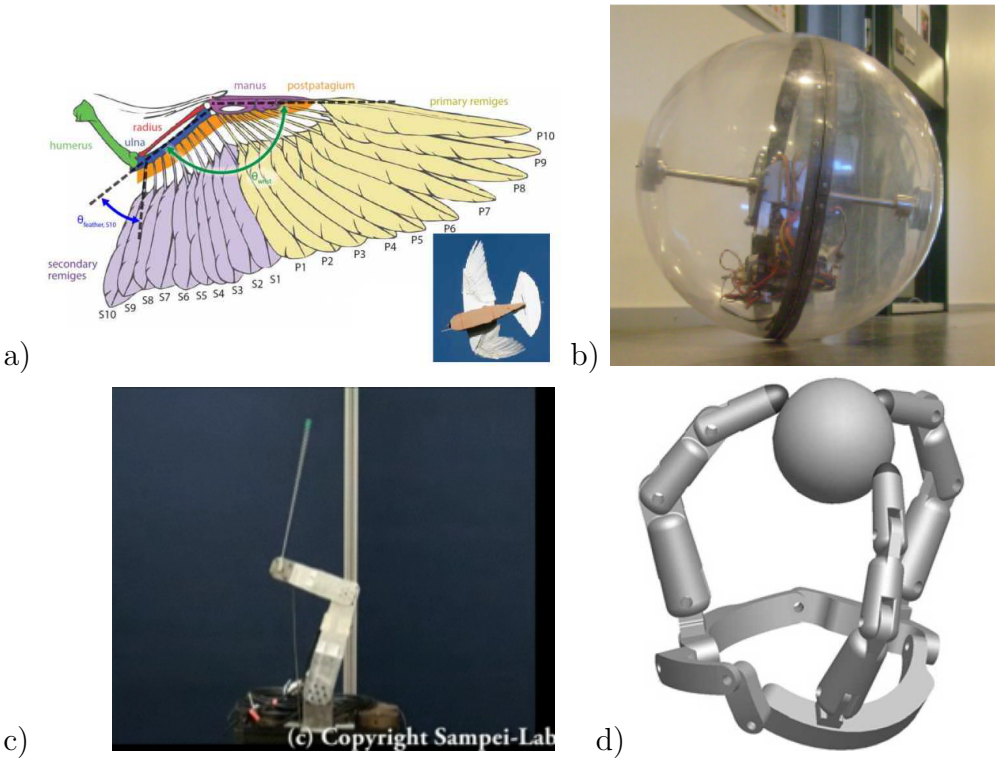

Figure 1.1: Example underactuated systems: a) the bird wing [27], b) Pendulum-actuated rolling robot [5,51,68], c) Manipulators with passive joints [89] d) Dexterous manipulation with fingertips [32, 35].

1.1], manipulators with passive joints [89,95] [see c-Fig. 1.1], the object manipulation with fingertips (Dexterous manipulation) [32, 35, 41, 62, 82] [see d-Fig. 1.1] and even in simple car parking problem.

By having the motivation to underactuated robots the literature review takes place in three main topics. At first, the spherical rolling robots are studied in Section 1.2 that they have different propulsion mechanisms. We will talk about the limitations of the rolling robots with different propulsion systems which include fully and partially actuated mechanisms. Then, we will discuss the control challenges of the underactuated systems (dynamic models of the rolling robots and planar manipulators) in Section 1.3. One of the main issues in the control of underactuated systems is the singularities due to inertial-coupling in inverse dynamics. These singularities are coming from inversed inertial matrices which results in serious limitation for the underactuated robot's controller design. Finally, the problem of motion control is studied for path planning of the spin-rolling sphere. The nonholonomic constraint that is

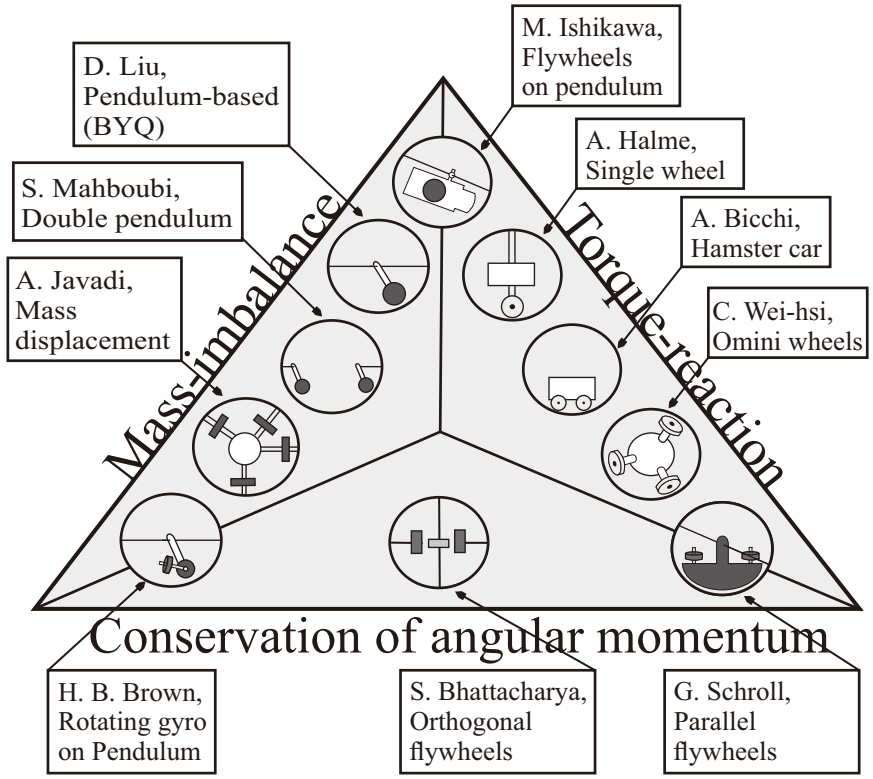

Figure 1.2: History of proposed different internal mechanisms for actuating spherical bots with solid shell.

combined with the underactuated system has been explained in previous studies and existing challenges in Section 1.4.

1.2 Spherical Mobile Robots

Currently, rolling robot's are getting more attention in the field of robotics. In particular, there is an interest in spherical rolling robots. These types of robot can move omni-directionally, and the inner gap of the outer shell provides a secure and safe placement of the actuators [28]. The shell minimizes the risk of a failure due to unstable configurations and robot does not face with complex propulsion scenarios to avoid the risk of damage. Therefore, they can operate in dangerous and chaotic environments in a better and agile way [5]. These strengths make them strong alternative for biologically inspired robots e.g., legged robots, or even wheel propelled robots.

Spherical robots can be divided into three main groups based on their actuation principles [see Fig. 1.2]: torque-reaction, mass-imbalance, and conservation of angular

momentum. Their actuation principles can be under- or fully-actuated mechanisms depending on their structural design.

1.2.1 Torque-reaction

Torque-reaction as the former actuation principle has rolling wheels to create a reactive torque at the inner shell. Haleme et al. [46] proposed a kinematic-based motion control in which the robot had a single direction turning wheel [see Fig. 1.2]. Also, a cart was placed inside the ball-shaped shell that was used as an alternative way to actuate the body [21]. To deal with the unstable cart-based system, a rolling robot can be equipped with omniwheel platforms [58, 121]. For this principle of propulsion, a nonlinear feedback controller inspired by the caterpillar-rolling gait model was applied to manipulate the cart in a spherical shell [31]. It is important to note that actuators realizing the torque-reaction principle [2, 21, 31, 46, 121] take the majority of the physical space inside the spherical carrier.

1.2.2 Mass-imbalance

The mass-imbalance principle was introduced by Javadi for moving the rolling robot named Glory [54]. In this robot, the driving force is created by unbalancing the center of mass (COM) by moving the masses along various axes. NASA researchers developed a spherical rover for outer space explorations named Tumbleweed [15]. Tumbleweed rover can use external wind energy to move via the mass-imbalance. Attaching a pendulum mechanism to change the center of mass was proposed by Liu et al. [68] and Mahboubi et al. [71]. This research was followed by trajectory tracking studies [8, 116] and relevant model design and simulations [64, 65]. These mechanisms have been developed for propelling the masses directly with gearboxes, which limit the spherical carrier velocity. Different control strategies for systems using the mass-imbalance were proposed in [25, 48, 53, 59]. Please note that the rolling robots can be implemented as hybrid mechanisms that combine torque-reaction and mass-imbalance driving principles [51].

1.2.3 Conservation of Angular Momentum

Another actuation principle is based on the conserving the angular momentum. A rolling robot with rotating internal gyroscope and two motor drivers for each direction was proposed in [24]. Bhattacharya and Agrawal [20] proposed a perpendicular pair of rotors to move the carrier body. A different design is reported in [22]. A hybrid robot that utilizes both the conservation of angular momentum and the reaction forces is designed by Schroll [91]. To control, Morinaga et al. [75] applied iterative steering by nilpotent approximations [83] for motion planning. Reduced attitude control of the sphere by three inertia discs was analyzed in [80]. These mechanisms use a physical principle similar to a spinning ice skater; hence, the low produced torque and sensitivity to the external forces are unavoidable.

The torque-reaction-based motion principle mostly requires direct contact with the outer-shell which makes this type fully-actuated in the majority of models [2,21,31,46, 121]. However, the rolling robots actuating by the mass-imbalance and conversation of angular momentum have underactuated models [20,24,51,54,68,71]. These mechanisms mainly do not have any direct input/control on the spherical outer shell which decreases the numbers of control inputs. Based on the aforementioned limitations for each principle of actuation, we observe that there has not been any mechanism that could encompass all the driving principles while it keeps the advantages of each specific method, namely, an isolated driving mechanism, the conservation of power and ability to accelerate/decelerate.

1.3 Inverse Dynamics in Underactuated Systems

Industrial machines and robots perform different tasks that require an accurate mathematical model of their system. In particular, underactuated mechanisms are getting more attention in this field due to their advantages [69]. Physically, a system is underactuated when the number of control inputs is less than the states related to the configuration variables. These systems with a promise in saving actuator numbers, power, and producing complex locomotion have serious challenges. For example, there are singularities in their inverse dynamics due to inertial coupling [97,113] which makes it harder to have accurate and continuous control strategies. This general issue

is predominant in underactuated rolling robots and manipulators.

In principle, the inverse dynamics can be described by inverting the inertia matrix and its sub-matrices in differential equations to obtain the torque of active joints as output. Also, the inverse of inertia matrices is required to solve the state equations [1] or control the underactuated systems [97, 115]. Thus, we can generalize the primary source of singularity to the inversed inertial matrix or its sub-matrices. These singularities can be found in the middle of configuration or certain neighborhood regions. In this neighborhood, the integration of a joint angle creates enormous changes. These large errors directly transferred to active joint torques where they are not physically able to be realized. [1] presented this problem in mass-point manipulators. The integration of differential equations in modeled manipulators was breaking if there were singular configurations in the inverse dynamics.

Initial studies for underactuated mechanisms started by the proposed robots as Pendubot [99] and Acrobat [98]. These two-link manipulators had one active and one passive joint without the control input. The inverse dynamics are described by inversing the inertial sub-matrices to obtain torque of active joints as output. [4] also showed that the inverse dynamics model in a 2 degree-of-freedom (DoF) underactuated manipulator contains the singular configurations that the constraint equation imposes from the passive body. As explained before, when the robot reaches the singular configuration control torque converge to infinity and this issue limits the domain of the control. Next, [97] proposed a strong inertial coupling condition for the underactuated mechanical system using the positive definiteness of the inertia matrix. This condition grants a singular free inverse dynamics for certain geometric properties at a 2-DoF Pendubot. This singularity problem was dominant in the non-collocated linearization method to control the passive primary joint [98]. In general, these mathematical singularities that originate from the inversed terms of the inertia matrix limit the mechanism to certain geometric parameters. Then, a coupling index was shown for different geometric parameters in underactuated manipulators [18]. This property was expressing the actuality of this system in different configurations. It is important to note that inertial coupling becomes more challenging to deal with when the number of passive joints increases to more than one. This issue is one of the main reasons that manipulators with multiple passive joints are not covered in

the literature. Additionally, the inertial-coupling problem was highlighted and control strategies were developed relative to this limitation for underactuated spherical robots [3,104]. Also, because the spherical carrier requires consecutive rotations without any angular limitations, the singularities due to inertial coupling become more challenging to deal with. However, a more insightful study is required to understand the root of the problem of developing an effective solution.

It is clear from previous studies that limiting the geometric parameters or the configuration of the robot due to inertial coupling (Refs. [18, 97] showed inertial coupling for 2-DoF linked systems) is not sufficient and practically acceptable. The problem becomes much harder to deal with in n-DoFs underactuated mechanisms with more than one constraint equations e.g., multi-DoFs manipulators with more than one passive joints.

1.4 Non-holonomic Path Planning of a Spin-rolling Sphere

Sphere is a unique geometrical object that can be visualized as a fingertip [32,35,41, 62,82], a convex object [38,44,102] or a rolling robot [2,43,52,55,107]. Manipulation of this sphere into the desired configurations is an open problem in the fields of control and robotics. Interestingly, path planning for a spin-rolling sphere on a plane with underactuated model is mostly untouched in the literature.

In the kinematics of the rolling contact, the pure-rolling motion has 2 degrees of freedom that the instantaneous rotation axis is located at the contact point. This axis is always parallel to the common tangent plane of two surfaces e.g., sphere and plane. However, spin-rolling motion, also known as twist-rolling, has 3 degrees of freedom with a similar instantaneous rotation axis that passes contact point. Also, its axis can be in any arbitrary direction because the spinning motion is normal to the rolling axis.

From a physical point of view, it is known that spin-rolling motions are possible to be realized in the mechanical systems which the Gimbal mechanic is the classic example. For example, if we imagine the fingertip of the hand like a hemisphere, angular spinning can be achieved by wrist rotation [32]. Another example is rotating the spherical object in multiple directions with control of the fingertips sometimes called as dexterous manipulation [35,62,82]. Also, there are mechanical actuators with

3 or more degrees of freedom in realizing spin-rolling motions which are developed for spherical mobile robots [2, 52, 107] and Ballbots [43, 55]. In particular, spherical robots can rotate multiple masses or use different cart-based actuators inside their shell to create spin-rolling locomotion. Additionally, rotating spherical particles have broad applications in the field of nano and micro manipulations [38, 44, 102].

In the conventional pure rolling, the sphere rotates with two degrees of freedom considered a ball-plate problem [56, 72]. Because the ball is sandwiched between a moving plane and the ground, the system binds with spinning constraint. Basically, the ball-plate definition doesn't fit the spin-rolling case when there is spinning around the perpendicular axis of the surface plane. Thus, our study excludes mechanisms that manipulate convex objects e.g., sphere, by planes [72,93] since rotating the plane around its normal axis cannot spin the sphere physically. To deal with this issue, Kiss et al. [62] proposed a kinematic model with three independent planes to manipulate the sphere, and controlled the relative angles by ignoring the plane configuration. Also, Date et al. used the advantage of spinning in an indirect way [37]. Their designed algorithm was shifting the coordinate of the actuating plane in iterations with respect to different base frames which was, in a sense, utilizing a third rotational virtual center. However, time scaling with the included coordinate transformation of the kinematic model can result in uncontrollable states [84]. Also, the practicality of the approach was not discussed for realizing the proposed virtual center by different propulsion mechanisms.

On the other hand, the Montana kinematic model [74] illustrated that spinning can be included in the rolling sphere on the surface. It is also clear that having one more input (spinning or twist) makes the kinematic model 5×3 which increases the level of accessibility in the given system. However, spinning of the rolling object creates a certain complexity because the spin angle changes all the rotational states. This new system leaves the conventional planning in geometric phase shifting [56, 66, 79, 106] hard to be applied.

Apart from spin-rolling motion, finding an optimal solution has serious challenges when reaching the sphere to its final states are desired. This issue becomes harder to achieve as smooth trajectories are required for the realization of a considered dynamical system. In literature of the pure rolling, different feed-forward [3, 36, 56]

and feedback control [37,78,84] methods were utilized. For example, Arthurs et al. [7] and Jurdjevic [56] proposed planning approaches based on the optimal control theories which feasibility of them was not tested. As an alternative, to stabilize the ball-plate system without a differentially flat model, iterative steering was formulated by Oriolo and Vendittelli [84]. Nevertheless, the solutions had serious fluctuations as trajectories converge to the desired states. Thus, their created trajectories were not easy to be realized by dynamical systems [76] and there are singularities in different regions of spherical manifold due to the locality. Beschastnyi [19] studied the optimality problem of the rolling sphere with twisting (spinning) on the plane. Certain extremal trajectories were parametrized, and their cut times were estimated for optimality. It was proposed that Maxwell time can be determined while the sphere follows the straight path for the optimal solution. Note that this research did not cover the control problem for arbitrary desired states.

1.5 Contributions

The main contributions of this work is an insightful study of underactuated mechanisms design and finding solutions for some of the theoretical challenges in these models. Indeed, previous studies took place for mechanism design, in particular spherical rolling robot [5], and developed different control strategies for underactuated robots [69], however, we take a look at certain problems from a different perspective and introduce a new planning problem.

We can list contributions as follows:

• We present a novel fluid-actuated rolling robot with an insightful study of literature in Section 1.2. After modeling the complete robot, its performance is studied analytically. This robot is propelled by rotating spherical masses (cores) inside designed circular pipes. This robot is able to encompass mass-imbalance and conservation of the angular momentum principles of actuation. Then, an inverse-dynamics based method is developed to control this underactuated robot.

• A sensor fusion filter is developed for motion tracking of the inertial measurement unit with onboard ferromagnetic materials. This was aimed to experimentally track the rotating core inside pipe for our previously proposed rolling system. However, we extend the study to verify this method for all the inertial measurement units under

soft and hard ferromagnetic materials effects. This tracking sensor can be used in developing a proper feedback control strategy to do motion tracking for the rolling robot under perturbations. Additionally, we show an observation that proper filter design with attached permanent magnetics, these magnets can work as a shield toward magnetic disturbances for improving motion tracking in robots and mechanisms. Also, the proposed filter was compared with the well-known QUEST filter [33, 73] for its performance.

• Next, we show a solution for avoiding inertial-coupling singularities in underactuated rolling robots and planar manipulators. The inverse of the inertial matrix is required to compute inverse dynamics or apply different control strategies [115]. However, underactuated mechanisms face geometric and configuration constraints due to existing singular configurations. We propose small-amplitude wave kinematics on the trajectory of mass-rotating bodies (active joints) to prevent inertial-coupling singularities. We check our approach for both underactuated rolling systems and multi-DoFs manipulators with more than one passive joints. In addition, we demonstrate that this predominant in the rolling system.

• Finally, a new Darboux-Frame-Based path planning strategy is developed for a spin-rolling sphere on the plane in kinematic level. This underactuated model is hardly studied in literature due to the challenges in planning the spin angle of the sphere [19] since it changes all the angular states. This makes the conventional path methods impractical for this problem [56, 66, 79, 106]. In our proposed geometric method, the sphere is able to follow the shortest path on the plane while the sphere has smooth and realizable. Since our geometric method was coordinate- and time-invariant, we were able to realize the obtained paths in different desired angular velocities. This method can be applied for planning the rolling robots and spherical particles as well as Dexterous manipulation problems e.g., box manipulation with fingers. By utilizing the Darboux-Frame-based model and solving it together with dynamics model a trajectory tracking strategy can be developed to realize the path planning approach for different mechanics.

1.6 Dissertation Outline

The Chapter 2 of the dissertation starts with introducing a novel fluid actuated rolling robot. After explaining the designed robot, rigid body dynamics are derived through the D'Alembert principle, and we find the driving mechanism's model. Then, the driving mechanism and rolling robot are studied analytically. Next studies are related to performance studies of this rolling robot. Finally, we propose a feedforward control strategy using inverse dynamics.

We begin studies on the sensor design of our proposed rolling system in Chapter 3. Because the proposed driving unit is novel, we propose a sensor tracking mechanism to track the core that rotates in the pipe. This tracking sensor lets us know the angular position of the rotating mass (core) in the pipe. This helps to develop proper feedback control strategies to control the rolling robot toward desired configurations under the perturbations. Next, a new motion tracking filter is developed based on the Kalman filter under ferromagnetic material effects. With observations from our experiments, we verify the performance of the new filter that does sensor fusion via an inertial measurement unit. Also, we explain how proper filter design with on-board ferromagnetic materials (magnets are for tracking the rotating core in the pipe) can work as a magnetic shield toward external disturbances.

In our early studies in Chapter 2, we observed that singularities in the inverse dynamics of underactuated rolling robots can create serious limitations for controlling. In Chapter 4, we introduce a solution for inertial-coupling singularities as one of the serious challenges in underactuated robots. We start by applying small-amplitude waves on the rotating mass kinematics. Next, the nonlinear dynamics of a general mass rotating rolling robot is derived. We demonstrate how a singular-free inverse dynamics can be obtained after explaining the singular configurations of the rolling systems. Also, we extend our solution for planar underactuated multi-degrees-of-freedom manipulators and studied the solution analytically.

Chapter 5 introduces a new geometric path planning approach for a spin-rolling sphere on a plane. The proposed spin-rolling sphere apart from its new deriving mechanism, its 3-DoFs rotational degree limits the conventional methods to be applied for planning. This nonholonomic path planning problem requires a different approach to have smooth and realizable trajectories which we propose in this chapter. At first,

the new Darboux Frame kinematics for the spin-rolling sphere on a plane is developed. Before explaining the constraints of this planning, we describe the path planning problem for the derived Darboux-Frame-based kinematic model and our objectives. Next, a virtual surface as a geometric controller is designed to converge the system to desired states. Additionally, we show our simulation results and capabilities of this proposed approach.

Chapter 6 is our final chapter where we conclude our findings and explains remaining open-problems and future works.

Chapter 2

Design and Analytical Studies on Novel Fluid Actuated Spherical Mobile Robot

2.1 Introduction

In this chapter, we analyze a novel underactuated spherical mobile robot. This rolling robot has two spherical masses moving inside two perpendicular circular pipes. Masses rotations create the required force to move the spherical robot based on the mass-imbalance. The driving force of rotating masses is generated by the internal driving unit (IDU) which circulates the incompressible fluid via a moving cylinder. The cylinder is connected to a linear actuator for controlling the injected fluid volume. Also, we propose a feed-forward control strategy for its planar locomotion through the inverse dynamics.

Our main contribution in this chapter is to propose a first driving unit that uses fluid actuation for rolling robots. We analyze the performance of the proposed driving unit analytically. Also, a nonlinear feed-forward control strategy is applied to control this system.

The novel rolling robot is proposed with the aim to overcome different limitations that previously designed mechanisms have in rolling robots as described in Chapter 1. The proposed robot is considered to encompass the majority of the driving principles without overusing the rolling robot's inner space. This issue was challenging in actuation principles of the torque-reaction-based and mass-imbalance. Also, we wanted to propose a driving mechanism that its DoF can easily be extended. As another advantage, the fluid in the driving unit will work as a mediator which will result in smooth and safe locomotion. Based on the literature, it is clear that every driving principle has particular advantages where we want to achieve them in this particular rolling robot. We believe this will increase the application ranges in rolling robots.

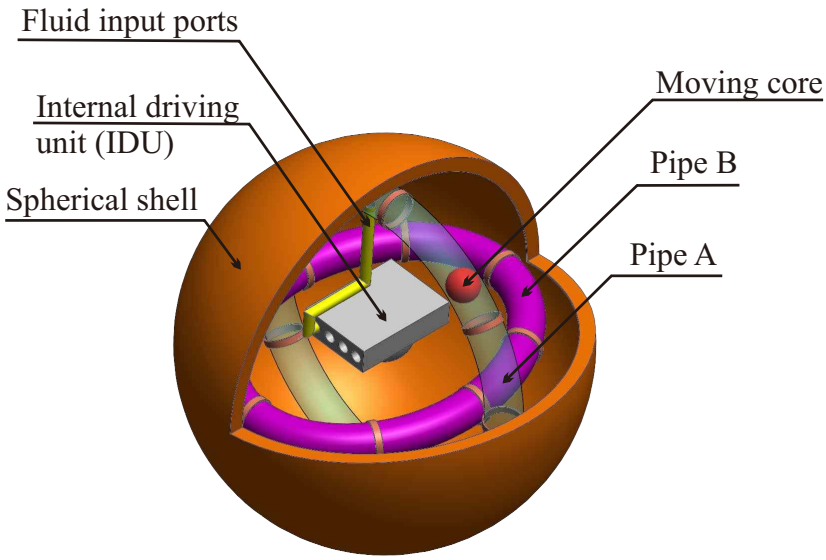

Figure 2.1: Proposed fluid-actuated spherical robot.

The chapter is organized as follows. In Section 2.2, we describe the main components of the proposed robot and derive its rigid body dynamics from the D'Alembert principle. In Section 2.3, the IDU is introduced. In Section 2.4, the performance of the IDU is assessed with respect to three critical parameters namely torque reliance, cylinder tank volume, and fluid characteristics. Also, the performance of the whole robot is then verified under simulations, which include its dynamic model and the IDU model. Next, we do parametric evaluation by mass-ratio of core-sphere design and robot's cost-of-transport (COT) in Section 2.5. Final Sections 2.6-2.7, we propose a feed-forward control based on inverse dynamics and study our simulated results.

2.2 Robot Feature and Rigid Body Model

2.2.1 Structure and Components of Rolling Robot

The outer cover of the rolling robot is a spherical plastic shell. We have two circular pipes, made from a solid material, e.g., acrylonitrile butadiene styrene, that are attached to the inner surface of the sphere. In the initial configuration, pipe A is placed vertically and pipe B is placed horizontally perpendicular to pipe A as shown in Fig. 2.1. For preventing the intersection of two pipes, the radius of pipe B is chosen smaller than that of pipe A. Two spherical masses (cores) are placed inside these

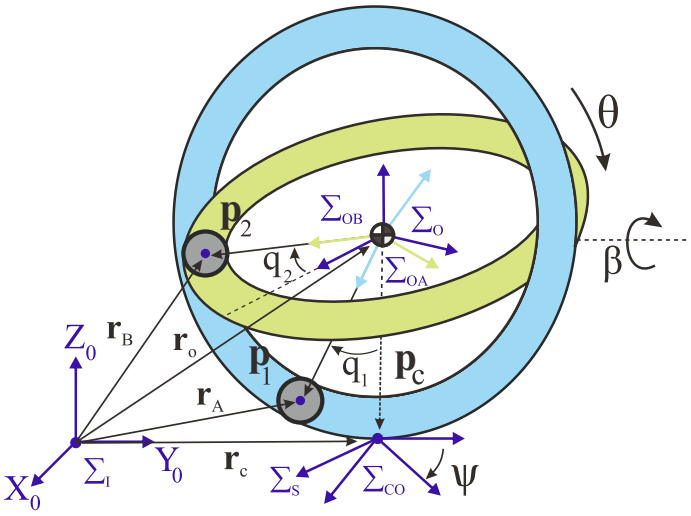

Figure 2.2: The rolling robot with introduced basic vectors.

circular pipes to propel the robot. The internal driving unit (IDU) is located at the center of the spherical shell. The IDU is producing the driving forces for moving the rotational masses (cores). This IDU circulates an incompressible fluid in the pipes through the input ports (injection line pipes). It works with cycles and it is connected to different parts of the pipes.

2.2.2 Rigid Body Dynamics

To obtain the nonlinear dynamics of the robot's rigid body, we use the geometric description shown in Fig. 2.2. Here, Σ_I represents the inertial frame. The moving frame connected to the center of the sphere is denoted as Σ_O. The contact coordinate frame on the plane is denoted as Σ_{CO}. Also, Σ_{OA} and Σ_{OB} are the rotating cores' A and B coordinate frames with respect to the sphere center Σ_O. Table 2.1 shows all the variables used in describing the kinematics of the rolling robot.

The position of contact point $\mathbf{p}_c$ with respect to Σ_O is given as

$$\mathbf{p}_c = \mathbf{R}_y(u_{co})\mathbf{R}_x(v_{co}) \begin{bmatrix} 0 \\ 0 \\ -R \end{bmatrix} = R \begin{bmatrix} -\sin u_{co} \cos v_{co} \\ \sin v_{co} \\ -\cos u_{co} \cos v_{co} \end{bmatrix}, \tag{2.1}$$

where R is the outer radius of the spherical shell and $\{u_{co}, v_{co}\}$ are the angles that describe the contact point on the sphere. By introducing the relative spinning angle

Table 2.1: Nomenclature.

θ, β, ψ	Orientation angles of the sphere with respect to X-, Y- and Z-axes
q_1, q_2	Rotation angles defining the position of the cores in A and B pipes
Ω_x, Ω_y, Ω_z	Angular velocities of sphere
r_1, r_2	Distances from the center of cores to the center of sphere
$\mathbf{r}_A, \mathbf{r}_B$	Positions of the cores with respect to Σ_I
$\mathbf{r}_o$	Position of the center of sphere Σ_O with respect to Σ_I
$\mathbf{r}_c$	Position of the contact point with respect to Σ_I
$\mathbf{p}_1,\ \mathbf{p}_2$	Positions of cores A and B with respect to Σ_O
$\mathbf{p}_c$	Position of the contact with respect to Σ_O
$\mathbf{V}_o,\ \boldsymbol{\Omega}_o$	Linear and angular velocities of the sphere
$\mathbf{V}_A,\ \mathbf{V}_B$	Linear velocities of the cores in pipes A and B with respect to Σ_I
$\boldsymbol{\Omega}_A,\ \boldsymbol{\Omega}_B$	Angular velocities of the cores in pipes A and B with respect to Σ_I
$\delta\pi_A$, $\delta\pi_B$	Infinitesimal rotations of cores with respect to Σ_I
$\delta\pi_o$	Infinitesimal rotation of the sphere with respect to Σ_I
$\delta\pi_1$, $\delta\pi_2$	Infinitesimal relative rotations of the cores with respect to Σ_O

ψ, the orientation matrix of the sphere with respect to Σ_I is constructed as $\mathbf{R}_o = \mathbf{R}_z^T(\psi)\mathbf{R}_x^T(v_{co})\mathbf{R}_y^T(u_{co})$. Now, the contact kinematic model of the sphere and plane can be expressed by Montana's equation as follows [103]

$$\begin{bmatrix} \dot{u}_{cs} \\ \dot{v}_{cs} \\ \dot{u}_{co} \\ \dot{v}_{co} \\ \dot{\psi} \end{bmatrix} = \begin{bmatrix} 0 & R & 0 \\ -R & 0 & 0 \\ -\sin\psi/\cos v_{co} & -\cos\psi/\cos v_{co} & 0 \\ -\cos\psi & \sin\psi & 0 \\ -\sin\psi\tan v_{co} & -\cos\psi\tan v_{co} & -1 \end{bmatrix} \begin{bmatrix} \Omega_x \\ \Omega_y \\ \Omega_z \end{bmatrix}, \tag{2.2}$$

where u_{cs} and v_{cs} are the coordinates of the contact point in the contact plane, and $\Omega_x, \Omega_y, \Omega_z$ are the components of the angular velocity of the sphere in projections onto the inertial frame.

The positions of the cores, $\mathbf{p}_1$ and $\mathbf{p}_2$, with respect to Σ_O are defined as

$$\mathbf{p}_1 = \begin{bmatrix} 0 \\ -r_1\sin q_1 \\ -r_1\cos q_1 \end{bmatrix},\ \mathbf{p}_2 = \begin{bmatrix} r_2\sin q_2 \\ r_2\cos q_2 \\ 0 \end{bmatrix}, \tag{2.3}$$

where r_1 and r_2 are the distances from the center of the cores to the center of the sphere, and q_1 and q_2 are the angles of the cores in pipe A and pipe B, respectively. It is assumed that in the frame Σ_O the cores rotate, respectively, along the unit vectors

$\mathbf{e}_1 = [1,0,0]^T$ and $\mathbf{e}_2 = [0,0,1]^T$. The kinematic equations that describe the motion of the cores in pipes A and B with respect to inertial frame Σ_I can now be presented as follows:

$$\begin{aligned}
&\delta\pi_A = \delta\pi_o + \delta\pi_1,\ \boldsymbol{\Omega}_A = \boldsymbol{\Omega}_o + \boldsymbol{\Omega}_1 \\
&\dot{\boldsymbol{\Omega}}_A = \dot{\boldsymbol{\Omega}}_o + \dot{\boldsymbol{\Omega}}_1 + \boldsymbol{\Omega}_o \times \boldsymbol{\Omega}_1, \\
&\dot{\mathbf{V}}_A = \dot{\mathbf{V}}_o + \dot{\boldsymbol{\Omega}}_A \times \mathbf{p}_1 + \boldsymbol{\Omega}_A \times (\boldsymbol{\Omega}_A \times \mathbf{p}_1)\,,
\end{aligned} \tag{2.4}$$

$$\begin{aligned}
&\delta\pi_B = \delta\pi_o + \delta\pi_2,\ \boldsymbol{\Omega}_B = \boldsymbol{\Omega}_o + \boldsymbol{\Omega}_2, \\
&\dot{\boldsymbol{\Omega}}_B = \dot{\boldsymbol{\Omega}}_o + \dot{\boldsymbol{\Omega}}_2 + \boldsymbol{\Omega}_o \times \boldsymbol{\Omega}_2, \\
&\dot{\mathbf{V}}_B = \dot{\mathbf{V}}_o + \dot{\boldsymbol{\Omega}}_B \times \mathbf{p}_2 + \boldsymbol{\Omega}_B \times (\boldsymbol{\Omega}_B \times \mathbf{p}_2)\,,
\end{aligned} \tag{2.5}$$

where the parameterizations of the virtual displacement are $\delta\pi_1 = \mathbf{e}_1\delta q_1,\ \delta\pi_2 = \mathbf{e}_2\delta q_2$, $\boldsymbol{\Omega}_1 = \mathbf{e}_1\delta\dot{q}_1,\ \boldsymbol{\Omega}_2 = \mathbf{e}_2\delta\dot{q}_2,\ \dot{\boldsymbol{\Omega}}_1 = \mathbf{e}_1\delta\ddot{q}_1$ and $\dot{\boldsymbol{\Omega}}_2 = \mathbf{e}_2\delta\ddot{q}_2$.

In here, we model each of the cores as a mass point. It is also assumed that the filling fluid is distributed uniformly inside the pipes i.e., cylinder, injection line and the pipe with the core. By applying the D'Alembert principle for the multi-body system, free from non-holonomic rolling constraints [122], one can obtain

$$\delta\mathbf{r}_o \cdot [M_o\,(\ddot{\mathbf{r}}_o - \mathbf{g})] + \delta\pi_o \cdot \left[\mathbf{J}_o\dot{\boldsymbol{\Omega}}_o + \boldsymbol{\Omega}_o \times \mathbf{J}_o\boldsymbol{\Omega}_o\right] + \sum_{i=1}^{2}\left[\delta\mathbf{r}_i \cdot (m_c\ddot{\mathbf{r}}_i - \mathbf{F}_i)\right] = 0, \tag{2.6}$$

where $\delta\mathbf{r}_o$ and $\delta\mathbf{r}_i$ are the virtual displacements of the center of the sphere and the cores, in the given order. Also, M_o stands for the total mass of the sphere, including the mass of the fluid; $\mathbf{J}_o$ is the inertia tensor of the sphere, m_c is the mass of the core, $\mathbf{g}$ is the gravity vector, and $\mathbf{F}_i$ is external force acting on the i-th core. It is important to note that the first two terms in (2.6) account for the sphere dynamics and the last term is for the dynamics of the two rotating cores. Then, the external forces in $\mathbf{F}_i$ are defined as

$$\mathbf{F}_i = \mathbf{F}_{d_i} + \mathbf{F}_{G_i} + \mathbf{F}_{v_i}, \tag{2.7}$$

where $\mathbf{F}_{d_i}$, $\mathbf{F}_{G_i}$, $\mathbf{F}_{v_i}$ are the driving forces, the body forces, and the viscous forces. We will define functions of the forces specifically in Section 2.3.

By expressing the absolute virtual displacements of the cores $\delta\mathbf{r}_i = \delta\mathbf{r}_o + \delta\pi_i \times \mathbf{p}_i$ through the virtual displacement of the sphere and the relative virtual displacements

of the cores as $\delta\mathbf{r}_A = \delta\mathbf{r}_o + \delta\pi_A \times \mathbf{p}_1$ for pipe A and $\delta\mathbf{r}_B = \delta\mathbf{r}_o + \delta\pi_B \times \mathbf{p}_2$ for pipe B, one transforms (2.6) to the following form

$$\begin{aligned}
&\delta\mathbf{r}_o \cdot \Big[M_o\Big(\dot{\mathbf{V}}_o - \mathbf{g}\Big) + \Big(m_c\dot{\mathbf{V}}_A - \mathbf{F}_1\Big) + \Big(m_c\dot{\mathbf{V}}_B - \mathbf{F}_2\Big)\Big] \\
&+ \delta\pi_o \cdot \big[\mathbf{J}_o\dot{\boldsymbol{\Omega}}_o + \boldsymbol{\Omega}_o \times \mathbf{J}_o\boldsymbol{\Omega}_o + \mathbf{p}_1 \times \Big(m_c\dot{\mathbf{V}}_A - \mathbf{F}_1\Big) \\
&+ \mathbf{p}_2 \times \Big(m_c\dot{\mathbf{V}}_B - \mathbf{F}_2\Big)\,\big] + \delta\pi_1 \cdot \big[\mathbf{p}_1 \times \Big(m_c\dot{\mathbf{V}}_A - \mathbf{F}_1\Big)\,\big] \\
&+ \delta\pi_2 \cdot \big[\mathbf{p}_2 \times \Big(m_c\dot{\mathbf{V}}_B - \mathbf{F}_2\Big)\,\big] = 0.
\end{aligned} \tag{2.8}$$

To take into account the rolling constraint, we first transform $\delta\mathbf{r}_o$ to the contact point between the sphere and the plane $\delta\mathbf{r}_c = \delta\mathbf{r}_o + \delta\pi_o \times \mathbf{p}_c$, where we have $\mathbf{r}_c = \mathbf{r}_o + \mathbf{p}_c$. Because there is no-sliding constraint $\delta\mathbf{r}_c = 0$ [57], we have the virtual displacement of the sphere as

$$\delta\mathbf{r}_o = -\delta\pi_o \times \mathbf{p}_c. \tag{2.9}$$

Then, we substitute (2.9) into (2.8), which results in

$$\begin{aligned}
&\delta\pi_o \cdot \big[-\mathbf{p}_c \times \Big(M_o\dot{\mathbf{V}}_o + m_c\Big(\dot{\mathbf{V}}_A + \dot{\mathbf{V}}_B\Big)\Big) + \mathbf{J}_o\dot{\boldsymbol{\Omega}}_o + \boldsymbol{\Omega}_o \times \mathbf{J}_o\boldsymbol{\Omega}_o + \mathbf{p}_1 \times \Big(m_c\dot{\mathbf{V}}_A - \mathbf{F}_1\Big) \\
&+ \mathbf{p}_2 \times \Big(m_c\dot{\mathbf{V}}_B - \mathbf{F}_2\Big)\,\big] + \delta\pi_1 \cdot \big[\mathbf{p}_1 \times \Big(m_c\dot{\mathbf{V}}_A - \mathbf{F}_1\Big)\,\big] \\
&+ \delta\pi_2 \cdot \big[\mathbf{p}_2 \times \Big(m_c\dot{\mathbf{V}}_B - \mathbf{F}_2\Big)\,\big] = 0,
\end{aligned} \tag{2.10}$$

Next, we take into account that $\dot{\mathbf{V}}_o = -\dot{\boldsymbol{\Omega}}_o \times \mathbf{p}_c$, which comes from differentiating the rolling constraint $\mathbf{V}_o + \boldsymbol{\Omega}_o \times \mathbf{p}_c = 0$. In addition, we replace $\dot{\mathbf{V}}_A$ and $\dot{\mathbf{V}}_B$ by the expressions defined in (2.4) and (2.5). As a result, we transform (2.10) to the following equation

$$\begin{aligned}
&\delta\pi_o \cdot \Big(\overline{\mathbf{M}}_{11}\dot{\boldsymbol{\Omega}}_o + \overline{\mathbf{M}}_{12}\dot{\boldsymbol{\Omega}}_1 + \overline{\mathbf{M}}_{13}\dot{\boldsymbol{\Omega}}_2 + \overline{\mathbf{N}}_{11} + \overline{\mathbf{G}}_{11}\Big) \\
&+ \delta\pi_1 \cdot \Big(\overline{\mathbf{M}}_{21}\dot{\boldsymbol{\Omega}}_o + \overline{\mathbf{M}}_{22}\dot{\boldsymbol{\Omega}}_1 + \overline{\mathbf{M}}_{23}\dot{\boldsymbol{\Omega}}_2 + \overline{\mathbf{N}}_{21} + \overline{\mathbf{G}}_{21}\Big) \\
&+ \delta\pi_2 \cdot \Big(\overline{\mathbf{M}}_{31}\dot{\boldsymbol{\Omega}}_o + \overline{\mathbf{M}}_{32}\dot{\boldsymbol{\Omega}}_1 + \overline{\mathbf{M}}_{33}\dot{\boldsymbol{\Omega}}_2 + \overline{\mathbf{N}}_{31} + \overline{\mathbf{G}}_{31}\Big) = 0,
\end{aligned} \tag{2.11}$$

where

$$\begin{aligned}
\overline{\mathbf{M}}_{11} &= \mathbf{J}_o + M_o\hat{\mathbf{p}}_c\hat{\mathbf{p}}_c + 2m_c\hat{\mathbf{p}}_c\hat{\mathbf{p}}_c - m_c\left(\hat{\mathbf{p}}_1\hat{\mathbf{p}}_c + \hat{\mathbf{p}}_c\hat{\mathbf{p}}_1\right) \\
&- m_c\left(\hat{\mathbf{p}}_2\hat{\mathbf{p}}_c + \hat{\mathbf{p}}_c\hat{\mathbf{p}}_2\right),\ \overline{\mathbf{M}}_{12} = m_c\hat{\mathbf{p}}_1\hat{\mathbf{p}}_1 - m_c\hat{\mathbf{p}}_c\hat{\mathbf{p}}_1, \\
\overline{\mathbf{M}}_{13} &= m_c\hat{\mathbf{p}}_2\hat{\mathbf{p}}_2 - m_c\hat{\mathbf{p}}_c\hat{\mathbf{p}}_2,\ \overline{\mathbf{M}}_{21} = m_c\hat{\mathbf{p}}_1\hat{\mathbf{p}}_1 - m_c\hat{\mathbf{p}}_1\hat{\mathbf{p}}_c, \\
\overline{\mathbf{M}}_{22} &= m_c\hat{\mathbf{p}}_1\hat{\mathbf{p}}_1,\ \overline{\mathbf{M}}_{23} = 0,\ \overline{\mathbf{M}}_{31} = m_c\hat{\mathbf{p}}_2\hat{\mathbf{p}}_2 - m_c\hat{\mathbf{p}}_2\hat{\mathbf{p}}_c, \\
\overline{\mathbf{M}}_{32} &= 0,\ \overline{\mathbf{M}}_{33} = m_c\hat{\mathbf{p}}_2\hat{\mathbf{p}}_2,
\end{aligned} \tag{2.12}$$

$$\begin{aligned}
\overline{\mathbf{N}}_1 &= m_c\mathbf{p}_1 \times \left[(\boldsymbol{\Omega}_o + \boldsymbol{\Omega}_1) \times ((\boldsymbol{\Omega}_o + \boldsymbol{\Omega}_1) \times \mathbf{p}_1) + \left(\boldsymbol{\Omega}_o + \boldsymbol{\Omega}_1\right) \times \mathbf{p}_1\right] \\
&+ m_c\mathbf{p}_2 \times \left[(\boldsymbol{\Omega}_o + \boldsymbol{\Omega}_2) \times ((\boldsymbol{\Omega}_o + \boldsymbol{\Omega}_2) \times \mathbf{p}_2) + (\boldsymbol{\Omega}_o + \boldsymbol{\Omega}_2) \times \mathbf{p}_2\right] \\
&- m_c\mathbf{p}_c \times \left[(\boldsymbol{\Omega}_o + \boldsymbol{\Omega}_1) \times \left(\left(\boldsymbol{\Omega}_o + \boldsymbol{\Omega}_1\right) \times \mathbf{p}_1\right)\right. \\
&+ (\boldsymbol{\Omega}_o + \boldsymbol{\Omega}_2) \times ((\boldsymbol{\Omega}_o + \boldsymbol{\Omega}_2) \times \mathbf{p}_2) \\
&+ \left.(\boldsymbol{\Omega}_o + \boldsymbol{\Omega}_1) \times \mathbf{p}_1 + (\boldsymbol{\Omega}_o + \boldsymbol{\Omega}_2) \times \mathbf{p}_2\right] + \boldsymbol{\Omega}_o \times \mathbf{J}_o\boldsymbol{\Omega}_o, \\
\overline{\mathbf{N}}_2 &= m_c\mathbf{p}_1 \times \left[(\boldsymbol{\Omega}_o + \boldsymbol{\Omega}_1) \times ((\boldsymbol{\Omega}_o + \boldsymbol{\Omega}_1) \times \mathbf{p}_1) + (\boldsymbol{\Omega}_o + \boldsymbol{\Omega}_1) \times \mathbf{p}_1\right], \\
\overline{\mathbf{N}}_3 &= m_c\mathbf{p}_2 \times \left[(\boldsymbol{\Omega}_o + \boldsymbol{\Omega}_2) \times ((\boldsymbol{\Omega}_o + \boldsymbol{\Omega}_2) \times \mathbf{p}_2) + (\boldsymbol{\Omega}_o + \boldsymbol{\Omega}_2) \times \mathbf{p}_2\right],
\end{aligned} \tag{2.13}$$

and

$$\overline{\mathbf{G}}_1 = -\left(\mathbf{p}_1 \times \mathbf{F}_1 + \mathbf{p}_2 \times \mathbf{F}_2\right),\ \overline{\mathbf{G}}_2 = -\mathbf{p}_1 \times \mathbf{F}_1,\ \overline{\mathbf{G}}_3 = -\mathbf{p}_2 \times \mathbf{F}_2. \tag{2.14}$$

In our equations, hat symbol corresponds to the skew-symmetric operator $\mathbf{a}\times\mathbf{b} \triangleq \hat{\mathbf{a}}\mathbf{b}$.

The dynamic equations can now be developed by treating the virtual displacements $\delta\pi_o$, $\delta\pi_1$, $\delta\pi_2$ in (2.11) as independent variations. By rearranging the terms with $\mathbf{F}_{d_i}$ (the fluid pressure forces driving the cores within the pipes) to the right-hand side, we will finally obtain

$$\begin{bmatrix} \mathbf{M}_{11} & \mathbf{M}_{12} & \mathbf{M}_{13} \\ M_{21} & M_{22} & M_{23} \\ M_{31} & M_{32} & M_{33} \end{bmatrix} \begin{bmatrix} \dot{\boldsymbol{\Omega}}_o \\ \ddot{q}_1 \\ \ddot{q}_2 \end{bmatrix} + \begin{bmatrix} \mathbf{N}_1 \\ N_2 \\ N_3 \end{bmatrix} + \begin{bmatrix} \mathbf{G}_1 \\ G_2 \\ G_3 \end{bmatrix} = \begin{bmatrix} 0 \\ \tau_1 \\ \tau_2 \end{bmatrix}, \tag{2.15}$$

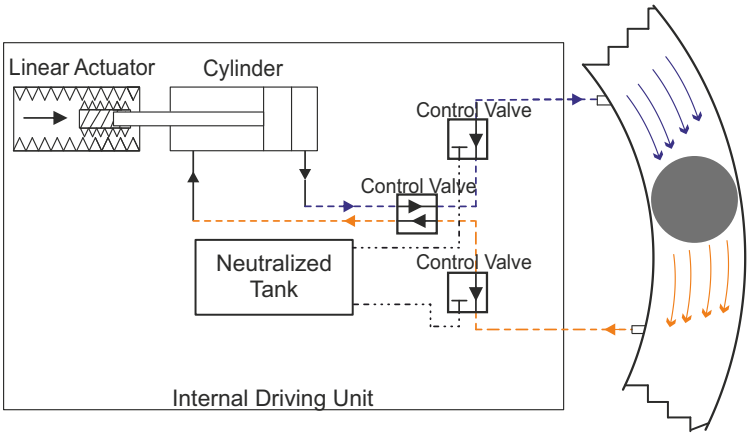

Figure 2.3: Schematic of the fluid actuated mechanism.

where

$$\begin{aligned}
\mathbf{M}_{11} &= \overline{\mathbf{M}}_{11}, \mathbf{M}_{12} = \overline{\mathbf{M}}_{12}\mathbf{e}_1, \mathbf{M}_{13} = \overline{\mathbf{M}}_{13}\mathbf{e}_2, \mathbf{N}_1 = \overline{\mathbf{N}}_1, \mathbf{G}_1 = \overline{\mathbf{G}}_1, \\
M_{21} &= \mathbf{e}_1^T\overline{\mathbf{M}}_{21}, M_{22} = \mathbf{e}_1^T\overline{\mathbf{M}}_{22}\mathbf{e}_1, M_{23} = \mathbf{e}_1^T\overline{\mathbf{M}}_{23}\mathbf{e}_2, N_2 = \mathbf{e}_1^T\overline{\mathbf{N}}_2, \\
G_2 &= -\mathbf{e}_1^T\left(\mathbf{p}_1 \times (\mathbf{F}_{G_1} + \mathbf{F}_{v_1})\right), M_{31} = \mathbf{e}_2^T\overline{\mathbf{M}}_{31}, M_{32} = \mathbf{e}_2^T\overline{\mathbf{M}}_{32}\mathbf{e}_1, \\
M_{33} &= \mathbf{e}_2^T\overline{\mathbf{M}}_{32}\mathbf{e}_2, N_3 = \mathbf{e}_2^T\overline{\mathbf{N}}_3, G_3 = -\mathbf{e}_2^T\left(\mathbf{p}_2 \times (\mathbf{F}_{G_2} + \mathbf{F}_{v_2})\right),
\end{aligned}$$

and also the input torques are computed as $\tau_1 = \mathbf{e}_1^T\left(\mathbf{p}_1 \times \mathbf{F}_{d_1}\right)$ and $\tau_2 = \mathbf{e}_2^T\left(\mathbf{p}_2 \times \mathbf{F}_{d_2}\right)$. With obtained derivations, equation (2.2) together with (2.15) define the total rigid body model of the rolling robot with 12 state $\{u_{cs}, v_{cs}, u_{co}, v_{co}, \psi, \omega_x^o, \omega_y^o, \omega_z^o, q_1, \dot{q}_1, q_2, \dot{q}_2\}$ and two control inputs τ_1 and τ_2.

2.3 Internal Driving Unit

The internal driving unit (IDU) is the main part of our proposed propulsion mechanism. The IDU is responsible for producing the required fluid pressure to move the spherical masses (cores) in the pipes. We have divided the modeling two parts: 1. The linear actuator part that creates fluid circulation 2. The motion generation part where the exiting fluid is transferred to the main pipe with the core.

2.3.1 Linear Actuator

To push the moving core, a high-density flow is produced by a multi-functional linear actuator connected to a cylinder (please see Fig. 2.3). The cylinder provides the

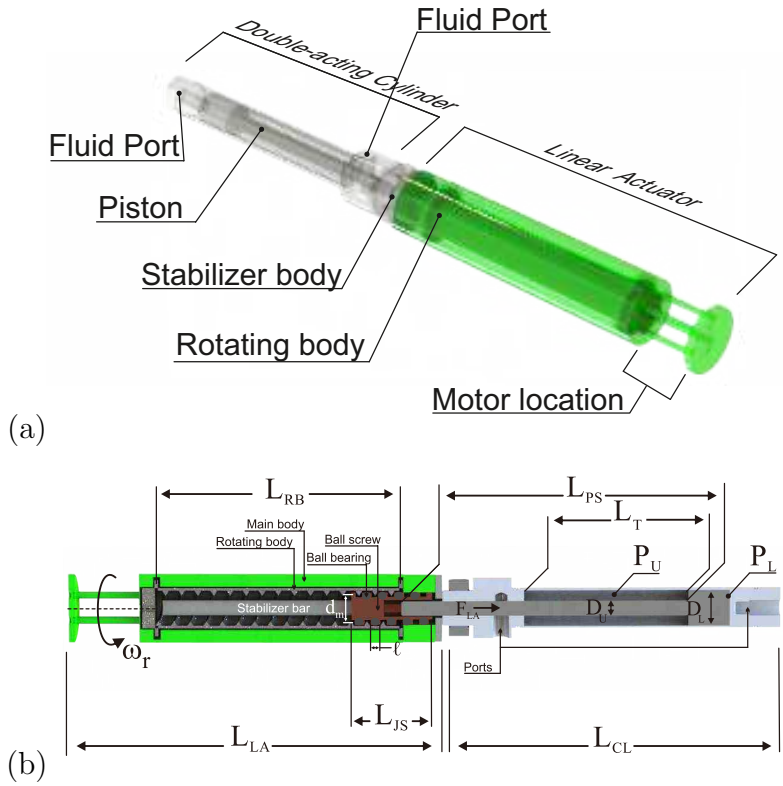

Figure 2.4: The structure of the linear actuator and the connected cylinder. The torque is carried through rotating body to move the joint that is connected to the cylinder rod.

fluid flow in the pipe while the designed control valves manipulate the flow direction within the sections of the pipe. Fig. 2.4 demonstrates the schematic for the designed linear actuator with the cylinder connection. We begin with modeling of the linear actuator connected to this cylinder, and then we define the size limitations of this mechanism inside the IDU box.

The displacing cylinder rod in the interconnected motor can be related to the axial force of the linear actuator by the following one-dimensional motion equation

$$F_{in} - F_{LA} + F_s = 0, \tag{2.16}$$

where F_{in}, F_{LA} and F_s are the inertia of the cylinder's rod, the transmitted torque on the rod, and the total friction between the screw and rotating body forces, respectively. The given forces are defined as [30, 96]

$$F_{in} = m_{LA} a_{LA},\ F_{LA} = 2\pi T_m \eta / \ell,\ F_s = \mu_{LA} F_{in}, \tag{2.17}$$

where m_{LA}, a_{LA}, T_m, η, ℓ and μ_{LA} are the total mass of the rod and the moving connected joints, the acceleration of the rod, the input torque of the motor, the efficiency of the linear actuator, the size of the lead, and the friction coefficient between rotating body and rod, respectively. The efficiency is defined as $\eta = (\cos\alpha - \mu_s \tan\lambda)/(\cos\alpha + \mu_s \cot\lambda)$ [30], where α, μ_s and λ are, respectively, the thread angle, the coefficient of friction (typically 0.15) in the screw, and the lead angle. The screw is considered to be a ball screw with minimal friction effect; hence η is approximated with 96%.

With the given defined forces in (2.16)-(2.17), the state-space model of the rod of the linear actuator can be described as follows,

$$\begin{aligned} \dot{D}_{LA} &= V_{LA}, \\ \dot{V}_{LA} &= \frac{2\pi\eta}{m_{LA}\ell(1+\mu_{LA})} T_m, \end{aligned} \tag{2.18}$$

where D_{LA} and V_{LA} are the displacement and the velocity of the moving rod, respectively. Note that the velocity of the connected bar of the linear actuator, V_{LA}, is the same as the velocity of the cylinder, V_{CL}. Also, we use a double-act cylinder in this modeling problem. Therefore, the cylindrical volume is shifting in cycles in order to provide continuous flow. As a result, the effective area of the cylinder that pushes the liquid in each cycle is defined as follows,

$$A_{CL} = \begin{cases} \pi D_L^2/4, & D_{LA} \text{ is increasing from 0 to } L_T \\ \pi\left(D_L^2 - D_U^2\right)/4, & D_{LA} \text{ is decreasing from } L_T \text{ to 0} \end{cases} \tag{2.19}$$

where D_U, D_L and L_T are the diameter of the rod, the diameter of the pusher in the cylinder, and the length of the rod, in the given order.

We have determine the size limitations on the actuation mechanism for fitting it in the IDU box with symmetric mass distribution (see Fig. 2.4-2.5). The cylinder volume is given as $\pi D_L^2 L_T$. The cylinder length $L_T \leq L_{CL}$ is constrained by the connected linear actuator length L_{LA} as $(L_{LA} + L_{CL}) < D_{IB}$, where D_{IB} is the diagonal length of the IDU box. Also, the diameter of cylinder tank D_L has to be within $d_m \leq D_L \leq [D_{IB} - (L_{LA} + L_{CL})]/2$ range, where d_m is the external diameter of the linear actuator joint. The upper limitation on D_L is the radius of the circle corresponding to the distance left in diagonally placed total actuator at the edge of the box. Also, we have

$L_{PS} = L_{RB} - L_{JS}$ for the linear actuator and the cylinder , where $L_{PS} = L_T$. These size limitations can be used when placing even numbers of actuators inside the IDU box. We use these relationships to determine the parameters of the IDU listed in Table 2.2.

2.3.2 Motion Generation

The main part of this propulsion mechanism (from the cylinder to the circulating core) operates in a liquid medium. In this operating system, a lightweight double-act pneumatic cylinder [10] is considered. This cylinder works as a pump actuator to create a continuous flow. The total IDU mechanism is placed inside the spherical shell. The system integrated actuator is shown in Fig. 2.3. The driving unit is completely closed; hence the fluid volume is constant in the whole structure. The flow is circulated through the pipes, cylinders and neutralized tank. Note that the liquid enters the neutralized tank for the proper control of the filling cycles of the cylinder.

Since pipes A and B are similar, it suffices to consider one of them in describing the motion of the core. The active input ports for the fluid and the effective forces acting on the core are sketched in Fig. 2.5 where the pipe is shown in the vertical configuration. It is assumed that the velocity of the liquid flow is the same as that of the core, $\mathbf{V}_i = r_i \dot{q}_i \mathbf{n}_i$, where r_i, $\dot{q}_i$ and $\mathbf{n}_i$ are the distance from the center of the sphere to the core i, the angular velocities of the core i, and the unit vector tangent to circular path of the pipe , respectively. Note that the relevant parameters have to be substituted for each pipe corresponding to q_i. For example, r_1 and $\dot{q}_1$ are taken for the core in pipe A, and r_2 and $\dot{q}_2$ are taken for the core in pipe B.

Since the proposed mechanism works in the liquid-solid medium, we combine the core forces (2.7) with the input fluid pressure via the momentum equation of the flow [101, 124], $d\left(m_c \mathbf{V}_i\right)/dt = \mathbf{F}_i$. In polar coordinates, the core has angular $\mathbf{a}_{q_i}(t) = d|\mathbf{V}_i|/dt\mathbf{n}_i = r_i \ddot{q}_i(t)\mathbf{n}_i$ and radial $\mathbf{a}_{r_i}(t)$ accelerations. The latter one can be ignored because it is constant with no effect on the core and the fluid. Therefore, all terms are defined with respect to $\mathbf{a}_{q_i}(t)$.

The first term in the right-hand side of (2.7) is the fluid pressure input along the

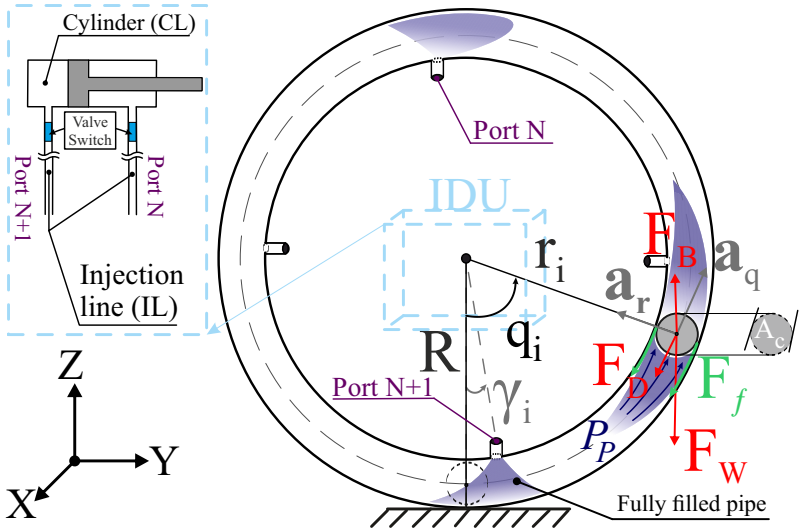

Figure 2.5: The acting forces on the rotating core at pipe A. In here, $\mathbf{F}_B$, $\mathbf{F}_D$, $\mathbf{F}_W$, $\mathbf{F}_f$ and $\mathbf{F}_d$ are the buoyancy, drag, weight, surface friction, and the dynamic pressure forces, respectively. Also, N and $N+1$ are the connecting ports to provide the liquid circulation with a single fluid actuator.

unit vector $\mathbf{n}_i$. This term can be represented as

$$\mathbf{F}_{d_i} = \oiint_{C.S.} P_P \mathbf{n}_i dA_P = P_P A_P \mathbf{n}_i, \tag{2.20}$$

where P_P, A_P and $C.S.$ stand for the fluid pressure in the pipe, the pipe's surface area, and the contour surface, in the given order. For this force (2.20), we assume that the distance gap between the pipe and the core surface is negligibly small, and thus $A_P = \pi D_i^2/4$, where D_i is the diameter of the rotating core. Upon substituting (2.20) into (2.7), the resultant cross-product of the core position vector $\mathbf{p}_i$ and the unit vector $\mathbf{n}_i$ becomes $\mathbf{p}_i \times \mathbf{n}_i = r_i \mathbf{e}_i$ (here $\mathbf{e}_i$ is the core's relative rotation vector) since $\mathbf{n}_i \perp \mathbf{p}_i$.

Next, the body force $\mathbf{F}_{G_i}$ in (2.7) can be decomposed to the gravity $\mathbf{F}_W$ and buoyancy $\mathbf{F}_B$ forces. Since the volume of the core $\nu_c = 4\pi D_i^3/3$, and gravity vector $\mathbf{g}$ is parallel to the vector of the contact position $\mathbf{p}_c$, we can define the body forces as follows

$$\mathbf{F}_W = -m_c g \mathbf{p}_c, \ \mathbf{F}_B = \rho_f \nu_c g \mathbf{p}_c, \tag{2.21}$$

where ρ_f is the density of the fluid, and g the gravitational acceleration.

The viscous force $\mathbf{F}_{v_i}$ in Eq. (2.7) is decomposed to the head loss of the flowing fluid $\mathbf{F}_f$ and the drag force $\mathbf{F}_D$ acting along the circular path of the core [101],

$$\mathbf{F}_f = -\text{sgn}(\dot{q}_i) f_P \frac{L'_P V_i^2}{2gD_i}\mathbf{n}_i,\ \mathbf{F}_D = -\text{sgn}(\dot{q}_i)\frac{1}{2}C_D\rho_f A_P V_i^2 \mathbf{n}_i, \tag{2.22}$$

where $V_i^2 = r_i^2\dot{q}_i^2$, and f_P, L'_P, D_i and C_D are the Darcy friction factor, the apparent length of the pipe, the pipe diameter, and the drag coefficient. The Darcy friction factor is defined as $f_P = 64/Re_P$ respectively. The Reynold number for the main pipe with the core in it is $Re_P = L_P V_P \rho_f/\mu_f$, where V_P is the fluid velocity in the entrance to the main pipe, L_P is the length of the pipe, and μ_f is the viscosity of the fluid.

In this model, the head loss $\mathbf{F}_f$ in (2.22) is a resistant force coming from the bending shape of the pipe and viscous friction [124]. In the bend of the pipe, a secondary flow is created by the centripetal acceleration of the rotating fluid; Hence, the apparent length through the main pipe is defined by [124]

$$L'_P = L_P + [(K_b D_i)/f_P], \tag{2.23}$$

where K_b is the resistance coefficient for 180° in the return bend.

The motion equations of the driving mechanism can be formed under the assumption that the flux of the linear momentum equilibrates with the external forces, including the pressure, the gravity and the viscous friction forces. In the state space form, we have

$$\begin{aligned}
&\mathbf{V}_i = r_i\dot{q}_i\mathbf{n}_i,\\
&\mathbf{a}_{q_i} = P_P A_P \mathbf{n}_i - \text{sgn}(\dot{q}_i)\frac{r_i^2\dot{q}_i^2}{2}\left(f_P\frac{L'_P}{D_i g} + C_D\rho_f A_P\right)\mathbf{n}_i\\
&+ \left[g(-m_c + \rho_f\nu_c)\mathbf{e}_i\cdot(\mathbf{p}_i\times\mathbf{p}_c)\right]\mathbf{n}_i.
\end{aligned} \tag{2.24}$$

Finally, the two-stage Bernoulli equation with the head loss [101] is applied within the streamline to derive the input pressure P_P. In the first stage, the fluid goes through the cylinder tank (P_{CL}, V_{CL}) to the injection line (P_{IL}, V_{IL}), where IL stands for the slim fluid carrier pipe. Then, the pressure of the fluid in the injection line P_{IL} is given as

$$P_{IL} = P_{CL} + \frac{\rho_f}{2}\left[V_{CL}^2 - V_{IL}^2\right] - \rho_f g h_L, \tag{2.25}$$

where P_{CL}, V_{CL}, V_{IL} and h_L are the pressure and the velocity of the fluid in the cylinder tank, the velocity of the fluid in the injection line pipe and the head loss, respectively. The distance between the cylinder and injection line is neglected ($h_L = 0$). To find out the pressure in the injection line P_{IL}, it is assumed that $V_{CL} = V_{LA}$, where V_{LA} is taken from the first state equation in (2.18). Next, the velocity of the fluid in the injection line pipe V_{IL} is defined by the continuity equation $V_{IL} = V_{CL}A_{CL}/A_{IL}$, where A_{IL} is the cross-section area of the injection line pipe. The cylinder pressure $P_{CL} = F_{LA}/A_{CL}$, where F_{LA} is defined by (2.17), is substituted into (2.25) in order to compute the injection line pressure P_{IL}.

The injection line pipes are connected to the main pipes from the IDU (refer to ports in Fig. 2.5), and the following Bernoulli equation gives the pressure of the fluid in the main pipe

$$P_P = P_{IL} + \frac{\rho_f}{2}\left[V_{IL}^2 - V_P^2\right] + \rho_f g\left[Z_{IL} - Z_P - h_m - h_f\right], \tag{2.26}$$

where V_P, Z_{IL}, Z_P, h_m and h_f are the fluid velocity in the entrance to the main pipe, the constant height of the injection port, the height of the port, the head loss of friction, and the sudden expansion loss, in the given order. Since the main pipe is get rotating, the height of the port will not stay constant. With given acknowledge, the height is defined as follows

$$Z_P = \mathbf{e}_i \cdot \left(\mathbf{p}_{\gamma_i} \times \mathbf{p}_c\right), \tag{2.27}$$

where

$$\mathbf{p}_{\gamma_i} = [0,\ (R - D_i)\sin\gamma_i,\ (R - D_i)\cos\gamma_i] \tag{2.28}$$

is the position of the port in rotating pipe and the angle γ_i is defined in Fig. 2.5.

Note that the velocity in the entrance of the pipe V_P in (2.26) is determined from the continuity equation $V_P = V_{IL}A_{IL}/A_P$. Also, the head loss of friction in the injection line h_f and the diameter change in the main pipe's entrance h_m are defined as [101]

$$h_f = f_{IL}\frac{L_{IL}V_{IL}^2}{2gD_{IL}},\ h_m = K_{SE}\frac{V_{IL}^2}{2g}, \tag{2.29}$$

where D_{IL}, f_{IL} and K_{SE} are, respectively, the diameter of the injection line pipe, the Darcy friction factor for the injection line pipe, and the loss coefficient through the transition from the injection line pipe to the main pipe. Here, the friction factor is

Table 2.2: Parameters of the designed IDU.

Variable	Value	Variable	Value
K_{SE}	0.9	D_L	0.0097 m
K_b	0.2	d_m	0.0097 m
ℓ	0.007 m	D_{IL}	0.00635 m
μ_{LA}	0.75	D_i	0.028 m
m_{LA}	0.2 kg	D_U	0.0047 m
η	96%	ρ_f	1000 kg/m^3
L_{IL}	0.145 m	γ_1	10^o
L_T	0.05 m	T_m	0.27 mN $\cdot$ m
L_P	0.411 m	μ_f	1.81×10^{-3} kg/m $\cdot$ s
L_{JS}	0.01 m	D_{IB}	0.10 m

defined as $f_{IL} = 0.316/Re_{IL}^{0.25}$, where $Re_{IL} = L_{IL}V_{IL}\rho_f/\mu_f$, and L_{IL} is the length of the injection line pipe.

2.4 Simulation Studies

2.4.1 Performance of the Internal Driving Unit (IDU)

In this section, the performance of the IDU is tested under the simulation. The control valves are ignored due to their minor contribution in the motion performance. We investigate the mechanism for the three main factors: the direct motor input, the cylinder volume changes, and the fluid properties. First, we examine the feasibility and limitations of the proposed actuator and also we determine whether it can create the required force to circulate the core in the pipe. Next, the tank size of the cylinder is varied to find its boundary values. Finally, we evaluate the performance of the IDU in different fluids properties.

In the simulation analysis, it is assumed that the pipe is fixed in the vertical configuration, as shown in Fig. 2.5, and therefore $Z_P = (R - D_1)[1 - \cos\gamma_1]$ in (2.26) with constant γ_1, and $\mathbf{e}_i \cdot (\mathbf{p}_i \times \mathbf{p}_c) = 1 - \cos q_1$. Thus, the differential equations (2.24) take the following form

$$\dot{q}_1 = \frac{1}{r_1} V_1, \tag{2.30}$$

$$\ddot{q}_1 = \frac{1}{r_1 m_c}\left[P_P A_P - \frac{\mathrm{sgn}\,(\dot{q}_1)\, r_1^2 \dot{q}_1^2}{2}\left(f_P \frac{L'_P}{D_1 g} + C_D \rho_f A_P\right)\right] + [-m_c + \rho_f \nu_c](1 - \cos q_1) g, \tag{2.31}$$

where the control input, the pressure of the transferred fluid in the pipe, is established from solving the algebraic equations (2.25)- (2.26). Note that in this structure, the gravity is involved in the driving equation, thus, we can evaluate the system with including all effected forces.

In the simulations, we solve the system (2.18), (2.31) by using Matlab ODE45 [40, 94] function with the integration step 0.001s. The mass of the core is set at 0.25 kg and the other parameters are taken from Table 2.2. In incoming Section 2.5.1, we evaluate what mass ratio between core and the rolling sphere is desirable with analytical studies. It should be noted that the characteristics of the IDU correspond to the commercially available 08GS61 DC motor [117] and A07020D pneumatic cylinder [10]. This cylinder has 0.05 kg weight and can work in a liquid medium. Also, the internal driving unit satisfies the derived size limitation defined in Section 2.3.1.

In all the simulations, the starting position of the core is at the bottom of the sphere, and the other state variables are initialized from zero values. Note that we evaluate the medium of the cylinder and main pipe with a low Reynolds number, but the injection line is in the turbulent regime as we considered in Eq. (2.29). The cycles of the cylinder tank change when the bore reaches the final point and reverse in accordance with (2.19).

Torque Reliance

The torque input generated by the DC motor is the main factor in controlling the complete robot. In this part, we analyze to what extent the motor can manipulate the core when the pipe is filled with distilled water. The model of driving mechanism is checked with respect to three torque example values $T_m = 0.24, 0.27$ and 0.3 mN·m. The simulation results are presented in Figs. 2.6 and 2.7. We clearly can see that the DC motor input T_m can directly change the pressure and the flow velocity. The pressure in all the pipes is changing with the constant shift in response to the change of the torque. Note that for the relatively higher torque input values the core displacement is nonlinear. Also, the slope of the fluid velocity in the injection line V_{IL} increases with the raise of the input torque. Also, the velocities of fluid have different peaks due to use of double-acting cylinder which contain different cross-section area in each cycle change as Eq. (2.19).

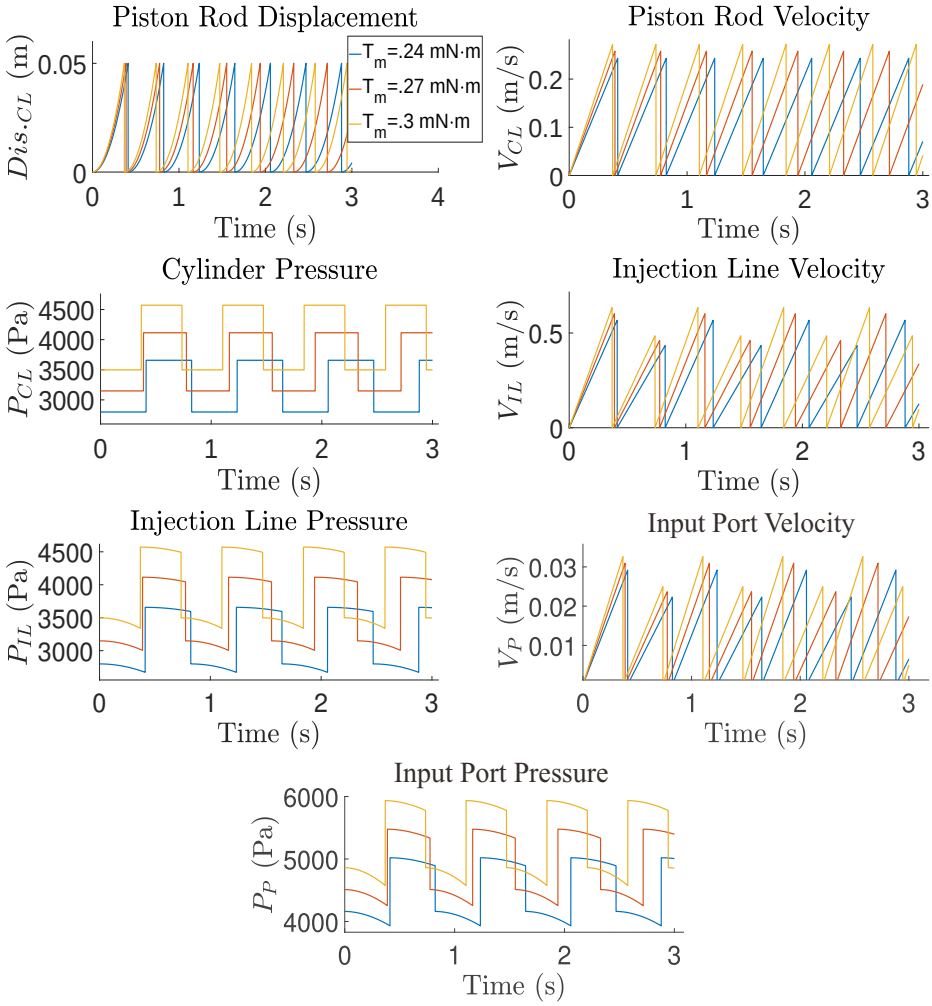

Figure 2.6: The fluid pressure and velocity from the cylinder tank to the main pipe with different input torques.

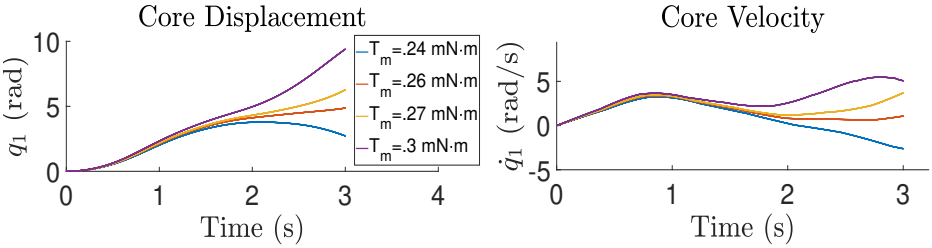

Figure 2.7: The core locomotion and velocity results with inclusion of the critical input torque T_{cr}.

With our obtained observations and modeling insight, the limits of the torque

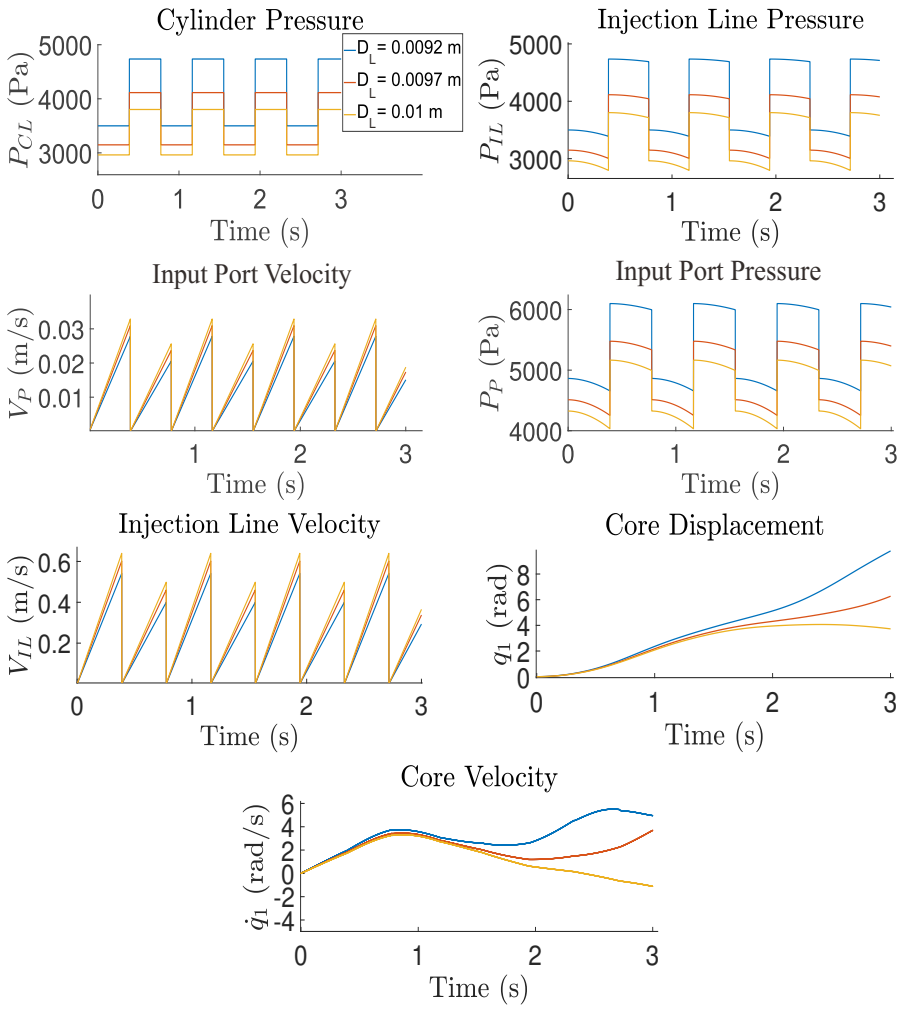

Figure 2.8: The IDU simulation results with different piston diameter D_L.

input generated by the DC motor can be set as follows:

$$\begin{cases} T_{nf} > T_m > T_{cr}, & \text{satisfactory torque} \\ T_m \leq T_{cr}, & \text{critical torque,} \end{cases} \tag{2.32}$$

where T_{nf} and T_{cr} are the maximum applicable and the critical motor torques. If the torque T_m is less than the critical one, the actuation mechanism cannot deliver the core to the zenith point of the sphere as the generated fluid flow cannot overcome the gravity, drag and head loss forces. Based on the simulation results, one can set $T_{cr} = 0.26$ mN·m. Overall, we observe from simulations that motor input can successfully manipulate the spherical mass in the liquid medium under the given property (2.32).

Note that the maximum applicable torque T_{nf} is constrained by the maximum

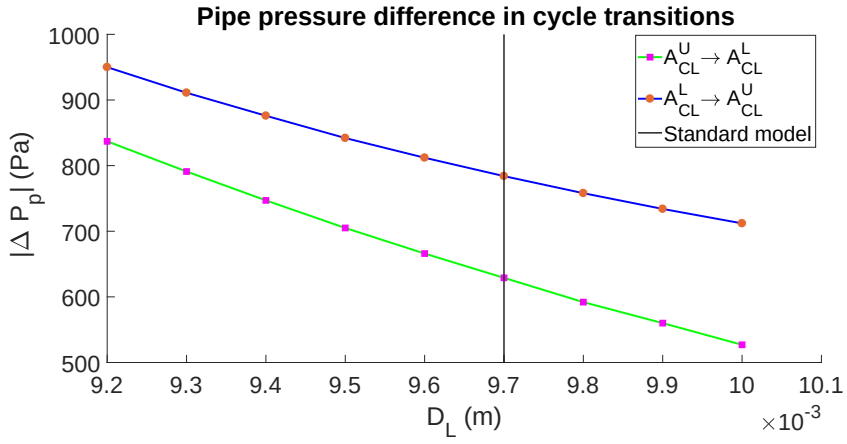

Figure 2.9: The pressure difference of the main pipe in the transition cycles of the cylinder versus different diameter D_L. Note that the blue graph shows the transition of cylinder tank with bore area A^U_{CL} to the covered plunger area A^L_{CL}. The red graph happens for the opposite process of the green one. Blackline refers to D_L with the reference value in Table 2.2.

natural frequency of the linear actuator. If the value of T_m exceeds T_{nf}, vibration will cause damage to the gears. This upper constraint can be established as follows. The constant torque generated by the DC motor is $T_m = 60E_aI_a/2\pi\omega_r$ [49], where the parameters I_a, E_a and ω_r are the input armature current, the armature voltage and the angular velocity of the motor. Thus, we can formulate as

$$T_{nf} = 60d_mE_aI_a/4\pi n_c, \tag{2.33}$$

where d_m and n_c are the diameter of the connecting joint and the natural frequency, respectively. The maximum natural frequency of the ball screw is $n_c = 4.76 \times 10^6 d_m C_s/L^2_{RB}$ [96], where C_s is the end-fixity factor for critical speed, and L_{RB} is the length between bearing supports. Because both sides of the rotating body are fixed completely [see Fig. 2.4], the value of C_s is set as 2.2 [96] while L_{RB} is 0.07 m. With the full-load current $I_a = 0.1$ A and the voltage input $E_a = 5$ V, the maximum applicable torque T_{nf} is found as 1.1 mN·m for the current actuator.

Cylinder Volume Diversity

Now, the IDU is examined with respect to the changes of the diameter of the cylinder tank D_L while its length L_T is kept constant. The IDU model is simulated for three distinct diameter values: $D_L = 0.0092$ m, $D_L = 0.0097$ m (reference value defined

in Table 2.2), and $D_L = 0.01$ m. The simulation results are presented in Fig. 2.8. As can be seen, for the higher volume of the cylinder ($D_L = 0.01$ m) the actuator cannot push the core to the zenith with the reference torque T_m defined in Table 2.2). On the other hand, for the lower volume of the cylinder ($D_L = 0.0092$ m), the peak velocity of the fluid in all the pipes is decreased. However, the fluid pressure in the pipes is raised, which have a great influence on moving the core into further distance compared to the reference value $D_L = 0.0097$ m.

Note that the volume of the cylinder cannot be set to arbitrarily small values due to the design limitations on the size of the cylinder tank. As the cylinder volume shifts in every cycle between A_{CL}^U and A_{CL}^L (refer to Eq. (2.19)), there appears a pressure difference ΔP_P between each cycle changes of the cylinder tank.

Fig. 2.9 shows the pressure difference while there is a transition from both cycles for different diameter values. It is understood that most severe drops happen while fluid circulation changes from the cylinder with bore included area (A_{CL}^U) to fully covered plunger area (A_{CL}^L). Also, the system faces an incremental pressure difference $|\triangle P_P|$ when D_L has a smaller size. Therefore, we have to limit the diameter of the cylinder tank as

$$D_{min} < D_L < D_{max},$$

with the specific values of $D_{min} = 0.0094$ m and $D_{max} = 0.011$ m found from the obtained simulation runs in Fig. 2.8 and Fig. 2.9.

Liquid Characteristics

The liquid characteristics are significant in determining the performance of the IDU. In this connection, we simulate the IDU for following three different liquids varying in their viscosity and density: distilled water ($\rho_f = 1000$ kg/m^3, $\mu_f = 1.81\times10^{-3}$ kg/m·s), ethylene glycol ($\rho_f = 1113.2$ kg/m^3, $\mu_f = 1.61\times10^{-2}$ kg/m·s), and silicone oil ($\rho_f = 971$ kg/m^3, $\mu_f = 9.71\times10^{-3}$ kg/m·s).

Fig. 2.10 illustrates that the viscosity and the density of the liquid have a direct effect on the core motion. This is obvious after passing the transient response of the core motion ($t > 1$ s). If a larger displacement of the core is required, ethylene glycol outperforms the distilled water and silicone oil as it has higher density and viscosity.

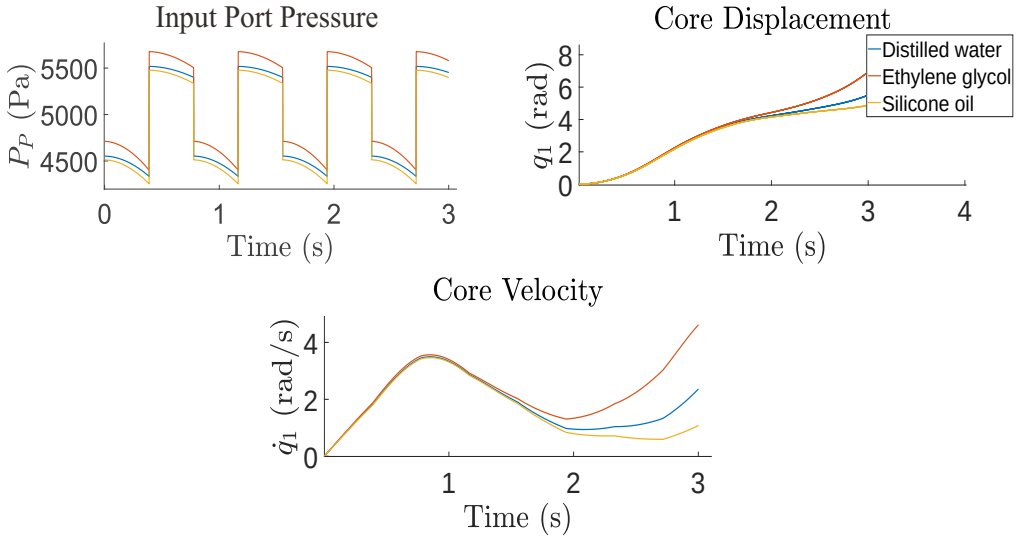

Figure 2.10: The input port pressure of the main pipe, the rotating core position and velocity for various fluids.

Although ethylene glycol results in bigger displacement of the core, the core velocity and the pipe pressure tend to be more nonlinear, featuring large slopes. Thus, if having a lesser slope of the pipe pressure is more important in evaluating the system performance, then the distilled water, which has high density and minimal viscosity, can be the better choice for the propulsion mechanism.

2.4.2 Motion Patterns in Forward Locomotion

Reduced Dynamic Model

In this section, we consider forward locomotion of the robot along Y axis, which corresponds to planar rolling along a line. This motion requires only one pipe and the motion equations established in Section 2.2 are simplified as follows. First, note that the core and the pipe rotate around the unit vector $\mathbf{i}$ of the coordinate frame Σ_O (X axis). The kinematic equations (2.4) are transformed to $\boldsymbol{\Omega}_o = \dot{\theta}\mathbf{i}$ and $\dot{\boldsymbol{\Omega}}_o = \ddot{\theta}\mathbf{i}$. The virtual displacement of the core and the sphere become $\delta\pi_1 = \delta q_1 \mathbf{i}$ and $\delta\pi_o = \delta\theta\mathbf{i}$. Then, the dynamic equations (2.15) are reduced to the following form:

$$\begin{bmatrix} M_{11} & M_{12} \\ M_{21} & M_{22} \end{bmatrix} \begin{bmatrix} \ddot{\theta} \\ \ddot{q}_1 \end{bmatrix} + \begin{bmatrix} N_1 \\ N_2 \end{bmatrix} + \begin{bmatrix} G_1 \\ G_2 \end{bmatrix} = \begin{bmatrix} 0 \\ \tau_1 \end{bmatrix}, \tag{2.34}$$

Table 2.3: Setup variables of the robot dynamics.

Variable	Value	Variable	Value
g	9.8 m/s^2	r_1	0.131 m
M_o	1 kg	R	0.145 m
m_c	0.25 kg	J_o	0.0140 kg·m^2

where $\tau_1 = r_1 F_{d_1}$, and

$$\begin{aligned}
M_{11} &= M_{12} + M_o R^2 + J_o + m_c R^2 - m_c R r_1 \cos(q_1 + \theta) \\
&= M_o R^2 + J_o + m_c R^2 - 2 m_c R r_1 \cos(q_1 + \theta) + m_c r_1^2, \\
M_{21} &= M_{22} - m_c R r_1 \cos(q_1 + \theta) = m_c r_1^2 - m_c R r_1 \cos(q_1 + \theta), \\
N_1 &= m_c R r_1 (\dot{q}_1 + \dot{\theta})^2 \sin(q_1 + \theta), \\
N_2 &= -\text{sgn}\,(\dot{q}_1)\, 0.5 r_1^2 \dot{q}_1^2 \left((f_P L'_P / D_1 g) + C_D \rho_f A_P \right), \\
G_1 &= G_2 = [m_c - \rho_f v_c] g r_1 \sin(q_1 + \theta).
\end{aligned} \tag{2.35}$$

Note that the gravity and buoyancy forces (2.21) and the viscous forces (2.22) are substituted into (2.14). The driving force F_{d_1} is defined as a scalar component in (2.20), i.e., as the product of the fluid pressure and the cross-sectional area. The reduced dynamic model (2.34)- (2.35) is coupled with the linear actuator dynamics (2.18), and the fluid pressure in the pipe is computed by solving algebraic Bernoulli equations (2.25)-(2.26).

Motion Pattern Analysis

In this section, the behavior of the robot controlled by the IDU is studied under simulations. The parameters of the robot are listed in Table 2.3, and the simulation time is set as 4 s. In solving the differential equations (2.18), (2.34) and (2.35), we use ODE45 Matlab solver [40, 94] running with integration step 0.001 s.

The simulation analysis is conducted for two cases. In the first case, the initial state conditions are set as $\left[\theta, \dot{\theta}, q_1, \dot{q}_1\right] = [0, 0, 0, 0]$, and the motor input torque is set constant: $T_m = 0.2$ mN·m, $T_m = 0.24$ mN·m, $T_m = 0.27$ mN·m, $T_m = 0.3$ mN·m. The results are illustrated in Fig. 2.11. We observe that the rolling sphere moves in the main direction (clockwise rotation) with the counterclockwise actuation of the core. The location of the core with respect to the base frame Σ_I, defined as

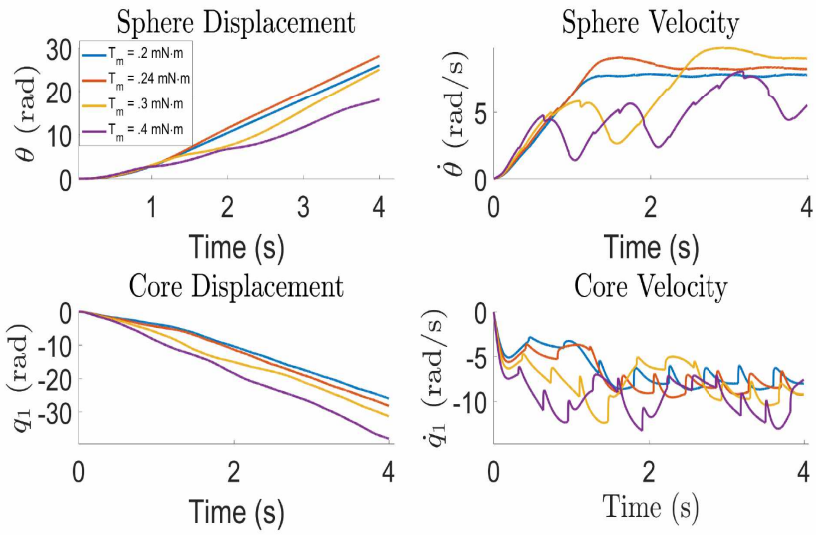

Figure 2.11: The position and velocity of the sphere and the core in the first simulation case.

$|q_1| - |\theta| \in [-\pi, \pi]$, is demonstrated in Fig. 2.12. Note that the fast fluctuations in the core velocity as observed in Fig. 2.11 may affect the physical system because the cylinder rod stops for switching cycles. This issue can be resolved by using multiple cylinders that fill the gap between cycle changes in the cylinder tank.

If the control goal is to bring the core to the north pole, one can define a critical torque T_m similar to what has been done in Section 2.4.1. Based on the obtained results, we can set $T_{cr} = 0.24$ mN·m. This property creates two different motion patterns. For $T_m \leq T_{cr}$ the core remains in the lower hemisphere, and for $T_m > T_{cr}$ the core circulates in the whole pipe.

Interestingly, the higher values of the constant input torque T_m do not necessarily lead to larger displacements of the sphere (see Fig. 2.11). This happens while the core velocity presents large impulse with the given high DC motor torque ($T_m \in [0.3, 0.4]$ mN·m). It can be interpreted that the core rotation in $q_1 \in [-\pi, 0]$ for $T_m > T_{cr}$ affects the clockwise rotation of the sphere aligned with main direction. This issue causes minor backward locomotion of the sphere (see Fig. 2.11). For example, when the core passes the north pole at around 0.6 s with $T_m = 0.4$ mN·m (see Fig. 2.12), the backward locomotion is clearly seen at around 1.5 s (the core arrives at bottom of the sphere) in Fig. 2.11.

In the second simulation case, the initial conditions are $\left[0, \dot{\theta}(0), 0, 0\right]$, where the

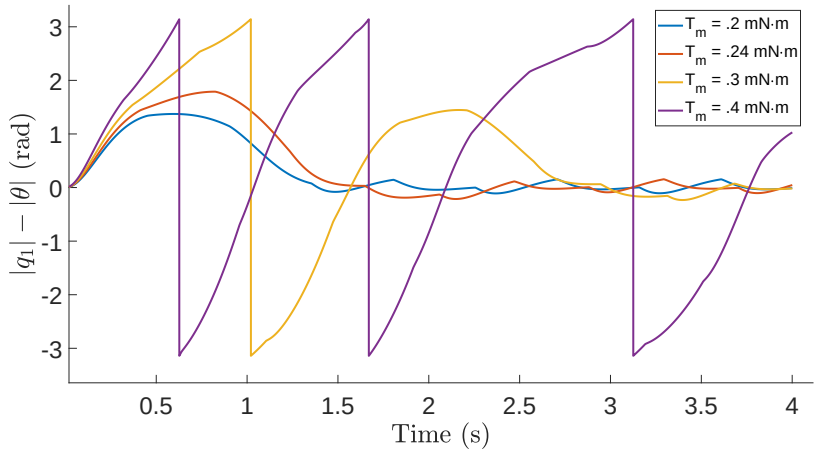

Figure 2.12: The location of the core on sphere with respect to the base frame Σ_I in first simulation case.

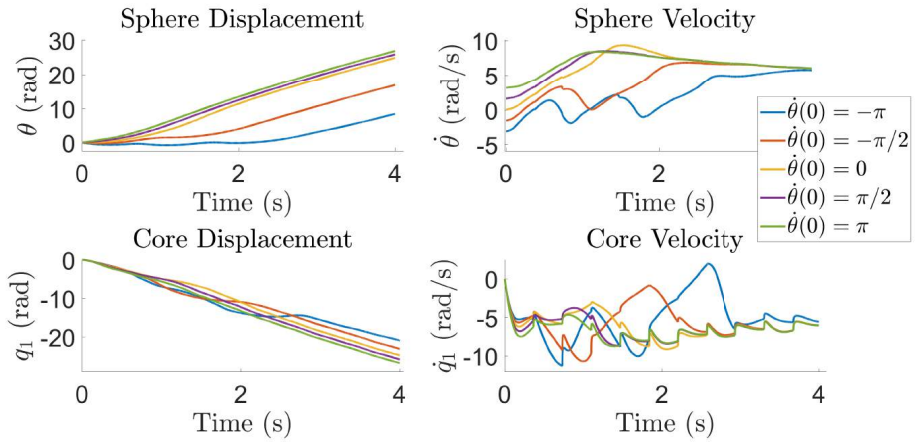

Figure 2.13: The position and velocity of the sphere and the core in the second simulation case.

initial velocity of the sphere $\dot{\theta}(0) \in [-\pi, \pi]$ is not necessarily zero. The control torque is exponentially decaying as $T_m = 0.3e^{-t/T}$ mN·m, where $T = 4$ s. The simulation results are presented in Fig. 2.13. The sphere reaches shorter distances as the initial velocity $\dot{\theta}(0)$ changes from π to $-\pi$. Also, the positive initial velocities of the rolling sphere keep the core in lower-hemisphere as observed from Fig. 2.14. This causes the sphere to reach maximal distances. However, negative velocities of the sphere boost the actuated core to the north pole of the sphere (see Fig. 2.14). This feature can have a negative effect on the final displacement of the sphere similar as it was observed in our first simulation case.

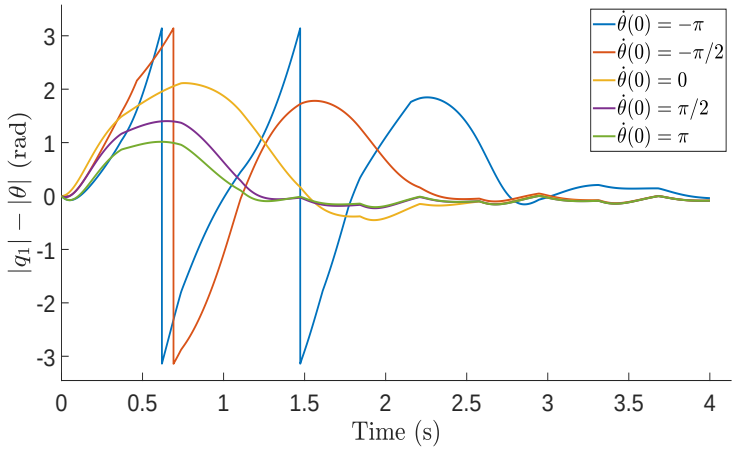

Figure 2.14: The location of the core on sphere with respect to the base frame Σ_I in second simulation case.

Overall, the core works as an effective actuator to locomote the sphere. The sphere can easily accelerate, but the feedback control of the core at higher velocities is indispensable for realizing accurate locomotion. Also, note that the core in the pipe can be imagined as a fish in water [118]. Then, the drag power in the moving core at high velocities becomes proportional to the power of three of the fluid velocity. This issue that may limit the performance of this type of actuation needs to be studied separately.

2.5 Parametric Evaluations on Developed System

2.5.1 Mass Ratio Evaluation

The rotating core in the sphere should have enough mass and momentum to produce the required force to rotate the spherical carrier. To see how this association works in our proposed actuation mechanism, we analyze this property analytically. To obtain an applicable domain of mass ratio for sphere and core

$$m^* = \frac{m_c}{M_o},$$

we study the simulated dynamics via two approaches. First approach evaluates the sphere maximum traversed distance for different m^* values in fixed time interval. In the latter, we change core mass to find a minimum force which brings the core to north state of sphere under the defined conditions.

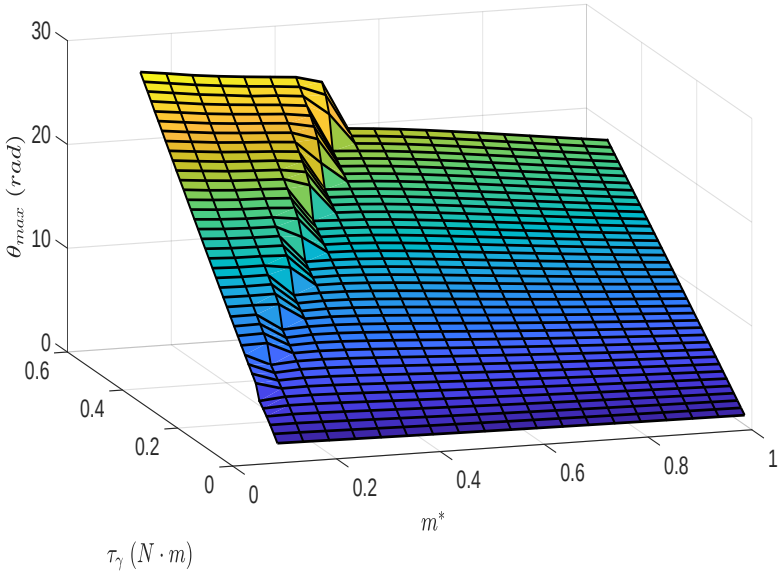

Figure 2.15: Maximum sphere displacement and velocity for different mass ratio within constant input torque range.

In the first approach, the main statement is to find a range with the maximum displacement under the desired physical properties of the mechanism. We check acceptable mass ratio m^* with including step torque input, $\tau_1 = r_1 F_{d_1} u(t)$ where $u(t) = 1$ for $t \geq 0$. Our main objective in this section is to study the rotating mass (core) effect on sphere motion including their inertia so F_{d_1} is constant for simplifying the problem to basic motion analysis. From Eq. (2.7), we know physical forces on the core. In here, we approximate control input as fluid pressure,

$$F_{d_1} \simeq \frac{F_{\Delta P}(A_{CL}^L) + F_{\Delta P}(A_{CL}^U)}{2}, \tag{2.36}$$

where $F_{d_1}(A_{CL}^L)$ and $F_{d_1}(A_{CL}^U)$ are the pressure forces when lower and upper cylinder tank are used, respectively.

Given fluid pressure force F_{d_1} and $M_o = 1$ Kg when mass ratio is $m^* \in [0, 1]$, designed IDU is dependent on our control input in the nonlinear dynamics. Furthermore, the non-dimensionality of m^* helps us to generalize the mass design for heavier M_o (the required core input force by IDU has to be recomputed) since both M_o and $m_c = m^* M_o$ are linearly dependent to state equations (2.34). Upper limit of injected fluid force to core is the maximum DC motor rotational torque and T_{nf} (2.33). Also, because the motor [49] is constrained with size and $0 < m_c \leq M_o$, $3I_a$

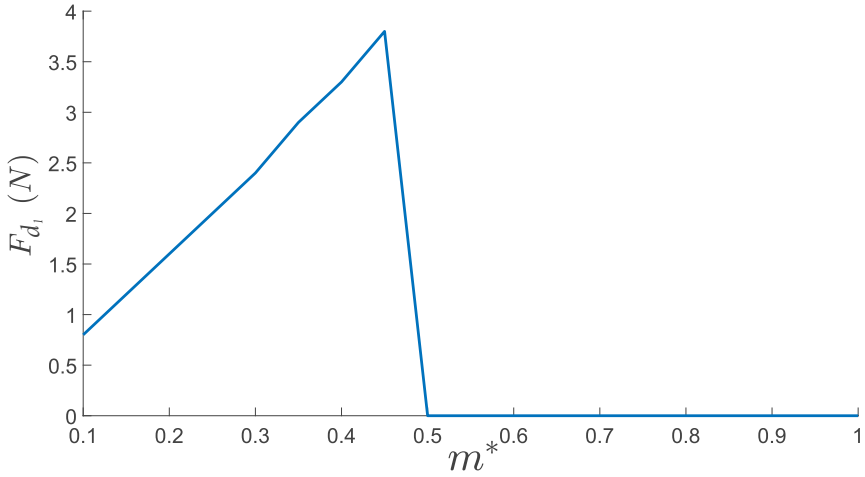

Figure 2.16: Minimum force for rising core to zenith point of sphere with different mass ratio.

becomes the maximum physical current of motor when other parameters are permanently constant i.e., ω_r and E_a. Nevertheless, to extent our study and also show that high motor power is not critical in determining mass ratio range, we check simulation till $10T_m$. To prepare the simulation, we run the dynamics in 2 s. The core starts from south pole of sphere with zero initial velocity, $[\theta \;\; \dot{\theta} \;\; q_1 \;\; \dot{q}_1] = [0 \;\; 0 \;\; 0 \;\; 0]$.

While $m^* < 0.5$, the maximum displacement have greatest range of movement distance [see Fig. 2.15]. Interestingly, increase in the mass of core despite the raise for torque input, does not result in the maximum displacement directly. We knew that with commercially available motors, it is not easy to satisfy the size and mass constraint, even if we ignore performance disadvantages. This means, ideal core mass with given $3I_a$ motor boost is $0.1 \leq m_1^* \leq 0.5$, for this novel rolling robot.

Next approach deals with acceptable range of mass ratio that let core reach north pole with minimum fluid force F_{d_1}. This is important since the robot is designed to circulate the core in pipes. This also means given force to core has to push it to north pole and maybe rotate it consecutive times. The model is simulated with same initial states. Additionally, the physical limit of DC motor is considered with same property of the previous approach. Within 2 s simulation time, we collect F_{d_1} from every iteration, to determine minimum value, if given force fluid let core reaches to north pole, $\max\{|q_1| - |\theta|\} \backsimeq \pi$.

The obtained results from simulation are shown in Fig. 2.16. Note that with given

$10T_m$ pure motor torque, the produced fluid force is not able to bring the core to north pole when $m^* \geq 0.5$. In other words, there is no force ($F_{d_1} = 0$) that can carry core to zenith point with given torque constraint. This is true even for simulation times that exceeds 2 s duration. Also, we see less mass ratio let us actuate the robot with minimum F_{d_1}. More importantly, this core circulation happens while there is $\dot{q}_1 > \dot{\theta}$ velocity relation. This modifies our mass range as

$$0.1 \leq m^* \leq 0.4. \tag{2.37}$$

This shows our reasoning of why we choose mass of the core m_c and mass ratio m^* as 0.25 kg and 0.25 from (2.37), given in Table 2.3. By displacement of designed cores inside tubes, the required robot motion is expected as a semi-linear movement.

2.5.2 Cost of Transport

We discuss the efficiency of robot by utilizing the cost of transport (COT) and power consumption. To know the efficiency of designed robot with novel propulsion mechanism, the cost of transport (COT) [118] is introduced as $\text{COT} = \text{CP}/\left[(M_o + m_c)gV_o\right]$, where CP stands for total consumed power by robot. For our robot, the total consumed power is defined as

$$\text{CP} \triangleq \text{Motor power} + \text{Fluid losses} + \text{Ground friction},$$

which

$$\begin{aligned}
&\text{Motor power} = T_m\omega_r + I_a^2 R_a,\\
&\text{Fluid losses} = \left(f_P \frac{L'_P}{2gD_P} + \frac{1}{2}C_D\rho_f A_P\right)\cdot|r_1\dot{q}_1|^3 + \left(f_{IL}\frac{L_{IL}}{D_{IL}} + K_{S.E.}\right)\cdot\frac{V_{IL}^3}{2g},\\
&\text{Rolling resistance} = \zeta_\theta\dot{\theta}^3.
\end{aligned} \tag{2.38}$$

Here, motor power consists of motor mechanical power and Joule heating. First term in fluid losses is calculated from drag and head loss forces in circular pipe (2.22). Furthermore, second term is head loss in injection line that comes from (2.29). Rolling resistance is obtained from ground-sphere dissipation function. Note that we calculate DC motor current I_a by $(E_a - K_b\omega_r)/R_a$ where K_b and R_a are back-EMF constant and terminal resistance. For chosen DC motor 08GS61, R_a and K_b are 52 ohm and 0.53 [117].

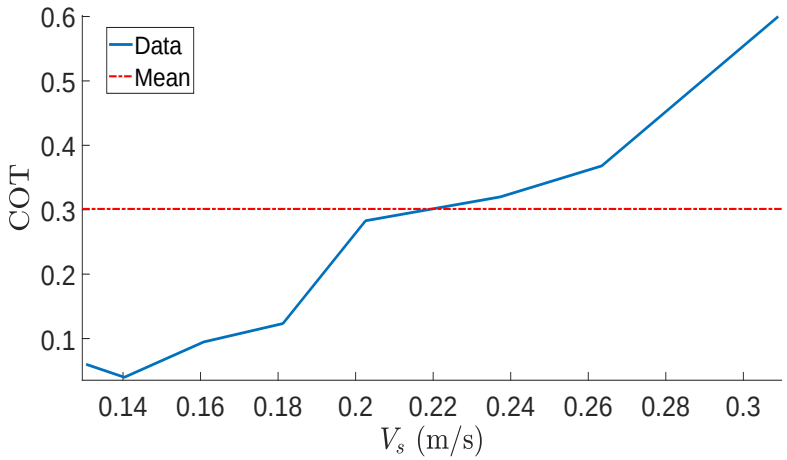

Figure 2.17: Cost of transport (COT) verses sphere linear velocity, V_o.

Fig. 2.17 is showing the achieved cost of transport for different sphere linear velocities by 1.5 sec simulation time. Please note that the input motor torque was $T_m \in [0, 0.17]$ mN·m where core is osculating in lower-hemisphere. It is interesting that robot has energy efficient model, mean COT of 0.3, in displacement along a straight path by comparison to other robot actuators [86, 118]. For example, legged robots such as Bigdog, ASIMO and MIT Cheetah robots have COT of 15 and 2, 0.5, respectively. Note that efficiency of these propellers are not good enough in low velocities like MIT Cheetah robot (COT $\approx$ 1) [92].

On the other hand, sphere can not conserve its angular momentum for higher velocities ($V_o > 0.3$ m/s). This issue comes from the lack of energy-based controller while accelerated core is circulating. Power consumption of robot for two actuation patterns shows this issue more clear as Fig. 2.18. For the case that core passes upper-hemisphere ($T_m = 0.23$ mN·m), the power consumption is twofold. Also, efficiency of robot drops as COT becomes 0.89. This is the consequence of sphere velocity drop in upper-hemisphere which confirms our interpretations in robot motion evaluations [see Fig. 2.11]. Also, we see that most of power consumption is about fluid circulation in injection line.

Overall, core works as an effective actuator to manipulate the sphere in given frame but to determine pros and cons of two motion patterns, system requires advance control study to improve displacement. This issue would improve the total efficiency by reaching higher velocities.

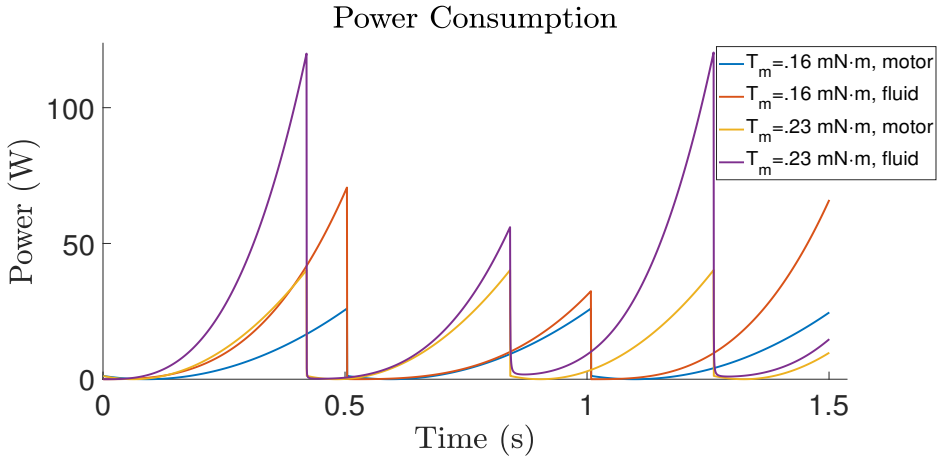

Figure 2.18: Power consumption of motor and circulating fluid for two patterns of sphere motion.

2.6 Inverse Dynamics-Based Motion Control

In this section, we consider an inverse-dynamics based motion planning for a rest-to-rest planar displacement of the robot. The planning problem can be formulated for two cases. In the first case, the motion of the core $(q_1(t),\ \dot{q}_1(t),\ \ddot{q}_1(t))$ is given, and in the second case, the motion of the sphere $(\theta(t),\ \dot{\theta}(t),\ \ddot{\theta}(t))$ is prescribed by our given time functions.

In the first case, the constraint equation in (2.34) is re-arranged as

$$\ddot{\theta} = -\frac{1}{M_{11}}\left(M_{12}\ddot{q}_1 + N_1 + G_1\right), \tag{2.39}$$

and the second equation in (2.34) is utilized for establishing the driving torque. The singularity (similar to the one established for pendulum driven rolling robots in [14, 61]) may appear in (2.39) when M_{11} becomes zero. It can be displaced that

$$M_{11} = (M_o R^2 + I_w + I_s) + m_c\Big(R^2 - 2Rr\cos(q_1+\theta) + r_1^2\Big),$$

and the condition $M_{11} > 0$ always holds true since

$$M_o R^2 + I_w + I_s > 0,$$

and then,

$$R^2 - 2Rr_1\cos(q_1+\theta) + r_1^2 \geq (R-r_1)^2 \geq 0.$$

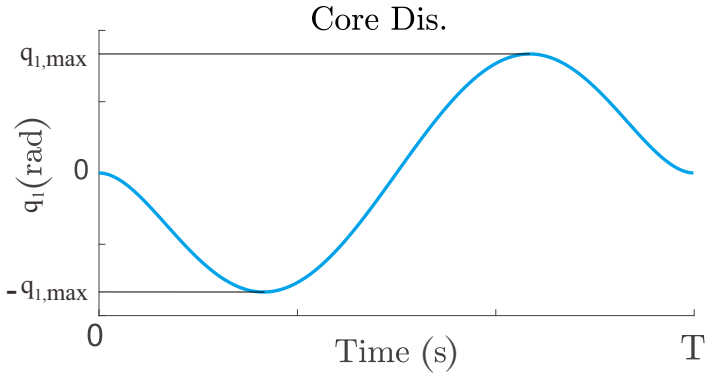

Figure 2.19: Two-phased motion of the rotating core with using the defined Beta function.

Similar to what has been developed in [104], we presume that the core follows a two-phased motion profile shown in Fig. 2.19. In the first phase of this scenario, the core moves counterclockwise to $-q_{1,max}$, and in the second step, it returns to zero states moving clockwise. This motion profile can be captured by the 2nd order derivative of the 4th order Beta function, that is

$$q_1(t) = a\left(-\frac{840}{T^7}t^5 + \frac{2100}{T^6}t^4 - \frac{1680}{T^5}t^3 + \frac{420}{T^4}t^2\right), \tag{2.40}$$

where T is the given movement duration, and the amplitude a is defined for the condition that $\theta(T) = \theta_{\text{des}}$, where θ_{des} is the desired displacement of the sphere. Then, we can show that with the selection of this motion pattern the condition $\dot{\theta}(T) = 0$ is always satisfied.

In the second case, when the motion of the rolling sphere is specified by a time function, first constraint in (2.34) is rearranged as

$$\ddot{q}_1 = -\frac{1}{M_{12}}\left(M_{11}\ddot{\theta} + N_1 + G_1\right), \tag{2.41}$$

and the second equation in (2.34) is used for establishing the driving torque.

We can shown that the singular free condition $M_{12} > 0$, that is

$$I_w + m_c r_1^2 - m_c R r_1 \cos(q_1 + \theta) = m_w r_1^2 + \frac{3}{16} m_w D_c^2 + m_c r^2 - m_c R r_1 \cos(q_1 + \theta) > 0. \tag{2.42}$$

It is important to note that this condition is harder to be satisfied since we have varying cosine which requires more strict condition for having singular free model.

Then, this condition is satisfied (Strong Inertial Coupling condition [97]) for any q_1 and θ if

$$\frac{m_w}{m_c}\Big(1+\frac{3D_c^2}{16r_1^2}\Big)+1>\frac{R}{r_1}. \tag{2.43}$$

Note that neglecting the mass of fluid ($m_w=0$) leads to $R/r_1<1$, which does not hold true and thus implies the existence of singular configurations when M_{12} becomes zero. However, the proper selection of the mass of the fluid so that condition (2.43) is satisfied, removes the singularity from consideration.

Next, the motion of the sphere in the second case can be specified with the use of the Beta function of the 4-th order, that is

$$\theta(t)=a\left(-\frac{20}{T^7}t^7+\frac{70}{T^6}t^6-\frac{84}{T^5}t^5+\frac{35}{T^4}t^4\right), \tag{2.44}$$

where $a=\theta(T)$. Having established motion of the robot, $\theta(t)$ and $q_1(t)$ (by integrating (2.39) or (2.41), depending on the chosen case) and having computed the driving torque $\tau_1(t)$, we define the the fluid pressure P_p in the circular pipe. Note that the driving torque τ_1 is related to P_p as [2]

$$\tau_1=r_1P_pA_c. \tag{2.45}$$

Thus, by substituting the second equation in (2.34) with the terms from (2.35) (apparent length L_p' and Darcy friction f_p) into (2.45), one obtains

$$\begin{aligned}P_p &= \frac{1}{r_1A_c}\Big(M_{21}\ddot{\theta}+M_{22}\ddot{q}_1+N_2+G_2\Big)=\frac{1}{r_1A_c}\Big[\left(m_cr_1^2-m_cRr\cos(q_1+\theta)\right)\ddot{\theta}\\ &+ m_cr_1^2\ddot{q}_1-0.5r_1^2\mathrm{sgn}(\dot{q}_1)\left((n_1/V_l)+n_2\right)\dot{q}_1^2+\left(m_c-\rho_f\nu_c\right)gr_1\sin(q_1+\theta)\Big], \end{aligned}\tag{2.46}$$

where the constant terms n_1 and n_2 are defined as follows,

$$n_1=\frac{64\mu_fA_c}{D_cg\rho_fA_{cl}}, n_2=K_b/g+C_D\rho_fA_c.$$

Note that the fluid pressure P_p in entering port depends on not only θ and q_1 and their derivatives, but also the velocity of the linear actuator V_l.

Having the fluid pressure P_p, we can then obtain the DC motor torque input T_m with the using the Bernoulli equation (2.26). Note that the pressure in the cylinder tank, P_{cl}, is related to the motor torque T_m as [2] $P_{cl}=F_{cl}/A_{cl}=(2\pi\eta/A_{cl})T_m$. Thus,

Table 2.4: Parameters of the robot.

Variable	Value	Variable	Value	Variable	Value
K_{se}	0.9	K_b	0.2	l	0.007 m
μ_l	0.75 kg	m_l	0.2 kg	η	96%
M_s	1 kg	r_1	0.131 m	L_T	0.05 m
μ_f	1.81×10^{-3} kg/m $\cdot$ s	γ_{il}	10^o	I_s	0.0140 kg$\cdot$m^2
D_c	0.028 m	D_{il}	0.00635 m	D_1	0.0047 m
C_D	0.8	m_c	0.25 kg	ρ_f	1000 kg/m^3
g	9.8 m/s^2	R	0.145 m	D_2	0.0097 m
L_p	0.411 m	L_{il}	0.145 m	I_w	0.0086 kg$\cdot$m^2

upon rearranging equation (2.26) with inclusion of the head-loss (2.29), it becomes as follow

$$T_m = \frac{1}{m_1}[P_p - m_2 V_l^2 + m_3 V_l^{\frac{7}{4}} - \rho_f g(Z_{il} - Z_p(1 - \cos\gamma_{il}))], \tag{2.47}$$

where

$$m_1 = \frac{2\pi\eta}{lA_{cl}},\ m_2 = \frac{\rho_f}{2}\left[1 - (A_{cl}/A_c)^2 - (A_{cl}^2 K_{se}/A_{il}^2)\right],$$
$$m_3 = \left[0.158\left(L_{il}^3 \rho_f^3 \mu_f A_{cl}^7\right)^{\frac{1}{4}}\right] / \left(A_{il}^{\frac{7}{4}} D_{il}\right).$$

When the expression of the motor torque is established, the states of the linear actuator, X_l and V_l, can be defined by integrating system (2.18).

2.7 Simulation Results of Feed-Forward Control

In this section, the two control strategies outlined in Section 2.6 are tested under simulation. In the simulations, the time duration is set as $T = 6$ s. The initial values for $q_1(0)$, $\dot{q}_1(0)$, $\theta(0)$, $\dot{\theta}(0)$, $X_l(0)$, and $V_l(0)$ are zero. The desired position of the sphere are set as $\theta(T) = 3$ rad and $\dot{\theta}(T) = 0$ rad/s. The desired position of the core are set as $q_1(T) = 0$ rad and $\dot{q}_1(T) = 0$ rad/s. We use the parameters of the rolling robot which are listed in Table 2.4. The integration of motion equations is done with the use of Matlab ODE45 function. The integration step in this simulation is set as 0.006 s and the relative accuracy is set as 0.001. In the simulations, the velocity of the linear actuator, V_L, is reset to zero every-time the rod reaches the end of the cylinder. The sign changes of V_L presents the flow direction inside the pipes as it comes from

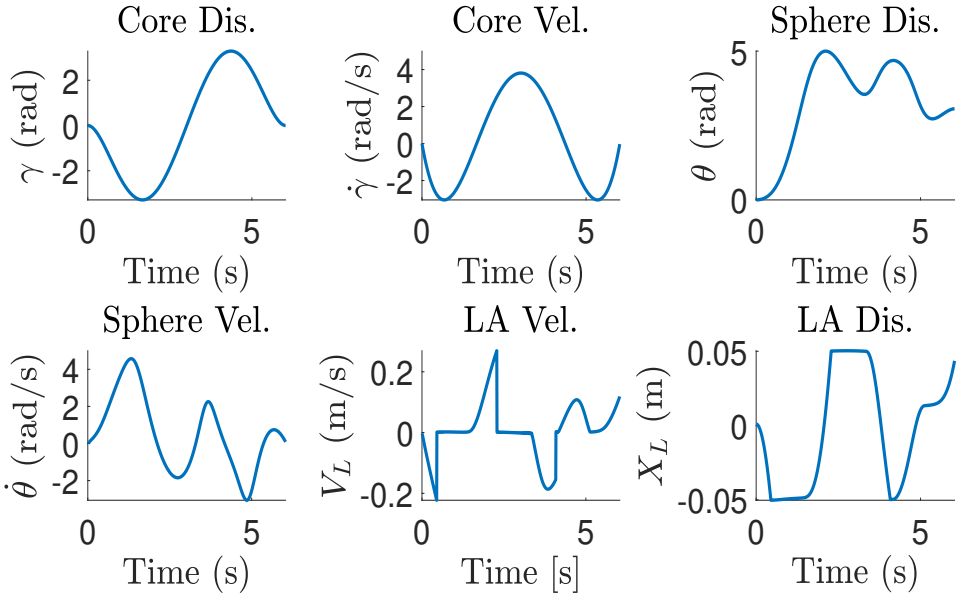

Figure 2.20: Results of inverse dynamics in simulation of the first case.

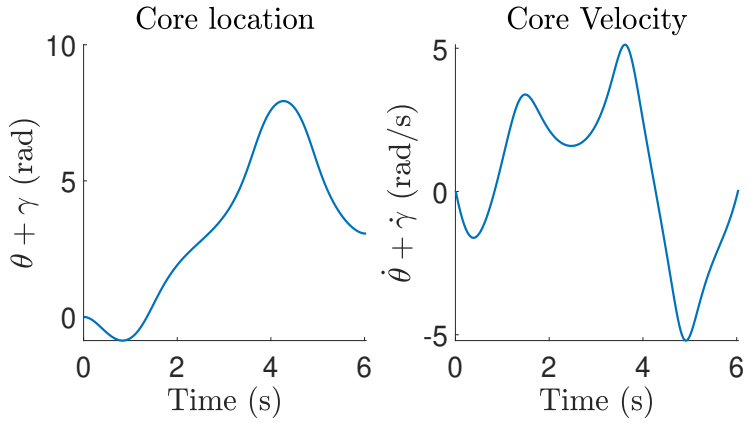

Figure 2.21: The core location and velocity respect to base frame in first case.

solving (2.47) with P_p and V_l as variables. When the fluid is sucked from the input port (it is connected to the circular pipe) by the cylinder, the states $\{X_l, V_l\}$ have negative values. However, when the circulating fluid is pushed from the cylinder to the circular pipe, they have positive values. In physical systems, the flow direction is controlled by control valves (see [2,107] for the control valves integrations as Fig. 2.3).

In the first case, the motion of the core is specified by (2.40) while one can find $a = -15.92$ rad from the condition $\theta(T) = 3$ rad. The simulation results are presented in Fig. 2.20-2.21. We can observe that the given motion of the core results in a desired

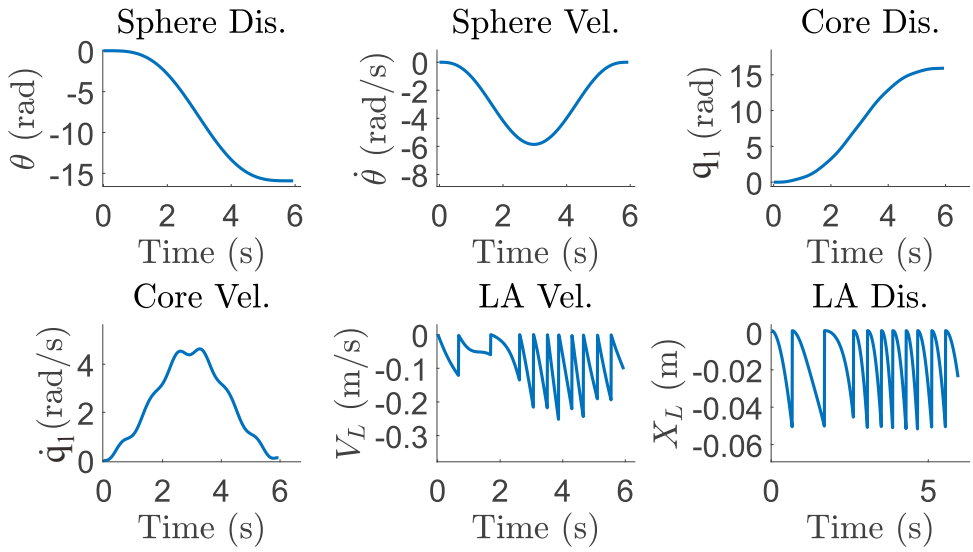

Figure 2.22: Results of the inverse dynamics in simulation of the second case.

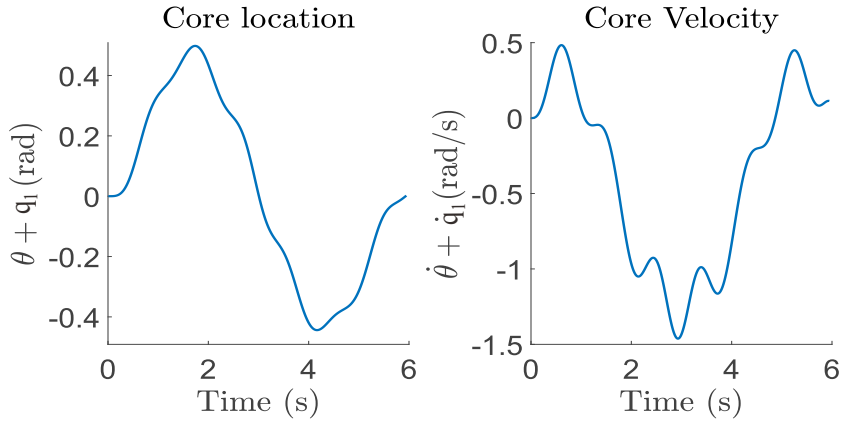

Figure 2.23: Core location and velocity respect to base frame in second case.

rest-rest displacement of the sphere. As the core moves to the upper-hemisphere, the core's circulation begins to dissipate the positive velocity of the sphere. In particular, after 2.5 s, where the core passes the highest point of the sphere (see Fig. 2.21), the rest of its rotation creates a negative sphere velocity as opposed to the positive one (see Fig. 2.20 for $\dot{\theta}$). The dynamics of the linear actuator states are illustrated in Fig. 2.20. The desired actuation of the sphere is successfully created by the driving mechanism. However, note that the dynamics of the linear actuator are not at rest at the final moment of simulation time.

In the second case, the motion of the sphere is specified by (2.44) where the

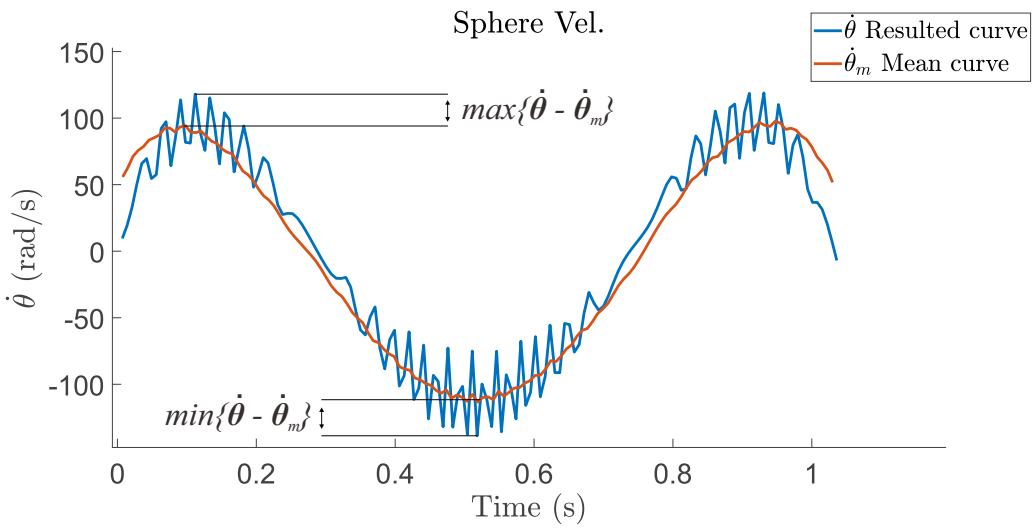

Figure 2.24: Example simulation to compute maximum amplitude change $\Delta\dot{\theta}$ for the case that the core states are specified.

parameter a is set to 3 rad. The motion of the core is obtained by integrating (2.41). The simulation results are obtained in Fig. 2.22 and Fig. 2.23. The absolute position of the core (q_1+θ) follows, the two-phased motion pattern as in the first case but with minor oscillations. Nevertheless, the core (q_1) stays at the lower-hemisphere (see Fig. 2.23). One can notice that the dynamics of the linear actuator are not at rest at the final moment of time. It is more important to note that the velocity of the core is not exactly zero (although very close to it). In contrast to the first case where the rest-to-rest motion is ensured (the formal proof can be constructed for the pendulum-actuated robot), the convergences of $\dot{q}_1$ to zero cannot be guaranteed.

To evaluate the performance of the feed-forward control strategies, we now simulate the motion of the robot for different time constants $T \in [1.5, 3]$ and desired sphere position $\theta_{des} \in [0, 10]$. The purpose of these simulations is to evaluate the level of oscillations in the velocity profiles of the core or the sphere depending on the selected control strategy. To generalize this study into a single scheme, we define x to be the variable which is the numerical integration (the variable that is not specified directly by a given function of time). Hence, x stands for either θ (calculated from solving Eq. (2.39) in the 1st control strategy) or q_1 (found from solving Eq. (2.41) in the 2nd control strategy).

Next, we define the maximum amplitude change $\Delta\dot{x}$ of the velocity signal via

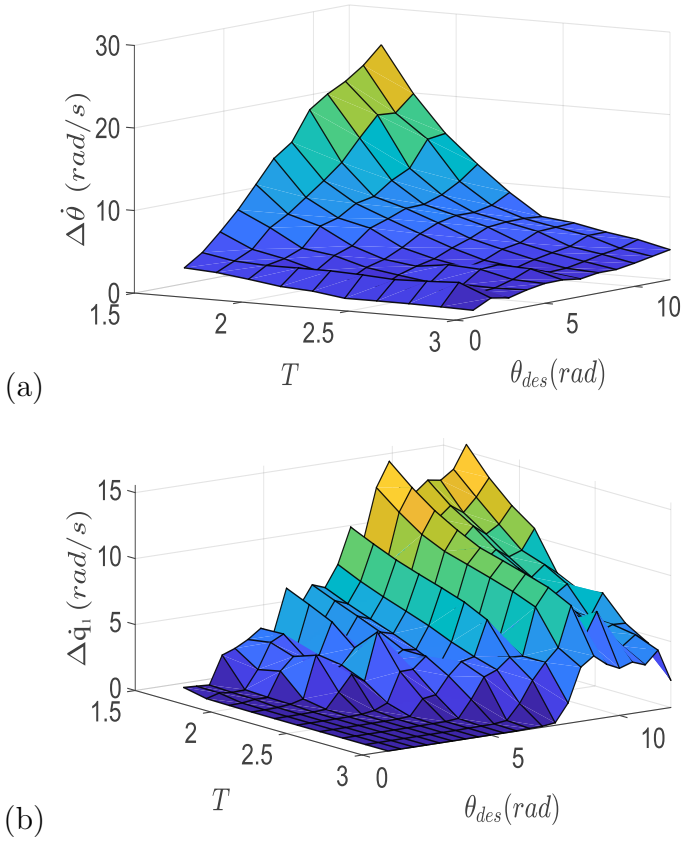

Figure 2.25: a) Velocity fluctuation of carrier state when core states are given, b) Velocity fluctuation of the core when carrier states are given.

comparing the value $\dot{x}(t)$ with the filtered curve (refers to Fig. 2.24 as an example of $x = \theta$) as

$$\Delta\dot{x} = \left| \max_{t\in[0,T]} \{\dot{x}(t) - \dot{x}_m(t)\} + \min_{t\in[0,T]} \{\dot{x}(t) - \dot{x}_m(t)\} \right| /2, \tag{2.48}$$

where $\dot{x}_m$ is the filtered curve of $\dot{x}$ found as the backward-looking moving average by

$$\dot{x}_m(t) = \frac{1}{w} \int_{t-w}^{t} \dot{x}(\tau) d\tau$$

where w is moving average window size set as 0.1 s in our simulations.

The simulation results are shown in Fig. 2.25. For the case when the motion of the core is given (see Fig. 2.25-a), the rolling sphere velocity does not have serious oscillations. However, as the movement duration T decreases, and the traveling distance θ_{des} increases, the sphere velocity has larger fluctuations. This feature also holds true for the case when the locomotion of the sphere is given (see Fig. 2.25-b),

however, the motion profile is more oscillating compared to the first movement strategy. As an exception, note that the peak value of the given core case $\Delta\dot{\theta}$ is very high in contrast to the given sphere case $\Delta\dot{q}_1$ at $T \leq 2$ s and $\theta_{des} > 8$ rad. Thus, if the motion of the core is assigned directly ($T > 2$ s), the amplitude of the oscillations of the speed is lesser compared to the case when the motion of the sphere is assigned. Finally, we can interpret that the control based on the Beta function (or any other continuous function used in specifying the desired motion) would not be suitable for a proportionally short movement duration and a relatively long traveling distance.

Chapter 3

Sensor Design for Tracking the Rolling Robot's Rotating Core in the Pipe by Inertial Measurement Unit

3.1 Introduction

This chapter a motion tracking system for the proposed rolling system is designed to track the rotating core inside the pipes. Also, we propose a generic compensatory filter to do the motion tracking by inertial measurement under the magnetic disturbances. In this mechanism, not only there are hard ferromagnetic materials as permanent magnets to properly track the core but also there are soft ferromagnetic effects due to magnetized stainless steel core. Thus, the sensor fusion is developed relatively to increase the accuracy of estimation.

Certain filters in the sensors fusion topic are designed with accelerometers and magnetometers for low-frequency gyroscopes to measure faster changes in the orientations [12, 33]. However, there have been important challenges due to magnetic disturbances which can come from the outside environment or obligatory ferromagnetic materials in the mechanisms and robots [13]. Roetenbergt et al. proposed a complementary filter to minimize the magnetic disturbances [87]. However, these works still face great deviations and errors when ferromagnetic items get involved as it was discussed in Refs. [13,87]. This makes great challenges for robotic applications when actuators or ferromagnetic mechanisms are placed in the near proximity of IMU sensors.

As the contribution of this chapter, an experimental setup to track rotating spherical mass (core) inside the pipe is designed. A generic filter to compensate the effects of magnetic disturbances based on the Kalman filter is designed. Another important contribution of this chapter is to raise a question in angular motion tracking by fused inertial sensors that consist of accelerometer, gyroscope, and magnetometer. We question whether having the on-board permanent magnets with proper filter design

work as a magnetic shield to increase the accuracy of estimation? We observe that our strategy can extend the application of inertial measurement units in the actuators and robots that magnetic disturbances are predominant. Because the core position in pipe can be determined by the following proposed tracking sensor, we can develop different feedback strategies to control the rotating mass (core) in the pipe to propel the rolling robot in a better way.

We have organized this chapter as follows. The experimental setup for verifying our findings is explained in Section 3.2. In Section 3.3, the models of the signals for each sensor are established. Next, the filter structure is described and the structure of fused sensor models is shown. The results of the proposed filter is compared with the QUEST filter about its performance with a developed experiment in Section 3.4.

3.2 Experimental Setup

In order to verify a motion tracking filter that tracks the rotating core in the pipes, we use a setup consisting of two identical IMU sensors [see Fig. 3.1]. This provides a better comparison regarding the performance of the proposed filter.

The setup contains a spherical rotating mass (core) with stainless-steel material (soft ferromagnetic material) inside a circular smooth plastic pipe. The goal is to track this rotating mass inside the pipe by an externally attached carrier S_t. This setup primary purpose is to study a fluid-actuated mechanism for rolling robots [2,107,109] which explicitly discussed in Chapter 2. This model of tracking sensor not only it has usage in the aforementioned propulsion mechanisms, but also it can have useful applications on the pipe crack detection systems [47] and inspection robots in the closed areas like pipes [11, 42, 81, 123]. Because placing a tracking sensor inside the spherical metallic core is not practically possible, the carrier should be placed outside of the pipe. This carrier contains two couple of Neodymium magnets. The purpose of the central magnets (each with 17.9 N magnetic force) is to produce the required force to follow the rotating core, and off-centered magnets with 7.6 N magnetic force each is to keep the tracking sensor always aligned with the core. Note that off-centered magnets can not minimize all the distortions that come from the vibrations of the magnetized core (varying magnetic flux density). Because this type of tracking mechanism requires a fast-tracking of the core location, the IMU sensor is placed

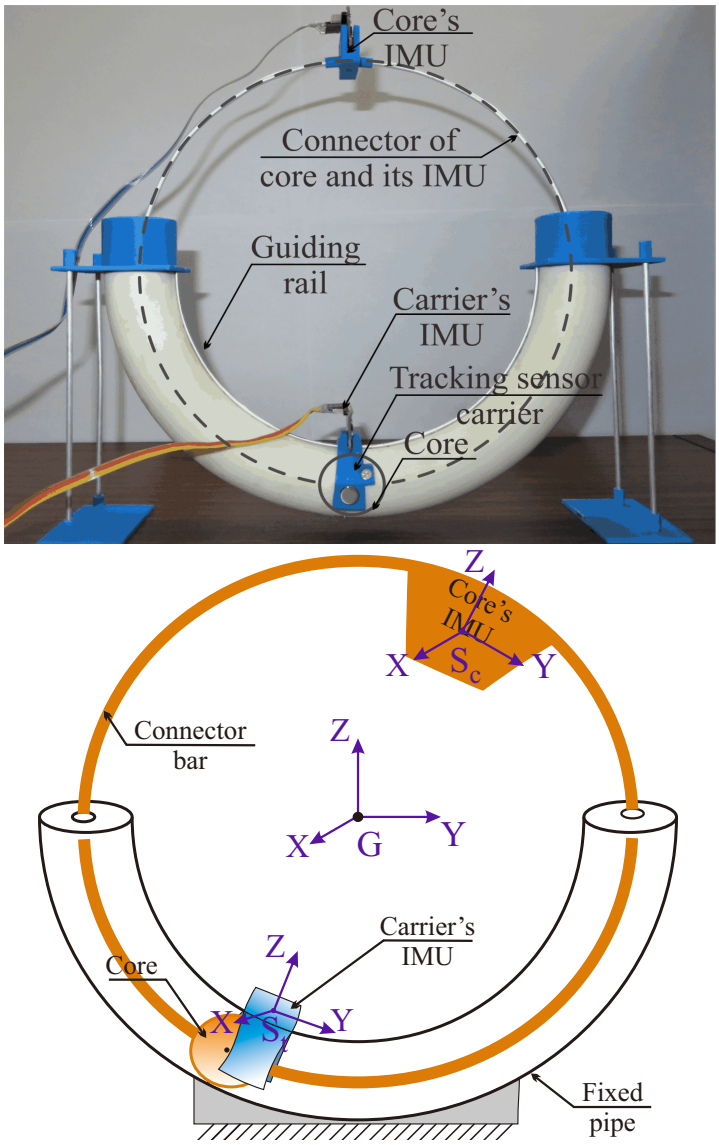

Figure 3.1: Experimental setup and frame transformations.

on the carrier sensor. Also, to verify our findings and compare the results with the second IMU sensor connected to the rotating core S_c, to know the true location of the core. Note that the core's IMU is free from any magnetic effects of the ferromagnetic materials since it always has an approximately 0.262 m distance from the core and magnets [13]. IMU consists of the gyroscope device with the model of L3GD20. Also, the LSM303D model is for the accelerometer and magnetometers.

Fig. 3.2 illustrates the simulation of the magnetic flux of the tracking carrier. The magnetic flux is simulated by using the EMS toolbox of the SolidWorks after

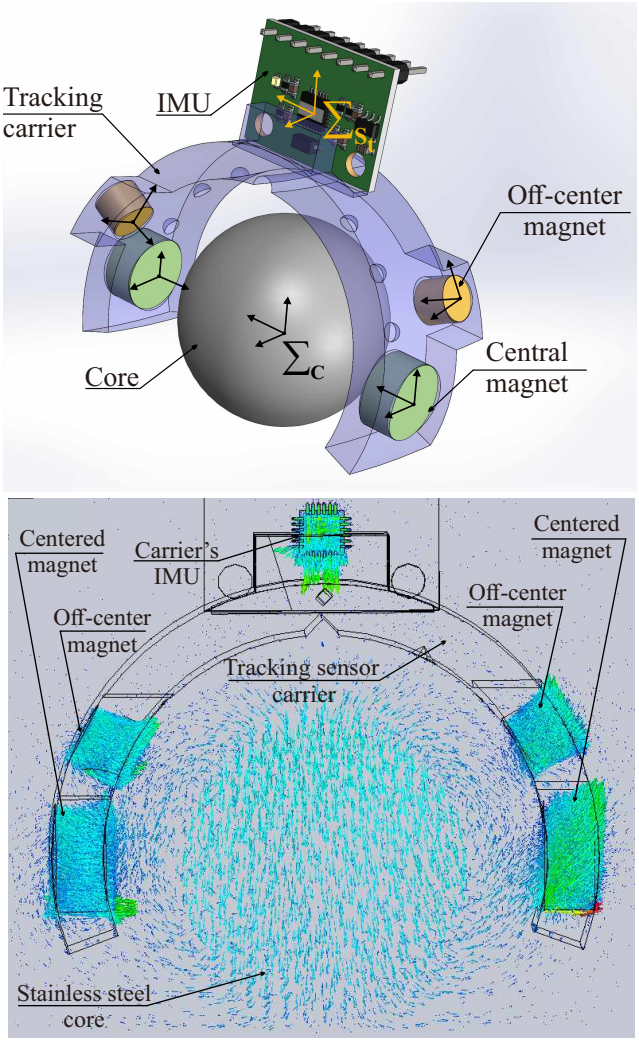

Figure 3.2: Schematic and magnetic flux map for the considered tracking carrier sensor.

designing the solid models of the bodies. It is clear that IMU is getting affected by the permanent magnets, in particular along the Z axis. Also, there is soft ferromagnetic material magnetization which creates the secondary flux. This means if the core deviates from its centralized location between the magnets, there will be magnetic disturbances depending on the distance of deviation from the central magnets.

3.3 Sensor Fusion

The angular position of a sensor carrier that has the mounted ferromagnetic materials require combing data of the different sensors. This problem also demands a new

approach in the model design of the complementary filter that not only the estimation uses the magnetic sensor feed, but also it should not be deviated due to strong disturbances and biases on the certain axes of the magnetometer. Thus, the filter is designed relatively by using a Kalman filter. In this section, we first explain the sensors in the IMU and their models before deriving the filter's model.

3.3.1 Models of the Sensor Signals

In order to track the orientation of the carrier, the inertial measurement unit (IMU) is utilized. Note that here we use two identical IMU sensors for verifying the proposed filter [see Fig. 3.1]. The IMU sensor consists of accelerometer $\mathbf{y}_a$, gyroscope $\mathbf{y}_g$ and magnetometer $\mathbf{y}_m$. The sensor data is captured with respect to the sensor frame S. The sensor that is under the magnetic disturbance as the core's tracking sensor has a coordinate frame of S_t. The second sensor has a coordinate frame of S_c that is for verifying our findings (in contrast to S_t) without permanent magnets' effects while it has the accurate location of the core. The IMU sensors are rotating with respect to global coordinate frame G as follows

$$^{GS}\mathbf{R} = \left[{}^{S}\mathbf{X} \;\; {}^{S}\mathbf{Y} \;\; {}^{S}\mathbf{Z} \right]. \tag{3.1}$$

The measured signals from magnetometer $\mathbf{y}_m$, gyroscope $\mathbf{y}_g$ and accelerometer $\mathbf{y}_a$ in k-th sample at sensor frame S are defined with following equations [87]

$$\mathbf{y}_m = \mathbf{h}_k + \mathbf{d}_k + \mathbf{v}_m, \tag{3.2}$$

$$\mathbf{y}_g = \boldsymbol{\omega}_k + \mathbf{b}_k + \mathbf{v}_g, \tag{3.3}$$

$$\mathbf{y}_a = \mathbf{a}_k - \mathbf{g} + \mathbf{v}_a, \tag{3.4}$$

where $\mathbf{h}_k$, $\boldsymbol{\omega}_k$, $\mathbf{a}_k$ and $\mathbf{v}$, $\mathbf{g}$ are the sum of magnetic fields including the earth, the angular velocity and acceleration terms of carrier sensor, the white noise in each signal and the gravity vector, respectively. Also, the bias of gyro $\mathbf{b}_k$, acceleration signal $\mathbf{a}_k$ with designed first-order low-pass filter and magnetic disturbance $\mathbf{d}_k$ designed with Markov scheme are

$$\mathbf{d}_k = c_d \cdot \mathbf{d}_{k-1} + \mathbf{w}_d, \tag{3.5}$$

$$\mathbf{b}_k = \mathbf{b}_{k-1} + \mathbf{w}_b, \tag{3.6}$$

$$\mathbf{a}_k = c_a \cdot \mathbf{a}_{k-1} + \mathbf{w}_a, \tag{3.7}$$

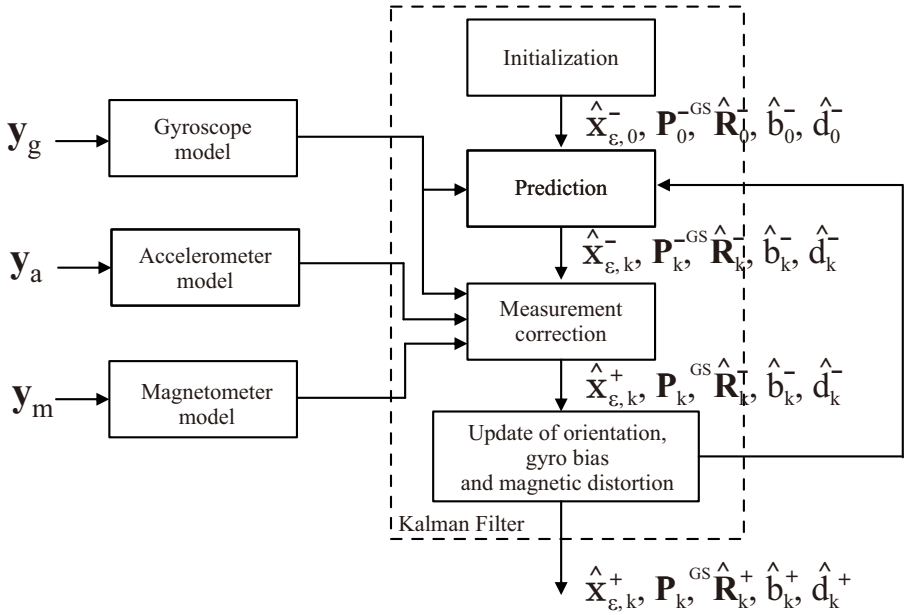

Figure 3.3: Structure of the filter in estimating the state vector $\mathbf{x}$ and covariance matrix $\mathbf{P}$.

where c_a, c_d and $\mathbf{w}$ are the cutoff frequencies for the acceleration and the magnetic field, and the Gaussian noise vector in each signal.

3.3.2 Filter Structure

It is aimed to have a filter that can accurately track the motion while there are deviations and biases on the magnetometer. The model is inspired by different studies [12, 87, 90]. However, these studies did not deal with magnetic deviations when there are ferromagnetic materials in the near vicinity of the IMU sensor.

General Model

We utilize the Kalman filter where it has error models in the state-space presentations for the estimations. Then, the model is presented as follows

$$\mathbf{x}_{\varepsilon,k} = \mathbf{A}\mathbf{x}_{\varepsilon,k-1} + \mathbf{w}_k, \tag{3.8}$$

$$\mathbf{z}_{\varepsilon,k} = \mathbf{H}\mathbf{x}_{\varepsilon,k} + \mathbf{v}_k, \tag{3.9}$$

where $\mathbf{A}$ and $\mathbf{H}$ are the state transition and measurement models, and state vector $\mathbf{x}_{\varepsilon,k} = [\boldsymbol{\theta}_{\varepsilon,k} \;\; \mathbf{b}_{\varepsilon,k} \;\; \mathbf{d}_{\varepsilon,k}]^T$ are defined by the orientation error $\boldsymbol{\theta}_{\varepsilon,k}$, the error of the gyroscope bias $\mathbf{b}_{\varepsilon,k}$ and the error of the magnetic disturbance $\mathbf{d}_{\varepsilon,k}$. The measurement states are the acceleration error $\mathbf{z}_a$, the inclination error $\mathbf{z}_i$ and the magnetic error inputs $\mathbf{z}_m$ as $\mathbf{z}_{\varepsilon,k} = [\mathbf{z}_a \;\; \mathbf{z}_i \;\; \mathbf{z}_m]^T$. Also, $\mathbf{w}_k$ and $\mathbf{v}_k$ variables are the process and measurement noises, respectively. The flowchart in Fig. 3.3 demonstrates the designed complementary Kalman filter for estimating the orientation.

Prediction

This step in the proposed filter [see Fig. 3.3] predicts the considered states $\mathbf{x}_{\varepsilon,k}$ and uncertainty matrix $\mathbf{P}_k^-$. To construct the state transition matrix $\mathbf{A}$, at first, the *priori* bias error of gyroscope is determine by

$$\hat{\mathbf{b}}_{\varepsilon,k}^- = \hat{\mathbf{b}}_k - \mathbf{b}_k, \tag{3.10}$$

where $\hat{\mathbf{b}}_k = \hat{\mathbf{b}}_{k-1}$ is the prediction of the gyroscope bias. Then, after substituting (3.6) and the relation of the prediction of the gyroscope bias $\hat{\mathbf{b}}_k$ into (3.10), one gets

$$\hat{\mathbf{b}}_{\varepsilon,k}^- = \hat{\mathbf{b}}_{\varepsilon,k-1}^+ - \mathbf{w}_b, \tag{3.11}$$

where $\mathbf{b}_{\varepsilon,k-1}^+$ is a *posteriori* error estimate of the bias which is presented with $+$ superscript. Also, the same calculations take place for predicting the error of the magnetic disturbances as follows

$$\hat{\mathbf{d}}_{\varepsilon,k}^- = \hat{\mathbf{d}}_{\varepsilon,k-1}^+ - \mathbf{w}_d, \tag{3.12}$$

where $\mathbf{d}_{\varepsilon,k-1}^+$ is a *posteriori* error estimate of the magnetic disturbances.

The estimated rotation of the carrier ${}^{GS}\hat{\mathbf{R}}$ with the sensor is assumed with minimum orientation error. Then, the *priori* estimated rotation ${}^{GS}\hat{\mathbf{R}}^-$ is defined by a linear model [23]

$${}^{GS}\hat{\mathbf{R}}_k^- = {}^{GS}\hat{\mathbf{R}}_{k-1}^+ \left(\mathbf{I}_3 + [\boldsymbol{\theta}_{\varepsilon,k-1}^+ \times]\right), \tag{3.13}$$

where $[\boldsymbol{\theta}_{\varepsilon,k-1} \times]$ is the skew-symmetric matrix that the skew presentation is as bellow, for an example

$$[\boldsymbol{\theta} \times] = \begin{bmatrix} 0 & -\boldsymbol{\theta}_z & \boldsymbol{\theta}_y \\ \boldsymbol{\theta}_z & 0 & -\boldsymbol{\theta}_x \\ -\boldsymbol{\theta}_y & \boldsymbol{\theta}_x & 0 \end{bmatrix}.$$

Next, the *priori* prediction of the orientation error $\hat{\boldsymbol{\theta}}^{-}_{\varepsilon,k}$ in k-th step is found by creating a relation between the previous and current state values. We apply the similar kinematic formulation in Ref. [90] as follows

$$\hat{\boldsymbol{\theta}}^{-}_{\varepsilon,k} = \left(\mathbf{I}_3 + T[\hat{\boldsymbol{\omega}}^{-}_{k}\times] + \frac{T^2}{2}[\hat{\boldsymbol{\omega}}^{-}_{k}\times]\right)\boldsymbol{\theta}^{+}_{\varepsilon,k-1} + \left(-T\,\mathbf{I}_3 - \frac{T^2}{2}[\hat{\boldsymbol{\omega}}^{-}_{k}\times]\right)\mathbf{b}^{+}_{\varepsilon,k-1}, \quad (3.14)$$

where Eq. (3.14) is derived by discretization of $\dot{\boldsymbol{\theta}}_{\varepsilon} = [\hat{\boldsymbol{\omega}}^{-}_{k}\times]\boldsymbol{\theta}_{\varepsilon} - \mathbf{b}_{\varepsilon}$ equation and T is the sampling time.

We can write the prediction equations as

$$\hat{\mathbf{x}}^{-}_{\varepsilon,k} = \mathbf{A}\hat{\mathbf{x}}^{+}_{\varepsilon,k-1} + \mathbf{w}_k, \quad (3.15)$$

$$\mathbf{P}^{-}_{k} = \mathbf{A}\mathbf{P}_{k-1}\mathbf{A}^{T} + \mathbf{Q}, \quad (3.16)$$

where $\mathbf{Q}$ is the covariance matrix of process noise. Based on our definitions, the state transition model $\mathbf{A}$ and process noise $\mathbf{w}_k$ are found by using (3.11), (3.12) and (3.14)

$$\mathbf{A} = \begin{bmatrix} \mathbf{I}_3 + T[\hat{\boldsymbol{\omega}}^{-}_{k}\times] + \frac{T^2}{2}[\hat{\boldsymbol{\omega}}^{-}_{k}\times] & -T\,\mathbf{I}_3 - \frac{T^2}{2}[\hat{\boldsymbol{\omega}}^{-}_{k}\times] & \mathbf{0}_{3\times3} \\ \mathbf{0}_{3\times3} & \mathbf{I}_3 & \mathbf{0}_{3\times3} \\ \mathbf{0}_{3\times3} & \mathbf{0}_{3\times3} & \mathbf{I}_3 \end{bmatrix},$$

$$\mathbf{w}_k = \left[\mathbf{0}_{1\times3}\ \mathbf{w}_b\ \mathbf{w}_d\right]^{T}.$$

Finally, we define the covariance matrix of process noise $\mathbf{Q}$ by using trapezoidal integration as [77, 85]

$$\mathbf{Q} = \frac{T}{2}\left[\mathbf{A}\mathbf{G}\mathbf{Q}_n\mathbf{G}^{T} + \mathbf{G}\mathbf{Q}_n\mathbf{G}^{T}\mathbf{A}^{T}\right], \quad (3.17)$$

where $\mathbf{G}$ and $\mathbf{Q}_n$ are the noise-input mapping matrix and our state noise constants.

Measurement Correction

In this step, the Kalman filter corrects the predictions. The measurement model is partially inspired by work in Ref. [87] where different model relations are utilized based on inclination and magnetic field errors. However, we extend this formula with one more term based on acceleration to minimize the effects of the magnetic disturbances. Also, note that the work in [87] did not consider the state transition $\mathbf{A}$ in its model.

The *posteriori* error estimates $\hat{\mathbf{x}}_{\varepsilon,k}^{+}$ in k-th step are updated based on the measurement information $\mathbf{z}_{\varepsilon,k}$ as follows

$$\hat{\mathbf{x}}_{\varepsilon,k}^{+} = \hat{\mathbf{x}}_{\varepsilon,k}^{-} + \mathbf{K}_k \left(\mathbf{z}_{\varepsilon,k} - \mathbf{H}\hat{\mathbf{x}}_{\varepsilon,k}^{-} \right), \tag{3.18}$$

where the Kalman gain matrix $\mathbf{K}_k$ is determined by

$$\mathbf{K}_k = \mathbf{P}_k^{-}\mathbf{H}^T \left(\mathbf{H}\mathbf{P}_k^{-}\mathbf{H}^T + \mathbf{R} \right)^{-1}, \tag{3.19}$$

where $\mathbf{R}$ is the measurement noise covariance. Next, the error covariance is updated for the next step by

$$\mathbf{P}_k = (\mathbf{I}_9 - \mathbf{K}_k\mathbf{H})\mathbf{P}_k^{-}(\mathbf{I}_9 - \mathbf{K}_k\mathbf{H})^T + \mathbf{K}_k\mathbf{R}\mathbf{K}_k^T. \tag{3.20}$$

In our observer model, the measurement inputs $\mathbf{z}_{\varepsilon,k}$ are defined with three different models as follows

$$\mathbf{z}_{\varepsilon,k} = \begin{bmatrix} \mathbf{z}_{a,k} \\ \mathbf{z}_{i,k} \\ \mathbf{z}_{m,k} \end{bmatrix} = \begin{bmatrix} \hat{\mathbf{Z}}_{a,k} - {}^{S}\mathbf{Z}_k \\ \hat{\mathbf{Z}}_{a,k} - \hat{\mathbf{Z}}_{g,k} \\ \hat{\mathbf{M}}_{m,k} - \hat{\mathbf{M}}_{g,k} \end{bmatrix}, \tag{3.21}$$

where ${}^{S}\mathbf{Z}_k$ is the correct inclination vector, $\hat{\mathbf{Z}}_{a,k}$ and $\hat{\mathbf{Z}}_{g,k}$ terms are the estimated inclination of the accelerometer and the gyro, and $\hat{\mathbf{M}}_{m,k}$ and $\hat{\mathbf{M}}_{g,k}$ are the measured magnetic vector subtracted by the estimated magnetic disturbance and estimated magnetic vector based on the gyroscope, which are obtained as follows [12, 87]

$$\hat{\mathbf{Z}}_{a,k} = \frac{\mathbf{y}_a - {}^{S}\hat{\mathbf{a}}_k}{|\mathbf{y}_a - {}^{S}\hat{\mathbf{a}}_k|} = {}^{S}\mathbf{Z}_k + \frac{1}{g}\big(-{}^{S}\hat{\mathbf{a}}_k^{-} \times \boldsymbol{\theta}_{\varepsilon,k}^{-} - c_a \cdot {}^{S}\hat{\mathbf{a}}_{\varepsilon,k-1}^{+} + \mathbf{w}_a + \mathbf{v}_a \big), \tag{3.22}$$

$$\begin{aligned} \hat{\mathbf{Z}}_{g,k} &= {}^{S}\hat{\mathbf{Z}}_{k-1}^{+} - T \cdot {}^{S}\hat{\boldsymbol{\omega}}_k^{-} \times {}^{S}\hat{\mathbf{Z}}_{k-1}^{+} \\ &\approx {}^{S}\mathbf{Z}_k + {}^{S}\hat{\mathbf{Z}}_{k-1} \times \hat{\boldsymbol{\theta}}_{\varepsilon,k}^{-} - T \cdot {}^{S}\hat{\mathbf{Z}}_{k-1} \times \hat{\mathbf{b}}_{\varepsilon,k}^{-} + {}^{S}\hat{\mathbf{Z}}_{k-1} \times T \cdot \mathbf{v}_G, \end{aligned} \tag{3.23}$$

$$\hat{\mathbf{M}}_{m,k} = \mathbf{y}_m - {}^{S}\hat{\mathbf{d}}_k = {}^{S}\mathbf{M}_k - {}^{S}\hat{\mathbf{d}}_k^{-} \times \hat{\boldsymbol{\theta}}_{\varepsilon,k}^{-} - c_d \cdot {}^{S}\hat{\mathbf{d}}_{\varepsilon,k-1}^{+} + \mathbf{w}_d + \mathbf{v}_m, \tag{3.24}$$

$$\begin{aligned} \hat{\mathbf{M}}_{g,k} &= {}^{S}\hat{\mathbf{M}}_{k-1}^{+} - T \cdot {}^{S}\hat{\boldsymbol{\omega}}_k^{-} \times {}^{S}\hat{\mathbf{M}}_{k-1}^{+} \\ &\approx {}^{S}\mathbf{M}_k + {}^{S}\hat{\mathbf{M}}_{k-1} \times \hat{\boldsymbol{\theta}}_{\varepsilon,k}^{-} - T \cdot {}^{S}\hat{\mathbf{M}}_{k-1} \times \hat{\mathbf{b}}_{\varepsilon,k}^{-} + {}^{S}\hat{\mathbf{M}}_{k-1} \times T \cdot \mathbf{v}_G. \end{aligned} \tag{3.25}$$

where ${}^{S}\mathbf{M}_k$ is the correct normalized magnetic field vector at k-th step, ${}^{S}\hat{\mathbf{a}}_{\varepsilon,k-1}^{+} = {}^{S}\hat{\mathbf{a}}_k^{-} - {}^{S}\mathbf{a}_k$ is the *posteriori* acceleration error where ${}^{S}\hat{\mathbf{a}}_k^{-}$ and ${}^{S}\mathbf{a}_k$ are the acceleration estimate which is updated with true orientation (3.13) and reference acceleration vector in S coordinate transformed from the global coordinate G. The equations

(3.23) and (3.25) related to inclination estimate and gyroscope-based estimation of the magnetic vector are found with substitution of the first-order approximation of the strapdown integration step as follows

$$\begin{aligned} {}^{GS}\hat{\mathbf{R}}_k^- &= {}^{GS}\hat{\mathbf{R}}_{k-1}^+ \left(\mathbf{I}_3 + \left[T \cdot \hat{\boldsymbol{\omega}}_k^- \times\right]\right) \\ &= {}^{GS}\hat{\mathbf{R}}_{k-1}^+ \left(\mathbf{I}_3 + \left[\left(\hat{\boldsymbol{\theta}}_{\varepsilon,k}^- - T \cdot \hat{\mathbf{b}}_{\varepsilon,k}^- + T \cdot \mathbf{v}_g\right) \times\right]\right). \end{aligned} \tag{3.26}$$

Finally, $\mathbf{H}$ and $\mathbf{v}_k$ matrices can be constructed by using (3.22)-(3.25)

$$\begin{aligned} \mathbf{H} &= \begin{bmatrix} -\frac{1}{g}[{}^S\hat{\mathbf{a}}_k^- \times] & \mathbf{0}_{3\times3} & \mathbf{0}_{3\times3} \\ [\,(-{}^S\hat{\mathbf{Z}}_k - \frac{1}{g}{}^S\hat{\mathbf{a}}_k^-\,)\times] & T \cdot [\hat{\mathbf{Z}}_k \times] & \mathbf{0}_{3\times3} \\ [\,(-{}^S\hat{\mathbf{M}}_k - {}^S\hat{\mathbf{d}}_k^-\,)\times] & T \cdot [\hat{\mathbf{M}}_k \times] & c_d \cdot \mathbf{I}_3 \end{bmatrix}, \\ \mathbf{v} &= \begin{bmatrix} \frac{1}{g}\left(-c_a \cdot {}^S\hat{\mathbf{a}}_{\varepsilon,k-1}^+ + \mathbf{v}_a + \mathbf{w}_a\right) \\ \frac{1}{g}\left(-c_a \cdot {}^S\hat{\mathbf{a}}_{\varepsilon,k-1}^+ + \mathbf{v}_a + \mathbf{w}_a\right) - {}^S\hat{\mathbf{Z}}_k \times T \cdot \mathbf{v}_g \\ \mathbf{v}_m + \mathbf{w}_d - {}^S\hat{\mathbf{M}}_k \times T \cdot \mathbf{v}_g \end{bmatrix}. \end{aligned} \tag{3.27}$$

In the last stage of the filter, the orientation, the gyro bias and the magnetic distortion are updated for the next step by

$${}^{GS}\hat{\mathbf{R}}_k^+ = {}^{GS}\hat{\mathbf{R}}_k^- \left(\mathbf{I}_3 - \left[\hat{\boldsymbol{\theta}}_{\varepsilon,k}^+ \times\right]\right), \tag{3.28}$$

$$\hat{\mathbf{b}}_k^+ = \hat{\mathbf{b}}_k^- + \hat{\mathbf{b}}_{\varepsilon,k}^+, \tag{3.29}$$

$$\hat{\mathbf{d}}_k^+ = \hat{\mathbf{d}}_k^- + \hat{\mathbf{d}}_{\varepsilon,k}^+. \tag{3.30}$$

3.4 Results and Discussion

In this section, we experiment with the proposed filter. Apart from verifying the proposed model, we will show that if the sensor fusion filter is designed properly, the attaching permanent magnets can work as a magnetic shield to minimize the disturbances. This solution can create a new approach in more accurate motion tracking of robots and mechanical actuators.

The setup explained in Section 3.2 is used. We use the Matlab program as the solver interface in our experimental study. In this study, we choose the QUEST filter based on the Wahba's problem to compare our findings [33, 73]. The acceleration and magnetometer weights of this filter are both set as 1 for the core sensor S_c, and 1

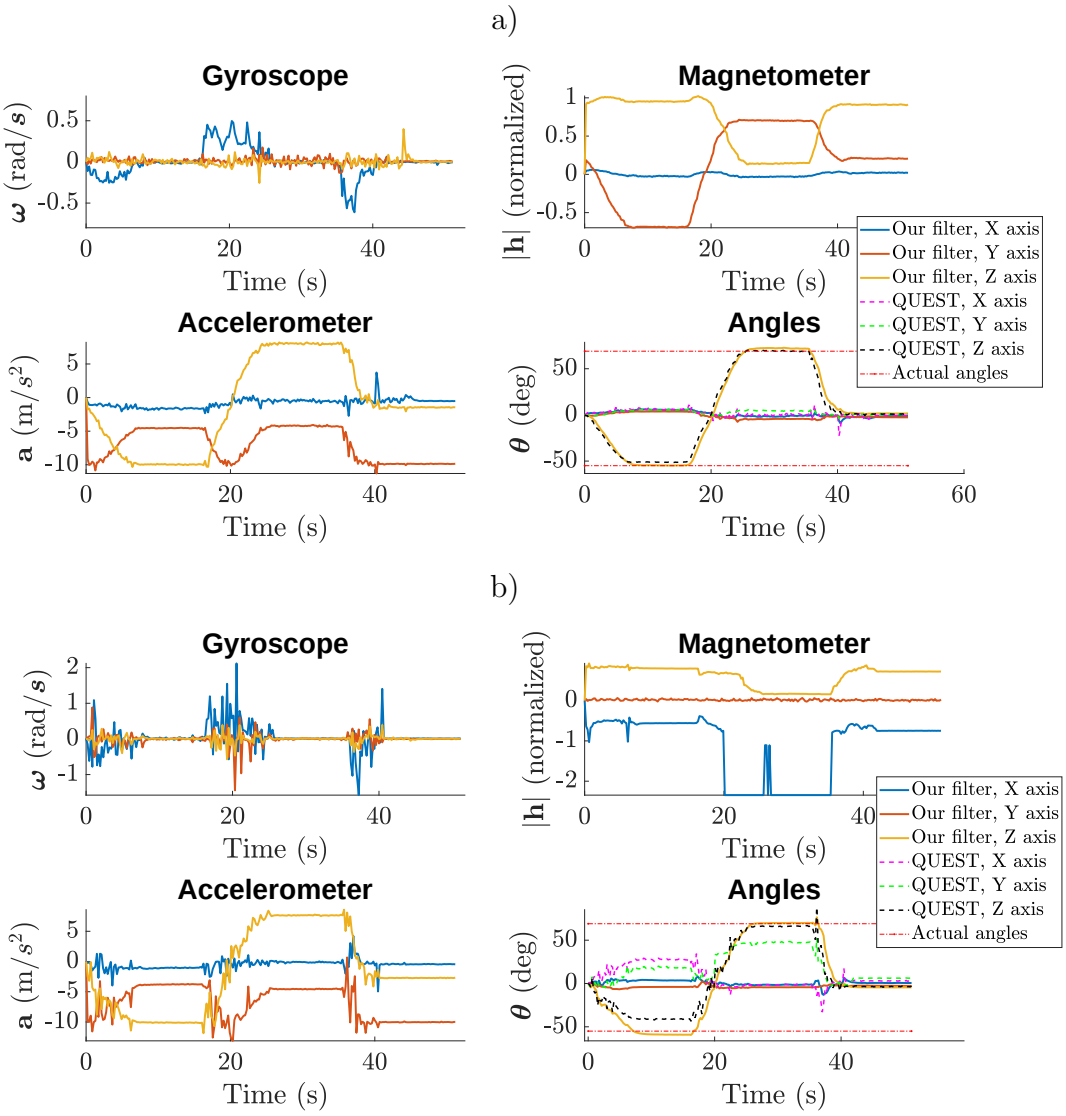

Figure 3.4: Experimental results of the proposed filter. a) Obtained results of the IMU for the moving core S_c, b) Obtained results of the IMU for the tracking carrier S_t with the on-board permanent magnet.

and 0.5 (smaller for less effect from the magnetic distortions) for the tracking sensor S_t, respectively. In the proposed filter, the cutoff frequencies of the acceleration and magnetic field signals in the Eqs. (3.5)-(3.7) are chosen 0.8 and 0.9 through calibrating our IMU devices. Next, the process noises standard deviations $\mathbf{w}_d$, $\mathbf{w}_b$ and $\mathbf{w}_a$ are considered 10^{-3}, 10^{-3} and 10^{-4}. Also, the measurement noises $\mathbf{v}_g$, $\mathbf{v}_m$ and $\mathbf{v}_a$ are chosen 10^{-3}, 10^{-4} and 10^{-3} based on static measurements and calibration process. The state noise constant $\mathbf{Q}_n = \text{diag}\,[10^{-5}, 10^{-25}, 10^{-5}]$ and the measurement noise

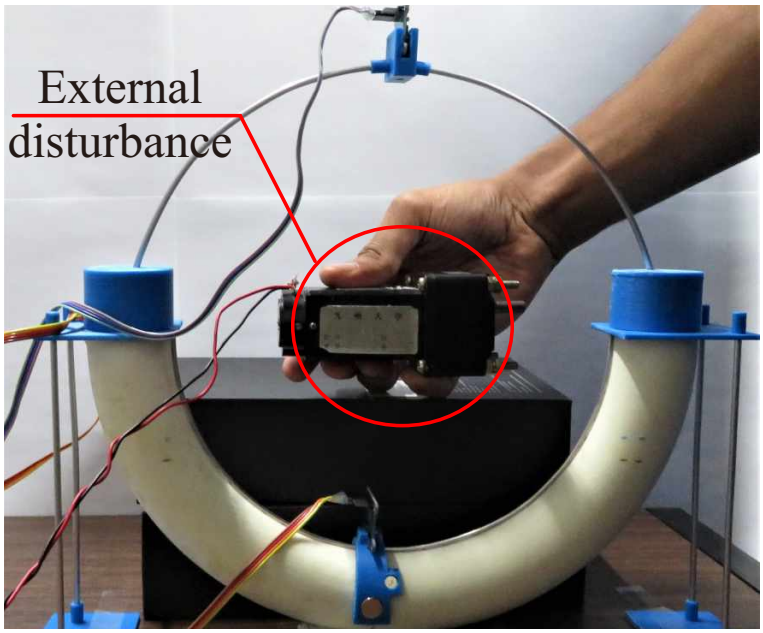

Figure 3.5: Evaluation of the system with external disturbances for the case C and D.

covariance $\mathbf{R} = \text{diag}\,[10^{-5}, 10^{-3}, 10^{-3}]$ are calculated with given values. Note that $\mathbf{Q}_n$ and $\mathbf{R}$ values are diagonal with values for each of the axes, and the noise input mapping matrix $\mathbf{G}$ is the identity matrix.

We do our experimental studies in two parts. At first, the performance of the filter is analyzed for our problem. Then, we do a case study to know that whether including the permanent magnets to the IMU sensor can be a solution for a well-known problem of the IMU sensors' high sensitivity toward the magnetic disturbances.

Fig. 3.4 demonstrates the results of our experiment. The core's IMU sensor is [see Fig. 3.4-a] showing that the performance of our filter is working similar to the QUEST filter with minimum disturbance in the orientation. However, when we check the behavior of filters for the tracking carrier S_t under the effect of ferromagnetic materials, the QUEST filter captures a great level of orientation errors (20-40^o deviations) including disturbance and biases in all the rotational axes. In contrast, our filter performs well with only 2-3^o error in X and Y axes. Also, note that there are minor physical vibrations that make 1-2^o angular errors in X and Y axes. In this setup, the complementary filter not only should remove the hard ferromagnetic biases due to permanent magnetic but also there are disturbances due to effects of the soft

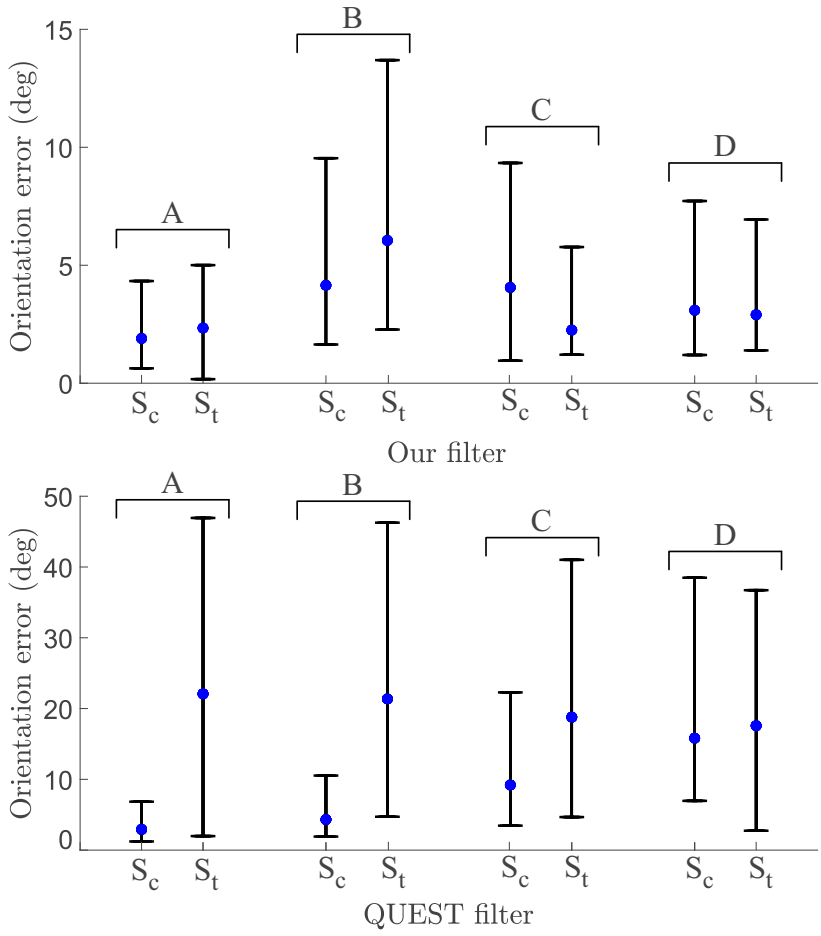

Figure 3.6: Orientation estimation means errors with different case studies. Case A is the motion tracking with normal angular speeds. Case B is the fast angular speed of the sensors. Case C has an external disturbance from an equally located DC motor. Case D has an external disturbance from a heater gun with the same position as Case C.

ferromagnetic materials. The rotating core as soft ferromagnetic material can create deviations in the magnetic field [see example points around 25 s in magnetometer S_c at Fig. 3.4-b] because it does not get aligned with the tracking sensor as well.

The second part of the experimental study is about checking the mean error of the orientation for our filter and the QUEST filter. Also, we show an important observation that permanent magnets with the proper design of the filter can work to be a magnetic shield toward other external magnetic disturbances. Here, we choose to evaluate our case studies in four different scenarios. In the first, case A, the error orientation is checked for normal motion tracking (average angular velocity is 10

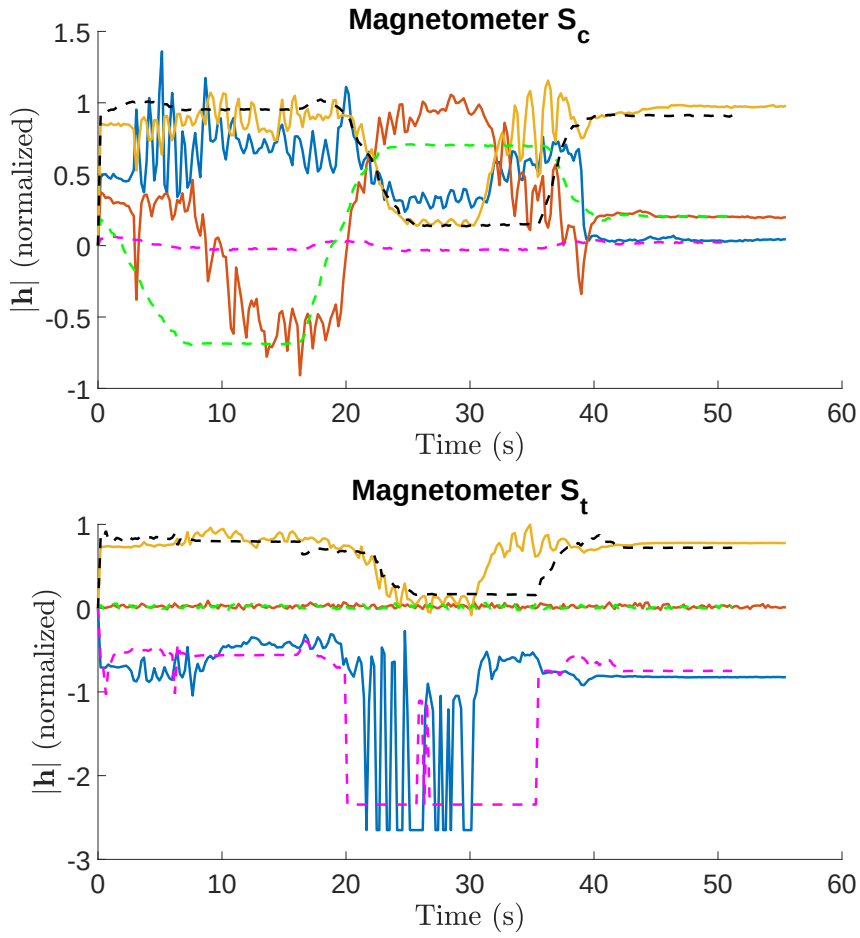

Figure 3.7: Example comparison between the core and tracking carrier IMU sensors when external disturbances are included. Note that the dashed and solid stand for the magnetic fields when there are no external disturbances and there are external disturbances. Also, this is recorded by the DC motor case (case C).

degree per seconds). In case B, the sensor tracking takes place for faster motions, around 25 degree per second speed. In the next two cases, we have included two external disturbances. To equally apply the disturbance to both of the IMU sensors, we place the external disturbance sources at the center of our experimental setup at G coordinate frame as Fig. 3.1 and Fig. 3.5. In these studies, a noisy motor with gearboxes working at 12 v input (5 W) is used for Case C. In these experiments, we have also tried to increase the effect of magnetic disturbance directions by rotating the motor continuously in different axes, while it is approximately centered in the G coordinate. A heater gun is also placed as the last case, case D, in our disturbance studies.

Fig. 3.6 illustrates the averaged orientation errors of all the axes in the described cases. It is clear that our filter outperforms the QUEST filter with a mean angular error of 2^o at case A. However, the QUEST filter despite our try to decrease the sensitivity of the filter toward the magnetic signal (0.5 weight), the mean angular error is over 22^o at tracking sensor S_t. Also, a similar pattern is true for case B that we have fast orientations. Case C shows that external disturbances do have a small deviation effect on our filter (2-3^o mean angular error increase). However, the QUEST filter presents that if we do not have proper filter design, adding permanent magnets does not always mean it will work as a magnetic shield to decrease disturbances. Because our filter uses a magnetic field disturbances to improve biases while not fully relying on it as Eq. (3.27), the filter uses permanent magnets at S_t like a shield to minimize the orientation errors with even 5^o smaller error length in contrast to S_c. Fig. 3.7 shows an example recorded magnetic field with/without external disturbances. This demonstrates that placing passive permanent magnets actually minimizes the disturbance amplitude. In the last experiment, we choose a much challenging noise producing object as a heater gun which creates disturbances including larger biases, the effect is great on the core sensor S_c when the applied filter is the QUEST filter.

Finally, we think our filter is an example solution for a well-known problem that previous studies highlighted regarding sensitivity to magnetic disturbances, such as putting IMUs 1 m away from different mechanical systems, which were making these sensors impractical [13, 87]. In the future, we will address more complex and faster motions with using alternative nonlinear filters rather than Kalman filter while the 3-dimensional magnetic disturbances exist to fully utilize the on-board permanent magnets. It is important to note that there is a limitation for the permanent magnets as well as the proposed filter to deal with magnetic distortions; Hence, if more than one axis of the magnetometer is saturated, the filter will fail to track.

Chapter 4

Singularity in the Inverse Dynamics of the Underactuated Robots

4.1 Introduction

In this chapter, we study the singularity problems in underactuated rolling systems and planar manipulators with inspiration from the previous chapter's studies [108]. Physically, the underactuated systems [see Fig. 4.2 for example] consist of two main parts: First, a rotating mass that moves by an actuator. Second, a passive body that displaces depending on the rotational mass. The control of these underactuated systems with passive bodies have inertial-coupling singularities that originate from the derived model [69, 97, 108].

As the contributions of this chapter, the singular configurations of the mass-rotating rolling robots due to inertial-coupling are described. This study encompasses the proposed fluid actuated spherical robot that is proposed in Chapter 2. Next, we propose a solution for avoiding inertial-coupling singularities in rolling systems. The solution is proposed by applying a sinusoidal wave along the rotational mass trajectory which is designed with singular-free conditions and positive definiteness of the inertial matrix. Next, the approach is studied for more generalized and important cases as an underactuated multi-degrees-of-freedom (DoFs) manipulator.

This chapter is organized as follows. We illustrate the kinematics of the wavy trajectory for the rotating mass system and then derive the modified non-linear dynamics of the general rolling system in Section 4.2. In Section 4.3, the singularity-free conditions for the rolling model are derived through the inverse dynamics. Also, the singularity configurations are studied for the rolling system with rotating mass. Section 4.4 shows example simulations for a mass rotating system with obtained singularity-free conditions and compares the modified model with the conventional one. Finally, we do analytical studies regarding the proposed approach for a 4-DoF underactuated

manipulator (2 passive and 2 active joints) in Section 4.5. Note that all the derivation and modeling studies for underactuated manipulators is presented in Appendix A.

4.2 Modified Dynamic Model of the Rolling System

In this section, we introduce a sinusoidal trajectory that is combined around a circle for the rotating mass. Next, the developed kinematics is substituted into the Lagrangian function of a rolling system. Finally, the Lagrangian method is utilized to find the nonlinear dynamics of this underactuated model. We will propose certain conditions that the singularities due to inertial coupling can be avoided through designing the included wave.

4.2.1 Rotating Mass Kinematics with a Combined Wave

Lets assume that a rotating mass-point has an orientation angle of γ with respect to the center of the spherical carrier with a radius of R [see Fig. 4.1]. Also, the spherical carrier is rolling with an angle of θ. Then, the position vector of the mass that rotates around a small-amplitude sinusoidal curve on the circle with a radius of r is defined as

$$\begin{aligned}\mathbf{D}_c = &-\left[(r + a\sin\left(n(\gamma+\theta)+\varepsilon\right))\cos(\gamma+\theta)\right]\mathbf{k} \\ &-\left[(r + a\sin\left(n(\gamma+\theta)+\varepsilon\right))\sin(\gamma+\theta)\right]\mathbf{j},\end{aligned} \tag{4.1}$$

where a, n and ε are the amplitude of sinusoidal wave, the frequency of created periodic wave on the circle of radius r and the constant phase shift of the curve, respectively. In the conventional mass-rotating models with circular trajectory, this trajectory becomes

$$\mathbf{D}_w = -r(\cos(\gamma+\theta)\mathbf{k} + \sin(\gamma+\theta)\mathbf{j}) \tag{4.2}$$

where a, n and ε are zero in (4.1) that results a circular rotation with radius r [111, 112]. We aim to design n, a and ε depending on the obtained relations from the inertial matrix to removes the inertial coupling singularity [1] while rotating mass follows around wavy circle. Also, the deviation of trajectory $\mathbf{D}_c$ with respect to

[1] Please check Theorem 4.3.1 for details.

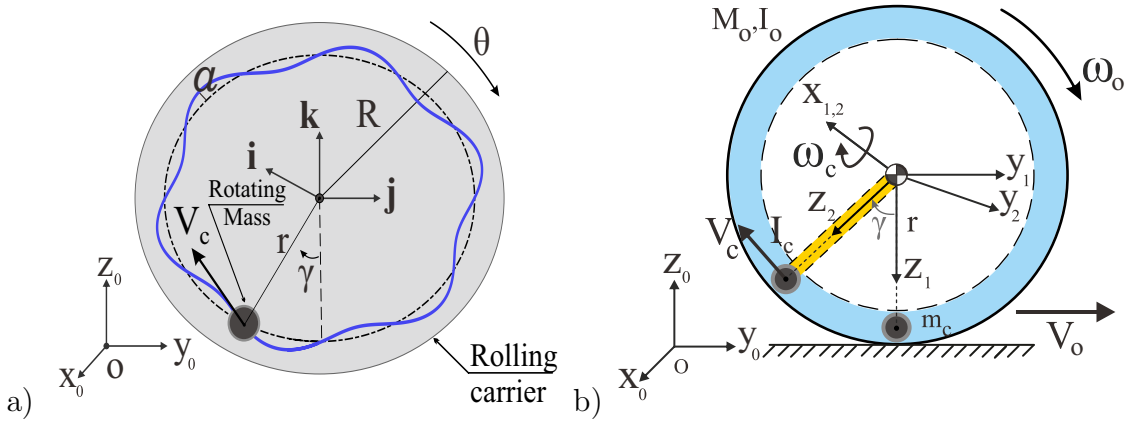

Figure 4.1: a) A rotating mass with the trajectory of a sine wave (blue color) on a circle with radius r (black dashed line). b) Rolling carrier motion along y axis and frame transformations.

circular radius r can be found as

$$\Delta D_c = r - \parallel \mathbf{D_c} \parallel = a\sin(n(\gamma+\theta)+\varepsilon), \tag{4.3}$$

where $\parallel \cdot \parallel$ operator is the module of the variable. The maximum value for this deviation ΔD_c is the amplitude of wave a, which we assume always $a \ll r$ and $a \ll R$. If the property $(a \ll r, R)$ is satisfied, the effect of the included wave can be ignored in dynamic models. However, the larger wave amplitudes a can be also realized in driving mechanisms. For instance, a prismatic joint can move the mass periodically on the lead of the pendulum-actuated systems (similar to Fig. A.2) [45,100] or fluid-actuated systems can have a pipe in the corresponding waveform.

In order to obtain the rolling kinematics, the coordinate frames are sketched as Fig. 4.1-b. Here, $x_0y_0z_0$ represents the reference frame. The moving frame connected to the center of the spherical carrier is $x_1y_1z_1$, which translates with respect to reference frame $x_0y_0z_0$. Finally, $x_2y_2z_2$ is a rotating frame for the rotating mass-point attached to the center of spherical carrier and it is rotating with respect to $x_1y_1z_1$. The rolling system kinematics with the rotational mass is

$$\boldsymbol{\omega}_o = \dot{\theta}\mathbf{i}, \mathbf{V}_o = R\dot{\theta}\mathbf{j},\ \boldsymbol{\omega}_c = \left(\dot{\gamma}+\dot{\theta}\right)\mathbf{i},\ \mathbf{V}_c = \mathbf{V}_o + \dot{\mathbf{D}}_c \tag{4.4}$$

where $\boldsymbol{\omega}_o$, $\mathbf{V}_o$, $\boldsymbol{\omega}_c$ and $\mathbf{V}_c$ are the angular and linear velocities of the carrier and the angular and linear velocities of the rotating mass.

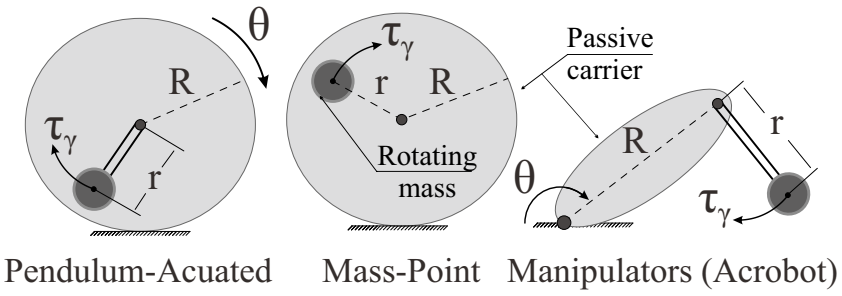

Figure 4.2: Different mass-rotating systems with passive body/carrier that their inertial matrices $\mathbf{M}(\boldsymbol{q})$ are primarily similar.

4.2.2 Nonlinear Dynamics

The non-linear dynamics of the rolling spherical carrier with a planar motion is derived from the proposed trajectory equation. To find the corresponding motion equations, the Lagrangian equations are utilized.

4.2.3 Dynamic Model of Underactuated Rolling System

The general motion equations of a passive and an active rotating bodies with rotational angles of $\boldsymbol{q} = [\theta, \gamma]^T$ can be presented as

$$\mathbf{M}(\boldsymbol{q})\ddot{\boldsymbol{q}} + \mathbf{h}(\boldsymbol{q}, \dot{\boldsymbol{q}}) = \mathbf{u}, \tag{4.5}$$

where inertial matrix $\mathbf{M}(\boldsymbol{q})$, velocity dependencies N_i and gravity terms G_i in $\mathbf{h}(\boldsymbol{q}, \dot{\boldsymbol{q}})$ and control inputs $\mathbf{u}$ are defined by

$$\mathbf{M}(\boldsymbol{q}) = \begin{bmatrix} M_{11} & M_{12} \\ M_{21} & M_{22} \end{bmatrix}, \mathbf{h}(\boldsymbol{q}, \dot{\boldsymbol{q}}) = \begin{bmatrix} N_1 + G_1 \\ N_2 + G_2 \end{bmatrix}, \mathbf{u} = \begin{bmatrix} 0 \\ \tau_\gamma \end{bmatrix}.$$

The underactuated systems (4.5) with two degrees of freedom [69] have a great common, similar inertial matrix $\mathbf{M}(\boldsymbol{q})$, with certain underactuated spherical robots [3, 60, 104, 111]. This inertial similarity help us to generalize our studying problem. The rolling spherical robots propel their passive carrier with a rotating mass-point [3, 50, 111] or pendulum [60, 104] as Fig. 4.2. Note that although we study a 2-DoFs rolling system, adding extra rotating masses (our previous study in Section 2.2.2 had spherical robot with two rotating masses as the cores) does not change our findings since each rotating mass-point has similar dynamic model as Eq. (2.15).

We consider a sphere as a passive carrier (passive joint) where it is propelled with the rotation of a spherical mass as Fig. 4.1. The carrier has a mass of M_o excluding the rotating mass. Also, the rotating mass with the mass m_c is assumed as a mass-point. The Lagrangian function of the rolling carrier with the rotating mass, including kinetic and potential energies, along y axis is described [112] as follows

$$E_L = \frac{1}{2}M_o \parallel \mathbf{V}_o \parallel^2 + \frac{1}{2}I_o \parallel \boldsymbol{\omega}_o \parallel^2 + \frac{1}{2}m_c \parallel \mathbf{V}_c \parallel^2 + \frac{1}{2}I_c \parallel \boldsymbol{\omega}_c \parallel^2 - m_c g d_c, \tag{4.6}$$

where $I_o = 2M_oR^2/3$, I_c, g and d_c are the inertia tensor of rolling passive carrier, an arbitrary inertia tensor I_c connected to the mass-point, the acceleration of gravity and the distance of the mass-point respect to the ground, respectively. We include the inertia tensor I_c for the sake of generality that its rotation is with the respect to carrier central frame $x_1y_1z_1$. This arbitrary inertia tensor I_c can be considered as either the lead of rotating pendulum [60, 104] (yellow pendulum in Fig. 4.1) or interacting fluid/gas inside pipes for the rotating spherical mass [3] (blue fluid/gas in Fig. 4.1). After the substitution of Eq. (2.4) into (4.6), one obtains

$$\begin{aligned}
E_L &= \frac{1}{2}R^2\dot{\theta}^2M_o + \frac{1}{2}I_o\dot{\theta}^2 + \frac{1}{2}I_c(\dot{\gamma}+\dot{\theta})^2 \\
&+ \frac{1}{2}m_c\Big[\big[R\dot{\theta} - \left(\dot{\gamma}+\dot{\theta}\right)(an\cos\left(n(\gamma+\theta)+\varepsilon\right))\sin(\gamma+\theta) \\
&+ (r + a\sin(n(\gamma+\theta)+\varepsilon))\cos(\gamma+\theta)\big]^2 \\
&+ \left(\dot{\gamma}+\dot{\theta}\right)^2\left[an\cos(n(\gamma+\theta)+\varepsilon)\cos(\gamma+\theta) - (r + a\sin\left(n(\gamma+\theta)+\varepsilon\right))\sin(\gamma+\theta)\right]^2\Big] \\
&- m_c g[r + a\sin(n(\gamma+\theta)+\varepsilon)](1-\cos(\gamma+\theta))
\end{aligned} \tag{4.7}$$

Finally, we apply the Lagrangian equations for planar translation of the rolling system along y axis as following

$$\frac{d}{dt}\left(\frac{\partial E_L}{\partial\dot{\gamma}}\right) - \frac{\partial E_L}{\partial\gamma} = \tau_\gamma,\ \frac{d}{dt}\left(\frac{\partial E_L}{\partial\dot{\theta}}\right) - \frac{\partial E_L}{\partial\theta} = \tau_\theta, \tag{4.8}$$

where τ_γ and τ_θ are the external torques for the rotating mass and the sphere, respectively. The acting external torque between the surfaces of the spherical mass (core) and carrier body is assumed zero, $\tau_\theta = 0$, because the mass-point does not have any spinning around itself and it only rotates with the respect to the carrier center $x_1y_1z_1$. After doing the necessary substitutions from Eqs. (4.7)-(4.8), the terms of the motion

equations (A.1) for this underactuated system becomes

$$
\begin{aligned}
&M_{11} = I_c + M_o R^2 + I_o + m_c R^2 - 2m_c R\mu_1 + m_c\mu_2,\\
&M_{12} = M_{21} = I_c - m_c R\mu_1 + m_c\mu_2, M_{22} = I_c + m_c\mu_2,\\
&N_1 = -m_c R(\dot{\gamma}+\dot{\theta})^2\mu_3 + m_c(\dot{\gamma}+\dot{\theta})^2\mu_4, N_2 = m_c(\dot{\gamma}+\dot{\theta})^2\mu_4, G_1 = G_2 = m_c g\mu_5.
\end{aligned}
\tag{4.9}
$$

while,

$$
\begin{aligned}
\mu_1 &= (an\cos(n(\gamma+\theta)+\varepsilon))\sin(\gamma+\theta) + (r + a\sin(n(\gamma+\theta)+\varepsilon))\cos(\gamma+\theta),\\
\mu_2 &= a^2n^2\cos^2(n(\gamma+\theta)+\varepsilon) + (r + a\sin(n(\gamma+\theta)+\varepsilon))^2,\\
\mu_3 &= -an^2\sin(n(\gamma+\theta)+\varepsilon)\sin(\gamma+\theta) + 2an\cos(n(\gamma+\theta)+\varepsilon)\cos(\gamma+\theta)\\
&- (r + a\sin(n(\gamma+\theta)+\varepsilon))\sin(\gamma+\theta),\\
\mu_4 &= -a^2n^3\sin(n(\gamma+\theta)+\varepsilon)\cos(n(\gamma+\theta)+\varepsilon)\\
&+ an\cos(n(\gamma+\theta)+\varepsilon)(r + a\sin(n(\gamma+\theta)+\varepsilon))\\
\mu_5 &= an\cos(n(\gamma+\theta)+\varepsilon)(1-\cos(\gamma+\theta)) + (r + a\sin(n(\gamma+\theta)+\varepsilon))\sin(\gamma+\theta).
\end{aligned}
$$

4.3 Inverse Dynamics and Singularity Regions of the Rolling System

In this section, the non-linear dynamics are illustrated in the inverse form. A general condition for removing the singularities is derived and the singularity regions are studied for the conventional rolling systems. Next, we propose our condition for determining the parameters of the combined wave to avoid the singularity regions that originate inertial-coupling. Finally, a time function as feed-forward control for specifying the spherical carrier rotation is defined.

The non-linear dynamics (A.1) with Eq. (4.9) are re-ordered with the goal to find the input torque τ_γ from the prescribed rolling carrier states ($\theta,\ \dot{\theta},\ \ddot{\theta}$); Hence, the rolling constraint of the carrier and the rotating mass differential equations in Eq. (A.1) becomes

$$
\begin{aligned}
\ddot{\gamma} &= -\frac{1}{M_{12}}\left(M_{11}\ddot{\theta} + N_1 + G_1\right),\\
\tau_\gamma &= M_{21}\ddot{\theta} + M_{22}\ddot{\gamma} + N_2 + G_2.
\end{aligned}
\tag{4.10}
$$

Now, we already know from Eq. (A.1) that inertial matrix $\mathbf{M}(q)$ is always a positive definite and symmetric matrix [1] where upper-left determinants grant this condition by $M_{11} > 0$ and $M_{11}M_{22} - M_{12}M_{21} > 0$. To extend these conditions to the derived inverse dynamics, the rolling constraint (first differential equation) in Eq. (4.10) is substituted into the second differential equation as follows

$$\overline{\tau}_\gamma = \overline{M}\ddot{\theta} + \overline{N} + \overline{G}, \tag{4.11}$$

where

$$\begin{aligned} &\overline{\tau}_\gamma = -\tau_\gamma,\ \overline{M} = M_{12}^{-1} \cdot (M_{11}M_{22} - M_{12}M_{21}), \\ &\overline{N} = M_{22}M_{12}^{-1}N_1 - N_2,\ \overline{G} = M_{22}M_{12}^{-1}G_1 - G_2. \end{aligned} \tag{4.12}$$

Because the mass-point and the spherical carrier rotation are opposite of each other in our motion and for the sake of the simplicity, we assume $\overline{\tau}_\gamma = -\tau_\gamma$. By relying on the Ref. [97], the coupled inertia matrix $\overline{M} > 0$ should be positive definite as well. However, the denominator in $\overline{M} > 0$ requires another extra condition that $M_{12}^{-1} > 0$. Under the condition of $M_{11}M_{22} - M_{12}M_{21} > 0$, there exist singularities in the solution of Eq. (4.11) for the cases when $M_{12} \leq 0$ ($\tau_\gamma \to \infty$) [1]. Thus, following proposition as the condition of the singular-free inverse dynamics is expressed.

Proposition 4.3.1 *Let the inverse non-linear dynamics (4.11)-(4.12) are for the rolling system with the trajectory* $\mathbf{D}_c$ *in (4.1). Given* $M_{12} > 0$*, the underactuated system does not hit any singularity, if following condition is satisfied*

$$\mu_{1a}^2 + \mu_{1b}^2 + \frac{I_c}{m_c} > R\left[\mu_{1a}\sin(\gamma+\theta) + \mu_{1b}\cos(\gamma+\theta)\right], \tag{4.13}$$

where μ_{1a} *and* μ_{1b} *are the first and second terms of* μ_1*.*

Proof Consider the inertia term M_{12} in (4.12) always positive to have no singular configuration as

$$M_{12} = I_c - m_c R\mu_1 + m_c\mu_2 > 0. \tag{4.14}$$

Then, μ_{1a} and μ_{1b} terms are defined from μ_1 in (4.10) as

$$\mu_{1a} = an\cos\left(n(\gamma+\theta)+\varepsilon\right),\ \mu_{1b} = r + a\sin(n(\gamma+\theta)+\varepsilon).$$

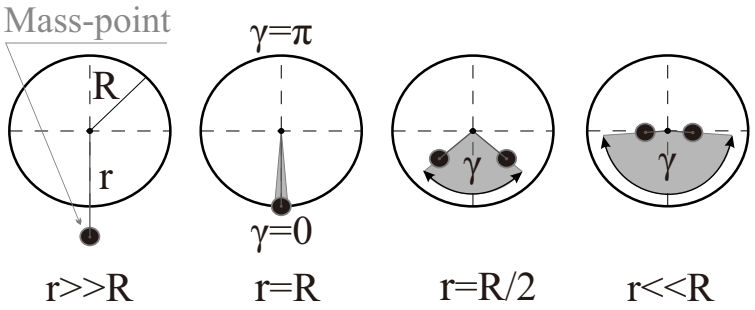

Figure 4.3: Singularity regions in gray color increases as mass-point distance r decreases while the carrier is steady ($\theta = 0$).

where there are $\mu_2 = \mu_{1a}^2 + \mu_{1b}^2$ and $\mu_1 = \mu_{1a}\sin(\gamma+\theta) + \mu_{1b}\cos(\gamma+\theta)$. Thus, μ_{1a} and μ_{1b} are substituted to inequality (4.14) as follows

$$m_c(\mu_{1a}^2 + \mu_{1b}^2) - m_c R(\mu_{1a}\sin(\gamma+\theta) + \mu_{1b}\cos(\gamma+\theta)) + I_c > 0 \tag{4.15}$$

Finally, the condition (4.13) is found by reordering inequality (4.15).

Before designing our combined wave model under the Proposition 4.3.1, we check the singularity regions for the different conventional underactuated rolling systems. Note that in these cases the trajectory is assumed as an ideal circle (4.2) without any consideration of our combined sinusoidal curve.

Example 4.3.1 The singularity regions of a conventional rotating mass-point system [111, 112], where $I_c = 0$, are analyzed using condition (4.13) in Proposition 4.3.1. Let the trajectory $\mathbf{D}_c$ be a perfect circle with radius r, which makes $\mu_{1a} = 0$ and $\mu_{1b} = r$ as (4.2) when $a = n = \varepsilon = 0$. From the given condition (4.13), the inequality is transformed to

$$r^2 > Rr\cos(\gamma+\theta) \tag{4.16}$$

By examining the maximum possible value for $\cos(\gamma+\theta) \approx 1$, one obtains a limitation on the geometric parametrization as

$$\frac{r}{R} > 1. \tag{4.17}$$

This means in designing this mass-point system, the inverse dynamics model (4.10) will hit singularity if the radius of rotating mass be less than the rolling carrier as

condition (4.17). Thus, this singularity disobeys the physical mechanics completely and makes the rolling system impossible to control. Fig. 4.3 shows how changes in the geometric parameters (r, R) in (4.16) affect singular configurations of the mass-point (4.2) on the steady spherical carrier ($\theta = 0$). This graphic clarifies that the rolling system without any angular constraint on γ and θ will hit the singularity. Otherwise, the solution of (4.10) will break many times while this singular region continuously changes by spherical carrier rotation, $\gamma + \theta$.

Example 4.3.2 A rotating mass system with arbitrary inertial tensor is chosen in this example. This inertia tensor I_c can be related to a rod that connects the mass to the center of the rolling body [60, 104] or an interacted water with the rotating mass in pipes [3, 111]. Thus, with a circular trajectory as the previous example, condition (4.17) is transformed to

$$m_c r^2 + I_c > m_c R r \cos(\gamma + \theta), \tag{4.18}$$

By sorting this condition based on the I_c with considering $\cos(\gamma + \theta) \approx 1$ (Strong Inertial Coupling [97]), we see that singularity can be avoided only when

$$I_c > m_c r(R - r). \tag{4.19}$$

Similar to the previous example, this singularity related condition limits the inverse dynamics for only certain mechanic configuration that can satisfy the following geometric condition.

To illustrate that our proposed approach removes the demonstrated singularity regions in Eq. (4.16) and Eq. (4.18), and how parameters of the included wave should be designed analytically a singular-free condition is developed.

Theorem 4.3.1 *The inverse dynamics (4.11) with a combined sinusoidal wave (4.1) never hit singularity and positive definiteness of $\overline{M} > 0$ is granted when variables a, n and ε of the small-amplitude wave ($a \ll r, R$ and $n > 2$) are satisfying following inequalities*

$$\begin{aligned}
r^2 + \frac{a^2}{2}\left[n^2 + (n^2 - 1)\cos 2\varepsilon + 1\right] + \frac{I_c}{m_c} &> \Delta\mu_1 \\
r^2 + \frac{a^2}{2}\left[n^2 + (n^2 - 1)\cos 2\varepsilon + 1\right] + \frac{I_c}{m_c} &> \frac{\sqrt{2}}{2} Rr + \Delta\mu_2 \\
r^2 + \frac{a^2}{2}\left[n^2 + (n^2 - 1)\cos 2\varepsilon + 1\right] + \frac{I_c}{m_c} &> Rr + \Delta\mu_3
\end{aligned} \tag{4.20}$$

where

$$\Delta\mu_1 = a \cdot \left| 2r \sin\left(\tan^{-1}\left(\frac{-2r}{Rn}\right)\right) - Rn\cos\left(\tan^{-1}\left(\frac{-2r}{Rn}\right)\right)\right|,$$
$$\Delta\mu_2 = \frac{\sqrt{2}a}{2}\Big|(2\sqrt{2}r - R)\sin\left(\tan^{-1}\left(\left(R - 2\sqrt{2}r\right)/Rn\right)\right)$$
$$- Rn\cos\left(\tan^{-1}\left(\left(R - 2\sqrt{2}r\right)/Rn\right)\right)\Big|,$$
$$\Delta\mu_3 = a \cdot |2r - R|.$$

Proof Let the singularity condition (4.13) from Proposition 4.3.1 be

$$\mu_{1a}^2 + \mu_{1b}^2 + (I_c/m_c) > R(\mu_{1a}\sin(\gamma+\theta) + \mu_{1b}\cos(\gamma+\theta)).$$

To have the left-hand side of the inequality always larger than the right-side, the absolute value of right-side in the three angular cases are found

$$\begin{aligned}
&1)\ \mu_{1a}^2 + \mu_{1b}^2 + \frac{I_c}{m_c} > R\cdot|\mu_{1a}|, && \zeta_1 = \frac{(2k+1)\pi}{2}\\
&2)\ \mu_{1a}^2 + \mu_{1b}^2 + \frac{I_c}{m_c} > \frac{\sqrt{2}R}{2}\cdot\left(|\mu_{1a}| + |\mu_{1b}|\right), && \zeta_2 = \frac{(2k+1)\pi}{4}\\
&3)\ \mu_{1a}^2 + \mu_{1b}^2 + \frac{I_c}{m_c} > R\cdot|\mu_{1b}|, && \zeta_3 = (k+1)\pi
\end{aligned} \tag{4.21}$$

where $\zeta_i = \gamma + \theta$. Next, we utilize the Fourier Transform equations [119] in following forms

$$\begin{aligned}
H(w) &= \frac{1}{\sqrt{2\pi}}\int_{-\infty}^{\infty}\mu(\zeta_i)e^{-jw\zeta_i}d\zeta_i,\\
\mu(\zeta_i) &= \frac{1}{\sqrt{2\pi}}\int_{-\infty}^{\infty}H(w)e^{jw\zeta_i}dw,
\end{aligned} \tag{4.22}$$

where $H(w)$ and w are the transformed term of μ and the frequency of corresponding μ. With applying the Fourier Transform (4.22) to each side of our inequalities in (4.21), under linearity property in the equations [119], one obtains

$$\begin{aligned}
&1)\ H_{1a}^2 + H_{1b}^2 + (I_c'(w)/m_c) > R\cdot|H_{1a}|,\\
&2)\ H_{1a}^2 + H_{1b}^2 + (I_c'(w)/m_c) > \sqrt{2}R\cdot\left(|H_{1a}| + |H_{1b}|\right)/2,\\
&3)\ H_{1a}^2 + H_{1b}^2 + (I_c'(w)/m_c) > R\cdot|H_{1b}|,
\end{aligned} \tag{4.23}$$

where $I_c'(w)$ is the Fourier Transform of the inertia tensor of I_c. Then, the terms in (4.23) become

$$\begin{aligned}
&H_{1a}^2 + H_{1b}^2 = \pi(a^2n^2 + a^2 + 2r^2)\delta(w) \\
&+ (\pi a^2(n^2-1)/2) \cdot \left[e^{-2j\varepsilon}\delta(2n+w) + e^{2j\varepsilon}\delta(2n-w)\right] \\
&+ 2\pi ar\left[e^{-j\varepsilon}\delta(n+w) - e^{j\varepsilon}\delta(n-w)\right]j, \\
&|H_{1a}| = \pi an\left[e^{-j\varepsilon}\delta(n+w) + e^{j\varepsilon}\delta(n-w)\right], \\
&|H_{1b}| = 2\pi r\delta(w) + \pi a\left[e^{-j\varepsilon}\delta(n+w) - e^{j\varepsilon}\delta(n-w)\right]j.
\end{aligned} \tag{4.24}$$

By using transformed equations (4.24), the corresponding terms are simplified to two base waves for comparison: the first term is the constant shift by $\delta(w)$ and the second is the sinusoidal waves, $\delta(n+w)+\delta(n-w)$. Because the angular rotation $\zeta(\gamma,\theta)$ of the waves in both sides of inequality is always same, each side of (4.23) can be compared relative to its multiplier δ with the same frequency w. By the known insight in the expressed property, all three inequality conditions in (4.23) are collected for each sinusoidal impulses δ in the given frequency w.

$$\begin{aligned}
&1)\ 2rj(e^{-j\varepsilon}\delta(n+w) - e^{j\varepsilon}\delta(n-w)) > Rn\left[e^{-j\varepsilon}\delta(n+w) + e^{j\varepsilon}\delta(n-w)\right] \\
&2)\ 4rj(e^{-j\varepsilon}\delta(n+w) - e^{j\varepsilon}\delta(n-w)) > \sqrt{2}R\left[e^{-j\varepsilon}\delta(n+w)(n+j) + e^{j\varepsilon}\delta(n-w)(n-j)\right] \\
&3)\ 2rj(e^{-j\varepsilon}\delta(n+w) - e^{j\varepsilon}\delta(n-w)) > Rj\left[e^{-j\varepsilon}\delta(n+w) - e^{j\varepsilon}\delta(n-w)\right]
\end{aligned} \tag{4.25}$$

Next, the minimum shift $\Delta\mu$ for having the left-hand side larger than the right-hand has to be computed by taking the Inverse Fourier Transform from (4.25). Therefore, the Inverse Fourier Transform of (4.25) is calculated by (4.22) for each inequality

$$\begin{aligned}
&1)\ 2ra\sin(n\zeta_1 + \varepsilon) > Ran\cos(n\zeta_1 + \varepsilon) \\
&2)\ 4ra\sin(n\zeta_2 + \varepsilon) > \sqrt{2}R\Big[a\sin(n\zeta_2 + \varepsilon) + an\cos(n\zeta_2 + \varepsilon)\Big] \\
&3)\ 2ra\sin(n\zeta_3 + \varepsilon) > Ra\sin(\zeta_3 + \varepsilon)
\end{aligned} \tag{4.26}$$

By analyzing (4.26), we can see that there are $\pi/2$ and $\pi/4$ phase differences between each side of sinusoidal curves in the conditions 1 and 2, respectively. To calculate the required shift for the first two conditions, the derivative of time-domain forms in

(4.26) are derived

$$
\begin{aligned}
&1)\frac{d}{d\zeta_1}\left[\frac{Rn\cos(n\zeta_1+\varepsilon)}{2r\sin(n\zeta_1+\varepsilon)}\right]=\frac{-Rn\sin(n\zeta_1+\varepsilon)}{2r\cos(n\zeta_1+\varepsilon)}=1,\\
&2)\frac{d}{d\zeta_2}\left[\frac{\sqrt{2}R[n\cos(n\zeta_2+\varepsilon)+\sin(n\zeta_2+\varepsilon)]}{4r\sin(n\zeta_2+\varepsilon)}\right]\\
&=\frac{\sqrt{2}R[-n\sin(n\zeta_2+\varepsilon)+\cos(n\zeta_2+\varepsilon)]}{4r\cos(n\zeta_2+\varepsilon)}=1.
\end{aligned}
$$

Then, we solve it for $\gamma_1 = n\zeta_1 + \varepsilon$ and $\gamma_2 = n\zeta_2 + \varepsilon$, and find the tangential point of two waves when their slopes are the same

$$
\gamma_1 = \tan^{-1}(-2r/Rn), \gamma_2 = \tan^{-1}\left(\left(R - 2\sqrt{2}r\right)/Rn\right). \tag{4.27}
$$

We define $\Delta\mu_1$ and $\Delta\mu_2$ as the minimum required shifts for the right-hand side of inequalities to be always larger than left in conditions 1 and 2 by equaling both sides of (4.26) as

$$
\begin{aligned}
&\Delta\mu_1 + Ran\cos(\gamma_1) = 2ra\sin(\gamma_1),\\
&\Delta\mu_2 + \frac{\sqrt{2}a}{2}R\left[\sin(\gamma_2) + an\cos(\gamma_2)\right] = 2ra\sin(\gamma_2).
\end{aligned} \tag{4.28}
$$

The third inequality condition in (4.26) is easier to compute because the waves of both sides are in the same phase, hence, we obtain $\Delta\mu_3$ by using the maximum amplitude difference

$$
\Delta\mu_3 = a \cdot |2r - R|. \tag{4.29}
$$

At the end, substituting (4.27) into (4.28) and reordering them with the respect to the minimum shifts $\Delta\mu_i$ results in

$$
\begin{aligned}
&1)\Delta\mu_1 = a\cdot\left|2r\sin\left(\tan^{-1}\left(\frac{-2r}{Rn}\right)\right) - Rn\cos\left(\tan^{-1}\left(\frac{-2r}{Rn}\right)\right)\right|\\
&2)\Delta\mu_2 = \frac{\sqrt{2}a}{2}\left|(2\sqrt{2}r - R)\sin\left(\tan^{-1}\left(\left(R - 2\sqrt{2}r\right)/Rn\right)\right)\right.\\
&\left. - Rn\cos\left(\tan^{-1}\left(\left(R - 2\sqrt{2}r\right)/Rn_i\right)\right)\right|\\
&3)\Delta\mu_3 = a\cdot|2r - R|
\end{aligned} \tag{4.30}
$$

By putting Eq. (4.30) back into inequalities (4.23) and taking the Inverse Fourier for single wave with $2n$ frequency and constant shift for $\delta(w)$, we have

$$\begin{aligned}
&1)\ \frac{a^2(n^2+1)}{2}+\frac{a^2(n^2-1)}{2}\cos(2(n\zeta_1+\varepsilon))+r^2+\frac{I_c}{m_c}>\Delta\mu_1(a,n),\\
&2)\ \frac{a^2(n^2+1)}{2}+\frac{a^2(n^2-1)}{2}\cos(2(n\zeta_2+\varepsilon))+r^2+\frac{I_c}{m_c}>\frac{\sqrt{2}}{2}Rr+\Delta\mu_2(a,n),\\
&3)\ \frac{a^2(n^2+1)}{2}+\frac{a^2(n^2-1)}{2}\cos(2(n\zeta_3+\varepsilon))+r^2+\frac{I_c}{m_c}>Rr+\Delta\mu_3(a,n),
\end{aligned} \tag{4.31}$$

In order to simplify the second term at right-hand side of inequalities (4.31), we choose $n>2$ which transfer $\cos(2(n\zeta+\varepsilon))$ to $\cos 2\varepsilon$ in all conditions $\{\zeta_1,\zeta_2,\zeta_3\}$. Under the given assumption ($n>2$), condition (4.20) can be derived from (4.31).

Remark 4.3.1 *Because the inertia tensor I_c of the rotating mass is normally related to geometric objects (connecting cylindrical bar of the pendulum) with a constant radius, it has been included as the constant value to the inequalities.*

Remark 4.3.2 *This Theory 4.3.1 can easily be extended for any underactuated system with two-link manipulators (for example the Acrobat) since M_{12} term is in common with all models and does not have the inertia tensor of carrier I_o.*

In this rolling system, we choose a 4th order time function [3, 104] to reach the carrier $\theta(t)$ toward its desired final configurations θ_{des} by

$$\theta(t)=k\left(-\frac{20}{T^7}t^7+\frac{70}{T^6}t^6-\frac{84}{T^5}t^5+\frac{35}{T^4}t^4\right), \tag{4.32}$$

where T and k are the time constant of designed motion and the value for the final arrived distance $\theta(T)=k=\theta_{\text{des}}$. We expect from this feed-forward control to actuate the rotating mass like $\gamma(t)=d^2\theta(t)/dt^2$ from (4.32) as a two-step motion. This two-step motion of rotating mass [see $\gamma+\theta$ at Fig. 4.5-b as an example of this motion pattern] is followed by a counterclockwise rotation till certain angle γ_{max} and a similar clockwise rotation for returning to the rest position. Note that similar to what has been developed in [3,104], one can show that with the selection of this motion scenario the condition $\dot{\theta}(T)=0$ is always satisfied.

Table 4.1: Value of parameters for the simulation studies.

Variable	Value	Variable	Value
m_c	0.4 kg	r	0.131 m
M_o	1 kg	R	0.145 m
g	9.8 m/s^2	I_o	0.0140 kg·m^2

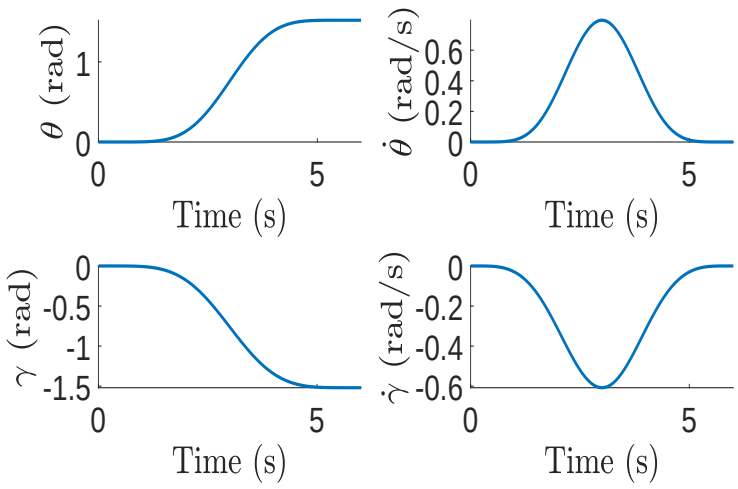

Figure 4.4: Example simulation for passive carrier $\{\theta, \dot{\theta}\}$ and rotating mass-point $\{\gamma, \dot{\gamma}\}$ states by the modified model.

4.4 Simulation Analysis of the Rolling System

In this section, the proposed condition for avoiding singularities is analyzed in the simulation space. At first, to evaluate our model in the worst-case scenario, a mass-point system with $I_c = 0$ is chosen. We find the singular-free model with satisfying the conditions of the proposed theorem. Next, to compare the modified model with the classic model, we compare both cases when there is an inertia tensor I_c as a pendulum system.

The geometric parameters of the considered physical system are like Table 4.1. Note that this system fails the singular-free coupling condition (4.17) by having $r < R$, as shown in Example 4.3.1, which makes the system to be in a singular region. To prescribe the angular orientation of the spherical carrier the introduced time functions in (4.32) is applied where $k = \theta_{des}$ is $\pi/2$ rad. The simulation is run for 6 s with $T = 6$. The robot begins from rest condition and it is expected to reach rest position at end of simulation time by the prescribed time function.

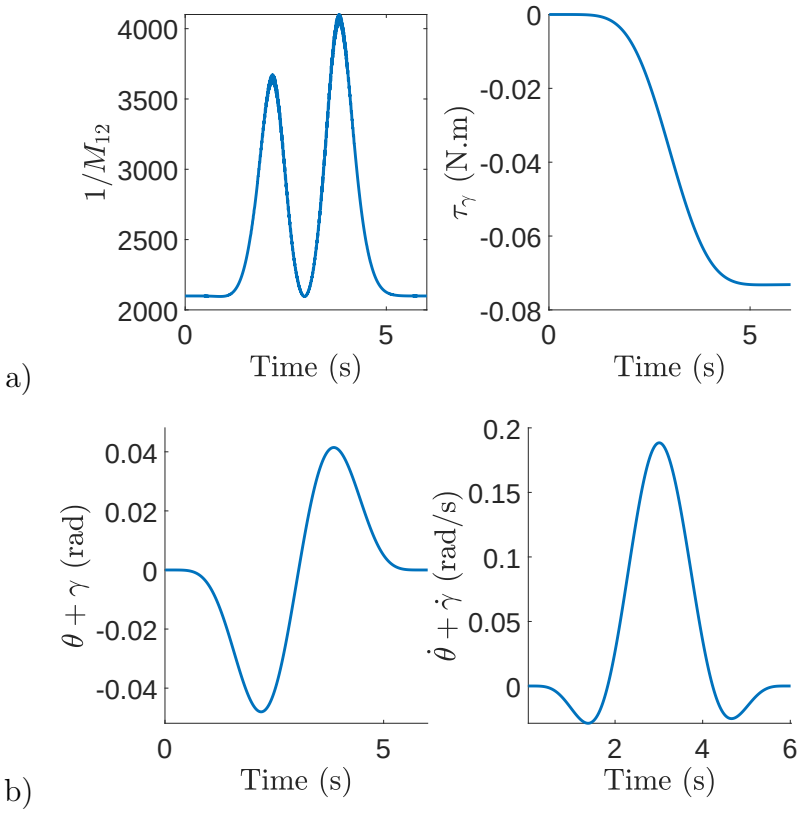

Figure 4.5: a) Inertia term and output torque results for modified inverse dynamics, b) the true location and velocity of the rotating mass respect to reference frame.

To solve the singularity, we use the proposed Theory 4.3.1 where a, n and ε are designed under the conditions of (4.20). By substituting the values of the geometric parameters from Table into the conditions (4.20), we choose our wave parameters with first maximum value as $a = 0.0055$, $n = 10$ and $\varepsilon = 0$ which satisfy all three inequalities. Note, if we have an inertia tensor I_c, depending on the designed mechanism, wave amplitude a can be chosen smaller as indicated in inequalities (4.20).

By running the simulation with obtained parameters, we see that the inverse dynamics are integrated without hitting any singularity [See Fig. 4.4-b and 4.5]. As expected, the rotating mass follows a smooth two-phase motion with the applied feed-forward control by our time function [see Fig. 4.5-b]. Also, the control torque τ_γ as the output is produced responsively with solving the modified nonlinear dynamics which displaces the spherical carrier to the desired angle with the rest-to-rest motion.

Finally, we illustrate a comparison between a conventional rotating pendulum

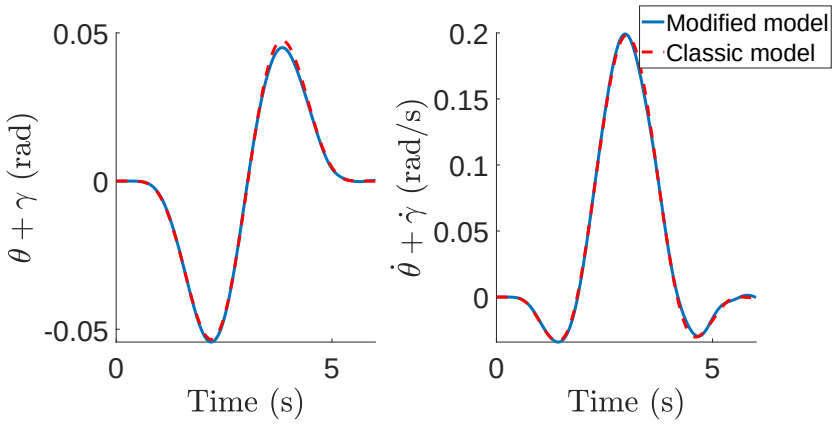

Figure 4.6: Compared results for a classic (conventional) and modified motion equations in a pendulum system with the inertia tensor I_c.

system with our modified singular-free model. We do this comparison for the sake of clarification that model with small-amplitude combined wave does not hurt/diverge the motion equations while it is removing the singularities due to coupling. All the simulation parameters are similar to the previous case-study except when we include an inertia tensor of cylindrical pendulum $I_c = m_l r^2/3 = 0.0057$ kg·m^2 that is connected to the mass-point as Fig. 4.1. Also, we simulate the classic (conventional) model of a pendulum system for the rolling sphere from Refs. [60, 104] which same model can be derived by prescribing $a = n = \varepsilon = 0$ at Eq. (4.10). Fig. 4.6 shows that our modified model does not have any dissimilarity with the classic model with included wave on the circular trajectory, $a \ll r, R$. In this case, note that the inclusion of I_c variable satisfies the singular-free coupling condition in Eq. (4.19). Our designed condition can easily work for the geometries that singular-free coupling conditions were limited by (4.16) and (4.19) (worst-case as a mass-point) conditions in previous studies.

4.5 Analytical and Simulation Studies for the Planar Manipulator

In this section, we first study our proposed singular-free condition for 4-Dof underactuated manipulator analytically that given in Proposition A.4.1. Next, we make a comparison of our modified inverse dynamics with the conventional systems without the combined wave kinematics.

Table 4.2: Chosen parameters for the analytical studies of a 4-DoFs underactuated manipulator that fails the Strong Inertial Coupling condition.

Variable	Value	Variable	Value
m_k	0.7 kg	l_k	0.11 m
$I_2 = I_4$	0.09 kg·m^2	g	9.8 m/s^2
$I_1 = I_3$	0.1 kg·m^2		

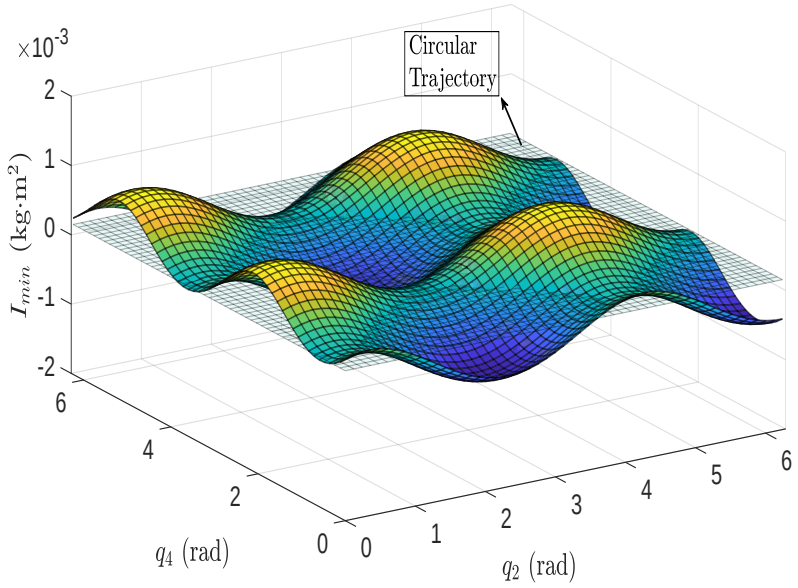

Figure 4.7: The minimum inertia verses manipulator configuration for singular-free regions.

4.5.1 Analytical Study of Minimum Inertial Condition

Here, We check how combined-wave kinematics changes the inertial-coupling condition and singularity regions. This will demonstrate the behavior of the proposed modeling method and the implications that it could have.

The geometric parameters of the chosen example model are presented in Table 4.2. With simple numerical analysis, we can see that the following system can not satisfy the inertial coupling conditions in Table A.1 for the 3rd one. The problem can be seen more vivid by using the proposed minimum inertial condition I_{min} in Proposition A.4.1. We choose our combined-wave parameters with some analytical studies as: $a_2 = -0.011$, $n_2 = 1.6$, $\varepsilon_2 = 1$ rad, $a_4 = -0.01$, $n_4 = -2$, $\varepsilon_4 = -0.41$ rad. Note that our derived minimum inertial condition is independent of q_1 and q_3 angles.

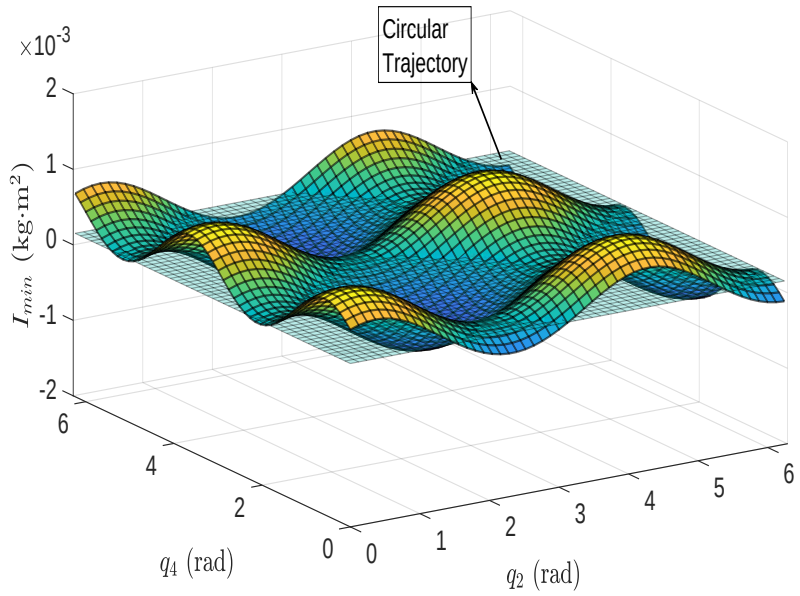

Figure 4.8: The minimum inertia verses manipulator configuration for singular free-regions ($a_2 = 0.011$ case).

Fig. 4.7 illustrates the minimum inertial coupling I_{min} with the respect to q_2 and q_4 angles of active joints. The blue plane shows the minimum value of the classic circular trajectory. It is clear that the minimum inertia value is near zero which is the main source of singularity. However, if there is combined wave kinematics, the minimum inertial condition rises. This is an interesting point that shows the property of our proposed modified inverse dynamics. It can be interpreted that depending on the desired region of action for the joint angles (actuability), the inertial coupling singularities can be avoided numerically. Nevertheless, there are singular regions in the configurations $\{q_2, q_4\}$ of manipulator, in here for the example case is $q_2 \in (\pi/2, \pi)$ and $q_4 \in (\pi/2, \pi)$, in the minimum inertial value I_{min}. This can be resolved easily by varying the sign of either a_2 or a_4 combined-waves amplitude which invert the minimum inertial value. Fig. 4.8 shows for $a_2 = 0.011$ at the current case. It is important to note that our chosen amplitudes of the combined waves are %10 of the link length. This value can be smaller or larger depending on our geometric parameters (m_k, l_k, I_k). Also, these parameters determine the singular-free configuration region for controlling if we limit our problem to $a_k < l_k$.

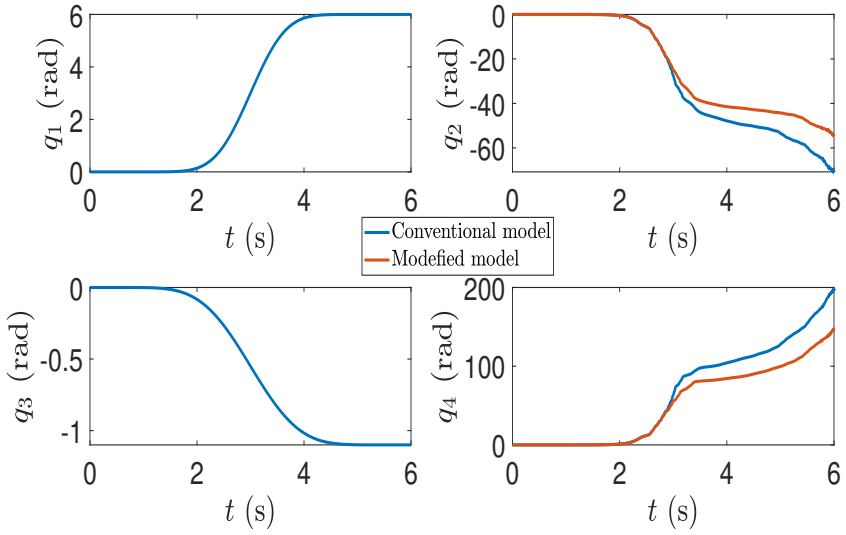

Figure 4.9: Angular displacements of joints for an example simulation.

4.5.2 Simulation of the Feed-Forward Control

The modified nonlinear dynamic model is checked using feed-forward control in Section A.4.2. Our aim is to show an example case that the singular configuration is prevented by applying our proposed approach. It is expected to converge the passive joints to their desired values while active joints angles are arbitrarily moving to reach the desired states.

Here, the accuracy of the Matlab solver for relative and absolute errors are 0.001 and 0.001, respectively. The geometric parameters of our physical system are similar to the previous part as Table 4.2. Also, we chose the same combined-wave kinematics values that we found in the previous section. To control the angular velocity and orientation of the active joints q_a, the given Beta functions (A.24)-(A.26) are applied. Note that the derivative of (A.24) gives the angular acceleration for these active joints. We choose our desired angular configuration as $\mathbf{q}_{f,p} = [q_{1,f},\ q_{3,f}] = [6,\ 1.1]$ rad. We consider this desired configuration to make joints cover the most of workspace. The simulation duration is set 6 s which means $T = 6$ in the Beta functions (A.24)-(A.26). Also, the order of functions for each of the actives are as follows: $\alpha_1 = 17$ and $\alpha_3 = 9$. The robot's passive joints begin from rest condition and it is expected to reach rest position at end of simulation time by the prescribed Beta functions. Also, initial angular positions and velocities are all zero in joints.

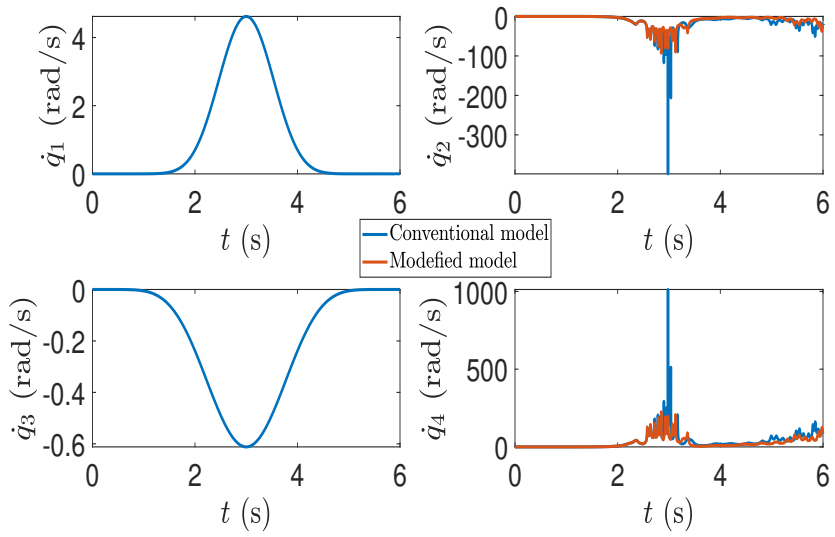

Figure 4.10: Angular velocities of joints for an example simulation.

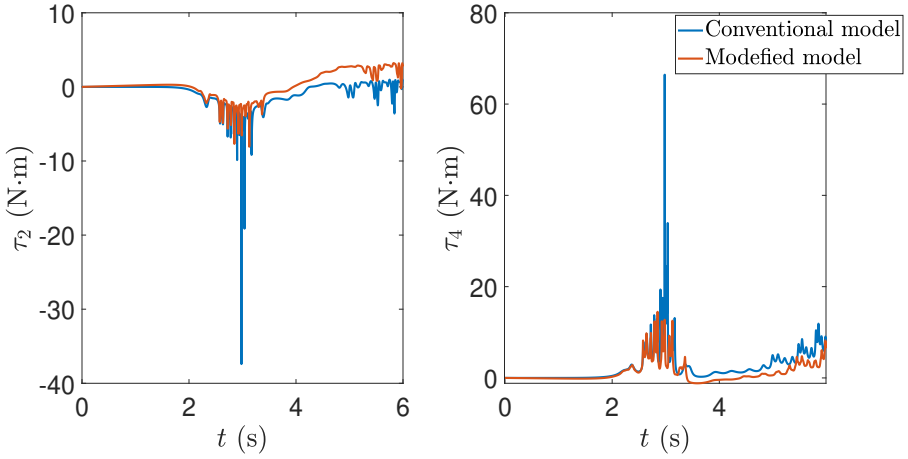

Figure 4.11: Active joints' torque outputs for a desired configuration.

The angular displacements of joints for the conventional manipulator with circular trajectory and our modified model (A.28)-(A.32) are shown in Fig. 4.9. Please note that singularity points can be hard to simulate and demonstrate in simulation/experiment since the integration solution converges to infinity. However, we choose a case that we just pass the local region of the singular point to have a more clear comparison based on Table A.1. This comparison becomes understandable when we have a look at angular velocity results in Fig. 4.10. It is clear that there are two singular points around 3 s which make huge spikes in the angular velocities of active

joints $\dot{\mathbf{q}}_a$. However, our designed combined-waves kinematics avoid the singular regions in inertial matrices and spikes do not appear anymore where the overall trend of motion is alike. Also, the inverse dynamics for the output torque of active joints ($\boldsymbol{\tau}_a$) similarly converge to large values in conventional models as Fig. 4.11. Thus, our proposed modeling method can resolve this issue and can be beneficial in continuous control strategies e.g., feedback control.

If the planning problem is aimed at the path planning of end-effector and condition $a_k \ll l_k$ is not satisfied, this could be an important issue to take care of in our proposed method. In that case, the wave has to be designed in a way that it converges to zero when it is reaching to the desired configuration. This can be done by making the amplitude $a_k(t)$ varying parameter. Alternatively, someone can find a suitable frequency n_k and phase ε_k to arrive the end-effector toward the exact desired position when a_k is constant.

Chapter 5

A Darboux-Frame-Based Approach for Path Planning of Spin-Rolling Sphere on Plane

5.1 Introduction

This chapter proposes a new geometric-based path planning method for a spin-rolling sphere on a plane. In the Chapter 2, we proposed a underactuated novel spherical robot. This robot had three rotational degrees known as a spin-rolling sphere which demonstrated a great challenge in doing the nonholonomic path planning with conventional methods. Because the spin angle diverge other local angular coordinates, the classic approaches face challenges like having a non-smooth trajectories.

Our planning problem is developed with two main contributions: considering a spin-rolling sphere on the plane and developing optimal smooth trajectories for the desired states. By our proposed geometric approach, the sphere with a nontrivial trajectory follows a straight path on the plane where the optimal solution for the desired states is achieved. Also, we propose a geometric model (the Darboux frame) where the control inputs are time- and coordinate-invariant with arc-length properties. Next, a virtual surface is introduced to manipulate the inputs of the kinematic model to the desired states. To the best of our knowledge, this is the first geometric arc-length-based control strategy that is proposed. Note that this geometric control separates the time scale from the kinematics, which gives the system freedom to converge with different convergence rates in the given time. Note that because we do planning at the kinematic level, the planning approach can be easily extended for other mechanisms like manipulation of the box with a fingertip (the sphere) that is famous for Dexterous manipulation. Thus, this method can be applied for particle manipulation apart from being used in spin-rolling spherical robots. It is important to note that we have not included the dynamics (such as our rolling robot dynamics) in the problem statement; Hence, we can keep the generality of the solution which is

realizable in different mechanisms.

This chapter is organized as follows. In Section 5.2, the Darboux-based kinematic model of a moving frame is derived with considering the curvature properties of surfaces. Next, the problem statement of our path planning approach is described in Section 5.3. Additionally, this section includes the design of the proved virtual surface as the geometric controller. In Section 5.4, the iterative algorithm with included tuning variables is explained. Simulations of this approach are demonstrated and discussed in Section 5.5.

5.2 Kinematic Model of a Moving Darboux Frame

The model of new Darboux frame at contact point of the spin-rolling sphere and plane is developed. Next, this Darboux kinematics are substituted to the Montana Kinematics [74]. As we derive the new geometric model, the kinematics readily suits both contact trajectories and arbitrary parameters of the surfaces [34]. Also, this transformation provides two significant benefits through our planning approach. First, the spin-rolling angular rotations explicitly appear on the relative curvature and torsion [34] that makes it easier for manipulation. Second, the Darboux frame separates the time variable from the planning due to its time- and coordinate-invariance.

Fig. 5.1 is depicted for rotating object and surface coordinates in the ball-plate system. Σ_o and Σ_s are the fixed coordinate frames on the rolling object (red sphere) and the plane. There are coordinates of the contact points for a sphere Σ_{co} and fixed traveled surface Σ_{cs}. Also, Σ_s coordinate is fixed relative to other coordinate frames. It is assumed that the sphere is rotating with no sliding constraint. The local coordinate systems for the sphere and plane are considered

$$\begin{aligned} &f_o : U_C \to \mathbb{R}^3 : c(u_o, v_o) \mapsto (-R_o \sin u_o \cos v_o, R_o \sin v_o, -R_o \cos u_o \cos v_o), \\ &f_s : U_S \to \mathbb{R}^3 : c(u_s, v_s) \mapsto (u_s, v_s, 0), \end{aligned} \tag{5.1}$$

where $c(u_o, v_o) \in [-\pi, \pi]$ and $c(u_s, v_s)$ are contact parameters of the sphere and plane. Additionally, the sphere is the rotating object U_C with curvature properties [66] as follows:

$$k^o_{nu} = k^o_{nv} = 1/R_o,\ \tau^o_{gu} = \tau^o_{gv} = 0, k^o_{gu} = \tan(v_o)/R_o,\ k^o_{gv} = 0, \tag{5.2}$$

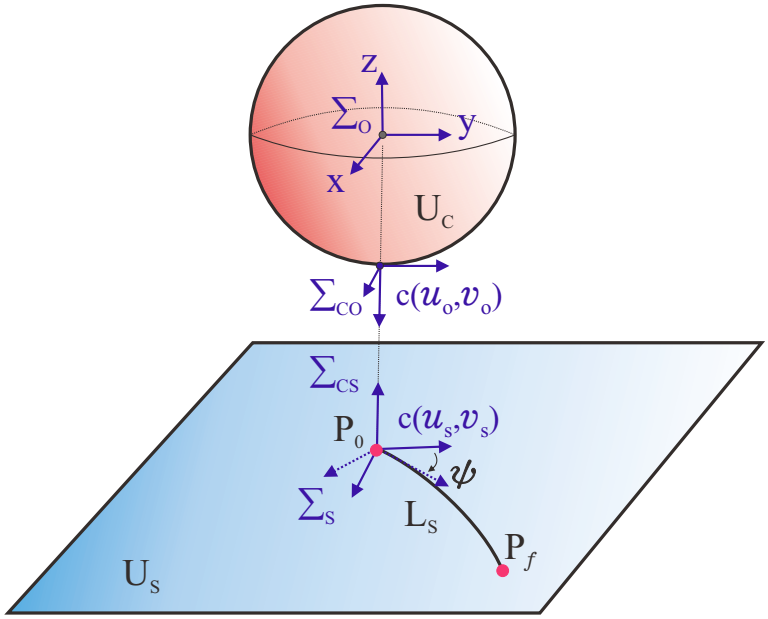

Figure 5.1: Kinematic model of rotating sphere. Note: ψ is the spin angle between sphere and plane surfaces.

where k^o_{nu}, k^o_{nv}, τ^o_{gu}, τ^o_{gv}, k^o_{gu}, k^o_{gv} are the normal curvature, geodesic torsion and geodesic curvature of the rotating body respect to u_o and v_o principles. Also, the curvature terms of the plane surface U_S are

$$k^s_{nu} = k^s_{nv} = \tau^s_{gu} = \tau^s_{gv} = k^s_{gu} = k^s_{gv} = 0, \tag{5.3}$$

where k^s_{nu}, k^s_{nv}, τ^s_{gu}, τ^s_{gv}, k^s_{gu}, k^s_{gv} are the normal curvature, geodesic torsion and the geodesic curvature of the fixed surface (plane) respect to u_s and v_s principles.

At first, we introduce a Darboux frame Σ_f, for deriving the kinematics in arc-length domain, that is on the contact coordinate of the plane Σ_{cs}. Let a traced curve $\mathbf{L}_s$ in Euclidean space be on the surface plane U_S [see Fig. 5.2]. Every contacted point $\mathbf{P} \in U_S$ has a unit-based Darboux frame $(\boldsymbol{e}^s_1, \boldsymbol{e}^s_2, \boldsymbol{e}^s_3)$ [26] where $\boldsymbol{e}^s_1$ is a tangent vector to the path $\mathbf{L}_s$, $\boldsymbol{e}^s_3$ is a normal vector to the U_S surface and $\boldsymbol{e}^s_2$ is perpendicular to the plane $\boldsymbol{e}^s_3 \times \boldsymbol{e}^s_1$ [see Appendix B.1 for the preliminary equations of the Darboux frame]. Apart from the Darboux frame attached to the plane trajectory $\mathbf{L}_s$, the angular velocities of the Darboux frame $\boldsymbol{\omega}^*$ is determined with including two more Darboux frames attached to the sphere trajectory $\mathbf{L}_o$ as $(\boldsymbol{e}^o_1, \boldsymbol{e}^o_2, \boldsymbol{e}^o_3)$ and trajectory of our defined virtual surface $\mathbf{L}_v$ as $(\boldsymbol{e}^v_1, \boldsymbol{e}^v_2, \boldsymbol{e}^v_3)$ on the contact point $\mathbf{P}$ [see Fig. 5.2]. Note that all these Darboux frames coincide with each other [34] due to no-sliding

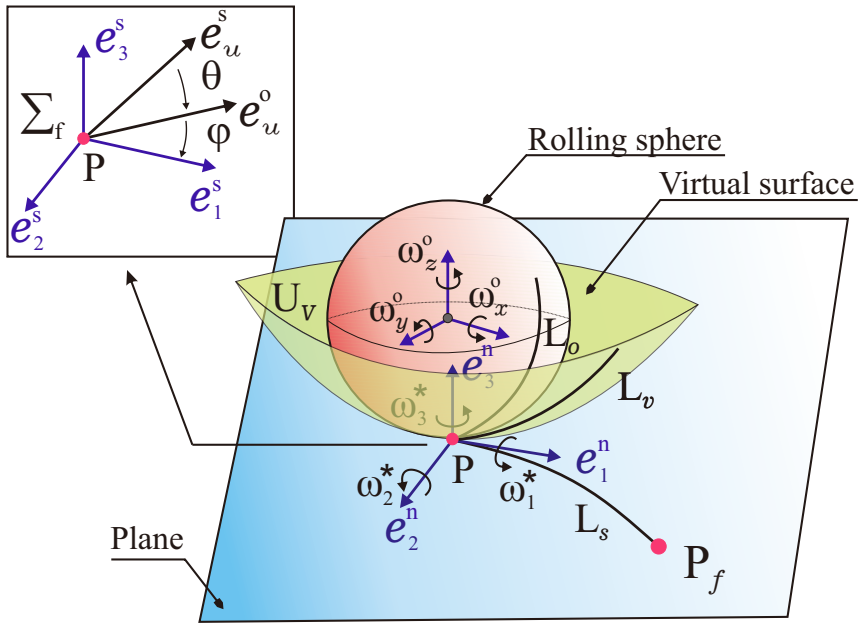

Figure 5.2: Frame transformations of the spin-rolling sphere on a moving frame Σ_f. Note that n superscript in $\{\boldsymbol{e}_1^n, \boldsymbol{e}_2^n, \boldsymbol{e}_3^n\}$ frame stands for the sphere $(n = o)$, the plane $(n = s)$ and the virtual surface $(n = v)$.

constraint. The detailed explanations and derivation are covered in Appendix B.2. Also, we have introduced this new virtual surface U_V with manipulative curvatures $(\alpha_s, \beta_s, \gamma_s)$ in purpose of controlling the sphere coordinates (u_o, v_o) in the arc-length domain (s-domain)[1]. This virtual surface can be imagined as a sandwiched surface that its curvatures variations (geometric controller) are projected onto both sphere and plane trajectories. This can be looked as bending the sheet of paper to rotate a ball on the plane. Thus, the angular velocities of the Darboux frame along $\mathbf{L}_s$ [the proof is in Appendix B.2] on $\mathbf{P}$ is shown

$$\boldsymbol{\omega}^* = \delta(-\tau_g^* \boldsymbol{e}_1^s + k_n^* \boldsymbol{e}_2^s - k_g^* \boldsymbol{e}_3^s). \tag{5.4}$$

where

$$\delta = ds/dt,\ k_g^* = k_g^o - k_g^s - \alpha_s, k_n^* = k_n^o - k_n^s - \gamma_s,\ \tau_g^* = \tau_g^o - \tau_g^s - \beta_s. \tag{5.5}$$

where δ is the derivation of the arc-length relative to time called the rolling rate, and k_g^*, k_n^* and τ_g^* are the induced geodesic curvature, normal curvature and geodesic torsion between two surfaces (sphere and plane) including a sandwiched virtual surface's

[1]The Eq. (5.24) will be our designed geometric control with using the introduced virtual surface that will be explained in Section 5.3.2

curvatures (α_s, β_s, γ_s). Also, $\{k_n^o, k_g^o, \tau_g^o\}$ and $\{k_n^s, k_g^s, \tau_g^s\}$ are the induced curvatures of the sphere and plane with respect to the Darboux frame of the plane ($\boldsymbol{e}_1^s$). In Refs. [34, 63], the angular velocities of the Darboux frame (5.4)-(5.5) was used in terms of $\delta\alpha_s$ only that it was defined as the compensatory spin rate. However, we have derived a general formulation with the defined virtual surface to control the pure-rolling velocity of the sphere by $\{\delta\gamma_s, \delta\beta_s\}$ and its spin velocity by $\delta\alpha_s$.

Next, there are the unit-based orthonormal frames of $(\boldsymbol{e}_u^o, \boldsymbol{e}_v^o, \boldsymbol{e}_3^o)$ and $(\boldsymbol{e}_u^s, \boldsymbol{e}_v^s, \boldsymbol{e}_3^s)$ induced by contact coordinates of the rotating object (sphere) Σ_{co} and fixed surface (plane) Σ_{cs}, respectively. These vectors can be found by taking derivative of local coordinates in (5.1). Here, always the unit normals of the surfaces ($\boldsymbol{e}_3^o$ and $\boldsymbol{e}_3^s$) and the Darboux frame of the plane are aligned with each other. Then, let the rotating sphere u-vector $\boldsymbol{e}_u^o$ makes an angle φ with the Darboux frame $\boldsymbol{e}_1^s$ vector [see Fig. 5.2] that is tangent to path $\mathbf{L}_s$. Also, θ is the angle between sphere $\boldsymbol{e}_u^s$ and plane $\boldsymbol{e}_u^o$ coordinates. Note that the general equations of the Darboux frame (trihedrons) with angle respect to induced coordinates of a surface is summarized as the preliminaries in Appendix B.1, which were also shown explicitly in Refs. [26,34,35]. Then, the induced curvature between the Darboux frame Σ_f and each of the contact coordinates of the sphere Σ_{co} and the plane Σ_{cs} can be developed [see Appendix B.3 for the details of calculation]. By using the general derived Darboux relation (B.22), the normal curvature k_n^o, the geodesic curvature k_g^o and geodesic torsion of τ_g^o of the contact coordinate of the sphere $\boldsymbol{e}_u^o$ in the direction of $\boldsymbol{e}_1^s$ becomes

$$\begin{aligned} k_n^o &= k_{nu}^o \cos^2\varphi + 2\tau_{gu}^o \cos\varphi \sin\varphi + k_{nv}^o \sin^2\varphi = 1/R_o, \\ \tau_g^o &= \tau_{gu}^o \cos 2\varphi + \frac{1}{2}(k_{nv}^o - k_{nu}^o)\sin 2\varphi = 0, \\ k_g^o &= k_{gu}^o \cos\varphi + k_{gv}^o \sin\varphi = \tan v_o \cos\varphi / R_o. \end{aligned} \tag{5.6}$$

The normal curvature k_n^s, the geodesic curvature k_g^s and the geodesic torsion of τ_g^s of the contact coordinate of the plane $\boldsymbol{e}_u^s$ in the direction of $\boldsymbol{e}_1^s$ ($\boldsymbol{e}_u^s - \boldsymbol{e}_1^s$ make the angle of $\varphi + \theta$ as Fig. 5.2) is

$$\begin{aligned} k_n^s &= k_{nu}^s \cos^2(\theta+\varphi) + 2\tau_{gu}^s \cos(\theta+\varphi)\sin(\theta+\varphi) + k_{nv}^s \sin^2(\theta+\varphi) = 0, \\ \tau_g^s &= \tau_{gu}^s \cos 2(\theta+\varphi) + \frac{1}{2}(k_{nv}^s - k_{nu}^s)\sin 2(\theta+\varphi) = 0, \\ k_g^s &= k_{gu}^s \cos(\theta+\varphi) + k_{gv}^s \sin(\theta+\varphi) = 0. \end{aligned} \tag{5.7}$$

Also, the induced curvatures in (5.5) become independent of each other for $\theta + \gamma = (k+1)\pi/2$ or $k\pi$ where $k \in N$.

Eq. (5.4) is the angular velocities of the Darboux frame. Transformation that expresses the Darboux frame $(\boldsymbol{e}_1^s, \boldsymbol{e}_2^s, \boldsymbol{e}_3^s)$ on the frame $(\boldsymbol{e}_u^o, \boldsymbol{e}_v^o, \boldsymbol{e}_3^o)$ of the sphere is

$$\begin{aligned} \boldsymbol{e}_1^s &= \cos(\varphi+\theta)\boldsymbol{e}_u^o + \sin(\varphi+\theta)\boldsymbol{e}_v^o, \\ \boldsymbol{e}_2^s &= -\sin(\varphi+\theta)\boldsymbol{e}_u^o + \cos(\varphi+\theta)\boldsymbol{e}_v^o, \\ \boldsymbol{e}_3^s &= \boldsymbol{e}_3^o \end{aligned} \tag{5.8}$$

The angular velocity of the Darboux frame $\boldsymbol{\omega}^*$ is equal to the angular velocity of the sphere. Thus, one gets the angular velocity of the sphere $\boldsymbol{\omega_o}$ by substituting (5.8) into (5.4), [see Fig. 5.2] as follows

$$\boldsymbol{\omega}^o = \omega_x^o \boldsymbol{e}_u^o + \omega_y^o \boldsymbol{e}_v^o + \omega_z^o \boldsymbol{e}_3^o, \tag{5.9}$$

where

$$\begin{aligned} \omega_x^o &= \delta(-\cos(\varphi+\theta)\tau_g^* - \sin(\varphi+\theta)k_n^*), \\ \omega_y^o &= \delta(-\sin(\varphi+\theta)\tau_g^* + \sin(\varphi+\theta)k_n^*), \\ \omega_z^o &= \delta(-k_g^*). \end{aligned} \tag{5.10}$$

The following angular velocities (5.10) are in terms of δ, θ and φ including the virtual surface where δ is rolling rate of the sphere and θ and φ angles are for assigning the direction of the sphere on plane. Because we use kinematics that gives the angular velocities $(\omega_x^o, \omega_y^o, \omega_z^o)$, all these input variables directly change the motion of the sphere on the plane.

The angular velocities of the Darboux frame in Eq. (5.10) have to be transferred to the states of the sphere and plane for motion planning. We utilize the Montana equation [74] with the inclusion of no-sliding constraints for this transformation. By knowing (5.2)-(5.3) properties, we can have the kinematic equations as follows

$$\begin{bmatrix} \dot{u}_s(t) \\ \dot{v}_s(t) \\ \dot{u}_o(t) \\ \dot{v}_o(t) \\ \dot{\psi}(t) \end{bmatrix} = \begin{bmatrix} 0 & R_o & 0 \\ -R_o & 0 & 0 \\ -\sin\psi/\cos v_o & -\cos\psi/\cos v_o & 0 \\ -\cos\psi & \sin\psi & 0 \\ -\sin\psi\tan v_o & -\cos\psi\tan v_o & -1 \end{bmatrix} \begin{bmatrix} \omega_x^o \\ \omega_y^o \\ \omega_z^o \end{bmatrix} \tag{5.11}$$

where ψ is the spin angle between the sphere and plane as Fig. 5.1. We use equation (5.11) as the spin-rolling sphere-plane kinematics. Next, we substitute the derived Darboux frame equations (5.10) into $(\omega_x^o, \omega_y^o, \omega_z^o)$ inputs at (5.11) with known curvature properties

$$\begin{bmatrix} u_s'(s) \\ v_s'(s) \\ u_o'(s) \\ v_o'(s) \\ \psi'(s) \end{bmatrix} = \begin{bmatrix} \sin(\theta+\varphi) \\ \sin(\theta+\varphi) \\ \frac{\sin(\theta+\varphi)[\sin\psi-\cos\psi]}{R_o\cos v_o} \\ \frac{\sin(\theta+\varphi)[\cos\psi+\sin\psi]}{R_o} \\ \frac{\tan v_o[\sin(\theta+\varphi)(\sin\psi-\cos\psi)+\cos\varphi]}{R_o} \end{bmatrix} + \begin{bmatrix} -R_o\sin(\theta+\varphi) \\ -R_o\sin(\theta+\varphi) \\ \frac{\sin(\theta+\varphi)[\cos\psi-\sin\psi]}{\cos v_o} \\ -\sin(\theta+\varphi)[\sin\psi+\cos\psi] \\ \tan v_o[\sin(\theta+\varphi)(\cos\psi-\sin\psi)] \end{bmatrix} \gamma_s + \begin{bmatrix} R_o\sin(\theta+\varphi) \\ -R_o\cos(\theta+\varphi) \\ \frac{-\sin(\psi+\theta+\varphi)}{\cos v_o} \\ -\cos(\psi+\theta+\varphi) \\ -\tan v_o\sin(\psi+\theta+\varphi) \end{bmatrix} \beta_s + \begin{bmatrix} 0 \\ 0 \\ 0 \\ 0 \\ -1 \end{bmatrix} \alpha_s. \tag{5.12}$$

The new kinematics in s-domain becomes a model with a drift term in which the sphere can be manipulated toward its desired rotations on the plane. This new model (5.12) apart from arc-length-based control inputs (α_s, β_s, γ_s), have angles $\{\theta(u_o, v_o, \psi), \varphi(\psi)\}$ in function of states, coming from (5.10), that we design them in our planning problem. Geometrically, if we have our virtual surface inputs (α_s, β_s, γ_s) zero, the drift term varies (change in $\{\theta, \varphi\}$ angles) the sphere velocity on plane with constant angular direction on plane (45^o). However, assigning larger $\{\theta, \varphi\}$ results in the sphere states (u_o, v_o, ψ) orientate faster to converge the required angular difference of $\{\theta, \varphi\}$. Note that the drift term appears due to the substituted sphere's normal and geodesic curvatures (5.2) which are dependent on $\{\theta, \varphi\}$ by our the Darboux frame (5.10). Also, this drift term vanishes in time-domain because rolling rate δ that provides rest-to-rest locomotion converges to zero. We have checked the controllability

of this system in Appendix B.4. Note that θ and φ angles from the derived Darboux frame will be assigned as the aforementioned rotation direction of the sphere on the plane. This means our planning will be easier with this parameterization. The three arc-length inputs (virtual surface) will be designed to converge the sphere desired rotational angles while assigned θ and φ angles keep the sphere in the desired direction on the plane as Fig. 5.2.

5.3 Path Planning

We first explain the outline of our planning problem for the sphere that moves along a straight path on the plane as Fig 5.3. This approach plans the path of the sphere to its final configuration while the rotating sphere follows the shortest path on the plane toward its desired position. Because the no-sliding constraint urges that the length of the curve on the sphere $\mathbf{L}_o$ has to be equal to the plane $\mathbf{L}_s$, curve may not be long enough to reach certain configurations on the sphere. This limitation is mainly due to our considered approach with a restricted path on the plane. To deal with this issue, we find a minimum distance constraint that determines the minimum length of the curve for reaching the sphere to its desired states. In other words, the length of the desired plane position respect to its initial value should always be chosen larger than the minimum distance constraint that we find on the sphere depending on the given desired states of the sphere. Note that this limitation only appears when the length between the initial and final states of the plane is less than the circumference of the sphere. We calculate this distance constraint for the plane via applying the Gauss-Bonnet theorem [39] to the created circular path on the desired angular states of the sphere. By finding the sphere's curve length as the distance constraint, the length between the initial and desired position of the plane is chosen larger than this value, without the limitation on the direction of the desired plane position. Thus, any full-configuration can be achieved under the given constraint.

Since we want to use the obtained kinematic model with arc-length-based inputs (5.12) in our planning approach, a virtual surface responsible for controlling these inputs is introduced in Section 5.3.2. The reason for introducing the virtual surface is to converge the curve toward the desired states of the sphere. This curvature-based variation simplifies the planning as manipulating a flexible rope (curve $\mathbf{L}_o$)

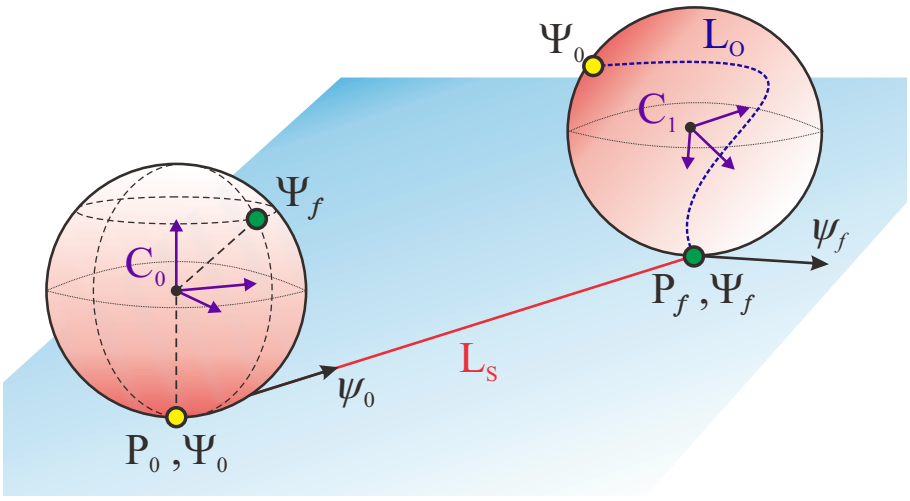

Figure 5.3: Statement of planning problem while the sphere with contact path of $\mathbf{L}_o$ follows a straight path $\mathbf{L}_s$ on plane.

with the constant length on the sphere. With reliance on the kinematic relation (5.5) in the s-domain (arc-length domain), we design a controller with the desired curvature relations of the obtained virtual surface. This geometric-based controller converges the rotating object (sphere) trajectory to the desired angular states of the sphere. Also, an algorithm will be proposed to tune this controller– to reach the desired full-configuration of the sphere– in the incoming section.

5.3.1 Problem Statement

Configuration of a sphere on a plane (see Fig. 5.3) is described with the sphere position on plane $\mathbf{P} = (u_s, v_s)$ and its local orientation $\mathbf{\Psi} = (u_o, v_o)$ which ψ is the spin angle between the sphere and plane. We consider our initial and final states with following notations $\{\mathbf{P}_0, \mathbf{\Psi}_0, \psi_0\} = \{u_{s,0}, v_{s,0}, u_{o,0}, v_{o,0}, \psi_0\}$ and $\{\mathbf{P}_f, \mathbf{\Psi}_f, \psi_f\} = \{u_{s,f}, v_{s,f}, u_{o,f}, v_{o,f}, \psi_f\}$, respectively. In this planning, the state equation (5.12) is solved in k iterations till finding admissible paths, where the traveled paths on the sphere and plane are noted as $\mathbf{L}_o$ and $\mathbf{L}_s$. We plan the sphere to reach its final configuration $C_0 \rightarrow C_1$ with a straight trajectory on $\mathbf{L}_s$ in the given t_f time. This planning problem can be looked as the optimal solution since the shortest trajectory on the plane $\mathbf{L}_s$ is always straight [19].

It is assumed that the initial states $\{\mathbf{P}_0, \mathbf{\Psi}_0, \psi_0\}$ and the final desired states of the sphere $\{\mathbf{\Psi}_f, \psi_f\}$ are given. However, final desired position on the plane $\mathbf{P}_f$ has to

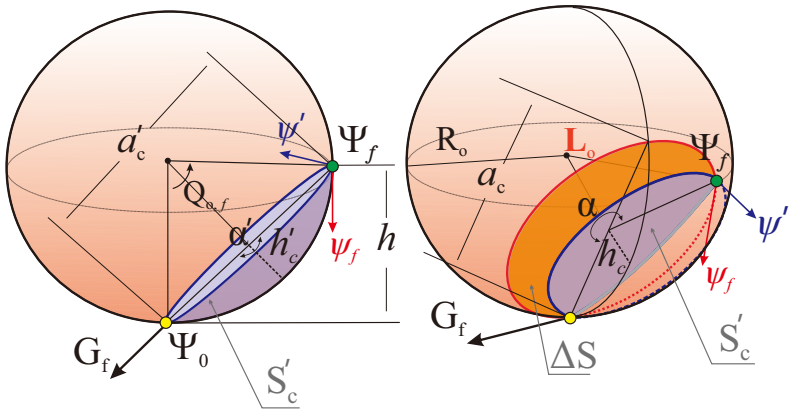

Figure 5.4: Limit of minimum distance d that is required to reach desired ψ_f. Note that G_f shows the desired goal angle on plane.

be specified under the consideration that the length between initial and final position $||\mathbf{P}_f - \mathbf{P}_0||_2 = [(u_{s,f} - u_{s,0})^2 + (v_{s,f} - v_{s,0})^2]^{\frac{1}{2}}$ is greater than the minimum distance constraint d where this constraint is calculated by the rest of desired and initial states. This length limitation appears because the total curve length of $\mathbf{L}_o$ on the sphere is always the same (no-sliding constraint) as $\mathbf{L}_s$ that goes in a straight trajectory. Also, the sphere has to arrive at desired local coordinate $\mathbf{\Psi}_f$ with different approaching angles, as the desired spin ψ_f, while it follows a straight optimal line rather than maneuvering freely through the plane U_S. Hence, by knowing the sphere desired states $\{\mathbf{\Psi}_f, \psi_f\}$, the $\mathbf{P}_f$ is chosen in any desired direction $\{u_{s,f}, v_{s,f}\}$ with the length $||\mathbf{L}_s|| = ||\mathbf{P}_f - \mathbf{P}_0||_2$ larger than minimum distance constraint as

$$d < ||\mathbf{P}_f - \mathbf{P}_0||_2, \tag{5.13}$$

where $||-||_2$ stands for the norm of the local coordinate points on $\mathbb{R}^2$. Note that this constraint d is not important and the sphere can reach all possible configurations, if the length of the desired position $||\mathbf{P}_f - \mathbf{P}_0||_2$ is set larger than sphere circumference $2\pi R_o$. To find the minimum distance d, a path is constructed as a circular segment on the sphere that passes $\mathbf{\Psi}_f$, and then the cap area is changed toward true desired ψ_f by Gauss-Bonnet theorem [39]. Then, by the trigonometric relations in the new under-cap area, we find the length of $\mathbf{L}_o$ as the minimum distance, where $||\mathbf{L}_s|| = ||\mathbf{L}_o||$.

Let the minimum distance $d = 2\pi a_c \alpha$ be the circumference of the orange cap-area that sphere travels, red line $\mathbf{L}_o$ on the right sphere at Fig. 5.4, where a_c and α are

the base diameter of this circumference and the angle of sector from $\mathbf{\Psi}_0$ to $\mathbf{\Psi}_f$ on the sphere U_C, respectively. First, we find the base diameter a_c of the cap with the following formulation

$$a_c = 2\sqrt{(S_t/\pi) - h_c^2},\ h_c = S_t/(2\pi R_o), \tag{5.14}$$

where S_t and h_c are the total area of the cap-shaped region [orange and blue regions in Fig. 5.4] and height of the cap area. Notice that the rotation of the sphere along the red path $\mathbf{L}_o$ doesn't cover the whole cap-shaped region. Thus, we find the total area as $S_t = 2S'_c + \triangle S$ where S'_c is the constructed cap area of the circular path by $\mathbf{\Psi}_f$ [see the blue cap-shaped region in Fig. 5.4] and $\triangle S$ is the area change [see the orange region in Fig. 5.4] for reaching from the spin angle ψ' with cap area of S'_c to desired spin angle ψ_f. Here, S_t has two parts which combining them gives the full segment of the circular cap (dashed and solid red line $\mathbf{L}_o$). First, the area of the cap-shaped region of S'_c is determined from the closed simple circle that passes $\mathbf{\Psi}_f$

$$S'_c = (\alpha'/2\pi) \cdot \left[(a'_c/2)^2 + {h'}_c^2\right] \tag{5.15}$$

where ${a'}_c$, ${h'}_c$ and α' are the diameter of cap's base, height of the cap and the sector angle from sphere initial to final configuration $\mathbf{\Psi}_f$ on the cap's base, α' equals to π. Following parameters in (5.15) are calculated with the help of Eq. (5.1) and trigonometric relations, shown in Fig. 5.4,

$$\begin{aligned}
h &= R_o\left[1 - \cos u_{o,f} \cos v_{o,f}\right], \\
{a'}_c &= \left[h^2 + R_o^2\left(\sin^2 v_{o,f} + \sin^2 u_{o,f} \cos^2 v_{o,f}\right)\right]^{1/2}, \\
{h'}_c &= \begin{cases} R_o\left[1 - \cos\left(Q_{o,f}/2\right)\right], & a'_c \le 2R_o \\ R_o\left[1 - a'_c \cos\left(Q_{o,f}/2\right)/2R_o\right], & a'_c > 2R_o \end{cases}
\end{aligned}$$

where $Q_{o,f}$ is the angle from initial contact point $\mathbf{\Psi}_0 = \{0, 0\}$ to desired local coordinates $\mathbf{\Psi}_f$ as

$$Q_{o,f} = \begin{cases} \pi - 2\cos^{-1}\left(h/a'_c\right), & h \le R_o \\ \frac{\pi}{2} - \sin^{-1}\left((h - R_o)/R_o\right), & h > R_o \end{cases}$$

Also, by knowing the a_c and a'_c, the new sector angle from $\mathbf{\Psi}_0$ to $\{\mathbf{\Psi}_f, \psi_f\}$ (red $\mathbf{L}_o$

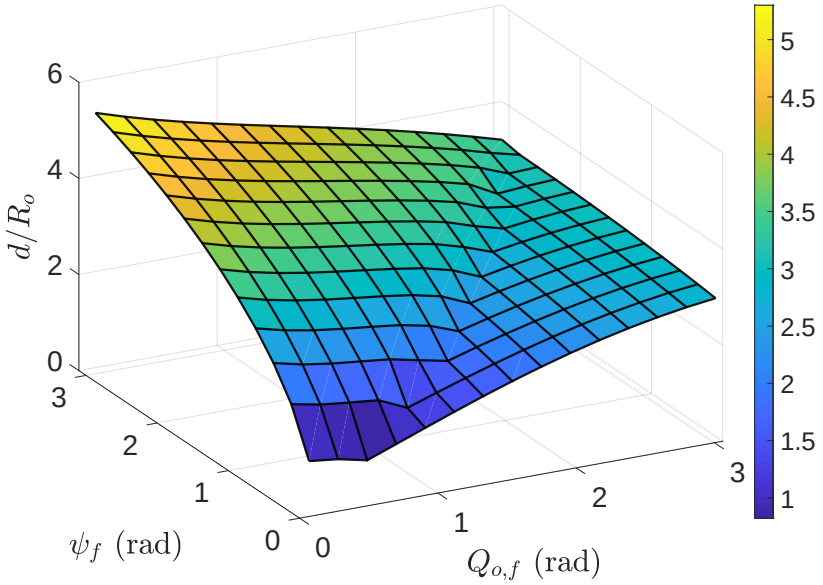

Figure 5.5: Normalized minimum distance d/R_o for different desired angles where $u_{o,f} \in [0, \pi]$ and $v_{o,f} = 0.01$.

line in Fig. 5.4) becomes

$$\alpha = \frac{1}{2\pi} \cdot \begin{cases} 1 - 2\sin^{-1}(a_c'/a_c), & \Delta S \geq 0 \\ 2\sin^{-1}(a_c'/a_c), & \Delta S < 0 \end{cases} \tag{5.16}$$

To find the achieved spin angle ψ' by the contacted S_c' cap-area, we use the Gauss-Bonnet theorem [39] while the sphere touches the circular closed blue path

$$\triangle\psi = \psi' - \psi_0 = \iint_{S_c'} \kappa_o \, dS = S_c'/R_o^2, \tag{5.17}$$

where $\kappa_o = 1/R_o^2$ is the Gaussian curvature and the initial spin angle is assumed $\psi_0 = 0$. Finding the spin angle ψ' also let us calculate ΔS in S_t. The required area-change ΔS for achieving ψ_f is calculated by the same Gauss-Bonnet theorem as follows

$$\triangle S = (\psi_f - \psi')/\kappa_o = R_o^2(\psi_f - \psi'). \tag{5.18}$$

After obtaining the total area S_t for reaching ψ_f, a_c in (5.14) and α in (5.16) give us the value of minimum distance d. Fig. 5.5 depicts the normalized minimum distance for different desired angles which shows how small $||\mathbf{P}_f - \mathbf{P}_0||_2$ can be for the example final configurations. It is clear that as the desired local coordinate $\mathbf{\Psi}_f$ moves to upper-hemisphere, $\mathbf{P}_f$ has to set for the longer length from $\mathbf{P}_0$. Also. the same property is

true for rising the spin angle ψ_f. Moreover, the largest distance requirement happens at lower points of $\mathbf{\Psi}_f$ ($Q_{o,f} \leq \pi/2$) with larger desired spin angles ψ_f. Note that this constraint d, with the assumption of a simple circular curve (5.13), is looked as the shortest length under the isoperimetric inequality, $4\pi S_t \leq d^2$.

5.3.2 Geometric Control by Virtual Surface

The Darboux-frame-based kinematics (5.12) that is developed with inputs in arc-length domain requires a geometric control for converging spin-rolling sphere to desired angular configuration $\mathbf{\Psi}_f$. We introduce a virtual surface U_V to produce these arc-length-based inputs $\{\alpha_s, \beta_s, \gamma_s\}$. As the key idea, the virtual surface is a surface sandwiched between sphere and plane by the kinematics (5.5) at the moving frame $\sum_f$. From a physical point of view, deformation (curvature changes) of this virtual surface is projected onto both sphere and plane trajectories [see Fig. B.2]. These changes in the curvature give us the ability to manipulate curve on the sphere $\mathbf{L}_o$ like a flexible rope. Note that to bend this rope-like curve toward the desired full-configuration, we will propose a tuning algorithm to update the variables of this virtual surface in the incoming section.

The curvature manipulation by virtual surface is directly giving the arc-length deviations at the three independent inputs $\{\alpha_s, \beta_s, \gamma_s\}$ [already proved in Appendix B.2]. In our case, the proposed virtual surface has normal and geodesic curvature of the sphere (sphere has zero geodesic torsion) and the geodesic torsion is in the shape of the helicoid. Note that the independence of the arc-length inputs (5.5), let us substitute curvature properties from different surfaces for each corresponding input. To geometrically control the sphere trajectory, we alter the radius and projection angles of the virtual surface through the developed desired curvature properties.

We here design the virtual surface for controlling the curve $\mathbf{L}_o$ on sphere manifold U_C when $\mathbf{L}_s$ is specified as a straight path. Before defining our geometric control based on the virtual surface, the following proposition is expressed for the controllability of the Darboux-based kinematic (5.12).

Proposition 5.3.1 *All three arc-length-based control inputs, in particular γ_s and β_s, always do exists in (5.12). Otherwise, rank of Lie bracket n for drift system becomes $n < 5$. This makes the kinematic model uncontrollable [see Appendix B.4].*

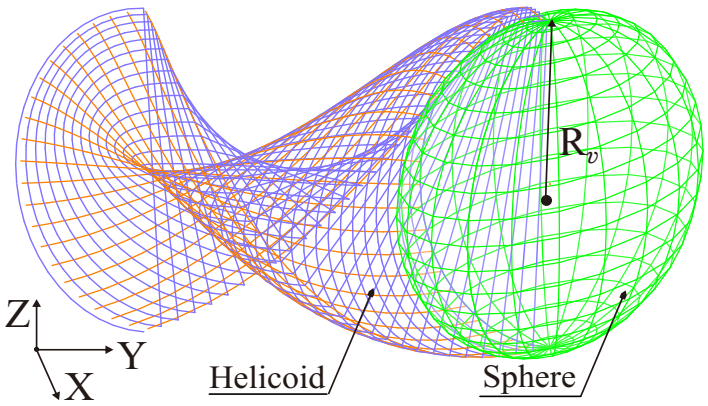

Figure 5.6: Geometric shape of the used virtual Surface U_V. Note: Green and blue surfaces are for $R_t = 0$ as the sphere and $R_t = R_v$ as the helicoid.

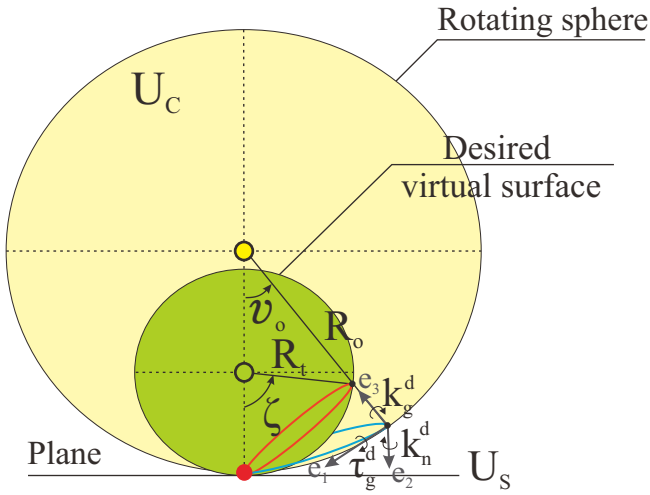

Figure 5.7: Design of the arc-length-based inputs by using desired virtual surface. Note that schematic is drawn for $u_o = 0$.

Definition 5.3.1 The curvature properties are designed with similarity to rotating object (sphere) manifold U_C for proper planning by virtual surface. However, the moving object is a sphere with $\tau_g^o = 0$. This contradicts with Proposition 5.3.1 because $\beta_s = 0$. As a solution, geodesic torsion of a helicoid shape is applied where the geometric shape is like Fig. 5.6 (see Appendix B.5 for details of derivation)

$$\tau_g^v = \frac{1}{R_v^2} |R_v^2 \cos^2 v_v(t) - R_t^2|^{\frac{1}{2}}, \tag{5.19}$$

where R_v, R_t and $v_v(t)$ are defined by main spherical radius, sum of spherical and

torsion radii and v-curve of helicoid surface, respectively. As a keynote, following surface as Fig. 5.6 is able to transform from the sphere to the helicoid surface by changing R_t. Next, we utilize Eq. (5.5) to construct the desired virtual surface [see Fig. 5.7] with the normal and geodesic curvature of the spherical surface $\{k_n^d(s), k_g^d(s)\}$ in (5.2)-(5.3) and the geodesic torsion of the helicoid surface $\tau_g^d(s)$ (5.19) as follows

$$\begin{aligned} k_n^d(s) &= 1/R_n = 1/R_o - \gamma_s, \\ k_g^d(s) &= \tan\zeta/R_t = \tan v_{o,f}/R_o - \alpha_s, \\ \tau_g^d(s) &= \frac{1}{R_o^2}\left|R_o^2\cos^2 v_o' - R_t^2\right|^{\frac{1}{2}} = \beta_s. \end{aligned} \tag{5.20}$$

where $R_t = R_n + R_g$ and $v_o' = v_{o,f} - v_o(t)$ are the total radius and the angle feed of v-curve in which R_n and R_g are the desired normal curvature and geodesic torsion radii. Also, we assume ζ is the desired stereographic projection angle for the spherical object along $k_g^d \boldsymbol{e}_3$ vector. By considering that the diameter of projected curve is same [red and blue curves in Fig. 5.7], $R_t \tan\zeta = R_o \tan v_o$, ζ is determined

$$\zeta = \tan^{-1}\left[R_o \tan\left(v_{o,f} + \zeta'\right)/R_t\right], \tag{5.21}$$

where ζ' is the constant angle shift that will be used during planning updates. Also, R_n and R_g are defined as

$$R_n(t) = R_g(t) = \left[R_i(t) + R_a\right]/2, \tag{5.22}$$

where R_i and R_a are the built-in incircle radius of u-curve and tuning constants that happens by algorithm, respectively. By using Fig. 5.8, built-in radius R_i is computed with the change of the designed incircle radius as follows

$$R_i(t) = \begin{cases} \left[\dfrac{(S_i - r_i)^2(S_i - l_i)}{S_i}\right]^{\frac{1}{2}}, & 0 \le u_o' < \dfrac{\pi}{2} \\ \dfrac{R_o}{\mu_r} + \left[\dfrac{(S_i - r_i)^2(S_i - l_i)}{S_i}\right]^{\frac{1}{2}}, & \dfrac{\pi}{2} \le u_o' \le \pi \end{cases} \tag{5.23}$$

where $S_i = (2r_i + l_i)/2$ is the area of encompassed triangle of the incricle, $u_o' = u_{o,f} - u_o(t)$ is the convergence of u-curve, μ_r is the scaler to limit the maximum built-in radius R_i, and also $r_i = R_o/\cos u_o'$ and $l_i = 2R_o \tan u_o'$ are adjacent and hypotenuse sides of isosceles triangle [see Fig. 5.8].

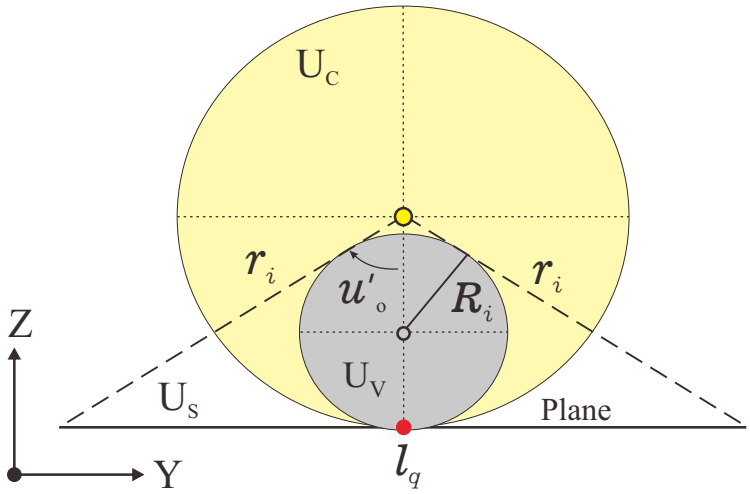

Figure 5.8: R_i determination by incircle of u'_o.

Remark 5.3.1 *The sphere curvature in Eq. (5.20) is included to cancel out the existing sphere U_C properties that drift terms is presenting in the kinematic model (5.12). Thus, this design gives a direct manipulation of virtual surface curvatures (s-domain) on $\mathbf{L}_o$ trajectory for $\mathbf{\Psi}_f$.*

Now, we can find the geometric control inputs from (5.20) in Definition 5.3.1 as

$$\begin{aligned} \gamma_s &= \frac{R_n - R_o}{R_n R_o}, \\ \beta_s &= \frac{1}{R_o^2}|R_o^2 \cos^2 v'_o - R_t^2|^{\frac{1}{2}}, \\ \alpha_s &= \tan v_{o,f}/R_o - \tan \zeta / R_t. \end{aligned} \tag{5.24}$$

By substituting the desired final values, the curves of $\mathbf{L}_o$ are constrained on the virtual surface with the projection on the rotating object, as the example of Fig. 5.7. This constrained curve is created from a conservative vector field in (5.24) where independent inputs act as force fields $\mathbf{F} = \nabla \mathbf{E}_{in}(u_o(t), v_o(t), u_{o,f}, v_{o,f}) = \{\alpha_s, \gamma_s, \beta_s\}$ to manipulate the moving frame Σ_f on U_C manifold [114]. By using kinematic (5.5), it is interpreted that the desired virtual surface bends this vector field towards the desired local coordinate $\mathbf{\Psi}_f$ [2] . Note that our curve manipulation on the sphere manifold U_C can be imagined as a flexible rope with length of $||\mathbf{P}_f - \mathbf{P}_0||_2$ that

[2]See the example result of the kinematic model with the designed geometric controller in Fig. 5.10.

$\{R_n, R_g\}$ and ζ terms change the curvature radius and angle of v-curve for the $\mathbf{L}_o$ on the spherical surface U_C.

We have to clarify, the proposed virtual surface is designed in a way that eases our planning problem with spherical curvature properties k_n^v and k_g^v. However, more complicated virtual surfaces with existing geodesic torsion τ_g^v can be applied to this planning approach for creating different contact paths but it can complicate planning problem, e.g., algorithm tuning, which requires a separate study.

5.4 Motion Planning Algorithm

5.4.1 Iterative Tuning Algorithm

We plan the rotating sphere with a straight curve $\mathbf{L}_s$ at the plane while the sphere reaches to its given configuration. The flowchart in Fig. 5.9 shows our proposed search algorithm that uses the control inputs (5.24) to do path planning. Geometrically, it is looked as manipulating curvature radii $\{R_n, R_g\}$ and angular location ζ' to bend the created rope-like curve $\mathbf{L}_o$ from (5.24) on the sphere. For example, constant raise in $\{R_n, R_g\}$ expand the curve $\mathbf{L}_o$ like enlarging the loops of the rope while its length is constant [see Fig. 5.10]. Also, constant changes on ζ' moves the $\mathbf{L}_o$ on the cutting plane of $u_{o,f}$. To do the convergence of this rope-like model, the proposed algorithm is solving (5.12) and (5.24) in iterations with the re-tuned constants in $\{R_n, R_g\}$ and ζ'.

To shift the curve of the sphere $\mathbf{L}_o$ by $\zeta'(k) = \zeta_q(k)+\zeta_u(k)$ on the cutting plane $u_{o,f}$, updates happen in Phase I and II by ζ_q and ζ_u, respectively. Also, constant change in the desired radius R_a is defined by the inclusion of all phases as $R_a(k) = R_q(k)+R_u(k)$, where R_q and R_u are tuning constants of radii in the steps of the Phase II. Our tuning algorithm consists of three primary steps:

The first step as the Phase I is the main part of the algorithm where the kinematic model (5.10)-(5.11) with designed arc-length-based inputs (5.24) is numerically solved in time domain. After obtaining $\mathbf{L}_o$ and $\mathbf{L}_s$ curves, the Phase I checks whether there is a point on $\mathbf{L}_o$ that passes the desired local coordinates on the sphere $\mathbf{\Psi}_f$. If $\mathbf{L}_o$ fails to reach $\mathbf{\Psi}_f$, ζ_q is re-tuned and kinematic model is resolved numerically. After succeeding the Phase I, the curve is checked whether the final point of local coordinate

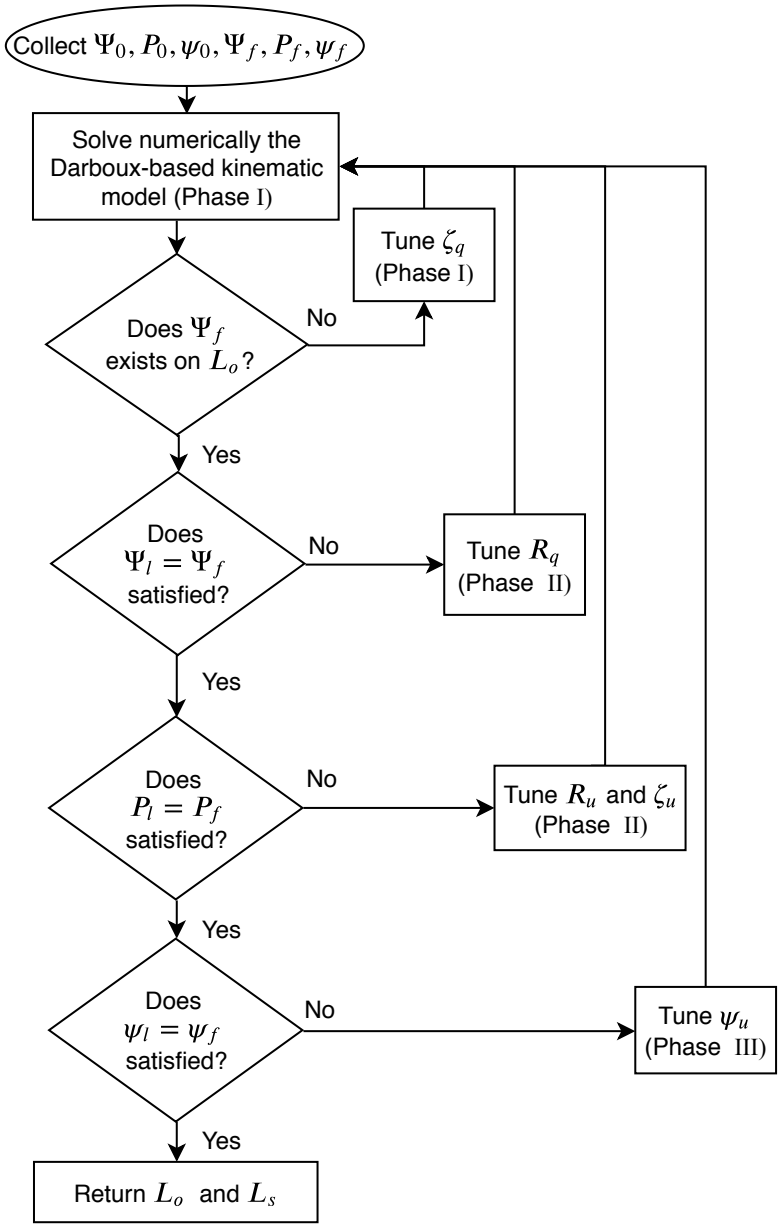

Figure 5.9: The flowchart of planning algorithm.

$\mathbf{\Psi}_l$ is at desired values of $\mathbf{\Psi}_f$ as Fig. 5.11. If the curve $\mathbf{L}_o$ fails from $\mathbf{\Psi}_l = \mathbf{\Psi}_f$, the radius of virtual desired surface R_q is increased by obtained error. Also, Phase II has a second extra step to reach the sphere final distance $\mathbf{P}_l$ to exact desired plane configuration $\mathbf{P}_l = \mathbf{P}_f$ by tuning R_u and ζ_u parameters. In the final step, the final state as the desired spin angle ψ_f is checked. Note that this algorithm requires to numerically solve differential equations in infinite k iterations till full convergence of

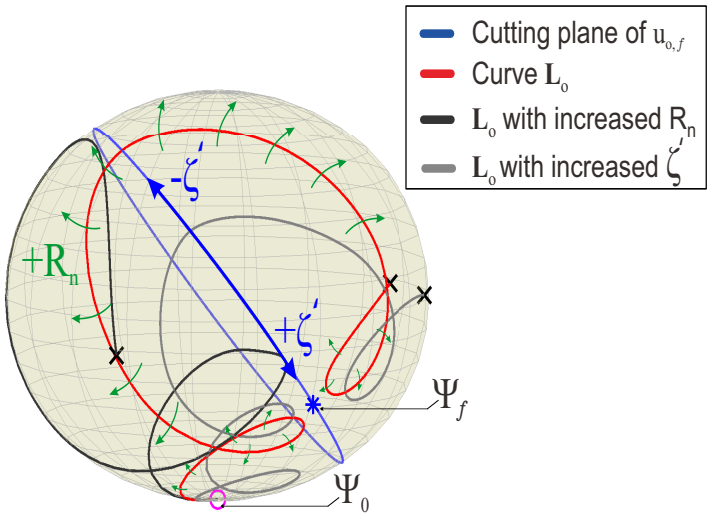

Figure 5.10: Manipulation of the rope-like $\mathbf{L}_o$ curve with the designed virtual surface.Note that following curves are obtained by using formulas in Phase I for ψ_q and δ in Eq. (5.28) and (5.29).

the chosen configuration.

Phase I

This phase solves the kinematic model first. Then, it finds the curve $\mathbf{L}_o$ on the rotating sphere that passes $\mathbf{\Psi}_f$ while the sphere moves toward the $\mathbf{P}_f$.

At first, the kinematic model (5.10)-(5.11) has to be solved with θ, φ and δ terms of the Darboux kinematics where we define their functions here. In the kinematic model (5.10)-(5.11), rotational angles θ and φ are the main factors for rotating the sphere in the desired direction $\mathbf{P}_f$ on plane via the designed Darboux frame. To move in the direction of $\mathbf{P}_f$ with the straight trajectory on $\mathbf{L}_s$, we find the θ from Eq. (5.12). Derivation happens by the definition of the goal angle on plane G_f in a small-time step dt from the Darboux-based kinematic model of the plane's local coordinate $c(u_s, v_s)$ as

$$G_f \triangleq \tan^{-1}\left(\frac{dv_s}{du_s}\right) = \tan^{-1}\left(\frac{\sin(\theta+\varphi) - R_o\sin(\theta+\varphi)\gamma_s - R_o\cos(\theta+\varphi)\beta_s}{\sin(\theta+\varphi) - R_o\sin(\theta+\varphi)\gamma_s + R_o\sin(\theta+\varphi)\beta_s}\right),$$

after factoring the numerator and denominator by $\sin(\theta+\varphi)$ and finding equation for $\theta+\varphi$, we have

$$\theta+\varphi = \cot^{-1}\left[\frac{1}{\beta_s}\left(\frac{1}{R_o}(1-\tan G_f) + \gamma_s(-1+\tan G_f) - \beta_s\tan G_f\right)\right]. \tag{5.25}$$

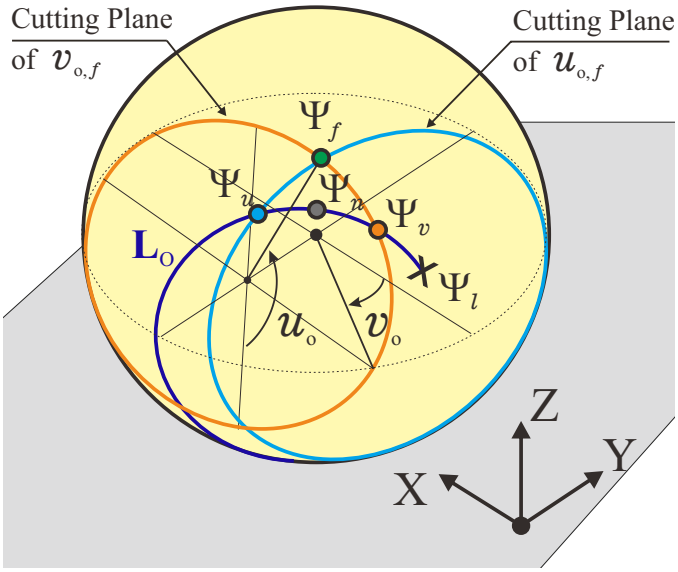

Figure 5.11: Parametrization of the curve $\mathbf{L}_o$ by cutting planes of $u_{o,f}$ and $v_{o,f}$.

Because θ is the angle between two surfaces $\boldsymbol{e}_u^o - \boldsymbol{e}_u^s$, we use (5.25) for this parameter only. Thus, θ and φ angles becomes

$$\theta(u_o, v_o, \psi) = \cot^{-1}\left[\frac{1}{\beta_s}\left(\frac{1}{R_o}(1-\tan G_f) + \gamma_s(-1+\tan G_f) - \beta_s \tan G_f\right)\right] - \psi_q, \tag{5.26}$$

$$\varphi(\psi) = \eta + \psi_q, \tag{5.27}$$

where ψ_q is defined as the spinning angle deviation and η is

$$\eta = \begin{cases} \pi, & -\frac{3\pi}{4} < G_f < 0 \quad \& \quad 0 \le G_f < \frac{\pi}{4} \\ 0, & -\pi < G_f < -\frac{3\pi}{4} \ \& \ -\pi \le G_f < \frac{\pi}{4} \end{cases}$$

From now on, we define the goal angle by $G_f = \tan^{-1}\left[(v_{s,f} - v_{s,0})/(u_{s,f} - u_{s,0})\right]$; hence, θ and φ will change relative to any values of arc-length inputs, for keeping the sphere always along G_f angle to reach $\mathbf{P}_f$. Therefore, the sphere stays in the prescribed straight direction by substituting constant value to G_f from the desired position on the plane $\mathbf{P}_f$.

Developing a converging state for the spin angle is not a straightforward way. It can make tracking unstable as the sphere may pass the same desired spin angle many times during its rotation. Thus, we develop an indirect convergence by using spinning angle deviation ψ_q to converge the desired spin angle ψ_f. During calculations

of minimum distance d at (5.13), we assumed that under-cap area S_t of traversed distance $\mathbf{L}_o$ is constant while $C_0 \to C_1$. Thus, the desired under-cap area is defined by $S_t = S'_c + R_o^2(\psi_f + \psi_u(k) - \psi')$ (only orange and blue cap areas excluding dashed-line part as Fig. 5.4), where $\psi_u(k)$ is the constant re-tuning spin angle for Phase III. Next, we extend the Gauss-Bonnet theorem between two points of $\{u_o(t), v_o(t), \psi(t)\}$ and $\{u_{o,f}, v_{o,f}, \psi_f\}$ in time t, as

$$\psi_q(t) = \frac{1}{R_o^2}\left[S_t - S_i(t)\right] = \frac{1}{R_o^2}\left[S_t - R_o^2\left(\psi(t) - \psi_0\right)\right], \tag{5.28}$$

where $S_i(t)$ and $\psi(t)$ are the changing cap area from the initial state till current time t and the current spin angle.

As the last parameter in the kinematic model, the rolling rate (arc-length derivation relative to the time $\delta(t)$) is the parameter that is multiplied to all three inputs and drift term. This variable is related to the time (ds/dt) and it varies the arc-length step of curve $\mathbf{L}_o$ and $\mathbf{L}_s$ in the given time t. Therefore, δ is defined to have a rest-to-rest motion by

$$\begin{aligned}\delta(t, u_o, u_s, v_s) &= ||\mathbf{P}_f - \mathbf{P}(t)||_2 \cdot \left|\frac{v_{o,f} \cdot u'_o}{T}\right| \\ &= \left[(u_{s,f} - u_s(t))^2 + (v_{s,f} - v_s(t))^2\right]^{\frac{1}{2}} \cdot \left|\frac{v_{o,f} \cdot u'_o}{T}\right|,\end{aligned} \tag{5.29}$$

where T is the time scaling constant.

Algorithm 1 shows the computations of Phase I. By solving the Darboux-based kinematic model, the geometric parameters [see Fig. 5.11] are determined from obtained $\mathbf{L}_o$ and $\mathbf{L}_s$. $\mathbf{\Psi}_l$ and $\mathbf{P}_l$ are the final arrived configuration by the numerical solution. Also, $\mathbf{\Psi}_n$, $\mathbf{\Psi}_u$ and $\mathbf{\Psi}_v$ are the nearest point on $\mathbf{L}_o$ to $\mathbf{\Psi}_f$ and existing nearest points on $\mathbf{L}_o$ that are obtained by cutting planes of $u_{o,f}$ and $v_{o,f}$ on the sphere. Note that all points are collected as the final existing values since there is possibility that curve passes the nearest point or cutting planes more than once.

In the algorithm 1, ϵ_n is a small value for breaking while loop, when required accuracy is achieved for Phase I. Additionally, error e_n is the euclidean distance of nearest $\mathbf{\Psi}_n$ and desired $\mathbf{\Psi}_f$ points in $\mathbb{R}^3$

$$\begin{aligned}e_n = ||\mathbf{\Psi}_n - \mathbf{\Psi}_f||_3 = R_o\big[&(\sin v_{o,f} - \sin v_{o,n})^2 + (\cos u_{o,f}\cos v_{o,f} - \cos u_{o,n}\cos v_{o,n})^2 \\ &+ (\sin u_{o,f}\cos v_{o,f} - \sin u_{o,n}\cos v_{o,n})^2\big]^{\frac{1}{2}}.\end{aligned} \tag{5.30}$$

Algorithm 1 Phase I

procedure CONFIGSOLVE($\mathbf{\Psi}_f, \mathbf{P}_f, \psi_f, \mathbf{\Psi}_0, \mathbf{P}_0, \psi_0$)
  while $e_n \geq \epsilon_n$ **do**
    Solve the kinematic model (5.12) numerically
    Collect $\mathbf{\Psi}_n$, $\mathbf{\Psi}_l$, $\mathbf{\Psi}_v$ and $\mathbf{\Psi}_u$
    Compute e_n and e'_n by (5.30) ▷ Error of nearest point to $\mathbf{\Psi}_f$
    if $e_n(k) > \epsilon_n$ **then**
      Apply the directional comparison by $\mathbf{\Psi}_n$, $\mathbf{\Psi}_v$ and $\mathbf{\Psi}_u$ ▷ Details in Appendix B.6
      Calculate $\zeta_q(k)$ by (5.31)
    end if
  end while
end procedure

Next, the absolute angle difference between $\mathbf{\Psi}_f$ and $\mathbf{\Psi}_n$ are utilized to update the $\zeta_q(k)$ angle in k-th iteration of Phase I as follows

$$\zeta_q(k) = \zeta_q(k-1) \pm \begin{cases} e'_n \cdot |Q_f^{zx} - Q_n^{zx}|, & Q_f^{zx} = Q_n^{zx} \\ e'_n \cdot |Q_f^{zy} - Q_n^{zy}|, & Q_f^{zx} \neq Q_n^{zx} \end{cases} \tag{5.31}$$

where $e'_n = \min\{e_n\}$ is smallest error of e_n till iteration k and the angle differences with respect to $Z - X$ plane Q^{zx} and $Z - Y$ plane Q^{zy} for either $\mathbf{\Psi}_f$ or $\mathbf{\Psi}_n$ are obtained by Eq. (5.1) as

$$\begin{aligned} Q^{zx} &= \left| \tan^{-1}\left(\frac{\sin u_o \cos v_o}{\cos u_o \cos v_o} \right) \right| = |u_o|, \\ Q^{zy} &= \left| \tan^{-1}\left(\frac{\sin u_o \cos v_o}{\sin v_o} \right) \right|. \end{aligned} \tag{5.32}$$

The sign of each update in (5.31) is chosen from the directional updates in Appendix B.6. The goal of the directional update is to always move the curve $\mathbf{L}_o$ toward $\mathbf{\Psi}_f$ on the spherical surface U_C.

Phase II and III

After finding the suitable curve $\mathbf{L}_o$ from Phase I that passes $\mathbf{\Psi}_f$, Phase II tunes variable for converging $\mathbf{L}_o$ and $\mathbf{L}_s$ final arrived points ($\mathbf{\Psi}_l$ and $\mathbf{P}_l$) to the desired

Algorithm 2 Complete Computation

procedure CONFIGCOM($\boldsymbol{\Psi}_f, \mathbf{P}_f, \psi_f, \boldsymbol{\Psi}_0, \mathbf{P}_0, \psi_0$)
  while $e_s \geq \epsilon_s$ **do** ▷ Phase III
    while $(e_n \geq \epsilon_n)$ & $(e_r \geq \epsilon_r)$ & $\mathbf{P}_l \neq \mathbf{P}_f$ **do** ▷ Phase II
      while $e_r \geq \epsilon_r$ **do** ▷ Phase II
        CONFIGSOLVE(.) ▷ Phase I
        Compute e_r, e'_r, n_s and d_s
        if $\boldsymbol{\Psi}_l \neq \boldsymbol{\Psi}_n$ **then** ▷ update R_q
          $R_q(k) \leftarrow +R_q(k-1)$ according to (5.34)
        else
          $R_q(k) \leftarrow -R_q(k-1)$ by $n_s \leq 1$ case according to (5.34)
        end if
      end while
      if $||\mathbf{P}_f - \mathbf{P}_l||_2 > \epsilon_p$ **then** ▷ Phase II
        Update R_u and ζ_u
      end if
    end while
    if $\psi_l \neq \psi_f$ **then** ▷ Phase III
      Update ψ_u
    end if
    Reset e_n, e'_n, e_r and e'_r
  end while
return $\mathbf{L}_o$ and $\mathbf{L}_s$
end procedure

configurations on $\boldsymbol{\Psi}_f$ and $\mathbf{P}_f$. Algorithm 2 depicts the overall computations, including all the phases using the flowchart of Fig. 5.9.

In Phase II, the error e_r of final arrival point $\boldsymbol{\Psi}_l$ with respect to desire values of $\boldsymbol{\Psi}_f$ is first determined by

$$e_r = ||\boldsymbol{\Psi}_l - \boldsymbol{\Psi}_f||_3 = R_o\big[(\sin v_{o,f} - \sin v_{o,l})^2 + (\cos u_{o,f} \cos v_{o,f} - \cos u_{o,l} \cos v_{o,l})^2 + (\sin u_{o,f} \cos v_{o,f} - \sin u_{o,l} \cos v_{o,l})^2\big]^{\frac{1}{2}}. \tag{5.33}$$

Next, the update of R_q is to enlarge the loops of $\mathbf{L}_o$ for shorting the distance between nearest $\mathbf{\Psi}_n$ and final arrived $\mathbf{\Psi}_l$ points; hence, the algorithm computes the R_q update for k-th iteration by using the error e_r as

$$R_q(k) = R_q(k-1) + R_o \cdot \begin{cases} d_s \cdot e'_r, & n_s \leq 1 \\ n_s \cdot d_s \cdot e'_r, & 1 < n_s \leq 2 \\ (d_s \cdot e'_r)/n_s, & n_s > 2 \end{cases} \tag{5.34}$$

where $e'_r = \min\{e_r\}$, d_s and n_s are the smallest error of e_r till iteration k, distance ratio of $\mathbf{L}_s$ for the loop on the curve $\mathbf{L}_o$ and the numbers of created full loops by spinning ψ, respectively. The distance ratio d_s and the number of created loops $n_s \in \mathbb{R}$ are calculated as follows

$$\begin{aligned} d_s &= \frac{||\mathbf{P}_n - \mathbf{P}_f||_2}{||\mathbf{P}_0 - \mathbf{P}_f||_2} = \left[\frac{(u_{s,n} - u_{s,f})^2 + (v_{s,n} - v_{s,f})^2}{(u_{s,0} - u_{s,f})^2 + (v_{s,0} - v_{s,f})^2}\right]^{\frac{1}{2}}, \\ n_s &= |\psi_l/\psi_n|. \end{aligned} \tag{5.35}$$

Note that n_s is computed with the assumption that ψ value can be greater than 2π which every 2π orientation represents a loop on spin angle [114].

As the final step of Phase II, because our arc-length-based inputs create curve $\mathbf{L}_o$ with multiple loops (specially for $d \ll ||\mathbf{P}_f - \mathbf{P}_0||_2$), we use R_u and ζ_u variable for shifting $\mathbf{L}_o$ away from $\mathbf{\Psi}_0$ on the surface of the sphere U_C (can be looked as decreasing the size of the enlarged R_q) with same expressed flexible rope model. This computation step with updating ζ_u and R_u tries to reach $\mathbf{\Psi}_l \to \mathbf{P}_f$ as previous loops try to keep $\mathbf{\Psi}_l = \mathbf{\Psi}_f$ condition true,

$$\begin{aligned} R_u(k) &= R_u(k-1) - R_q(k) \cdot \frac{||\mathbf{P}_l - \mathbf{P}_f||_2}{||\mathbf{P}_l - \mathbf{P}_0||_2}, \\ \zeta_u(k) &= \zeta_u(k-1) + \begin{cases} -\tan^{-1}\left(\frac{R_u(k)\tan\zeta_q(k-1)}{R_o}\right), & \text{for } v_{o,f} \geq 0 \\ \tan^{-1}\left(\frac{R_u(k)\tan\zeta_q(k-1)}{R_o}\right), & \text{for } v_{o,f} < 0 \end{cases} \end{aligned} \tag{5.36}$$

Final phase is to update the tuning variable of the spinning angle ψ_u in Eq. (5.28) with

$$\psi_u(k) = \psi_u(k-1) - e'_s \text{sgn}[\psi_f - \psi_l], \tag{5.37}$$

where $e'_s = \min\{\psi_f - \psi_l\}$ is the smallest error till iteration k. Also, ϵ_s, ϵ_r and ϵ_p are the accuracies of each designated step in Algorithm 2.

5.4.2 Global Convergence of Algorithm

To prove the convergence of proposed iterative Algorithm 2, the Zangwill's convergence theorem is utilized as [126]

Theorem 5.4.1 *Let the iterative algorithm* $\mathbf{A}: \mathbb{R}^5 \to \mathbb{R}^3$*, showed in the flowchart at Fig. 5.9, be on* $\mathbf{X} = \mathbf{X}_I \circ \mathbf{X}_{II} \circ \mathbf{X}_{III}$ *compact set where* $\mathbf{X}_I$*,* $\mathbf{X}_{II}$ *and* $\mathbf{X}_{III}$ *are sets of phase I, II and phase III computation steps, respectively. Given* $\mathbf{x}_0 \in \mathbf{X}$*, the created sequence* $\{\mathbf{x}_k\}_{k=1}^{\infty}$ *satisfies* $\mathbf{x}_{k+1} \in \mathbf{A}(\mathbf{x}_k)$*. Then,* $\mathbf{A}$ *is globally convergent to a solution* $\mathbf{\Gamma} \subset \mathbf{X}$ *with following conditions*

- $\exists$ *a descent function* $\mathbf{z}$ *for* $\mathbf{\Gamma}$ *and* $\mathbf{A}$,
- *The squence* $\{\mathbf{x}_k\}_{k=0}^{\infty} \subset S$ for $S \subset \mathbf{X}$ *is a compact set,*
- *The mapping* $\mathbf{A}$ *is closed at all points of* $\mathbf{X}/\mathbf{\Gamma}$.

Regarding the first condition in Theorem 5.4.1, the designed line search algorithm $\mathbf{A}$ have descent function $\mathbf{z} = \{R_q, \zeta_q, R_u, \zeta_u, \psi_u\}$ which roughly can be presented as

$$\mathbf{z}(x) = \mathbf{x}_k + \mathbf{h}_k \mathbf{d}_k \tag{5.38}$$

where $\mathbf{d}_k$ and $\mathbf{h}_k = \text{diag}\{h(1), h(2), h(3), h(4), h(5)\}$ are the direction of iteration and step size of iterations. Note that ζ_u is updated in the same way with others, only because R_u changes the curve $\mathbf{L}_o$, the new angular location shift happens by ζ_u. Next, the given descent function $\mathbf{z}(x)$ has following properties:

$$\begin{cases} \text{If } \mathbf{x} \notin \mathbf{\Gamma} \text{ and } \mathbf{y} \in \mathbf{X},\ \mathbf{z}(y) < \mathbf{z}(x), \\ \text{If } \mathbf{x} \in \mathbf{\Gamma} \text{ and } \mathbf{y} \in \mathbf{X},\ \mathbf{z}(y) \leq \mathbf{z}(x), \end{cases}$$

hence, the first condition of Theorem 5.4.1 is satisfied. Next, $\mathbf{A}$ is on the compact manifold of the sphere U_C and the plane U_S so $\mathbf{h}_k$ norms as the error e.g., e_r, $\mathbb{R}^n \to \mathbb{R}$ become a compact set as well. This can be clearly extended for the second condition about all produced sequences $\{\mathbf{x}_k\}_{k=0}^{\infty}$ on $\mathbf{X}$. Now, we provide a proposition to satisfy final condition as

Proposition 5.4.1 *Let* f *be a real continues function on* $\mathbf{X}$*. Then, Algorithm* $\mathbf{A}$ *with solution set* $\mathbf{\Gamma}$ *of*

$$\mathbf{\Gamma}(\mathbf{x}, \mathbf{d}) = \{\mathbf{y} \in \mathbb{R}^n \mid \mathbf{y} = \mathbf{x} + \mathbf{h}\mathbf{d},\ \mathbf{h} > 0, \text{ and } f(\mathbf{y}) = \min\ f(\mathbf{x} + \mathbf{h}\mathbf{d})\}$$

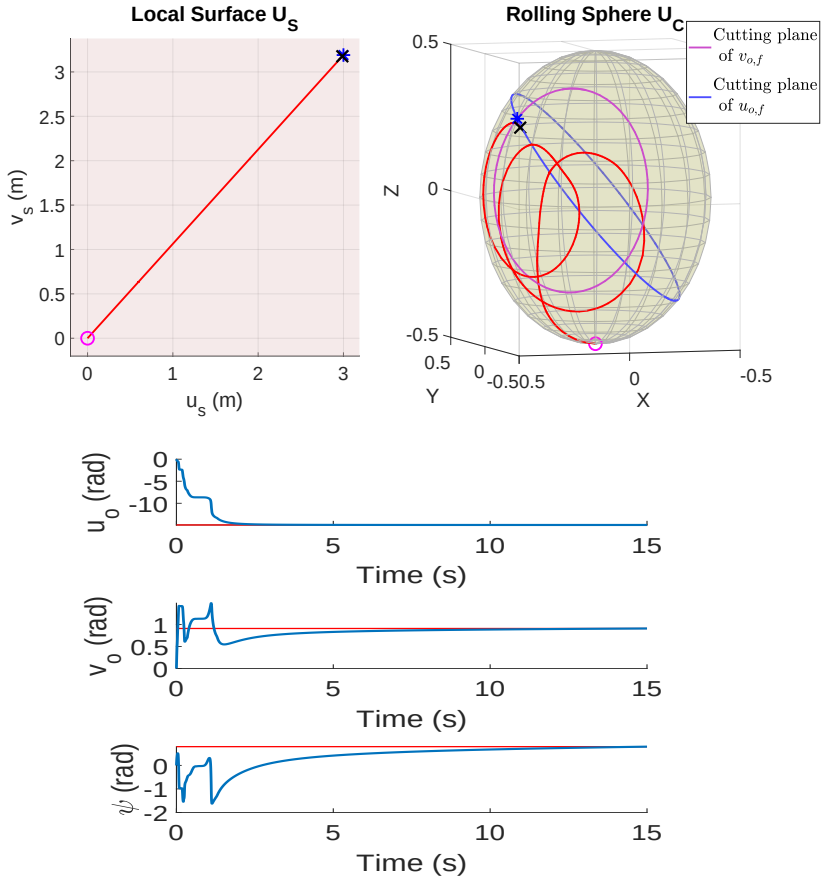

Figure 5.12: Simulation results of proposed approach for a case study with $\{u_{s,f}, v_{s,f}, u_{o,f}, v_{o,f}, \psi_f\} = \{3, 3.2, -\frac{\pi}{2} - 0.8, 0.8, 0.8\}$ final configuration.

is closed at any point $(\mathbf{x}, \mathbf{d})$ *at which always* $\mathbf{d} \neq 0$.

Check Appendix B.7 for the proof of given proposition. By satisfying all the three conditions in Theorem 5.4.1, the proposed line search algorithm is always convergent to a solution for the desired configuration.

5.5 Results and Discussion

The operation and performance of the proposed planning approach are tested under different simulations. At first, we check how algorithmic phases work to achieve a successful convergence. Next, we study the simulation results for different desired spin angles while the rest of the configuration is the same.

The planning method in Fig. 5.9 is analyzed for an example configuration. The

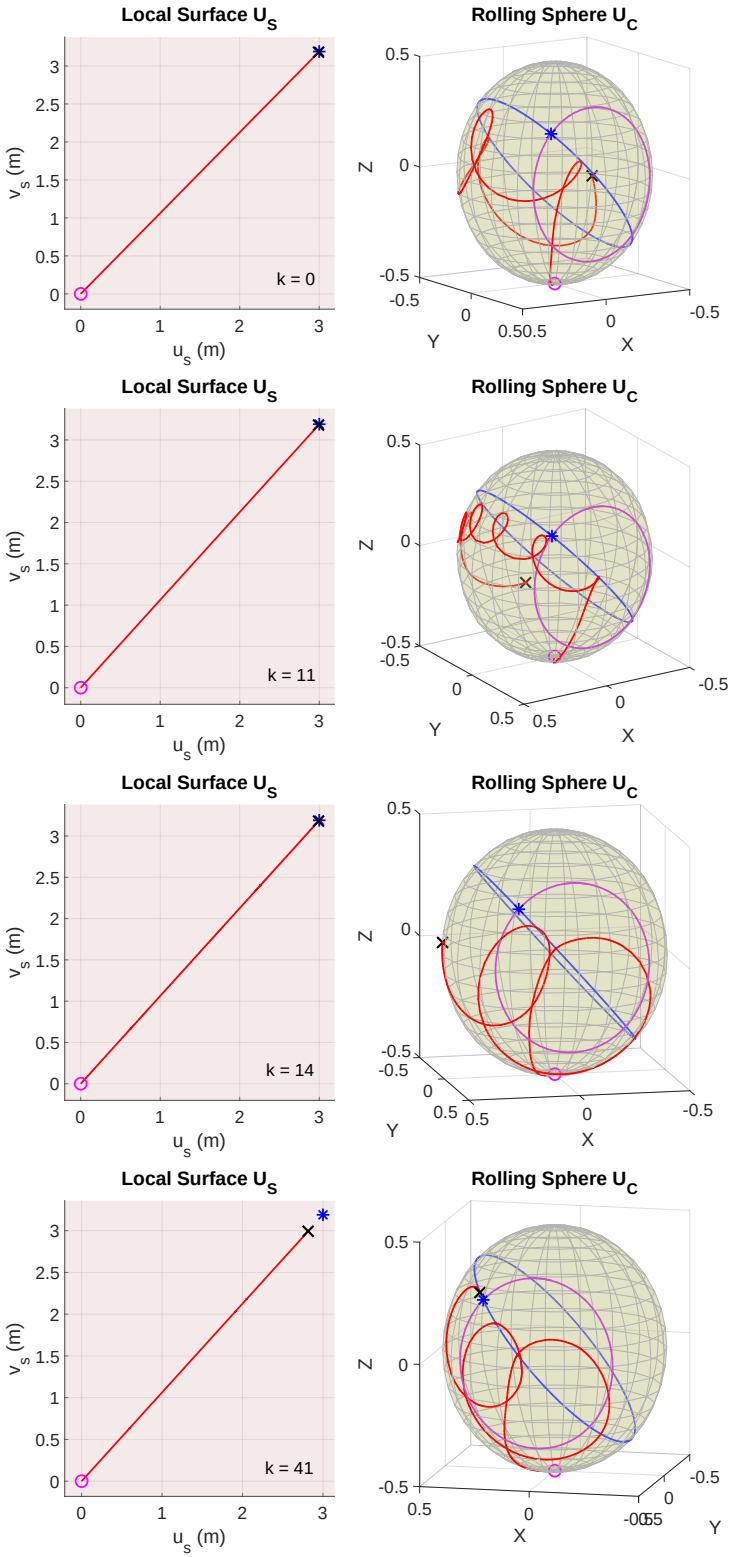

Figure 5.13: Collected iterations of the given final configuration: 1. The first solution of system ($k = 0$), 2. The first successful results of Phase I, 3. Converging Phase II, 4. The first results before applying Phase III.

Matlab is used to run this algorithm by utilizing ODE45. The kinematic model (5.10)-(5.11) is solved together with (5.24), (5.27) and (5.29). The numerical solutions happen with 0.0001 and 0.001 relative and absolute errors. The specifications of the calculating computer are 2.8 GHz Intel(R) Core i7 with maximum possible memory of 7.2 GB. We set the initial and final configurations as $\{u_{s,0}, v_{s,0}, u_{o,0}, v_{o,0}, \psi_0\} = \{0, 0, 0, 0, 0\}$ and $\{u_{s,f}, v_{s,f}, u_{o,f}, v_{o,f}, \psi_f\} = \{3, 3.2, -\frac{\pi}{2} - 0.8, 0.8, 0.8\}$. Note that our plane's final configuration satisfies the minimum distance constraint (5.13) where d for our case is $2.15 \leq ||\mathbf{P}_f - \mathbf{P}_0||_2$, and to see curve with multiple loops, we have $||\mathbf{P}_f - \mathbf{P}_0||_2 = 4.38$ m. For this case, the simulation time is set to $t_f = 15$ s and time constant T in (5.29) is 1. The accuracy of phases in Algorithm 2 are $\epsilon_n = \epsilon_r = 0.07$, $\epsilon_p = 0.12$ and $\epsilon_s = 0.05$. As expressed in the controllability analysis at Appendix B.4, there is a uncontrollable point at $\pi/4$. For this case, we chose it away from point with $G_f = 0.754$ rad to see our approach abilities. The initial value of R_q is 0.005 to prevent any computation singularities. Also, we set the sphere radius and maximum divider as $R_o = 0.5$ m and $\mu_r = 4$.

After running the simulation, the final results are shown as Fig. 5.12. The calculation steps k for this case is achieved with 48 iterations. The computation process takes about 7.2 s. By the achieved successful final iteration, we can interpret that while the sphere is rolling along the given desired final position $\mathbf{P}_f$, it spins with smooth trajectories toward its final configuration for $\{\mathbf{\Psi}_f, \psi_f\}$.

To understand better how the algorithm works by utilizing the derived virtual surface, we plot four collected iteration steps [see Fig. 5.13]. From the initial iteration ($k = 0$), it is clear that $\mathbf{L}_o$ moves by virtual surface toward desired $\mathbf{\Psi}_f$ but because $\mathbf{P}_f$ is far, $\mathbf{L}_o$ curve moves along the $u_{o,f}$ cutting plane. A rope on a sphere explains the way that the achieved curve $\mathbf{L}_o$ on U_C can be imagined. So, algorithm tunes the virtual surface and this bends the obtained curve $\mathbf{L}_o$ in loops, like a rope, toward the desired $\mathbf{\Psi}_f$. Here, Phase I rises the $\mathbf{L}_o$ to move $\mathbf{\Psi}_n$ near to $\mathbf{\Psi}_f$ as the result of succeeded iteration $k = 11$. To move $\mathbf{\Psi}_l$ on $\mathbf{\Psi}_f$, Phase II enlarges the radius of the rope-like curve $\mathbf{L}_o$, as the example iteration $k = 14$ shows. The iteration $k = 41$ in Fig. 5.13 satisfies $\mathbf{\Psi}_l = \mathbf{\Psi}_f$ condition while the next step is tuning the plain configuration to achieve $\mathbf{P}_l = \mathbf{P}_f$ using Eq. (5.36). Finally, the Phase III condition is satisfied by the desired ψ_f value; the algorithm gives the results of Fig. 5.12.

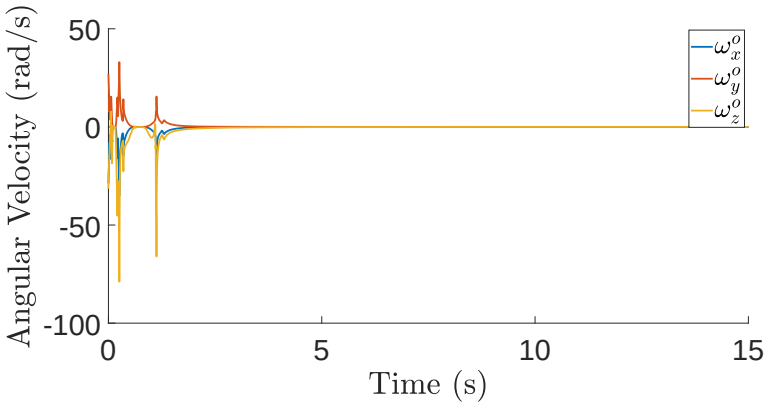

Figure 5.14: Angular velocities of the sphere with the designed arc-length-based based controller.

The angular velocities of the sphere collected by search algorithm are presented in Fig. 5.14 but there are certain fast accelerations in the angular velocities. Note that the problem is considered in kinematics level without any slipping; Hence, arriving longer distances in a short amount of time results in faster velocities. However, we can use the aforementioned advantage in the derived kinematic model (5.12) where the time domain is separated from the kinematics by the rolling rate δ. Thus, We alter the sphere angular velocities in two cases:

In the initial case, to decrease the overall velocity, the time span can be enlarged without affecting the achieved paths $\mathbf{L}_o$ and $\mathbf{L}_s$. For the considered example, we increase the time scaling constant T (it is at δ in Eq. (5.29)) and simulation time t_f to 160 s while the kinematic model is solved with the succeeded parameters in ζ' and R_q+R_u from the algorithm. Clearly, the overall velocities decreased by expanding them in time as Fig. 5.15-b (dashed line velocities). However, there are fast accelerations (around 3 s and 21 s) that makes it harder to be applied practically. To solve this issue, we keep the simulation time t_f same as 160 s but a smooth function is chosen for T as the second case study. With the known relation of $\omega_z^o = \delta k_g^* \triangleq \delta \alpha_s$ from (5.10) and (5.29), we define T as

$$T \triangleq (c \cdot \omega_s)/\alpha_s, \tag{5.39}$$

where $c = |v_{o,f} \cdot u_o'| \cdot ||\mathbf{P}_f - \mathbf{P}(t)||_2$ and ω_s is the desired smooth angular velocity. The

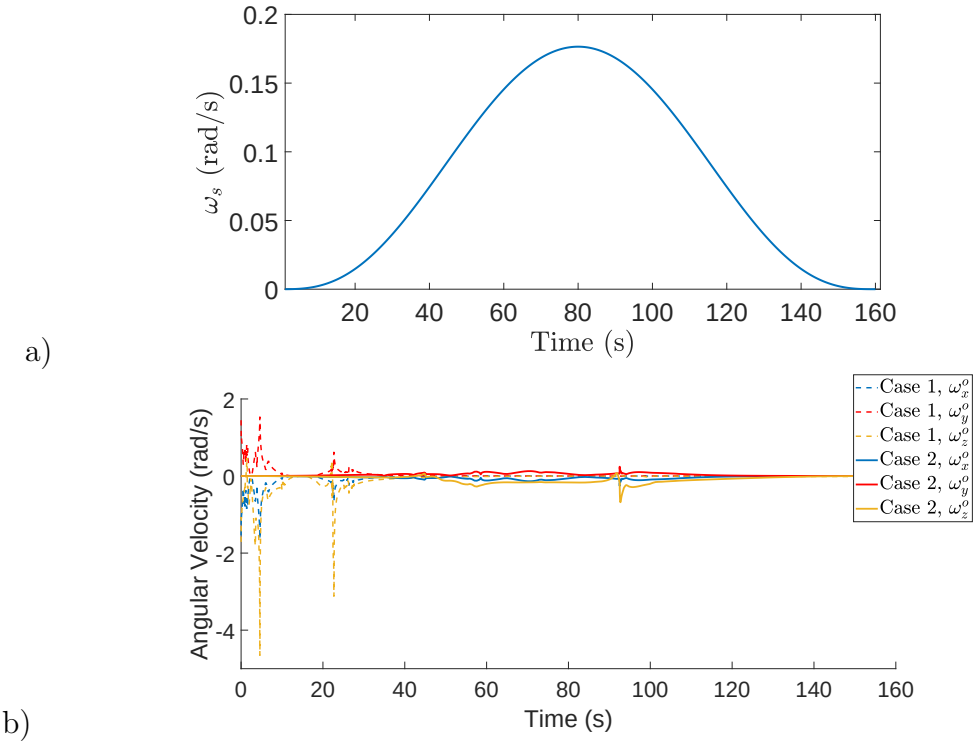

Figure 5.15: a) The designed function ω_s in time, b) Smoothed angular velocities of the sphere in two different cases of time scaling T.

desired smooth velocity ω_s is created with a symmetric time function as

$$\omega_s = a\left(-\frac{140}{T_s^7}t^7 + \frac{420}{T_s^6}t^6 - \frac{420}{T_s^5}t^5 + \frac{140}{T_s^4}t^4\right), \tag{5.40}$$

where $a = 12.91$ and $T_s = 160$ are the time constant and the amplitude. Fig. 5.15-a shows the rest-to-rest function behavior of Eq. (5.40). After running the same simulation with our defined T, we get the results in Fig. 5.15-b (solid lines velocities). It is clear that the second case has smooth angular velocities which are practical without large accelerations at the same time span of t_f. The angular displacement in Fig. 5.16 also demonstrate how the desired angles of the sphere get expanded with the same convergence trend ($\mathbf{L}_o$ trajectory is the same as Fig. 5.12). Note that more complex functions can be defined for T to have different angular velocities convergences without effecting the trajectories of $\mathbf{L}_o$ and $\mathbf{L}_s$.

Next, we analyze the patterns of the created curves $\mathbf{L}_o$ for different desired spin angles with the same final configuration. In here, the final configuration is considered $\{u_{s,f}, v_{s,f}, u_{o,f}, v_{o,f}\} = \{3, 3.2, 0.6, 0.7\}$ besides $\psi_f = \{-1.7, 1.3, 2.3\}$. To have these

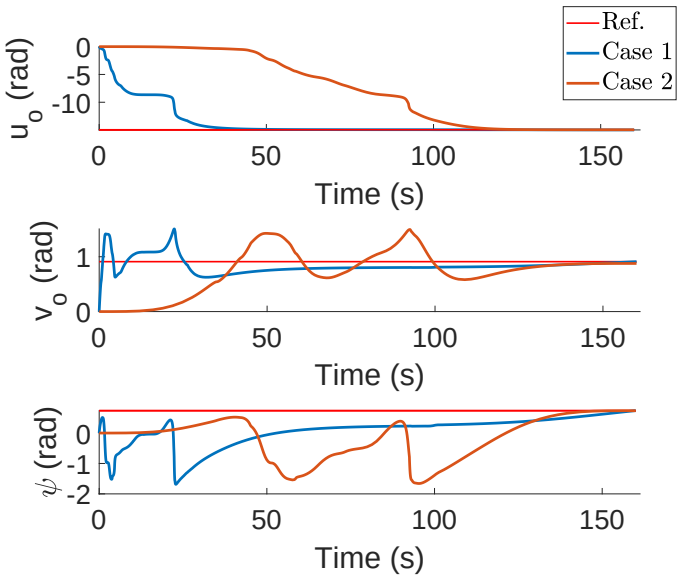

Figure 5.16: Comparing angular convergence of $\mathbf{\Psi}_f$ at two cases.

different curves approximately on same configuration, the ϵ_n and ϵ_r accuracies are chosen $\{0.045, 0.05\}$, $\{0.048, 0.034\}$ and $\{0.048, 0.05\}$ for $\psi_f = \{-1.7, 1.3, 2.3\}$ cases, in the given order. Also, simulation time is set for $t_f = 20$ s with $T = 1$. Note that the rest of the initial conditions are the same as the previous case study.

Our planning approach gives the following results in Fig. 5.17 with the chosen final configuration. The algorithm converges successfully to desired states with different trajectories. The average process time for these simulations was about 40 s. Note that the rise in the average process time is due to exceptional computation for $\psi_f = -1.7$ rad. This happens depending on the accuracy and how near the desired $\mathbf{\Psi}_f$ angles are to $\mathbf{\Psi}_0$ which causes larger iterations (110 s process time).

Also, for the case of $\psi_f = -1.7$ rad, the curve creates multiple loops to reach the desired goal. As mentioned before, the reason is that some spin angles are not easy to be converged by the designed approach. To achieve it, we had to change the region of attraction for the desired configuration. This happens by adding $+\frac{\pi}{2}$ to v-curve for the $\alpha_s(v_{o,f} + \frac{\pi}{2})$ arc-length-based input for this configuration. On the other hand, this becomes a power of our algorithm. Because we have already guarantied the convergence of the desired goal by the Theorem 5.4.1, we can have regional shifts in the $v_{o,f}$ and $u_{o,f}$. Note that this can be the interesting property of proposed algorithm

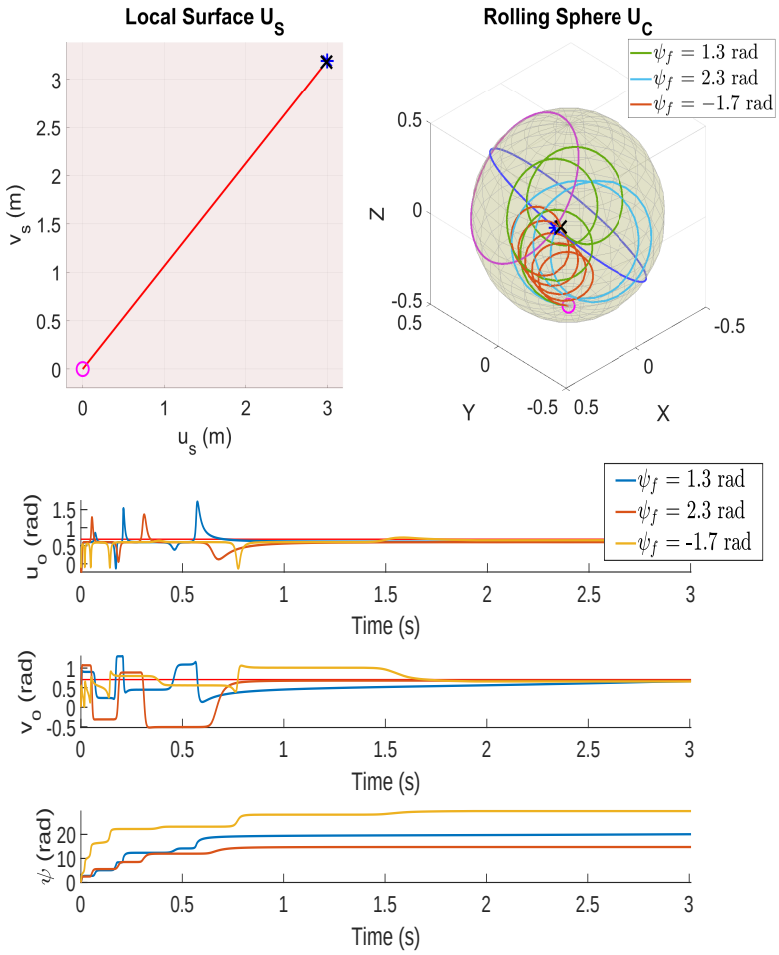

Figure 5.17: The simulation results for having different final spin angles $\psi_f = \{-1.7, 1.3, 2.3\}$.

since multiple solutions would be achievable for the same configuration that with changing the time constant T and region of attraction on u- and v-curves happen; Hence, configuring the same states with different trajectories would be achievable which itself requires a separate study. Also, choosing the accuracy of the algorithm as well as the final local configuration on the sphere $\mathbf{\Psi}_f$ mainly decides how minimum k iterations can be.

Chapter 6

Conclusion

6.1 Summary of Dissertation

The summary of this study is as follows:

In Chapter 1, an introduction was provided about the underactuated systems. We began by explaining different under- and fully-actuation principles in spherical robots. Next, the literature of different control methods for the underactuated systems was covered with a main focus on the inertial-coupling problem. Finally, the path planning problem for a spin-rolling sphere on a plane was discussed in previous studies and we compared it to the pure-rolling ball-plate system.

In Chapter 2, we proposed a novel actuation mechanism for rolling robots. The robot motion is produced through rotating spherical masses (cores) inside circular pipes. To provide the push force for the rotating cores, a fluid-actuated mechanism is utilized. The overall dynamical model of the underactuated rolling robot was developed. Then, analytical studies took place for understanding the performance and motion behavior of this robot. Also, there were detailed studies on proper mass-ratio (core-sphere) design and the cost-of-transport (COT) for this system. Finally, we developed a feed-forward control strategy based on inverse dynamics. It was presented that the planar motion of the robot can be controlled to desired states.

The reason for proposing the fluid-actuated rolling robot is to overcome certain disadvantages that exist in previously proposed actuation principles. The main advantage of the proposed actuation scheme is that the driving unit does not occupy the whole space within the spherical shell in contrary to, for example, the pendulum actuated robots [68, 71] or wheel-actuated robots (torque-reaction-based principle) [2, 21, 31, 46, 121]. Therefore, extra tools and sensors can be placed within the shell. In addition, the proposed actuator can accelerate/decelerate with nearly zero-backlash and minimal load inertia of the connected motor because the fluid works as a mediator between the driver (linear actuator) and the core in our mechanism. This

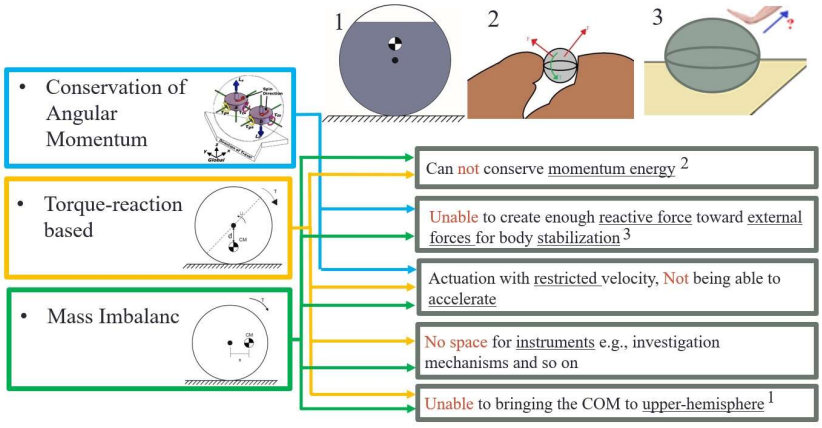

Figure 6.1: The limitations of the some well-known driving mechanisms for the rolling robots [5].

is challenging for mechanisms that the motors are directly connected to the payload. Additionally, the robot features a smooth and safe motion due to the circulation of the fluid.

Fig. 6.1 depicts a graphical presentation for the related limitation in different driving mechanisms that is preventable in our proposed robot. Based on the structure of the proposed robot, the number of pipes (they include the core) can be increased without affecting the internal workspace. This would increase the DoF of the rolling robot based the requirement. This property was one of the challenges in torque-reaction-based mechanisms [2,5,21,31,121]. Also, the proposed robot is able to bring its center of mass to upper-hemisphere which is not applicable for previous pendulum-based models [68,71]. Moreover, recent researches by NASA/JPL [9] on rolling robots with a mass-imbalance mechanism showed that they can use the actuation mechanism to restore the power in batteries while the sphere freely moves by the wind where the mounted masses generate electricity. This can be applicable to our mechanism with the proper design since it has spherical masses (cores) which can rotate and push the fluid back to the cylinder to generate the electricity for re-storing the batteries. However, as depicted in Cost-of-Transport studies, the fluid-actuated robot would not be power efficient in very high velocities because of existing drag (energy loss is the power of three of the fluid velocity) between spherical masses (cores) and circulating fluid.

In Chapter 3, we designed a Kalman-based compensatory filter for motion tracking of the rotating core of our proposed spherical robot. This problem requires a proper sensor fusion of the inertial measurement unit (accelerometer, gyroscope and magnetometer sensors) to do motion tracking with a minimum angular error. Not only the located permanent magnets had serious biases on a certain axis of the magnetometer but also there was a magnetic distortion due to the soft ferromagnetic material i.e., steel. After defining each measured signal of the inertial/magnetic sensors, the process and measurement models were described for the Kalman filter. Next, the proposed filter experimented on a setup about its performance in comparison to the well-known QUEST filter. This proposed filter application can be extended to different motion tracking applications in actuators of the robots with magnetic parts and the environment under magnetic distortions. Finally, we raised a question about whether attaching permanent magnets to inertial measurement sensors as a magnetic shield improves the motion tracking of the mechanisms and robots.

The tracking sensor that is developed for rolling robot apart from its general new findings can help in developing better motion control strategies for our rolling robot. For example, because we now can know the location of the rotating mass (core) and can determine the amount of fluid volume that is injected to the pipe, we can propose a feedback control strategies e.g., Hybrid control to manipulate robot properly. Also, the disturbances on the spherical robot can be minimized with a feedback controller which was not considered in our previous study in Chapter 2.

In Chapter 4, the inertial-coupling problem of underactuated systems was taken into consideration. This coupling creates configuration and geometric parameter limitations with the following "Strong Inertial Coupling" condition [97] which makes it harder to apply control strategies that require the inverse of the inertial matrices. At first, the singular-free model was derived by the applied small-amplitude sine wave on the trajectory of rotational mass. The nonlinear dynamics of the mass-rotating rolling sphere was derived. Before obtaining a singular-free model from the positive definiteness of inertial matrices, the singular configurations were presented in classical systems i.e., mass-point and pendulum-actuated rolling robots. Then, the modified model was clarified in simulation and we compared our proposed model to the classical pendulum-actuated rolling system about differences. We extended the method

to multi-DoF underactuated manipulators with more than one passive joints. We illustrated how conventional models faced with serious inertial-coupling singularities which prevented proper controller design by using the inverse of inertial matrices. Finally, we presented the singular-free model for the 4-DoF underactuated manipulators (two passive and two active joints). Also, analytically the simulation behavior of the singular-free condition and model at singular configuration were discussed and evaluated.

In Chapter 5, we presented a new approach for path planning of the spin-rolling sphere on a straight plane trajectory. The planning was mainly constructed by the introduced geometric control. In the beginning, the kinematic model of the moving frame was derived from the contact point of the sphere and plane. Next, a virtual surface was designed to produce arc-length-based control inputs. The problem is imagined as manipulating a flexible rope-like curve on the sphere with a constant length. Thus, we proposed an iterative algorithm to tune the traversed curve toward desired configurations. The achieved simulations clarified the performance of the proposed planning approach.

The proposed path planning method was at a kinematic level for a generalized problem statement. In order to implement the path planning for a particular mechanism such as our proposed rolling robot different strategies, including the mechanisms that can realize spin-rolling motion, can be followed. As the first way, the desirable paths for both sphere and plane can be obtained off-line and because we know the angular velocities as well, a trajectory tracking controller can be used with integrated nonlinear dynamics of the fluid-actuated rolling robot. Another alternative solution can be a semi on-line path planning. Our off-line search algorithm only tunes the geometric controller's constants, this means after obtaining the suitable constants for the geometric controller, the geometric controller together with the Darboux-frame-based kinematics can be solved on-line. Thus, a feedback controller can be developed that based on the rotating object's current states (here is our spherical robot) and effecting external perturbations, the controller re-tune the geometric controller from new state values with existing planned paths. Note that the angular velocities can be changed without affecting the desired paths as shown in our studies.

6.2 Future Works

In this dissertation, we shed light on some of the well-known problems in underactuated systems. The existing challenges and possible future works are depicted for each topic as follows

6.2.1 Fluid-Actuated Spherical Robot

In this dissertation, we proposed a novel fluid-actuated mechanism for rolling systems in Chapter 2. We were able to show that this rolling robot has interesting advantages in contrast to other propulsion mechanisms. We also solved sensory problem to track the rotating core inside pipes in Chapter 3.

While the simulations demonstrate the feasibility of the proposed actuation system, several issues need to be addressed and tested under experiments in future research. These include the unmodeled gap between the cores and the pipes (the diameter of the cores and the pipes were assumed equal in our model) and the effect of possible leakage that would cause deviation of the fluid and cores' velocities. The relative rotation of the cores with respect to their centers of masses may also contribute to the unmodeled dynamics which corresponds to torque-reaction-based actuation principle.

In future, we plan to develop a proper nonlinear controller with sensor feed from the core position for the driving mechanisms of the robot. We think we will be able to verify our driving mechanism performance experimentally.

6.2.2 Underactuated Systems without Inertial-Coupling Singularities

Our proposed solution for avoiding singularities covered in Chapter 4 that did not contain a complex algorithm and multiple space transformations. This solution resolved the limitations of the physical mechanism design and reachable configuration due to the inertial coupling in the underactuated systems. One challenging problem related to this method was the dependency of wave parameters, in particular the amplitude, to the geometric parameters and considered the region of the workspace by links in planar manipulators. Thus, there are possible cases that wave motion must be realized by mechanisms when the amplitude of a wave is not extremely smaller

than the link length. A similar issue is relevant to the rolling robots. This realization can be done with the example mechanisms mentioned in the dissertation or other alternative propulsion mechanisms. Also, this model can facilitate various advanced feedback control strategies.

Future researches can take place to find out how we can make the wave combinations virtually in a way that there wouldn't be any necessity for realizing mechanisms physically in certain geometric values. Moreover, the constrained waves on the rotational trajectory of active joints (mass-points with direct control) can be researched in the different phase-shifted combinations where the final model did not have any physical implications for the real system. This will require an in-depth study on the Lagrangian functions to minimize the deviation in the energy formula before deriving the motion equations with combined waves.

6.2.3 Darboux-frame-based Parametrization and Planning Challenges

The developed path planning method for spin-rolling sphere on plane in Chapter 5 with the achieved smooth nontrivial trajectories looks promising in practical applications. Also, this method can open a new topic in control studies due to the newly introduced geometric-based controller. For instance, changing the topology of the virtual surface can create different trajectories in converging desired states. Also, the planning problem becomes easier to be solved because this time- and coordinate-invariant method is utilizing the curvature of surfaces. Furthermore, the derived general Darboux frame is possible to be applied for more complex manifolds rather than a plane surface. While the algorithm process time is fast enough for practical implementations, there is a way to change the achieved angular velocities of the rotating body in any desired convergence rate. The reason is that the algorithm tunes parameters of designed geometric inputs with constant values. However, on-line algorithms applied in Refs. [37,93,106] have an advantage since they their real-time computation is fast. Furthermore, some control strategies can deal with perturbations [37, 78, 84] which is not applicable for our method due to the existing off-line search algorithm that tunes the geometric controller.

After a detailed study of an on-line control method for this new kinematic system, the applications can be extended to advance studies in dexterous manipulations.

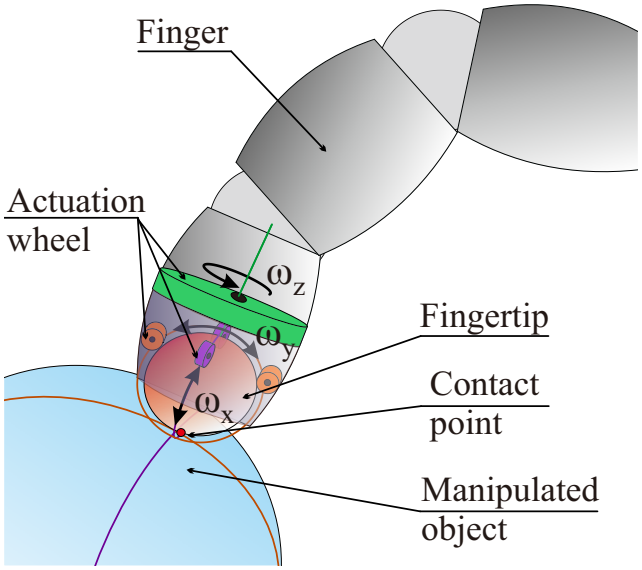

Figure 6.2: Manipulation with agile fingertips.

Recently, agile grasping with the aim for more advanced manipulation through fingertips is starting to get more attention [125]. Because the Darboux-frame-based model gives a transformation that lets us arbitrarily change the spin-rolling sphere in an arbitrary direction on a fixed surface (can be the manipulated objects), we can create a feedback loop to track spin-rolling fingertip in real-time. We plan to study a 3 Dofs fingertips where it is attached to a flexible finger as Fig. 6.2. Because we are able to extend the Darboux-frame-based kinematics with this new mechanism to arbitrary surfaces, the manipulation of smooth non-uniform objects can be the next objective of future researches.

Appendices

Appendix A

Singularity-Free Model Derivations

A.1 Planar n-DoF Underactuated Manipulators

This and incoming sections study the underactuated manipulators regarding singularities in their inverse dynamics and we apply our approach for it. Note that for the sake of simplicity the notation of this section is different from the previous study, rolling systems.

The general motion equations for an underactuated manipulator with n number of links that has an equal $n/2$ numbers of passive and active rotating joints with their rotational angles of $\boldsymbol{q} = [\mathbf{q}_p, \mathbf{q}_a]^T$ is

$$\mathbf{M}(\boldsymbol{q})\ddot{\boldsymbol{q}} + \mathbf{h}(\boldsymbol{q}, \dot{\boldsymbol{q}}) = \mathbf{u}, \tag{A.1}$$

where the inertia matrix $\mathbf{M}(\boldsymbol{q})$, the velocity dependencies and gravity terms $\mathbf{h}(\boldsymbol{q}, \dot{\boldsymbol{q}})$ and the control inputs $\mathbf{u}$ are defined by

$$\mathbf{M}(\boldsymbol{q}) = \begin{bmatrix} \mathbf{M}_{pp} & \mathbf{M}_{pa} \\ \mathbf{M}_{ap} & \mathbf{M}_{aa} \end{bmatrix}, \mathbf{h}(\boldsymbol{q}, \dot{\boldsymbol{q}}) = \begin{bmatrix} \mathbf{h}_p & \mathbf{h}_a \end{bmatrix}^T, \mathbf{u} = \begin{bmatrix} \mathbf{0}_{n\times 1} & \boldsymbol{\tau}_a \end{bmatrix}^T.$$

Definition A.1.1 The inverse dynamics can be presented from the constraint equations in (A.1) by

$$\ddot{\mathbf{q}}_a = -\mathbf{M}_{pa}^{-1}\left[\mathbf{M}_{pp}\ddot{\mathbf{q}}_p + \mathbf{h}_p\right]. \tag{A.2}$$

In this motion planning problem, the specified states of $n/2$ number of the passive joints $\{\mathbf{q}_p(t), \dot{\mathbf{q}}_p(t), \ddot{\mathbf{q}}_p(t)\}$ are the inputs to converge the system toward its desired states $\{\mathbf{q}_{f,p}, \dot{\mathbf{q}}_{f,p}, \ddot{\mathbf{q}}_{f,p}\}$. The output torques $\boldsymbol{\tau}_a(t, \mathbf{q}_p, \dot{\mathbf{q}}_p, \ddot{\mathbf{q}}_p)$ on $n/2$ number of the active joints are coming from (A.1) that is as follows

$$\boldsymbol{\tau}_a = \mathbf{M}_{ap}\ddot{\mathbf{q}}_p + \mathbf{M}_{aa}\ddot{\mathbf{q}}_a + \mathbf{h}_a. \tag{A.3}$$

Also, the first and second integrations of differential constraint equations (A.2) give the states of the active joints $\{\dot{\mathbf{q}}_a(t),\mathbf{q}_a(t)\}$.

We can understand that the inertia matrix $\mathbf{M}_{pa}^{-1}\mathbf{M}_{pp}$ of the constraint equation (A.2) should be non-singular plus satisfying the positive definiteness of $\mathbf{M}$. Nevertheless, the previous studies proved that this may not be true for all the geometric parameters and configurations due to the inertial coupling of the passive joints [97,113]. By a simple operation, the sub-matrix of inertia becomes $(\mathbf{M}_{pa}^{*}\mathbf{M}_{pp})/|\mathbf{M}_{pa}| > 0$ where $\mathbf{M}_{pa}^{*}$ and $|\mathbf{M}_{pa}|$ present the adjoint matrix and determinant of the matrix $\mathbf{M}_{pa}$. Thus, we can conclude that if $|\mathbf{M}_{pa}| > 0$, the singularity-free condition of inverse dynamics (A.2)-(A.3) are satisfied. Please note that because $\ddot{\mathbf{q}}_a$ also appears in (A.3), failing the $|\mathbf{M}_{pa}| > 0$ condition due to singularities will result the torque of active joints ($\boldsymbol{\tau}_a \to \infty$) to converge infinity as well as active joint states $\{\ddot{\mathbf{q}}_a, \dot{\mathbf{q}}_a, \mathbf{q}_a\}$. The inertial coupling is the main reason that makes inverse of inertia matrices practically limited and hard to be applied.

A.2 Wave on the Trajectory of the Rotational Joints

A.2.1 Kinematics of Small-Amplitude Wave

The kinematics and properties of a proposed combined small-amplitude wave on the active joints are introduced here. The main objective of this combined-wave is to design its parameters to avoid the singularities due to inertial coupling as studied for rolling systems.

First, we assume a single sine wave trajectory on the rotational mass [see Fig A.1 as example]. Here, $x_0y_0z_0$ shows the reference frame. The k-th link has the frame connected to the center of joint as $x_ky_kz_k$, which rotates with the respect to reference frame $x_0y_0z_0$. The position vector of the link that rotates with angle q around a small-amplitude sinusoidal curve on the circle with a link radius of l is defined similar to Eq. (4.1) [113]

$$\mathbf{D} = -\left(l + a\sin\left(nq + \varepsilon\right)\right)\left[\cos q\mathbf{k} + \sin q\mathbf{j}\right], \tag{A.4}$$

where a, n and ε are the amplitude of sinusoidal wave, the frequency of created periodic wave on the circle of the link radius l and constant phase shift of the curve,

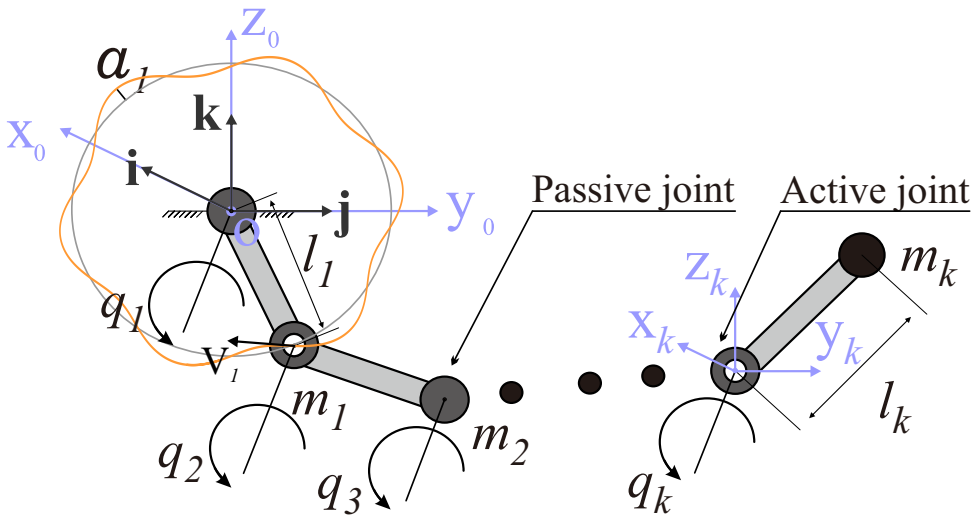

Figure A.1: General model of the underactuated manipulator. Note that the orange trajectory presents the combined wave trajectory.

respectively. In the conventional manipulators with circular trajectory, Eq. (A.4) transforms to Eq. (4.2) where a, n and ε are zero in (A.4) that gives a circular rotation with radius l for the rotational links. Next, we can extend equation (A.4) for the position vector of k-th link in multi-joint manipulators as follows

$$\mathbf{D}_k = \sum_{i=1}^{k} -\left(l_i + a_i \sin\left(n_i q_i + \varepsilon_i\right)\right)\left[\cos q_i \mathbf{k} + \sin q_i \mathbf{j}\right]. \tag{A.5}$$

Similarly, it is aimed to design n_i, a_i and ε_i depending on the obtained relations from the inertia matrix to removes the inertial coupling singularity[1] while rotating link follows around wavy circle. Also, the deviation of trajectory $\mathbf{D}_k$ with respect to constant link length l_k can be found for each link k with the combined wave as

$$\Delta D_k = \| \mathbf{D}_k \| - \| \mathbf{D}_{k-1} \| - l_k = a_k \sin(n_k q_k + \varepsilon_k), \tag{A.6}$$

where $\| \cdot \|$ stands for the module of the variable.

The maximum value for this deviation ΔD_k will be the amplitude of wave a_k, which we assume in our study that $a_k \ll l_k$. If the property $(a_k \ll l_k)$ is satisfied, the effect of the included sine wave can be ignored in dynamic models and there is

[1]Please check the Proposition A.4.1 for the details of parameter design.

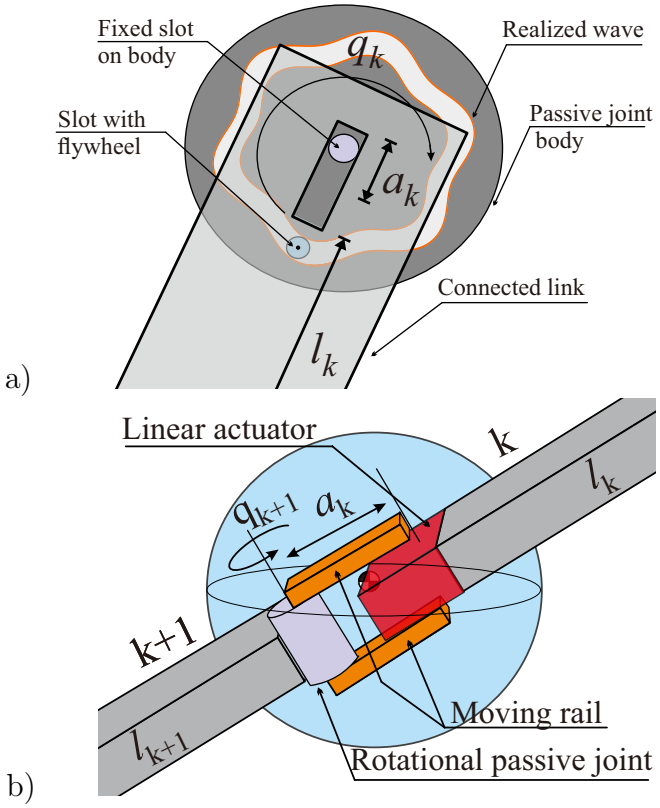

Figure A.2: Example mechanism realizations for the wavy displacements of the joints in the cases that $a_k \leq l_k$, a) The trajectory realization with passive mechanical slot. b) The trajectory realization by linear actuator.

no need to realize it mechanically. For the cases that geometric parameters especially a_k be $a_k \leq l_k$, then, the wave motion can be realized in driving mechanisms of manipulators as the given examples in Fig. A.2. We will show how robot geometry choice and inertial coupling changes the a_k be $a_k \leq l_k$ choices. In order to realize this wave, a passive flywheel slot as Fig. A.2-a can be placed to follow the derived sine wave trajectory. Also, the flywheel slot and wave path can be replaced with eccentric interacting gears to realize the motion. As a second alternative, a prismatic (telescope) joint can move the rest of the body periodically [see Fig. A.2-b] at the end of the lead in the manipulator. This method of actuation is also studied for time-varying inertia pendulum mechanisms [16, 29, 45, 100]. Please note that we chose the proposed first passive slot mechanism in this study [see Fig. A.2-a], if $a \ll l$ is not satisfied. However, for the case of linear actuator mechanism, the actuator model can be solved together with our rigid body model where variables will become $\{a_k, \dot{a}_k\}$.

Note that the rigid-body model will be the same since the mass of the linear actuator will be on the previous link and there is no need for extra mass definition as Fig. A.2-b.

The linear and angular velocities of k-th link with using (A.5) become

$$\begin{aligned}
\mathbf{V}_k &= \sum_{i=1}^{k} \dot{q}_i \big[-a_i n_i \cos\left(n_i q_i + \varepsilon_i\right) \cos q_i + \left(l_i + a_i \sin\left(n_i q_i + \varepsilon_i\right)\right) \sin q_i \big] \mathbf{k} \\
&- \dot{q}_i \big[a_i n_i \cos\left(n_i q_i + \varepsilon_i\right) \sin q_i + \left(l_i + a_i \sin\left(n_i q_i + \varepsilon_i\right)\right) \cos q_i \big] \mathbf{j}, \\
\boldsymbol{\omega}_k &= \sum_{i=1}^{k} \dot{q}_i \mathbf{i}.
\end{aligned} \tag{A.7}$$

A.2.2 Lagrangian Dynamics of the Manipulator

This section is dedicated to derive the general motion equation of n number of links with the included combined-wave kinematics in every joint. The model is found by using the Lagrangian equations.

We consider each link has its center of mass located at end of the k-th link with mass of m_k as Fig. A.1. Also, each link has its own inertia tensor I_k with respect to its coordinate frame. Note that these links are free to have full rotations as rotating-mass system, e.g., pendulums. Then, the Lagrangian function of this manipulator, including kinetic and potential energies, is described as follows

$$L = \frac{1}{2} \sum_{k=1}^{n} m_k \parallel \mathbf{V}_k \parallel^2 + \frac{1}{2} \sum_{k=1}^{n} I_k \parallel \boldsymbol{\omega}_k \parallel^2 - \sum_{k=1}^{n} m_k g y_k, \tag{A.8}$$

where $\mathbf{D}_k = x_k \mathbf{j} + y_k \mathbf{k}$ and g is the acceleration of gravity. After substituting Eq. (A.5) and Eq. (A.7) from defined kinematics, the Lagrangian function (A.8) is simplified

to following form

$$
\begin{aligned}
L = & \frac{1}{2}\sum_{k=1}^{n} m_k \Big[\sum_{i=1}^{k} \dot{q}_i^2 \big[a_i^2 n_i^2 \cos^2(n_i q_i + \varepsilon_i) + (l_i + a_i \sin(n_i q_i + \varepsilon_i))^2 \big] \\
& + 2 \sum_{i=1}^{k-1} \dot{q}_i \dot{q}_k \big[(l_i + + a_i \sin(n_i q_i + \varepsilon_i))(l_k + a_k \sin(n_k q_k + \varepsilon_k)) \cos(q_i - q_k) \\
& + a_i n_i a_k n_k \cos(n_i q_i + \varepsilon_i) \cos(n_k q_k + \varepsilon_k) \cos(q_i - q_k) \\
& + a_i n_i (l_k + a_k \sin(n_k q_k + \varepsilon_k)) \cos(n_i q_i + \varepsilon_i) \sin(q_i - q_k) \\
& + a_k n_k (l_i + a_i \sin(n_i q_i + \varepsilon_i)) \cos(n_k q_k + \varepsilon_k) \sin(q_k - q_i) \big] \Big] \\
& + \frac{1}{2} \sum_{k=1}^{n} I_k \left(\sum_{i=1}^{k} \dot{q}_k \right)^2 + \sum_{k=1}^{n} \sum_{i=1}^{k} m_k g \left(l_i + a_i \sin\left(n_i q_i + \varepsilon_i \right) \right) \cos q_i .
\end{aligned}
\tag{A.9}
$$

Note that a_0, n_0 and q_0 are set zero. Next, we utilize following Lagrangian equation for every k-th joint

$$
\frac{d}{dt}\left(\frac{\partial L}{\partial \dot{q}_k} \right) - \frac{\partial L}{\partial q_k} = \tau_k, \tag{A.10}
$$

The derived motion equation has its general inertia matrix $\mathbf{M}^*$ and velocity dependency and gravity matrix $\mathbf{h}^*$ in the following form

$$
\begin{aligned}
\mathbf{M}^* &= \begin{bmatrix} M_{11} & M_{12} & \cdots & M_{1n} \\ M_{21} & M_{22} & \cdots & M_{2n} \\ \vdots & & \ddots & \vdots \\ M_{n1} & M_{n2} & \cdots & M_{nn} \end{bmatrix}, \mathbf{h}^* = \begin{bmatrix} h_1 & h_2 & \ldots & h_n \end{bmatrix}^T, \\
\mathbf{u} &= \begin{bmatrix} \tau_1 & \tau_2 & \ldots & \tau_n \end{bmatrix}^T .
\end{aligned}
\tag{A.11}
$$

where terms of the matrices are as follows

$$
\begin{aligned}
M_{11} &= (m_1 + \cdots + m_n)\mu_{a,1} + I_1 + \cdots + I_n, \\
M_{12} &= (m_2 + \cdots + m_n)\mu_{b,12} + I_2 + \cdots + I_n, M_{1n} = m_n \mu_{b,1n} + I_n, \\
M_{n1} &= m_n \mu_{b,n1} + I_n, M_{n2} = m_n \mu_{b,n2} + I_n, \; M_{nn} = m_n \mu_{a,n} + I_n, \\
h_1 &= (m_1 + \cdots + m_n)\mu_{c,1}\dot{q}_1^2 + (m_2 + \cdots + m_n)\mu_{d,12}\dot{q}_2^2 + \cdots + m_n \mu_{d,1n}\dot{q}_n^2, \\
h_2 &= (m_2 + \cdots + m_n)\mu_{d,12}\dot{q}_1^2 + (m_2 + \cdots + m_n)\mu_{c,2}\dot{q}_2^2 \cdots + (m_2 + \cdots + m_n)\mu_{d,n2}\dot{q}_n^2, \\
h_n &= m_n \mu_{d,1n}\dot{q}_1^2 + m_n \mu_{d,2n}\dot{q}_2^2 + ... + m_n \mu_{c,n}\dot{q}_n^2,
\end{aligned}
\tag{A.12}
$$

while,

$$
\begin{aligned}
\mu_{a,s} &= \left[a_s^2 n_s^2 \cos^2(n_s q_s + \varepsilon_s) + (l_s + a_s \sin(n_s q_s + \varepsilon_s))^2\right], \\
\mu_{b,ss'} &= [(l_s + a_s \sin(n_s q_s + \varepsilon_s))(l_{s'} + a_{s'} \sin(n_{s'} q_{s'} + \varepsilon_{s'})) \cos(q_s - q_{s'}) \\
&+ a_s n_s (l_{s'} + a_{s'} \sin(n_{s'} q_{s'} + \varepsilon_{s'})) \cos(n_s q_s + \varepsilon_s) \sin(q_s - q_{s'}) \\
&+ a_{s'} n_{s'} (l_s + a_s \sin(n_s q_s + \varepsilon_s)) \cos(n_{s'} q_{s'} + \varepsilon_{s'}) \sin(q_{s'} - q_s) \\
&+ a_s n_s a_{s'} n_{s'} \cos(n_s q_s + \varepsilon_s) \cos(n_{s'} q_{s'} + \varepsilon_{s'}) \cos(q_s - q_{s'})], \\
\mu_{c,s} &= a_s n_s \cos(n_s q_s + \varepsilon_s)(l_s + a_s \sin(n_s q_s + \varepsilon_s)) - a_s^2 n_s^3 \sin(n_s q_s + \varepsilon_s) \cos(n_s q_s + \varepsilon_s),
\end{aligned}
$$

$$
\begin{aligned}
\mu_{d,ss'} &= 2 a_{s'} n_{s'} \cos(n_{s'} q_{s'} + \varepsilon_{s'})(l_s + a_s \sin(n_s q_s + \varepsilon_s)) \cos(q_s - q_{s'}) \\
&+ 2 a_s n_s a_{s'} n_{s'} \cos(n_s q_s + \varepsilon_s) \cos(n_{s'} q_{s'} + \varepsilon_{s'}) \sin(q_s - q_{s'}) \\
&+ (l_s + a_s \sin(n_s q_s + \varepsilon_s))(l_{s'} + a_{s'} \sin(n_{s'} q_{s'} + \varepsilon_{s'})) \sin(q_s - q_{s'}) \\
&- a_s n_s a_{s'} n_{s'}^2 \sin(n_{s'} q_{s'} + \varepsilon_{s'}) \cos(n_s q_s + \varepsilon_s) \cos(q_s - q_{s'}) \\
&- a_s n_s (l_{s'} + a_{s'} \sin(n_{s'} q_{s'} + \varepsilon_{s'})) \cos(n_s q_s + \varepsilon_s) \cos(q_s - q_{s'}) \\
&- a_{s'} n_{s'}^2 (l_s + a_s \sin(n_s q_s + \varepsilon_s)) \sin(n_{s'} q_{s'} + \varepsilon_{s'}) \sin(q_{s'} - q_s).
\end{aligned}
$$

The following general motion equation is derived with including every joint with combined wave kinematics. One can find the motion equation for different passive and active joints with their combined waves. Also, by equaling the $\{a_k, n_k, \varepsilon_k\}$ to zero results in the joint k to be the conventional circular trajectory.

A.3 The Dynamic Model of 4-DoFs Underactuated Manipulator

We study the singularity problems due to the inertial-coupling in a conventional underactuated manipulator. A 4-DOFs manipulator with two passive and two active joints is considered as Fig. A.3. To our best knowledge, there has not been any study on double passive joints because the coupling problem becomes more challenging to tackle with [4, 18]. This 4-DoFs underactuated model can be looked, for an example, as the model of the human body [17] where the head, body, leg and feet are the consisting bodies of each links.

We choose our combined wave kinematics to be on the active joints, the second and fourth joints $k = \{2, 4\}$. The variables of first and third joints as the passive

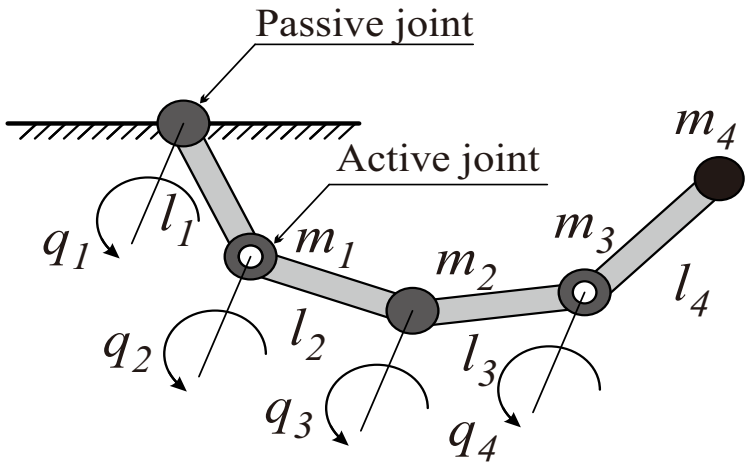

Figure A.3: 4-DoFs underactuated manipulator.

joints are set $a_1 = a_3 = 0$, $n_1 = n_3 = 0$ and $\varepsilon_1 = \varepsilon_3 = 0$ with circular trajectory in motion equation. In Appendix A.5, we have summarized the terms of the motion equation for this 4-DoF manipulator. Now, the derived matrices in (A.29) should be re-ordered based on the passive and active joints as (A.1) to obtain the inverse of motion equations, which are

$$\begin{aligned}
&\mathbf{M}_{pp} = \begin{bmatrix} M_{11} & M_{13} \\ M_{31} & M_{33} \end{bmatrix}, \mathbf{M}_{pa} = \begin{bmatrix} M_{12} & M_{14} \\ M_{32} & M_{34} \end{bmatrix}, \mathbf{M}_{ap} = \begin{bmatrix} M_{21} & M_{23} \\ M_{41} & M_{43} \end{bmatrix}, \\
&\mathbf{M}_{aa} = \begin{bmatrix} M_{22} & M_{24} \\ M_{42} & M_{44} \end{bmatrix}, \mathbf{u} = \begin{bmatrix} 0 & 0 & \tau_2 & \tau_4 \end{bmatrix}^T.
\end{aligned} \tag{A.13}$$

We first demonstrate the inertial coupling in the conventional model without the combined wave trajectory (A.5) ($a_1, \cdots, a_k = 0$, $n_1, \cdots, n_k = 0$). The configuration singularities with relation to geometric parameters ($l_k,\ m_k,\ I_k$) based on $|\mathbf{M}_{pa}|>0$ inertial coupling condition from (A.13) and (A.31) is

$$\begin{aligned}
&|\mathbf{M}_{pa}| = M_{12}M_{34} - M_{14}M_{32} = I_2I_4 + (I_2 + I_3 + I_4)m_4l_3l_4\cos(q_4 - q_3) \\
&+ I_4l_2\big[(m_2 + m_3 + m_4)l_1\cos(q_2 - q_1) - (m_3 + m_4)l_3\cos(q_2 - q_3)\big] \\
&- (I_3 + I_4)m_4l_1l_4\cos(q_4 - q_1) + m_4l_1l_2l_3l_4\big[(m_2 + m_3 + m_4)\cos(q_2 - q_1)\cos(q_4 - q_3) \\
&- (m_3 + m_4)\cos(q_4 - q_1)\cos(q_2 - q_3)\big] > 0
\end{aligned} \tag{A.14}$$

In order to find the constraint that comes from inertial coupling, we can analytically check the inequalities (A.14) as Table A.1 for different minimum values of

Table A.1: Singular configurations that have be satisfied due to the inertial coupling [97].

$q_2 - q_1$	$q_4 - q_3$	$q_4 - q_1$	$q_2 - q_3$	$\lvert\mathbf{M}_{pa}\rvert$
$(2k+1)\pi$	$\frac{(2k+1)}{2}\pi$	$-\frac{(2k+1)}{2}\pi$	$2k\pi$	$I_2I_4 - I_4l_2\big[(m_3+m_4)l_3$ $+(m_2+m_3+m_4)l_1\big]$
$\frac{(2k+1)}{2}\pi$	$-\frac{(2k+1)}{2}\pi$	$2k\pi$	$2k\pi$	$I_2I_4 - I_4l_2l_3(m_3+m_4)$ $-(I_3+I_4)m_4l_1l_4 - m_4l_1l_2l_3l_4(m_3+m_4)$
$(2k+1)\pi$	$(2k+1)\pi$	$2k\pi$	$2k\pi$	$I_2I_4 - (I_2+I_3+I_4)m_4l_3l_4$ $-(I_3+I_4)m_4l_1l_4$ $-I_4l_2\big[(m_2+m_3+m_4)l_1+(m_3+m_4)l_3\big]$ $+m_2m_4l_1l_2l_3l_4$
$(2k+1)\pi$	$2k\pi$	$(2k+1)\pi$	$2k\pi$	$I_2I_4 + (I_2+I_3+I_4)m_4l_3l_4$ $+(I_3+I_4)m_4l_1l_4$ $-I_4l_2\big[(m_2+m_3+m_4)l_1+(m_3+m_4)l_3\big]$ $-m_2m_4l_1l_2l_3l_4$
$2k\pi$	$(2k+1)\pi$	$2k\pi$	$(2k+1)\pi$	$I_2I_4 - (I_2+I_3+I_4)m_4l_3l_4$ $-(I_3+I_4)m_4l_1l_4$ $+I_4l_2\big[(m_2+m_3+m_4)l_1+(m_3+m_4)l_3\big]$ $-m_2m_4l_1l_2l_3l_4$

inertial term $|\mathbf{M}_{pa}|$ on the joint angles q_k. To have a singular-free model, the following conditions as the strong inertial coupling [97] should be satisfied with always values greater than zero. These conditions create a great level of limitations in the configuration and geometric parameters. For instance, simpler conditions were studied for the 2-DoF linked manipulators by [97] and for the rolling spherical systems in Examples 4.3.1-4.17 [113].

In Table A.1, the angle $q_2 - q_3$ is dependent on the chosen values of $q_2 - q_1$, $q_4 - q_3$ and $q_4 - q_1$ angles. It is clear that example conditions should be satisfied with chosen particular geometric parameters for l_k, m_k, and I_k to avoid singularities. However, these strongly singular configurations are not possible to be satisfied while we are changing the geometric parameters because the complete singular model requires the model to have a very large I_2I_4 in comparison to other terms. Otherwise, conditions will always fail non-singular condition (A.14) for (A.2)-(A.3) during the solving procedure of the inverse dynamics. We have to emphasize that we have chosen only 5 configurations with the most negative values in here. Many more conditions should be checked that we left them for the reader to have full configuration without singularity. Also, as the DoFs increases with multiple joints, the inertial coupling limits the

system configuration and geometric parameters with highly integrated singularities. This is one of the reasons why high DoFs underactuated manipulators with more than one passive joints are hardly covered in literature.

A.4 Design of Small-Amplitude Waves on Rotational Joints

A.4.1 Singular-Free Model of the underactuated manipulator

In this section, we develop our inertia-based condition for singular-free inverse dynamics. We will use this condition to design our combined wave parameters for avoiding inertial coupling singularities.

By applying the combined waves (A.5) on the active joints q_2 and q_4, we have a different interpretation to the inertial coupling condition as follows

$$
\begin{aligned}
&|\mathbf{M}_{pa}| = M_{12}M_{34} - M_{14}M_{32} = +I_2I_4 + m_4\big[c_1\big(l_3(I_2+I_3+I_4)\cos(q_4-q_3)\\
&- l_1(I_3+I_4)\cos(q_4-q_1)\big) + c_2\big(l_3(I_2+I_3+I_4)\sin(q_4-q_3) - l_1(I_3+I_4)\sin(q_4-q_1)\big)\big]\\
&+ I_4\big[c_3\big(l_1(m_2+m_3+m_4)\cos(q_2-q_1) - l_3(m_3+m_4)\cos(q_2-q_3)\big)\\
\\
&+ c_4\big(l_1(m_2+m_3+m_4)\sin(q_2-q_1) - l_3(m_3+m_4)\sin(q_2-q_3)\big)\\
&+ \frac{1}{2}m_4l_1l_3\Big[m_2\big[(c_1c_3-c_2c_4)\cos(q_2+q_4-q_1-q_3) + (c_2c_3+c_1c_4)\sin(q_2+q_4-q_1-q_3)\big]\\
&+ (c_1c_3+c_2c_4)[(m_2+m_3+m_4)\cos(q_2+q_3-q_1-q_4)\\
&- (m_3+m_4)\cos(q_4+q_3-q_1-q_2)]\\
&+ (c_1c_4-c_2c_3)[(m_2+m_3+m_4)\sin(q_2+q_3-q_1-q_4)\\
&+ (m_3+m_4)\sin(q_4+q_3-q_1-q_2)]\Big] > 0
\end{aligned}
\tag{A.15}
$$

where

$$
\begin{aligned}
&c_1 = l_4 + a_4n_4\cos(n_4q_4+\varepsilon_4), c_2 = a_4n_4\cos(n_4q_4+\varepsilon_4),\\
&c_3 = l_2 + a_2\sin(n_2q_2+\varepsilon_2), c_4 = a_2n_2\cos(n_2q_2+\varepsilon_2).
\end{aligned}
\tag{A.16}
$$

Because the inequality (A.15) is complex due to the included combined-waves, we have to check the minimum possible values to determine combined-wave parameters $(a_k, n_k, \varepsilon_k)$ properly. Thus, we define the following proposition.

Proposition A.4.1 *Let the inverse dynamics model be (A.2)-(A.3) with combined sinusoidal wave trajectories (A.4). This system does not hit singularity and* $|\mathbf{M}_{pa}| > 0$ *condition is satisfied while the small-amplitude waves parameters* a_k*,* n_k *and* ε_k *for* $k = \{2, 4\}$ *are designed with satisfying the minimum inertial condition*

$$
\begin{aligned}
I_{min} &= I_2 I_4 - m_4 l_1 (I_2 + I_3 + I_4) \left[c_1 \cos\left(\tan^{-1}\left(\frac{c_2}{c_1} \right) \right) + c_2 \sin\left(\tan^{-1}\left(\frac{c_2}{c_1} \right) \right) \right] \\
&- I_4 l_3 (m_3 + m_4) \left[c_3 \cos\left(\tan^{-1}\left(\frac{c_4}{c_3} \right) \right) + c_4 \sin\left(\tan^{-1}\left(\frac{c_4}{c_3} \right) \right) \right] \\
&+ f_1 + f_2 + \frac{1}{2} m_2 m_4 l_1 l_3 \left[(c_1 c_3 - c_2 c_4) \cos\left(\tan^{-1}\left(\frac{c_2 c_3 + c_1 c_4}{c_1 c_3 - c_2 c_4} \right) \right) \right. \\
&\left. + (c_2 c_3 + c_1 c_4) \sin\left(\tan^{-1}\left(\frac{c_2 c_3 + c_1 c_4}{c_1 c_3 - c_2 c_4} \right) \right) + f_3 \right] > 0,
\end{aligned}
\tag{A.17}
$$

where

$$
\begin{aligned}
f_1 &= -m_4 l_3 (I_2 + I_3 + I_4) \cdot \max\left\{ |c_1|, |c_2|, \frac{\sqrt{2}}{2}(|c_1| + |c_2|) \right\}, \\
f_2 &= -(m_2 + m_3 + m_4) l_1 I_4 \cdot \max\left\{ |c_3|, |c_4|, \frac{\sqrt{2}}{2}(|c_3| + |c_4|) \right\}, \\
f_3 &= -\frac{m_2 + m_3 + m_4}{m_2} \cdot \max\left\{ |c_1 c_3 - c_2 c_4|, |c_2 c_3 + c_1 c_4| \right. \\
&\quad \left. , \frac{\sqrt{2}}{2}(|c_1 c_3 - c_2 c_4| + |c_2 c_3 + c_1 c_4|) \right\} \\
&- \quad \frac{m_3 + m_4}{m_2} \cdot \max\left\{ |c_1 c_3 - c_2 c_4|, |c_2 c_3 + c_1 c_4|, \frac{\sqrt{2}}{2}(|c_1 c_3 - c_2 c_4| - |c_2 c_3 + c_1 c_4|) \right. \\
&\quad \left. , \frac{\sqrt{2}}{2}(-|c_1 c_3 - c_2 c_4| + |c_2 c_3 + c_1 c_4|) \right\}.
\end{aligned}
\tag{A.18}
$$

Proof Considering the condition $|\mathbf{M}_{pa}| > 0$ in (A.15), we have to determine the minimum value in the multivariable (q_k) function. Inequality (A.15) is re-ordered in

following way

$$
\begin{aligned}
|\mathbf{M}_{pa}| &= I_2 I_4 + m_4\big[l_3(I_2+I_3+I_4)\big(c_1\cos(q_4-q_3)+c_2\sin(q_4-q_3)\big)\\
&- l_1(I_3+I_4)\big(c_1\cos(q_4-q_1)+c_2\sin(q_4-q_1)\big)\big]\\
&+ I_4\big[l_1(m_2+m_3+m_4)\big(c_3\cos(q_2-q_1)+c_4\sin(q_2-q_1)\big)\\
&- l_3(m_3+m_4)\big(c_3\cos(q_2-q_3)+c_4\sin(q_2-q_3)\big)\big]\\
&+ \frac{1}{2}m_4 l_1 l_3\Big[m_2\big[(c_1c_3-c_2c_4)\cos(q_2+q_4-q_1-q_3)+(c_2c_3+c_1c_4)\sin(q_2+q_4-q_1-q_3)\big]\\
&+ (m_2+m_3+m_4)\big[(c_1c_3+c_2c_4)\cos(q_2+q_3-q_1-q_4)+(c_1c_4-c_2c_3)\sin(q_2+q_3-q_1-q_4)\big]\\
&+ (m_3+m_4)\big[-(c_1c_3+c_2c_4)\cos(q_4+q_3-q_1-q_2)\\
&+ (c_1c_4-c_2c_3)\sin(q_4+q_3-q_1-q_2)\big] > 0
\end{aligned}
\tag{A.19}
$$

The third, fifth and sixth terms are chosen to make them independent of (q_k) angles. Note that these angles (q_4-q_1), (q_2-q_3) and $(q_2+q_4-q_1-q_3)$ are chosen to be independent. Then, the derivatives of these terms are taken respect to their angles

$$
\begin{aligned}
&\frac{d}{d(q_4-q_1)}\big[-l_1(I_3+I_4)\big(c_1\cos(q_4-q_1)+c_2\sin(q_4-q_1)\big)\big]\\
&= -c_1\sin(q_4-q_1)+c_2\cos(q_4-q_1)=0,\\
&\frac{d}{d(q_2-q_3)}\big[-l_3(m_3+m_4)\big(c_3\cos(q_2-q_3)+c_4\sin(q_2-q_3)\big)\big]\\
&= -c_3\sin(q_2-q_3)+c_4\cos(q_2-q_3)=0,\\
&\frac{d}{d(q_2+q_4-q_1-q_3)}\big[m_2\big[(c_1c_3-c_2c_4)\cos(q_2+q_4-q_1-q_3)\\
&+ (c_2c_3+c_1c_4)\sin(q_2+q_4-q_1-q_3)\big]\\
&= -(c_1c_3-c_2c_4)\sin(q_2+q_4-q_1-q_3)+(c_2c_3+c_1c_4)\cos(q_2+q_4-q_1-q_3)=0.
\end{aligned}
\tag{A.20}
$$

Next, we solve each term for its angle in (A.20) as

$$
\begin{aligned}
q_4-q_1 &= \tan^{-1}\left(\frac{c_2}{c_1}\right),\ q_2-q_3=\tan^{-1}\left(\frac{c_4}{c_3}\right)\\
q_2+q_4-q_1-q_3 &= \tan^{-1}\left(\frac{c_2c_3+c_1c_4}{c_1c_3-c_2c_4}\right),
\end{aligned}
\tag{A.21}
$$

These angles in (A.21) are substituted back to the inequality condition (A.19). The remaining terms are calculated for their smallest possible values. In order to find

the smallest values in the second and fourth terms, we choose three largest possible points with negative signs as follows

$$f_1 = -l_3(I_2 + I_3 + I_4)\begin{cases} |c_1|, & (q_4 - q_3) = (k+1)\pi \\ |c_2|, & (q_4 - q_3) = \frac{(2k+1)\pi}{2} \\ \frac{\sqrt{2}}{2}(|c_1| + |c_2|), & (q_4 - q_3) = \frac{(2k+1)\pi}{4} \end{cases}$$
$$f_2 = -l_1(m_2 + m_3 + m_4)\begin{cases} |c_3|, & (q_2 - q_1) = (k+1)\pi \\ |c_4|, & (q_2 - q_1) = \frac{(2k+1)\pi}{2} \\ \frac{\sqrt{2}}{2}(|c_3| + |c_4|), & (q_2 - q_1) = \frac{(2k+1)\pi}{4} \end{cases} \tag{A.22}$$

Next, the remaining final term is also calculated for its smallest value as follows:

$$f_3 = -(m_2 + m_3 + m_4)\begin{cases} |c_1c_3 + c_2c_4|, & (q_2 + q_3 - q_1 - q_4) = (k+1)\pi \\ |c_1c_4 - c_2c_3|, & (q_2 + q_3 - q_1 - q_4) = \frac{(2k+1)\pi}{2} \\ \frac{\sqrt{2}}{2}(|c_1c_3 + c_2c_4| & \\ +|c_1c_4 - c_2c_3|), & (q_2 + q_3 - q_1 - q_4) = \frac{(2k+1)\pi}{4} \end{cases}$$
$$-(m_3 + m_4)\begin{cases} |c_1c_3 + c_2c_4|, & (q_4 + q_3 - q_1 - q_2) = (k+1)\pi \\ |c_1c_4 - c_2c_3|, & (q_4 + q_3 - q_1 - q_2) = \frac{(2k+1)\pi}{2} \\ \begin{cases} \frac{\sqrt{2}}{2}(-|c_1c_3 + c_2c_4| + |c_1c_4 - c_2c_3|), & \\ \qquad (q_2 + q_3 - q_1 - q_4) = \frac{(2k+1)\pi}{4} \\ \frac{\sqrt{2}}{2}(|c_1c_3 + c_2c_4| - |c_1c_4 - c_2c_3|), & \end{cases} & \end{cases} \tag{A.23}$$

Now, because the c_k terms are the combined waves with continues sign changes, we find the maximum value of functions (A.22)-(A.23) which result in our derived condition in (A.17).

Remark A.4.1 *The combined wave variables should be designed with condition (A.17) under the assumption of $a_k n_k < l_k$, based on equation (A.16), because maximum values of terms in (A.18) are derived with respect to this property.*

Remark A.4.2 *The following way of derivation for obtaining a singular-free condition (A.17) can be extended to other n-DoFs manipulators where the determinant*

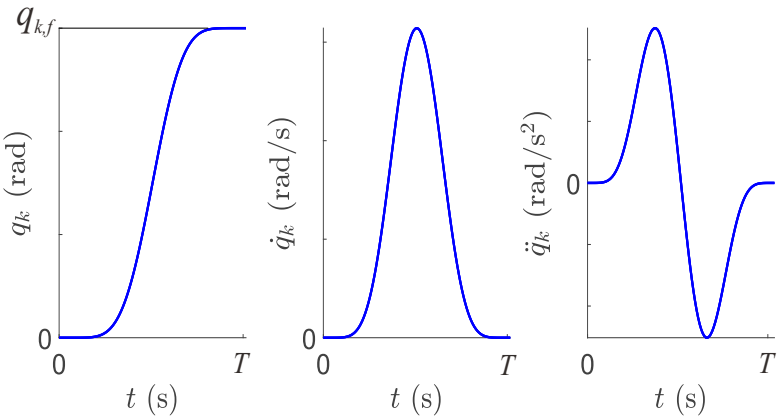

Figure A.4: The designed Beta function for the specified passive joints.

of $|\mathbf{M}_{pa}|$ *matrix is utilized. Note that this property mainly comes from non-singular condition [97, 113] under the positive definiteness of inertia matrix. Additionally, the problem dimension is* $n/2$ *when we have* n *number of joints, which is 2-dimensional problem (*q_2 *and* q_4*) here.*

A.4.2 Feed-Forward Control for Active Joints

A feed-forward control method is selected to converge the specified passive joints to desired states while the active joints follow the required motions. The Beta functions are utilized for giving the motion of the passive joints.

The passive joints are prescribed by using a general equation of the symmetric Beta functions [3, 105, 113] which considered as a sub-optimal solution in motion planning. For k-th passive joint (they are $k = \{1, 3\}$ here), the angular velocity of the passive joint is assigned as follows

$$\dot{q}_k(\zeta) = \frac{\zeta^{\alpha_k - 1}(1-\zeta)^{\alpha_k - 1}}{B}, \tag{A.24}$$

where $\zeta = t/T$, B is the Beta function and α_k is the order of k-th joint function, which t is the time variable and T is the time constant for the desired state arrival. The Beta function B is expressed in following form [105]

$$B = \frac{(\alpha_k - 1)!(\alpha_k - 1)!}{(2\alpha_k - 1)!}. \tag{A.25}$$

By taking integration of equation (A.24), the convergence function $q_k(\zeta)$ is defined

toward its desired state $q_{k,f}$ as follows

$$q_k(\zeta) = \frac{q_{k,f}}{T} \int_0^{\zeta} \dot{q}_k(\zeta)\, dt. \tag{A.26}$$

Fig. A.4 shows the behavior of considered function for the passive joints.

Note that similar to what has been developed in [3], one can show that with the selection of this motion scenario for the passive joints, the condition $\dot{q}_k(T) = 0$ is always satisfied. However, we do not consider any particular characteristic of active joints in these control strategies. Therefore, this feed-forward control is proposed for the sake of study on the singularity problem in the inertial matrix and see can our designed inverse dynamics avoid singularities due to inertial coupling.

A.5 Dynamics of the 4-DoF Manipulator

We show the 4-DoF nonlinear dynamics of manipulator by the derived general formulation.

In our study, we consider our system with two passive and two active joints. The active joints on second and forth links have the wavy trajectory with variables of $\{a_2, n_2, \varepsilon_2\}$ and $\{a_4, n_4, \varepsilon_4\}$. The passive joints in first and third link do not have the wave functions $a_1 = n_1 = \varepsilon_1 = 0$ and $a_3 = n_3 = \varepsilon_3 = 0$. By the considered system, the Lagrangian function in (A.9) becomes

$$\begin{aligned}
L &= \frac{1}{2}(m_1+m_2+m_3+m_4)l_1^2\dot{q}_1^2 + \frac{1}{2}(m_3+m_4)l_3^2\dot{q}_3^2 \\
&+ \frac{1}{2}(m_2+m_3+m_4)\dot{q}_2^2\big[a_2^2n_2^2\cos^2(n_2q_2+\varepsilon_2) + (l_2+a_2\sin(n_2q_2+\varepsilon_2))^2\big] \\
&+ \frac{1}{2}m_4\dot{q}_4^2\big[a_4^2n_4^2\cos^2(n_4q_4+\varepsilon_4) + (l_4+a_4\sin(n_4q_4+\varepsilon_4))^2\big] \\
&+ (m_2+m_3+m_4)\dot{q}_1\dot{q}_2\big[l_1(l_2 \\
&+ a_2\sin(n_2q_2+\varepsilon_2))\cos(q_1-q_2) + a_2n_2l_1\cos(n_2q_2+\varepsilon_2)\sin(q_2-q_1)\big] \\
&+ (m_3+m_4)\dot{q}_1\dot{q}_3l_1l_3\cos(q_1-q_3) \\
&+ (m_3+m_4)\dot{q}_2\dot{q}_3\big[l_3(l_2+a_2\sin(n_2q_2+\varepsilon_2))\cos(q_2-q_3) \\
&+ a_2n_2l_3\cos(n_2q_2+\varepsilon_2)\sin(q_2-q_3)\big] \\
&+ m_4\dot{q}_1\dot{q}_4\big[l_1(l_4+a_4\sin(n_4q_4+\varepsilon_4))\cos(q_1-q_4) \\
&+ a_4n_4l_1\cos(n_4q_4+\varepsilon_4)\sin(q_4-q_1)\big] + m_4\dot{q}_2\dot{q}_4\big[(l_2 \\
&+ a_2\sin(n_2q_2+\varepsilon_2))\cdot(l_4+a_4\sin(n_4q_4+\varepsilon_4))\cos(q_2-q_4) \\
&+ a_2n_2a_4n_4\cos(n_2q_2+\varepsilon_2)\cdot\cos(n_4q_4+\varepsilon_4)\cos(q_2-q_4) \\
&+ a_2n_2(l_4+a_4\sin(n_4q_4+\varepsilon_4))\cdot\cos(n_2q_2+\varepsilon_2)\sin(q_2-q_4) \\
&+ a_4n_4(l_2+a_2\sin(n_2q_2+\varepsilon_2))\cdot\cos(n_4q_4+\varepsilon_4)\sin(q_4-q_2)\big]
\end{aligned} \tag{A.27}$$

$$\begin{aligned}
&+ m_4\dot{q}_3\dot{q}_4\big[l_3(l_4+a_4\sin(n_4q_4+\varepsilon_4))\cos(q_3-q_4) \\
&+ a_4n_4l_3\cos(n_4q_4+\varepsilon_4)\sin(q_4-q_3)\big] \\
&+ \frac{1}{2}\sum_{k=1}^{4} I_k\left(\sum_{i=1}^{k}\dot{q}_k\right)^2 + \sum_{k=1}^{4}\sum_{i=1}^{k} m_k g\left(l_i + a_i\sin\left(n_iq_i+\varepsilon_i\right)\right)\cos q_i.
\end{aligned} \tag{A.28}$$

Furthermore, by using the equation (A.28) and the Lagrangian equations (4.8), the motion equation terms of (A.11) become

$$\mathbf{M}^* = \begin{bmatrix} M_{11} & M_{12} & M_{13} & M_{14} \\ M_{21} & M_{22} & M_{23} & M_{24} \\ M_{31} & M_{32} & M_{33} & M_{34} \\ M_{41} & M_{42} & M_{43} & M_{44} \end{bmatrix}, \mathbf{h}^* = \begin{bmatrix} h_1 & h_2 & h_3 & h_4 \end{bmatrix}^T,$$
$$\mathbf{u}^* = \begin{bmatrix} 0 & \tau_2 & 0 & \tau_4 \end{bmatrix}^T. \tag{A.29}$$

where

$$\begin{aligned}
M_{11} &= I_1 + I_2 + I_3 + I_4 + (m_1 + m_2 + m_3 + m_4) l_1^2, \\
M_{22} &= I_2 + I_3 + I_4 + (m_2 + m_3 + m_4)\big[a_2^2 n_2^2 \cos^2(n_2 q_2 + \varepsilon_2) + (l_2 + a_2 \sin(n_2 q_2 + \varepsilon_2))^2\big] \\
M_{33} &= I_3 + I_4 + (m_3 + m_4) l_3^2, \\
M_{44} &= I_4 + m_4\big[a_4^2 n_4^2 \cos^2(n_4 q_4 + \varepsilon_4 + (l_4 + a_4 \sin(n_4 q_4 + \varepsilon_4))^2\big], \\
M_{12} &= M_{21} = I_2 + I_3 + I_4 + (m_2 + m_3 + m_4) \cdot \big[l_1 (l_2 + a_2 \sin(n_1 q_1 + \varepsilon_1)) \cos(q_1 - q_2) \\
&+ a_2 n_2 l_1 \cos(n_2 q_2 + \varepsilon_2) \sin(q_2 - q_1)\big], \\
M_{13} &= M_{31} = I_3 + I_4 + (m_3 + m_4) l_1 l_3 \cos(q_1 - q_3), \\
M_{23} &= M_{32} = I_3 + I_4 + (m_3 + m_4) \cdot \big[l_3 (l_2 + a_2 \sin(n_2 q_2 + \varepsilon_2)) \cos(q_2 - q_3) \\
&+ a_2 n_2 l_3 \cos(n_2 q_2 + \varepsilon_2) \sin(q_2 - q_3)\big], \\
M_{34} &= M_{43} = I_4 + m_4 \cdot \big[l_3 (l_4 + a_4 \sin(n_4 q_4 + \varepsilon_4)) \cos(q_3 - q_4) \\
&+ a_4 n_4 l_3 \cos(n_4 q_4 + \varepsilon_4) \sin(q_4 - q_3)\big], \\
M_{14} &= M_{41} = I_4 + m_4 \cdot \big[l_1 (l_4 + a_4 \sin(n_4 q_4 + \varepsilon_4)) \cos(q_1 - q_4) \\
&+ a_4 n_4 l_1 \cos(n_4 q_4 + \varepsilon_4) \sin(q_4 - q_1)\big],
\end{aligned} \tag{A.30}$$

$$\begin{aligned}
M_{24} &= M_{42} = I_4 + m_4\big[(l_2 + a_2 \sin(n_2 q_2 + \varepsilon_2))(l_4 + a_4 \sin(n_4 q_4 + \varepsilon_4)) \cos(q_2 - q_4) \\
&+ a_2 n_2 a_4 n_4 \cos(n_2 q_2 + \varepsilon_2) \cos(n_4 q_4 + \varepsilon_4) \cos(q_2 - q_4) \\
&+ a_2 n_2 (l_4 + a_4 \sin(n_4 q_4 + \varepsilon_4)) \cos(n_2 q_2 + \varepsilon_2) \sin(q_2 - q_4) \\
&+ a_4 n_4 (l_2 + a_2 \sin(n_2 q_2 + \varepsilon_2)) \cos(n_4 q_4 + \varepsilon_4) \sin(q_4 - q_2)\big]
\end{aligned} \tag{A.31}$$

Additionally, the velocity dependencies and gravitational terms h_k in each link are obtained by using (A.12)

$$
\begin{aligned}
h_1 &= (m_2+m_3+m_4)\dot{q}_2^2\big[2a_2n_2l_1\cos(n_2q_2+\varepsilon_2)\cos(q_1-q_2)\\
&+ l_1(l_2+a_2\sin(n_2q_2+\varepsilon_2))\sin(q_1-q_2)-a_2n_2^2l_1\sin(n_2q_2+\varepsilon_2)\sin(q_2-q_1)\big]\\
&+ (m_3+m_4)\dot{q}_3^2\big[l_1l_3\sin(q_1-q_3)\big]\\
&+ m_4\dot{q}_4^2\big[2a_4n_4l_1\cos(n_4q_4+\varepsilon_4)\cos(q_1-q_4)+l_1(l_4+a_4\sin(n_4q_4+\varepsilon_4))\sin(q_1-q_4)\\
&- a_4n_4^2l_1\sin(n_4q_4+\varepsilon_4)\sin(q_4-q_1)\big]\\
&+ (m_1+m_2+m_3+m_4)g\big[(l_1+a_1\sin(n_1q_1+\varepsilon_1))\sin q_1\\
&- a_1n_1\cos(n_1q_1+\varepsilon_1)\cos q_1\big],\\
h_2 &= (m_2+m_3+m_4)\dot{q}_1^2\big[2a_2n_2l_1\cos(n_2q_2+\varepsilon_2)\cos(q_1-q_2)+l_1(l_2+a_2\sin(n_2q_2+\varepsilon_2))\\
&\quad\cdot\sin(q_1-q_2)-a_2n_2^2l_1\sin(n_2q_2+\varepsilon_2)\sin(q_2-q_1)\big]\\
&+ (m_2+m_3+m_4)\dot{q}_2^2\big[a_2n_2\cos(n_2q_2+\varepsilon_2)(l_2+a_2\sin(n_2q_2+\varepsilon_2))\\
&- a^2n_2^3\sin(n_2q_2+\varepsilon_2)\cos(n_2q_2+\varepsilon_2)\big]\\
&+ (m_3+m_4)\dot{q}_3^2\big[l_3(l_2+a_2\sin(n_2q_2+\varepsilon_2))\\
&\quad\cdot\sin(q_2-q_3)-a_2n_2l_3\cos(n_2q_2+\varepsilon_2)\cos(q_2-q_3)\big]\\
&+ m_4\dot{q}_4^2\big[2a_4n_4\cos(n_4q_4+\varepsilon_4)(l_2+a_2\sin(n_2q_2+\varepsilon_2))\\
&\quad\cdot\cos(q_2-q_4)+2a_2n_2a_4n_4\cos(n_2q_2+\varepsilon_2)\cos(n_4q_4+\varepsilon_4)\sin(q_2-q_4)\\
&+ (l_2+a_2\sin(n_2q_2+\varepsilon_2))(l_4+a_4\sin(n_4q_4+\varepsilon_4))\sin(q_2-q_4)\\
&- a_2n_2a_4n_4^2\sin(n_4q_4+\varepsilon_4)\cos(n_2q_2+\varepsilon_2)\cos(q_2-q_4)\\
&- a_2n_2(l_4+a_4\sin(n_4q_4+\varepsilon_4))\cos(n_2q_2+\varepsilon_2)\cos(q_2-q_4)\\
&- a_4n_4^2(l_2+a_2\sin(n_2q_2+\varepsilon_2))\sin(n_4q_4+\varepsilon_4)\sin(q_4-q_2)\big]\\
&+ (m_2+m_3+m_4)g\big[(l_2+a_2\sin(n_2q_2+\varepsilon_2))\sin q_2-a_2n_2\cos(n_2q_2+\varepsilon_2)\cos q_2\big],
\end{aligned}
$$

And,

$$
\begin{aligned}
h_3 &= (m_3+m_4)\dot{q}_1^2\big[l_1 l_3 \sin(q_1-q_3)\big] \\
&+ (m_3+m_4)\dot{q}_2^2\big[l_3(l_2+a_2\sin(n_2q_2+\varepsilon_2))\sin(q_2-q_3) \\
&- a_2 n_2 l_3 \cos(n_2q_2+\varepsilon_2)\cos(q_2-q_3)\big] \\
&+ m_4\dot{q}_4^2\big[2a_4n_4l_3\cos(n_4q_4+\varepsilon_4)\cos(q_3-q_4)+l_3(l_4+a_4\sin(n_4q_4+\varepsilon_4))\sin(q_3-q_4) \\
&- a_4n_4^2l_3\sin(n_4q_4+\varepsilon_4)\sin(q_4-q_3)\big] \\
&+ (m_3+m_4)g\big[(l_3+a_3\sin(n_3q_3+\varepsilon_3))\sin q_3 - a_3n_3\cos(n_3q_3+\varepsilon_3)\cos q_3\big], \\
h_4 &= m_4\dot{q}_1^2\big[2a_4n_4l_1\cos(n_4q_4+\varepsilon_4)\cos(q_1-q_4)+l_1(l_4+a_4\sin(n_4q_4+\varepsilon_4))\sin(q_1-q_4) \\
&- a_4n_4^2l_1\sin(n_4q_4+\varepsilon_4)\sin(q_4-q_1)\big] \\
&+ m_4\dot{q}_2^2\big[2a_4n_4\cos(n_4q_4+\varepsilon_4)(l_2+a_2\sin(n_2q_2+\varepsilon_2))\cos(q_2-q_4) \\
&+ 2a_2n_2a_4n_4\cos(n_2q_2+\varepsilon_2)\cos(n_4q_4+\varepsilon_4)\sin(q_2-q_4) \\
&+ (l_2+a_2\sin(n_2q_2+\varepsilon_2))(l_4+a_4\sin(n_4q_4+\varepsilon_4))\sin(q_2-q_4) \\
&- a_2n_2a_4n_4^2\sin(n_4q_4+\varepsilon_4)\cos(n_2q_2+\varepsilon_2)\cos(q_2-q_4) \\
&- a_2n_2(l_4+a_4\sin(n_4q_4+\varepsilon_4))\cos(n_2q_2+\varepsilon_2)\cos(q_2-q_4) \\
&- a_4n_4^2(l_2+a_2\sin(n_2q_2+\varepsilon_2))\sin(n_4q_4+\varepsilon_4)\sin(q_4-q_2)\big] \\
&+ m_4\dot{q}_3^2\big[2a_4n_4l_3\cos(n_4q_4+\varepsilon_4)\cos(q_3-q_4) \\
&+ l_3(l_4+a_4\sin(n_4q_4+\varepsilon_4))\sin(q_3-q_4) \\
&- a_4n_4^2l_3\sin(n_4q_4+\varepsilon_4)\sin(q_4-q_3)\big] \\
&+ m_4\dot{q}_4^2[a_4n_4\cos(n_4q_4+\varepsilon_4)(l_4+a_4\sin(n_4q_4+\varepsilon_4)) \\
&- a_4^2n_4^3\sin(n_4q_4+\varepsilon_4)\cos(n_4q_4+\varepsilon_4)] \\
&+ m_4g\big[(l_4+a_4\sin(n_4q_4+\varepsilon_4))\sin(q_4) \\
&- a_4n_4\cos(n_4q_4+\varepsilon_4)\cos(q_4)\big], \qquad \text{(A.32)}
\end{aligned}
$$

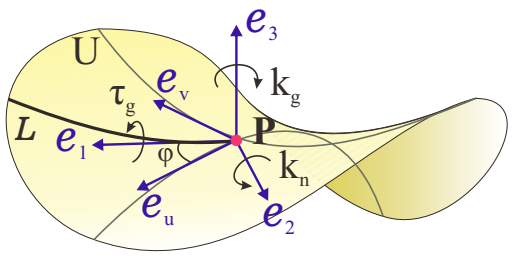

Figure B.1: Two coordinate frames related by φ rotational angle about $\boldsymbol{e}_3$.

Appendix B

Geometric Path Planning

B.1 Moving Darboux Frame Preliminaries

The structural equations of a Darboux frame, which is known for the trihedron, are explained on an arbitrary surface U as Fig. B.1. Let every contacted point $\mathbf{P} \in U$ is defined by a unit-based Darboux frame $(\boldsymbol{e}_1, \boldsymbol{e}_2, \boldsymbol{e}_3)$ [26] where $\boldsymbol{e}_1$ is a tangent vector to the path $\mathbf{L}$, $\boldsymbol{e}_3$ is a normal vector to the U surface and $\boldsymbol{e}_2$ is perpendicular to the plane $\boldsymbol{e}_3 \times \boldsymbol{e}_1$. The Darboux frame motion along the curve $\mathbf{L}$ on surface U becomes [26]

$$\begin{aligned} d\mathbf{P} &= \omega_1^f \boldsymbol{e}_1, \\ d\begin{bmatrix} \boldsymbol{e}_1 \\ \boldsymbol{e}_2 \\ \boldsymbol{e}_3 \end{bmatrix} &= \begin{bmatrix} 0 & \omega_{12}^f & \omega_{13}^f \\ -\omega_{12}^f & 0 & \omega_{23}^f \\ -\omega_{13}^f & -\omega_{23}^f & 0 \end{bmatrix} \begin{bmatrix} \boldsymbol{e}_1 \\ \boldsymbol{e}_2 \\ \boldsymbol{e}_3 \end{bmatrix}. \end{aligned} \tag{B.1}$$

where ω_1^f, ω_{12}^f, ω_{23}^f and ω_{13}^f are the one-forms of the Darboux frame $(\boldsymbol{e}_1, \boldsymbol{e}_2, \boldsymbol{e}_3)$. Based on Cartan [26], if the curve $\mathbf{L}$ is parametrized by arc-length s, ω_1^f is the component of translation of the Darboux frame (trihedron) in arc-length domain. Also, ω_{12}^f, ω_{23}^f and ω_{13}^f are the components of rotation of the Darboux frame (trihedron) in arc-length domain. The curvature dependencies along the curve $\mathbf{L}$ are defined for the Darboux frame by (B.1) by using these one-form differential relations as [63]

$$k_g = \omega_{12}^f/\omega_1^f, \quad k_n = \omega_{13}^f/\omega_1^f, \quad \tau_g = \omega_{23}^f/\omega_1^f, \tag{B.2}$$

where k_g, k_n and τ_g are the geodesic curvature, normal curvature and geodesic torsion of the Darboux frame, respectively.

Now, consider an angle φ between the Darboux frame $\boldsymbol{e}_1$ and the induced contact coordinate of the arbitrary surface $(\boldsymbol{e}_u, \boldsymbol{e}_v, \boldsymbol{e}_3)$ about aligned $\boldsymbol{e}_3$, then the structural equations are parameterized by

$$\begin{aligned} \boldsymbol{e}_1 &= \cos\varphi\, \boldsymbol{e}_u + \sin\varphi\, \boldsymbol{e}_v, \\ \boldsymbol{e}_2 &= -\sin\varphi\, \boldsymbol{e}_u + \cos\varphi\, \boldsymbol{e}_v, \\ \boldsymbol{e}_3 &= \boldsymbol{e}_3, \end{aligned} \tag{B.3}$$

which differentiating both sides of given transformation, results

$$\begin{bmatrix} \omega_{12}^f \\ \omega_{13}^f \\ \omega_{23}^f \end{bmatrix} = \begin{bmatrix} 1 & 0 & 0 \\ 0 & \cos\varphi & \sin\varphi \\ 0 & -\sin\varphi & \cos\varphi \end{bmatrix} \begin{bmatrix} \omega_{12} \\ \omega_{13} \\ \omega_{23} \end{bmatrix}, \tag{B.4}$$

where ω_{12}, ω_{13} and ω_{23} are the one-forms for an induced coordinates of an arbitrary surface. Note that we apply this to the arbitrary rotating object with the angle φ with respect to the Darboux frame. These properties are also applied to derive the fixed surface (plane) and rotating sphere equation with the inclusion of angle θ. We will use these kinematics relations to develop curvature equations between the Darboux frame and the induced contact coordinates of an arbitrary surface in Appendix B.3.

B.2 Proof of Darboux Frame Kinematics with Sandwiched Virtual Surface

The induced curvatures between the rotating object (sphere) and fixed surface (plane) including a sandwiched virtual surface (5.5) is proved here. We show the proof by using the preliminary study on the induced curvature for two surfaces [34]. Here, we develop a new virtual surface that is sandwiched between two surfaces (sphere and plane in our case). This virtual surface relates our arc-length-based inputs with derived curvatures in (B.22) to manipulate the spin-rolling sphere angular coordinates.

We propose a spin-rolling object U_C on the surface U_S where a virtual moving surface U_V is sandwiched as Fig. B.2. It is assumed that always three objects keep

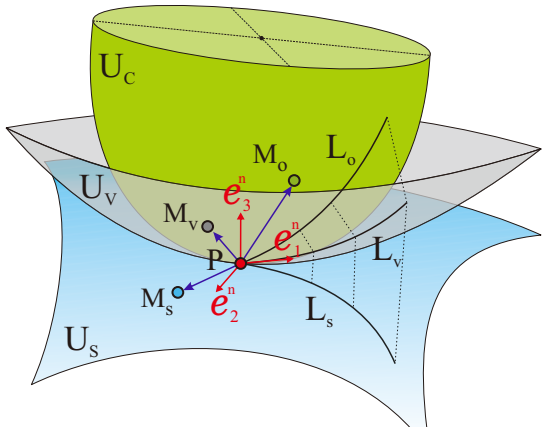

Figure B.2: Rotating object U_C on the fixed surface U_S with sandwiched virtual surface U_V. Note that n in $\{\boldsymbol{e}_1^n, \boldsymbol{e}_2^n, \boldsymbol{e}_3^n\}$ frame stands for fixed surface (plane) s, virtual surface v and rotating object (sphere) o at each of these compact surfaces.

having the same contact point $\mathbf{P}$. The moving Darboux frame at the contact point $\mathbf{P}$ contains a general motion equation as:

$$\begin{aligned} \frac{d\mathbf{P}}{ds} &= \boldsymbol{e}_1, \\ d\begin{bmatrix} \boldsymbol{e}_1 \\ \boldsymbol{e}_2 \\ \boldsymbol{e}_3 \end{bmatrix} &= \begin{bmatrix} 0 & k_g & k_n \\ -k_g & 0 & \tau_g \\ -k_n & -\tau_g & 0 \end{bmatrix} \begin{bmatrix} \boldsymbol{e}_1 \\ \boldsymbol{e}_2 \\ \boldsymbol{e}_3 \end{bmatrix}, \end{aligned} \tag{B.5}$$

where, regardless of coordinate dependency, s is the arc-length of path $\mathbf{L}_s$, and also k_g, k_n and τ_g are geodesic curvature, the normal curvature and geodesic torsion of the Darboux frame. Also, the right-handed orthonormal unit vectors are aligned in same direction for all objects with respective subscripts, for example, the object U_C has $(\boldsymbol{e}_1^o, \boldsymbol{e}_2^o, \boldsymbol{e}_3^o)$ [see Fig. B.2]. Initially, the position of an arbitrary fixed point $\mathbf{M}_o$ on body U_C is

$$\mathbf{M}_o = \mathbf{P} + \sigma_1^o \boldsymbol{e}_1^o + \sigma_2^o \boldsymbol{e}_2^o + \sigma_3^o \boldsymbol{e}_3^o, \tag{B.6}$$

where σ is a scaler coordinate for the considered object, here is $\{\sigma_1^o, \sigma_2^o, \sigma_3^o\}$ for the rotating sphere. Differentiating this position matrix (B.6) with respect to s besides using Eq. (B.5) gives

$$\frac{d\mathbf{M}_o}{ds} = \begin{bmatrix} 1 + d\sigma_1^o/ds - \sigma_2^o k_g^o - \sigma_3^o k_n^o \\ d\sigma_2^o/ds + \sigma_1^o k_g^o - \sigma_3^o \tau_n^o \\ d\sigma_3^o/ds + \sigma_1^o k_n^o + \sigma_2^o \tau_n^o \end{bmatrix}^T \begin{bmatrix} \boldsymbol{e}_1^o \\ \boldsymbol{e}_2^o \\ \boldsymbol{e}_3^o \end{bmatrix}. \tag{B.7}$$

Because the $\mathbf{M}_o$ is a fixed point, the derivative with respect to the arc-length is $d\mathbf{M}_o/ds = 0$. This fact is true for all three surfaces. Then, we can conclude followings for the rotating surface U_C

$$d\sigma_1^o/ds = \sigma_2^o k_g^o + \sigma_3^o k_n^o - 1,\ d\sigma_2^o/ds = -\sigma_1^o k_g^o + \sigma_3^o \tau_n^o,\ d\sigma_3^o/ds = -\sigma_1^o k_n^o - \sigma_2^o \tau_n^o. \quad \text{(B.8)}$$

By using the same steps of derivation, a differentiated model at (B.7) can be found for a fixed point $\mathbf{M}_v$ at surface U_V with arc-length of s',

$$\frac{d\mathbf{M}_v}{ds} = \begin{bmatrix} 1 + d\sigma_1^v/ds' - \sigma_2^v k_g^v - \sigma_3^v k_n^v \\ d\sigma_2^v/ds' + \sigma_1^v k_g^v - \sigma_3^v \tau_n^v \\ d\sigma_3^v/ds' + \sigma_1^v k_n^v + \sigma_2^v \tau_n^v \end{bmatrix}^T \begin{bmatrix} \boldsymbol{e}_1^v \\ \boldsymbol{e}_2^v \\ \boldsymbol{e}_3^v \end{bmatrix}, \quad \text{(B.9)}$$

which helps us to have same conclusion for $\mathbf{M}_v$ point as

$$d\sigma_1^v/ds' = \sigma_2^v k_g^v + \sigma_3^v k_n^v - 1,\ d\sigma_2^v/ds' = -\sigma_1^v k_g^v + \sigma_3^v \tau_n^v,\ d\sigma_3^v/ds' = -\sigma_1^v k_n^v - \sigma_2^v \tau_n^v. \quad \text{(B.10)}$$

$\mathbf{L}_o$ and $\mathbf{L}_v$ are traversed with the same velocity and always the Darboux frame units coincide because of the rolling constraint with no-slippage. Then, the following conditions should exist $\sigma_q^o = \sigma_q^v$ and $\sigma_q^o/ds = \sigma_q^v/ds'$ for $q \in [1, 3]$ that arc-length of two curves with the same time period is the same. With given assumptions and substitution of Eq. (B.8) into Eq. (B.9), the differentiated point $\mathbf{M}_v$ becomes

$$\frac{d\mathbf{M}_v}{ds} = \begin{bmatrix} \sigma_2^v k_g^{ov} + \sigma_3^v k_n^{ov} \\ -\sigma_1^v k_g^{ov} + \sigma_3^v \tau_g^{ov} \\ -\sigma_1^v k_n^{ov} - \sigma_3^v \tau_g^{ov} \end{bmatrix}^T \begin{bmatrix} \boldsymbol{e}_1^v \\ \boldsymbol{e}_2^v \\ \boldsymbol{e}_3^v \end{bmatrix}, \quad \text{(B.11)}$$

where $k_g^{ov} = k_g^o - k_g^v$, $k_n^{ov} = k_n^o - k_n^v$ and $\tau_g^{ov} = \tau_g^o - \tau_g^v$. Next, the same derivation is repeated to virtual surface U_V with respect to fixed surface U_S with $\mathbf{L}_v$ and $\mathbf{L}_s$ trajectories that ultimately results in

$$\frac{d\mathbf{M}_s}{ds} = \begin{bmatrix} \sigma_2^s k_g^{vs} + \sigma_3^s k_n^{vs} \\ -\sigma_1^s k_g^{vs} + \sigma_3^s \tau_g^{vs} \\ -\sigma_1^s k_n^{vs} - \sigma_3^s \tau_g^{vs} \end{bmatrix}^T \begin{bmatrix} \boldsymbol{e}_1^s \\ \boldsymbol{e}_2^s \\ \boldsymbol{e}_3^s \end{bmatrix}, \quad \text{(B.12)}$$

where $k_g^{vs} = k_g^v - k_g^s$, $k_n^{vs} = k_n^v - k_n^s$ and $\tau_g^{vs} = \tau_g^v - \tau_g^s$. From (B.12), we can rearrange the curvature properties as:

$$k_g^v = k_g^{vs} + k_g^s,\ k_n^v = k_n^{vs} + k_n^s, \tau_g^v = \tau_g^{vs} + \tau_g^s, \quad \text{(B.13)}$$

Substituting back (B.13) to Eq. (B.11), while we assume $k_g^{vs} = \alpha_s$, $k_n^{vs} = \gamma_s$ and $\tau_g^{vs} = \beta_s$, results in the Darboux frame angular velocity in point $\mathbf{P}$ as

$$\boldsymbol{\omega}^* = \delta(-\tau_g^* \boldsymbol{e}_1 + k_n^* \boldsymbol{e}_2 - k_g^* \boldsymbol{e}_3), \tag{B.14}$$

where

$$k_g^* = k_g^o - k_g^s - \alpha_s, k_n^* = k_n^o - k_n^s - \gamma_s, \tau_g^* = \tau_g^o - \tau_g^s - \beta_s. \tag{B.15}$$

Eq. (B.15) shows the parametrized kinematics with a virtual surface that is related to induced curvatures of the moving object and fixed surface. For our case, the sphere curvature properties are subtracted from the virtual surface to create the corresponding angular velocities (B.14). Note that changes in the virtual surface's curvatures are projected on both sphere and plane traveling paths, $\mathbf{L}_o$ and $\mathbf{L}_s$. Also, this formula describes the physical meaning of arc-length-based inputs $\{\gamma_s, \alpha_s, \beta_s\}$ in Eq. (5.7).

B.3 The Curvatures Variation in a Given Direction

We derive a relation between angular rotation of the Darboux frame along $\boldsymbol{e}_3$ [see Fig. B.1] and the normal curvature, geodesic torsion and geodesic curvature on an arbitrary surface. Let a differentiable manifold $f_l(u, v)$ in $S \subset \mathbb{R}^3$ exists where $\boldsymbol{e}_v$ and $\boldsymbol{e}_u$ present the unit vector along v and u curves on a moving point $\mathbf{P} \subset S$. The differentiated map of the point $\mathbf{P}$ is [26]

$$d\mathbf{P} = \mathbf{r}_u du + \mathbf{r}_v dv = \omega_1 \boldsymbol{e}_u + \omega_2 \boldsymbol{e}_v,$$

hence, by defining $\omega_1 = \sqrt{E}du, \omega_2 = \sqrt{G}du$, we have

$$\begin{bmatrix} \mathbf{r}_u \\ \mathbf{r}_v \\ \Lambda \end{bmatrix} = \begin{bmatrix} \sqrt{E} & 0 & 0 \\ 0 & \sqrt{G} & 0 \\ 0 & 0 & 1 \end{bmatrix} \begin{bmatrix} \boldsymbol{e}_u \\ \boldsymbol{e}_v \\ \boldsymbol{e}_3 \end{bmatrix} = A \begin{bmatrix} \boldsymbol{e}_u \\ \boldsymbol{e}_v \\ \boldsymbol{e}_3 \end{bmatrix}, \tag{B.16}$$

where $E = \mathbf{r}_u \cdot \mathbf{r}_u$, $G = \mathbf{r}_v \cdot \mathbf{r}_v$ and Λ are the coefficients for the first fundamental form and normal vector of the surface S, respectively. Differentiating the left side of Eq.

(B.16) results in

$$
\begin{aligned}
d\begin{bmatrix} \mathbf{r}_u \\ \mathbf{r}_v \\ \Lambda \end{bmatrix} &= du\begin{bmatrix} \mathbf{r}_{uu} \\ \mathbf{r}_{uv} \\ \Lambda_u \end{bmatrix} + dv\begin{bmatrix} \mathbf{r}_{uv} \\ \mathbf{r}_{vv} \\ \Lambda_v \end{bmatrix} = \\
&\left(du\begin{bmatrix} \Gamma_{11}^1 & \Gamma_{11}^2 & L \\ \Gamma_{12}^1 & \Gamma_{12}^2 & M \\ W_1^1 & W_1^2 & 0 \end{bmatrix} + dv\begin{bmatrix} \Gamma_{12}^1 & \Gamma_{12}^2 & M \\ \Gamma_{22}^1 & \Gamma_{22}^2 & N \\ W_2^1 & W_1^2 & 0 \end{bmatrix} \right)\begin{bmatrix} \mathbf{r}_u \\ \mathbf{r}_v \\ \Lambda \end{bmatrix}
\end{aligned}
\tag{B.17}
$$

where Γ_{ij}^k, W_i^j, L, M and N are coefficients of Gauss and Weingarten equations, and rest of the three coefficients are the second fundamental form of surface, in which are [39]

$$
\begin{aligned}
\Gamma_{11}^1 &= \frac{GE_u - 2FF_u + FE_v}{2(EG-F^2)},\ \Gamma_{11}^2 = \frac{2EF_u - EE_v + FE_u}{2(EG-F^2)} \\
\Gamma_{12}^1 &= \frac{GE_v - FG_u}{2(EG-F^2)},\ \Gamma_{12}^2 = \frac{EG_u - FE_v}{2(EG-F^2)}, \\
\Gamma_{22}^1 &= \frac{2GF_v - 2GG_u - FG_v}{2(EG-F^2)},\ \Gamma_{22}^2 = \frac{EG_v - 2FF_v + FG_u}{2(EG-F^2)}, \\
W_1^1 &= \frac{MF-LG}{EG-F^2}, W_1^2 = \frac{LF-ME}{EG-F^2}, \\
W_2^1 &= \frac{NF-MG}{EG-F^2}, W_2^2 = \frac{MF-NE}{EG-F^2}.
\end{aligned}
$$

Next, differentiating Eq. (B.16)'s right side gives

$$
\begin{aligned}
d\left(\mathbf{B}\begin{bmatrix} \boldsymbol{e}_u \\ \boldsymbol{e}_v \\ \boldsymbol{e}_3 \end{bmatrix}\right) &= \left(d\mathbf{B}\begin{bmatrix} \boldsymbol{e}_u \\ \boldsymbol{e}_v \\ \boldsymbol{e}_3 \end{bmatrix} + \mathbf{B}d\left(\begin{bmatrix} \boldsymbol{e}_u \\ \boldsymbol{e}_v \\ \boldsymbol{e}_3 \end{bmatrix}\right)\right) \\
&= \left(d\mathbf{B} + \mathbf{B}\begin{bmatrix} 0 & \omega_{12} & \omega_{13} \\ -\omega_{12} & 0 & \omega_{23} \\ -\omega_{13} & -\omega_{23} & 0 \end{bmatrix}\right)\begin{bmatrix} \boldsymbol{e}_u \\ \boldsymbol{e}_v \\ \boldsymbol{e}_3 \end{bmatrix}.
\end{aligned}
\tag{B.18}
$$

where ω_{12}, ω_{13} and ω_{23} are the one-forms for $(\boldsymbol{e}_u, \boldsymbol{e}_v, \boldsymbol{e}_3)$ here. Also, Eqs. (B.17)-(B.18) yield the angular velocities of rotating body $(\boldsymbol{e}_u, \boldsymbol{e}_v, \boldsymbol{e}_3)$ for isometric surfaces ($F = 0$ assumption)

$$
\omega_{12} = \frac{-E_v du + G_u dv}{2\sqrt{EG}},\ \omega_{13} = \frac{Ldu + Mdv}{\sqrt{E}},\ \omega_{23} = \frac{Mdu + Ndv}{\sqrt{G}},
\tag{B.19}
$$

where obtained ones are used besides the defined ω_1 and ω_2. By the derived formulation, for each u and v principle curves the curvature properties in Eq. (B.2) are calculated. For each principle, the derivative of perpendicular curve becomes zero, therefore, u-curve has

$$\begin{aligned} k_{gu} &= \frac{\omega_{12}}{\omega_1} = \frac{-E_v du}{2\sqrt{EG}} \cdot \frac{1}{\sqrt{E}du} = -\frac{E_v}{2E\sqrt{G}}, \\ k_{nu} &= \frac{\omega_{13}}{\omega_1} = \frac{L du}{\sqrt{E}} \cdot \frac{1}{\sqrt{E}du} = \frac{L}{E}, \\ \tau_{gu} &= \frac{\omega_{23}}{\omega_1} = \frac{M du}{\sqrt{G}} \cdot \frac{1}{\sqrt{E}du} = \frac{M}{\sqrt{EG}}. \end{aligned} \tag{B.20}$$

Also, the same operation for the v-curve gives

$$k_{gv} = \frac{G_u}{2G\sqrt{E}},\ k_{nv} = \frac{N}{G},\ \tau_{gv} = -\frac{M}{\sqrt{EG}}, \tag{B.21}$$

while the v-curve vector is $(\boldsymbol{e}_v, -\boldsymbol{e}_u, \boldsymbol{e}_3)$ and φ in Eq. (B.4) equals $\pi/2$. Lastly, the curvature in a given direction of trajectory $\mathbf{L}_s$ on a surface of object, is obtained using Eq. (B.1) and Eq. (B.4) where curvature properties are derived dependent on the arc-length s [39]

$$\begin{aligned} k_n &= \frac{\omega_{13}^f}{ds} = \frac{\omega_{13}\cos\varphi + \omega_{23}\sin\varphi}{ds} = k_{nu}\cos^2\varphi + 2\tau_{gu}\cos\varphi\sin\varphi + k_{nv}\sin^2\varphi, \\ \tau_g &= \frac{\omega_{23}^f}{ds} = \frac{-\omega_{13}\sin\varphi + \omega_{23}\cos\varphi}{ds} = \tau_{gu}\cos 2\varphi + \frac{1}{2}(k_{nv} - k_{nu})\sin 2\varphi, \\ k_g &= \frac{\omega_{12}^f}{ds} = \frac{\omega_{12}}{ds} = k_{gu}\cos\varphi + k_{gv}\sin\varphi, \end{aligned} \tag{B.22}$$

As a keynote, this formula is designed for the induced curvature of a general surface where its curvature coefficients are changing depending on the rotating arbitrary angle φ with respect to the Darboux frame as Fig B.1.

B.4 Controllability of the Darboux Frame-Based Kinematic Model

We check the controllability of the derived kinematic model in Eq. (5.12). This model can be represented as

$$\dot{\mathbf{x}} = \mathbf{f}(x) + \sum_{i=1}^{3} \mathbf{g}_i(x)\mathbf{u}_i, \tag{B.23}$$

where $\mathbf{f}(x)$ and $\mathbf{g}_i(x)$ are our drift term and the control input coefficients. Also, we know $\mathbf{x} = \{u_s, v_s, u_o, v_o, \psi\}$ and $\mathbf{u}_i = \{\gamma_s, \beta_s, \alpha_s\}$.

Theorem B.4.1 *System (B.23) is controllable in time-domain if* $\mathbf{f}(x)$ *be weakly positively Poisson stable (WPPS) and Lie algebra rank condition (LARC) is satisfied for local accessibility [67, 120].*

To proof the former (WPPS) in given Theorem B.4.1, we find whether the volume of phase space inside the given vector field for the drift term $\mathbf{f}(x)$ is preserved by Liouville's theorem [6]

$$\nabla \cdot \mathbf{f}(x) = \sum_{i=1}^{5} \frac{\partial f^i}{\partial x^i} = \delta \sin(\theta + \varphi)(\sin\psi + \cos\psi)\frac{\tan v_o}{R_o} = 0. \tag{B.24}$$

Because we will assign $\delta \geq 0$ as (5.29) in time-domain that always

$$\lim_{\mathbf{P}\to\mathbf{P}_f} \delta(u_s, v_s, u_o) = 0,$$

the property (B.24) is always true. Thus, our considered drift system becomes WPPS. δ term is similar to the time-scaling control method that was used for the ball-plate system in Ref. [37].

Remark B.4.1 *The Liouville's theorem is a sufficient condition to grant the WPPS property of our drift term. Moreover, Lobry proved that compact orientable manifold i.e., sphere, is Poisson stable [70] since every point on* $\mathbb{R}^2$ *of topological space is reachable. Then, Ref. [67] already proved that Poisson stable dense manifold is equivalent to WPPS.*

To find the Lie brackets of (B.23), we have four vector fields in total. In our planning, spin orientation of the sphere is an important control input which roughly

corespondents to $\mathbf{g}_3$ matrix. Thus, we find the Lie brackets as follows

$$\mathbf{f} = \begin{bmatrix} \sin(\theta+\varphi) \\ \sin(\theta+\varphi) \\ \frac{\sin(\theta+\varphi)[\sin\psi-\cos\psi]}{R_o\cos v_o} \\ \frac{\sin(\theta+\varphi)[\cos\psi+\sin\psi]}{R_o} \\ \frac{\tan v_o[\sin(\theta+\varphi)(\sin\psi-\cos\psi)+\cos\varphi]}{R_o} \end{bmatrix}, \mathbf{g}_1 = \begin{bmatrix} -R_o\sin(\theta+\varphi) \\ -R_o\sin(\theta+\varphi) \\ \frac{\sin(\theta+\varphi)[\cos\psi-\sin\psi]}{\cos v_o} \\ -\sin(\theta+\varphi)[\sin\psi+\cos\psi] \\ \tan v_o[\sin(\theta+\varphi)(\cos\psi-\sin\psi)] \end{bmatrix},$$

$$\mathbf{g}_2 = \begin{bmatrix} R_o\sin(\theta+\varphi) \\ -R_o\cos(\theta+\varphi) \\ \frac{-\sin(\psi+\theta+\varphi)}{\cos v_o} \\ -\cos(\psi+\theta+\varphi) \\ -\tan v_o\sin(\psi+\theta+\varphi) \end{bmatrix}, \mathbf{g}_3 = \begin{bmatrix} 0 \\ 0 \\ 0 \\ 0 \\ -1 \end{bmatrix},$$

$$[\mathbf{f},\mathbf{g}_3] = \begin{bmatrix} 0 \\ 0 \\ -\frac{\sin(\theta+\varphi)[\cos\psi+\sin\psi]}{R_o\cos v_o} \\ -\frac{\sin(\theta+\varphi)[\cos\psi-\sin\psi]}{R_o} \\ -\frac{\tan v_o\sin(\theta+\varphi)[\cos\psi+\sin\psi]}{R_o} \end{bmatrix}, [\mathbf{f},[\mathbf{f},\mathbf{g}_3]] = \begin{bmatrix} 0 \\ 0 \\ \frac{\sin(\theta+\varphi)[-\sin\psi+\cos\psi]}{R_o\cos v_o} \\ -\frac{\sin(\theta+\varphi)[\cos\psi+\sin\psi]}{R_o} \\ \frac{\tan v_o\sin(\theta+\varphi)[-\sin\psi+\cos\psi]}{R_o} \end{bmatrix}, \tag{B.25}$$

It is clear that the necessary condition for controllability in Theorem B.4.1 is satisfied since $\dim(\mathbf{L_3}) = \dim\{\mathbf{g}_1,\mathbf{g}_2,\mathbf{g}_3,[\mathbf{f},\mathbf{g}_3],[\mathbf{f},[\mathbf{f},\mathbf{g}_3]]\} = 5$, which its determinant is

$$\det(\mathbf{L_3}) = -2\frac{\sin v_o}{\cos^2 v_o}\cos\varphi\sin^3(\theta+\varphi)\left[\sin(\theta+\varphi)+\cos(\theta+\varphi)\right]. \tag{B.26}$$

Note that the determinant (B.26) has singular points at $\theta+\varphi = k\pi,\ \pi(2k+1)/2$ and $\varphi = \pi(2k+1)/2$ which have to be avoided when we are choosing our desired configuration on the plane. Also, the third singularity is at the local coordinate of the sphere manifold at $v_o = \pi(2k+1)/2$ angles that cause the determinant to converge infinity and controllability is lost. This can be solved with avoiding the physical desired angles $v_{o,f}$ near to $\pm\pi/2$ (two points located at two sides of the sphere's equator when u_o is an arbitrary angle).

In this kinematic model all three inputs always exists. In particular, if one of the

inputs is removed e.g., $\beta_s = 0$, the the kinematic model becomes uncontrollable

$$\begin{aligned}\dim(\mathbf{L}) = \dim \big\{ & \mathbf{g}_1, \mathbf{g}_3, [\mathbf{g}_1, \mathbf{g}_3], [\mathbf{f}, \mathbf{g}_3], [\mathbf{f}, \mathbf{g}_1], [\mathbf{f}, [\mathbf{g}_1, \mathbf{g}_3]] \\ & [\mathbf{f}, [\mathbf{f}, \mathbf{g}_3]], [\mathbf{f}, [\mathbf{f}, \mathbf{g}_1]], [\mathbf{g_1}, [\mathbf{g}_1, \mathbf{g}_3]], [\mathbf{g_1}, [\mathbf{f}, \mathbf{g}_3]], [\mathbf{g_1}, [\mathbf{f}, \mathbf{g}_1]], \\ & [\mathbf{g_3}, [\mathbf{g}_1, \mathbf{g}_3]], [\mathbf{g_3}, [\mathbf{f}, \mathbf{g}_3]], [\mathbf{g_3}, [\mathbf{f}, \mathbf{g}_1]], [\mathbf{f}, [\mathbf{f}, [\mathbf{g}_1, \mathbf{g}_3]]], \\ & [\mathbf{f}, [\mathbf{f}, [\mathbf{f}, \mathbf{g}_3]]], [\mathbf{f}, [\mathbf{f}, [\mathbf{f}, \mathbf{g}_1]]], [\mathbf{f}, [\mathbf{g_1}, [\mathbf{g}_1, \mathbf{g}_3]]], [\mathbf{f}, [\mathbf{g_1}, [\mathbf{f}, \mathbf{g}_3]]], \\ & [\mathbf{f}, [\mathbf{g_1}, [\mathbf{f}, \mathbf{g}_1]]], [\mathbf{f}, [\mathbf{g_3}, [\mathbf{g}_1, \mathbf{g}_3]]], [\mathbf{f}, [\mathbf{g_3}, [\mathbf{f}, \mathbf{g}_3]]], \\ & [\mathbf{f}, [\mathbf{g_3}, [\mathbf{f}, \mathbf{g}_1]]], [\mathbf{f}, [\mathbf{g_3}, [\mathbf{f}, \mathbf{g}_1]]] \big\} = 4 \neq 5,\end{aligned} \tag{B.27}$$

where proves the Proposition 5.3.1. To save the space, we leave the computation of the remaining Lie groups in (B.27) to the reader.

B.5 Geodesic Torsion Design of the Virtual Surface

The rotating object and plane do not have geodesic torsion, $\tau_g^* = -\beta_s$. It makes the kinematic model (5.12) uncontrollable. Thus, a helicoid virtual surface with similar curvature properties with rotating object [see Fig. 5.6] is proposed as

$$f_v : U_V \to R^3 : c(u_v, v_v) \mapsto (-R_v \sin u_v \cos v_v, R_v \sin v_v + R_t u_v, -R_v \cos u_v \cos v_v), \tag{B.28}$$

where R_v and R_t are defined by main spherical and sum of spherical and torsion radii, respectively. The curvature properties can be obtained as

$$k_n^v = \frac{1}{R_v},\ k_g^v = \frac{R_v \cos v_v \sin v_v}{R_v^2 \cos^2 v_v + R_t^2}, \tau_g^v = \frac{1}{R_v^2}(R_v^2 \cos^2 v_v + R_t^2)^{\frac{1}{2}} \tag{B.29}$$

where $k_n^v,\ k_g^v,\ \tau_g^v$ are normal curvature, geodesic curvature and geodesic torsion. We here mainly care about $\tau_g^v(R_v, R_t, v_v)$ and $k_n^v(R_v)$ to understand relation of geodesic torsion design. Thats why we related them with separate corresponding radii. To proof that this surface let us manipulate τ_g by using R_t, we consider $R_t = nR_v$ where $n > 1$, which results

$$\tau_g^v = \frac{1}{R_v}(\cos^2 v_v + n^2)^{\frac{1}{2}}. \tag{B.30}$$

Theorem B.5.1 *At an arbitrary point P on a surface, geodesic torsion relation with normal curvature is defined as [26]*

$$\tau_g = \frac{1}{2}(k_{nu} - k_{nv}) \sin 2\Omega \tag{B.31}$$

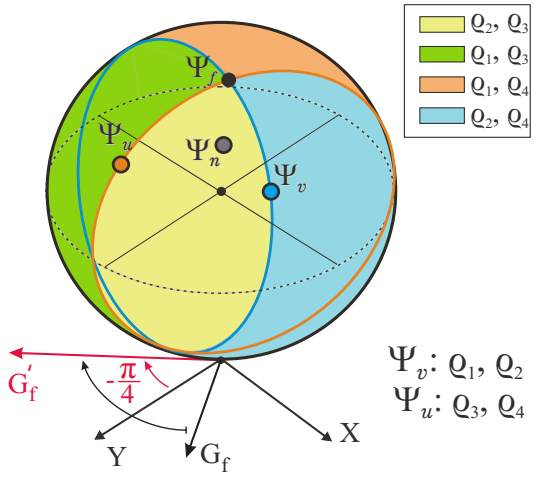

Figure B.3: Sectioned sphere based on the $\mathbf{\Psi}_v$ and $\mathbf{\Psi}_u$ cutting planes for directional updates of ζ_q. Note that $\mathbf{\Psi}_v$ and $\mathbf{\Psi}_u$ are on ϱ_2 and ϱ_3 as an example.

where k_{nu} and k_{nv} are the principle curvatures. Also, Ω is the counterclockwise angle from the direction of minimum curvature k_{nu} on the tangent plane.

By relying on the Theorem 1, it is clear that sphere tangent plane angle Ω is $\pi/4$. Now, we can do some algebraic operations on (B.31) with considering $k_{nu} = 1/R_v$ and Eq. (B.30),

$$k_{nv} = 1/R_v \left[1 + (\cos^2 v_v + n^2)^{\frac{1}{2}}\right] \tag{B.32}$$

where k_{nv} is second principle curvature of virtual surface. This support our assumption that designed geodesic torsion is inverse of sphere radius with similar unity of normal curvature $R_t = nR_v$. We do this for sake of separating radius of geodesic torsion and normal curvature in Eq. (5.20) as we use two separate surfaces (sphere and helicoid) in arc-length-based inputs.

B.6 Phase I Directional Update

We can separate the sphere regions to four by $c(u_{o,f}, v_{o,f})$ cutting planes [see example in Fig. B.3] for the desired configuration where ζ_q is calculated for its directional updates. Because we need to find directional updates in different G_f angles on plane, we apply a sphere rotational transformation to ease our regional computation. To find corresponding local points' right location for the directional update from plane angle G_f respect to v_s, we use an arbitrary local coordinate $c(u_o, v_o)$ rotation respect

to $-\pi/4$ base angle, $G'_f = G_f - \pi/4$, where gives new coordinate $c(u^r_o, v^r_o)$ as

$$\begin{aligned} v^r_o &= \sin^{-1}\left[-\sin G'_f \sin u_o \cos v_o + \cos G'_f \sin v_o \right] \\ u^r_o &= \sin^{-1}\left[(\cos G'_f \sin u_o \cos v_o + \sin G'_f \sin v_o)/\cos v^r_o \right] \end{aligned} \tag{B.33}$$

Next, to avoid the numerical solution of following Eqs. (B.33), we present it in algebraic operation depending on $c(u_o, v_o)$ location by

$$\begin{cases} \left\{ \begin{array}{ll} u^r_o \leftarrow -u^r_o, & \\ v^r_o \leftarrow \pi - v^r_o, & \text{for } \Big[\left(0 \le |v_o| \le \frac{\pi}{2} \;\&\; \frac{\pi}{2} \le |u_o| \le \pi\right) \end{array} \right. \\ \quad || \left(\frac{\pi}{2} < |v_o| \le \pi \;\&\; 0 \le |u_o| < \frac{\pi}{2}\right) \Big] \\ \left\{ \begin{array}{ll} u^r_o \leftarrow u^r_o, & \\ v^r_o \leftarrow v^r_o, & \text{for } \Big[\left(0 < |v_o| < \frac{\pi}{2} \;\&\; 0 < |u_o| < \frac{\pi}{2}\right) \end{array} \right. \\ \quad || \left(\frac{\pi}{2} < |v_o| < \pi \;\&\; \frac{\pi}{2} < |u_o| < \pi\right) \Big] \end{cases} \tag{B.34}$$

The operation by Eqs. (B.33)-(B.34) are applied to rotate the $\mathbf{\Psi}_f$, $\mathbf{\Psi}_u$, $\mathbf{\Psi}_v$ and $\mathbf{\Psi}_n$ relative to angle G_f to find them always in one G'_f direction. Now, the sectioned sphere as Fig. B.3 is obtained by cutting planes $\mathbf{\Psi}_v$ and $\mathbf{\Psi}_u$ where they create $\{\varrho_1, \varrho_2\}$ and $\{\varrho_3, \varrho_4\}$ regions, respectively. Note that for nearest point $\mathbf{\Psi}_n$ on $\mathbf{L}_o$, the corresponding ϱ are shown as ϱ_{n1}, ϱ_{n2}, ϱ_{n3}, ϱ_{n4}. We design our directional updates by comparing $\mathbf{\Psi}_n$ with $\mathbf{\Psi}_u$, $\mathbf{\Psi}_v$ as following computation

Calculate G'_f depending on the $\{u_{s,f}, v_{s,f}\}$
Calculate rotated coordinates of $\mathbf{\Psi}_f$, $\mathbf{\Psi}_u$, $\mathbf{\Psi}_v$ and $\mathbf{\Psi}_n$ by (B.34)
Calculate Q^{zy}_f, Q^{zx}_f, Q^{zy}_n and Q^{zx}_n according to (5.32)
if $\varrho_2 = 1$ & $\varrho_4 = 1$ **then** ▷ Exceptional regional updates
  if only $\varrho_{n2} = 1$ **then**
    $\zeta_q(k) \leftarrow +\zeta_q(k-1)$
  else if ($\varrho_{n2} = 1$ & $\varrho_{n4} = 1$) || (only $\varrho_{n4} = 1$) **then**
    if $v^r_{o,f} \ge 0$ **then**
      if $u^r_{o,f} \ge 0$ **then**
        $\zeta_q(k) \leftarrow +\zeta_q(k-1)$
      else
        $\zeta_q(k) \leftarrow -\zeta_q(k-1)$

end if

else

$\zeta_q(k) \leftarrow -\zeta_q(k-1)$

end if

end if

else if $(\varrho_{n2} = 1 \;\&\; \varrho_{n3} = 1) \,||\, (\varrho_3 = 1 \;\&\; \varrho_{n2} = 1 \;\&\; \varrho_{n4} = 1)$ **then**

if $u^r_{o,f} \geq 0$ **then**

$\zeta_q(k) \leftarrow +\zeta_q(k-1)$

else

$\zeta_q(k) \leftarrow -\zeta_q(k-1)$

end if

else if $\varrho_1 = \varrho_2 = \varrho_3 = \varrho_4 = 0$ **then**

if $v^r_{o,f} \geq 0$ **then**

$\zeta_q(k) \leftarrow -\zeta_q(k-1)$

else

$\zeta_q(k) \leftarrow +\zeta_q(k-1)$

end if

else ▷ Normal regional updates

if only $(\varrho_{n1} = 1)$ || $(\varrho_{n4} = 1)$ **then**

if $v^r_{o,f} \geq 0$ **then**

$\zeta_q(k) \leftarrow +\zeta_q(k-1)$

else

$\zeta_q(k) \leftarrow -\zeta_q(k-1)$

end if

else if only $(\varrho_{n2} = 1)$ || $(\varrho_{n3} = 1)$ **then**

if $v^r_{o,f} \geq 0$ **then**

$\zeta_q(k) \leftarrow -\zeta_q(k-1)$

else

$\zeta_q(k) \leftarrow +\zeta_q(k-1)$

end if

end if

end if

where condition with equality of 1 means the following points are in the given region. For example, $\varrho_{1n} = 1$ means $\mathbf{\Psi}_n$ existing in region 1 respect to $\mathbf{\Psi}_f$. We have to say that complexity of regional comparison is mainly due to non-holonomic characteristics of this system (sphere symmetry) that cause each region behave differently due to location of extracted points. Normal updates mainly find the curve's $\mathbf{\Psi}_n$ and compares it to the location of desired goal $\mathbf{\Psi}_f$ to find true direction of update. However, exceptional updates are designed to run away from loop traps of $\mathbf{\Psi}_n$ and brings the $\mathbf{L}_o$ curve always downward direction to $\mathbf{\Psi}_0$.

B.7 Proof of Closed Set

Let $\mathbf{x}_k \rightarrow \mathbf{x}_0$ and $\mathbf{d}_k \rightarrow \mathbf{d}_0$ be the convergence to desired values as $k \rightarrow \infty$ via sequences of $\{\mathbf{x}_k\}_{k=1}^{\infty}$ and $\{\mathbf{d}_k\}_{k=1}^{\infty}$. Also, suppose $\{\mathbf{y}_k\}_{k=1}^{\infty}$ is a sequence where $\mathbf{y} \in \Gamma(\mathbf{x}_k, \mathbf{d}_k)$ for all k while it has convergence of $\mathbf{y}_k \rightarrow \mathbf{y}_0$ as $k \rightarrow \infty$. We want to illustrate that $\mathbf{y}_0 \in \Gamma(\mathbf{x}_0, \mathbf{d}_0)$ for having a closed set.

In each iteration k, $\mathbf{y}_k = \mathbf{x}_k + \mathbf{h}_k\mathbf{d}_k$ for $\mathbf{h}_k > 0$. Thus, by knowing fact that $||\mathbf{d}_k|| = [1 \; .. \; 1]^T$, there is

$$\mathbf{h}_k = ||\mathbf{y}_k - \mathbf{x}_k|| = \begin{bmatrix} ||\mathbf{y}_k(1) - \mathbf{x}_k(1)|| & ... \\ ... & ||\mathbf{y}_k(n) - \mathbf{x}_k(n)|| \end{bmatrix} \rightarrow \mathbf{h}^* = ||\mathbf{y}_0 - \mathbf{x}_0||,$$

hence it implies that $\mathbf{y}_0 = \mathbf{x}_0 + \mathbf{h}^*\mathbf{d}_0$.

Now, to show $\mathbf{y}_0$ minimizes the f along the $\mathbf{x}_0 + \mathbf{h}\mathbf{d}_0$, we know for each k and $\mathbf{h}$, $0 < \mathbf{h} < \infty$, there is

$$f(\mathbf{y}_k) \leq f(\mathbf{x}_k + \mathbf{h}\mathbf{d}_k).$$

Therefore, by continuity of f, $k \rightarrow \infty$ leads to $f(\mathbf{y}_0) \leq f(\mathbf{x}_0 + \mathbf{h}\mathbf{d}_0)$ for all $\mathbf{h}$ in which shows

$$f(\mathbf{y}_k) \leq \min \; f(\mathbf{x}_k + \mathbf{h}\mathbf{d}_k).$$

This proves the definition of $\mathbf{y}_0 \in \Gamma(\mathbf{x}_0, \mathbf{d}_0)$ for having a closed set.

Bibliography

[1] S. K. Agrawal, "Inertia matrix singularity of planar series-chain manipulators," in *IEEE International Conference on Robotics and Automation*, 1991, pp. 102–107.

[2] P. Akella, O. O'Reilly, and K. Sreenath, "Controlling the locomotion of spherical robots or why BB-8 works," *ASME J. Mech. Robot.*, vol. 11, no. 2, pp. 024 501–024 501–4, 2019.

[3] F. Alouges, Y. Chitour, and R. Long, "A motion-planning algorithm for the rolling-body problem," *IEEE Trans. Robot.*, vol. 5, no. 26, pp. 827–836, 2010.

[4] H. Arai and S. Tachi, "Position control of manipulator with passive joints using dynamic coupling," *IEEE Transactions on Robotics and Automation*, vol. 7, no. 4, pp. 528–534, 1991.

[5] R. H. Armour and J. F. Vincent, "Rolling in nature and robotics: A review," *J. of Bionic Eng.*, vol. 3, no. 4, pp. 195 – 208, 2006.

[6] V. I. Arnol'd, *Mathematical methods of classical mechanics*. Springer Science & Business Media, 2013, vol. 60.

[7] A. Arthurs and G. Walsh, "On hammersley's minimum problem for a rolling sphere," in *Math. Proc. Cambridge Philos. Soc.*, vol. 99, no. 3. Cambridge University Press, 1986, pp. 529–534.

[8] J. Asama, M. R. Burkhardt, F. Davoodi, and J. W. Burdick, "Design investigation of a coreless tubular linear generator for a moball: A spherical exploration robot with wind-energy harvesting capability," in *IEEE International Conference on Robotics and Automation (ICRA)*, 2015, pp. 244–251.

[9] ——, "Design investigation of a coreless tubular linear generator for a moball: A spherical exploration robot with wind-energy harvesting capability," in *2015 IEEE International Conference on Robotics and Automation (ICRA)*, 2015, pp. 244–251.

[10] AutomationDirect. (2018) "A-series double-act pneumatic cylinders". Accessed November 19, 2018, www.automationdirect.com.

[11] T. Baba, Y. Kameyama, T. Kamegawa, and A. Gofuku, "A snake robot propelling inside of a pipe with helical rolling motion," in *Proceedings of SICE Annual Conference*, 2010, pp. 2319–2325.

[12] E. R. Bachmann, "Inertial and magnetic tracking of limb segment orientation for inserting humans into synthetic environments," Ph.D. dissertation.

[13] E. R. Bachmann, X. Yun, and A. Brumfield, "Limitations of attitude estimnation algorithms for inertial/magnetic sensor modules," *IEEE Robotics & Automation Magazine*, vol. 14, no. 3, pp. 76–87, 2007.

[14] D. Balandin, M. Komarov, and G. Osipov, "A motion control for a spherical robot with pendulum drive," *Journal of Computer and Systems Sciences International*, vol. 52, no. 4, pp. 650–663, 2013.

[15] A. Behar, J. Matthews, F. Carsey, and J. Jones, "NASA/JPL tumbleweed polar rover," in *Proc. IEEE Aerospace Conf.*, vol. 1, March 2004, p. 395.

[16] A. Bellino, A. Fasana, E. Gandino, L. Garibaldi, and S. Marchesiello, "A time-varying inertia pendulum: analytical modelling and experimental identification," *Mechanical Systems and Signal Processing*, vol. 47, no. 1-2, pp. 120–138, 2014.

[17] M. Benallegue, J.-P. Laumond, and A. Berthoz, "On the mechanical contribution of head stabilization to passive dynamics of anthropometric walkers," *The International Journal of Robotics Research*, vol. 39, no. 4, pp. 461–475, 2020.

[18] M. Bergerman, C. Lee, and Y. Xu, "A dynamic coupling index for underactuated manipulators," *Journal of Robotic Systems*, vol. 12, no. 10, pp. 693–707, 1995.

[19] I. Y. Beschatnyi, "The optimal rolling of a sphere, with twisting but without slipping," *Mat. Sb.*, vol. 205, no. 2, p. 157, 2014.

[20] S. Bhattacharya and S. Agrawal, "Spherical rolling robot: a design and motion planning studies," *IEEE Trans. Robot. Autom.*, vol. 16, no. 6, pp. 835–839, 2000.

[21] A. Bicchi, A. Balluchi, D. Prattichizzo, and A. Gorelli, "Introducing the "SPHERICLE": an experimental testbed for research and teaching in nonholonomy," in *Proc. IEEE Conf. Robot. Autom.*, vol. 3, Apr 1997, pp. 2620–2625.

[22] A. V. Borisov, A. A. Kilin, and I. S. Mamaev, "How to control Chaplygin's sphere using rotors," *Regul. Chaotic Dyn.*, vol. 17, no. 3, pp. 258–272, 2012.

[23] J. E. Bortz, "A new mathematical formulation for strapdown inertial navigation," *IEEE transactions on aerospace and electronic systems*, no. 1, pp. 61–66, 1971.

[24] J. Brown, H.B. and Y. Xu, "A single-wheel, gyroscopically stabilized robot," in *Proc. IEEE Int. Conf. on Robot. and Autom.*, vol. 4, Apr 1996, pp. 3658–3663.

[25] Y. Cai, Q. Zhan, and X. Xi, "Path tracking control of a spherical mobile robot," *Mech. Mach. Theory*, vol. 51, pp. 58–73, 2012.

[26] E. Cartan, *Riemannian Geometry in an Orthogonal Frame*, 1st ed. World Scientific Pub Co Inc, 2002.

[27] E. Chang, L. Y. Matloff, A. K. Stowers, and D. Lentink, "Soft biohybrid morphing wings with feathers underactuated by wrist and finger motion," *Science Robotics*, vol. 5, no. 38, 2020.

[28] R. Chase and A. Pandya, "A review of active mechanical driving principles of spherical robots," *Robotics*, vol. 1, no. 1, pp. 3–23, 2012.

[29] H. Chenarani and T. Binazadeh, "Flexible structure control of unmatched uncertain nonlinear systems via passivity-based sliding mode technique," *Iranian Journal of Science and Technology, Transactions of Electrical Engineering*, vol. 41, no. 1, pp. 1–11, 2017.

[30] P. R. Childs, *Mechanical Design*, 2^{nd} ed. Butterworth-Heinemann, 2003.

[31] A. R. Chowdhury, G. S. Soh, S. Foong, and K. L. Wood, "Implementation of caterpillar inspired rolling gait and nonlinear control strategy in a spherical robot," *J. of Bionic Eng.*, vol. 15, no. 2, pp. 313–328, 2018.

[32] A. B. A. Cole, J. E. Hauser, and S. S. Sastry, "Kinematics and control of multifingered hands with rolling contact," *IEEE Trans. Autom. Control*, vol. 34, no. 4, pp. 398–404, April 1989.

[33] J. L. Crassidis, F. L. Markley, and Y. Cheng, "Survey of nonlinear attitude estimation methods," *Journal of guidance, control, and dynamics*, vol. 30, no. 1, pp. 12–28, 2007.

[34] L. Cui and J. S. Dai, "A darboux-frame-based formulation of spin-rolling motion of rigid objects with point contact," *IEEE Trans. Robot.*, vol. 26, no. 2, pp. 383–388, April 2010.

[35] L. Cui, J. Sun, and J. S. Dai, "In-hand forward and inverse kinematics with rolling contact," *Robotica*, vol. 35, no. 12, p. 2381–2399, 2017.

[36] T. Das and R. Mukherjee, "Exponential stabilization of the rolling sphere," *Automatica*, vol. 40, no. 11, pp. 1877–1889, 2004.

[37] H. Date, M. Sampei, M. Ishikawa, and M. Koga, "Simultaneous control of position and orientation for ball-plate manipulation problem based on time-state control form," *IEEE Trans. Robot.*, vol. 20, no. 3, pp. 465–480, 2004.

[38] E. Diller, M. Sitti *et al.*, "Micro-scale mobile robotics," *Found. Trends Robot.,*, vol. 2, no. 3, pp. 143–259, 2013.

[39] M. P. do Carmo, *Differential Geometry of Curves and Surfaces*, 2nd ed. Prentice-Hall, 1976.

[40] J. Dormand and P. Prince, "A family of embedded Runge-Kutta formulae," *J. Comput. Appl. Math.*, vol. 6, no. 1, pp. 19–26, 1980.

[41] L. Droukas and Z. Doulgeri, "Rolling contact motion generation and control of robotic fingers," *J. Intell. Robot. Syst.*, vol. 82, no. 1, pp. 21–38, 2016.

[42] O. Duran, K. Althoefer, and L. D. Seneviratne, "Automated pipe defect detection and categorization using camera/laser-based profiler and artificial neural network," *IEEE Transactions on Automation Science and Engineering*, vol. 4, no. 1, pp. 118–126, 2007.

[43] P. Fankhauser and C. Gwerder, "Modeling and control of a ballbot," B.S. thesis, Eidgenössische Technische Hochschule Zürich, 2010.

[44] A. Fernández-Pacheco, R. Streubel, O. Fruchart, R. Hertel, P. Fischer, and R. P. Cowburn, "Three-dimensional nanomagnetism," *Nat. Commun.*, vol. 8, p. 15756, 2017.

[45] E. Gandino, S. Marchesiello, A. Bellino, A. Fasana, and L. Garibaldi, "Damping effects induced by a mass moving along a pendulum," *Shock and Vibration*, vol. 2014, 2014.

[46] A. Halme, T. Schonberg, and Y. Wang, "Motion control of a spherical mobile robot," in *Proc. 4th Int. Workshop Adv. Motion Control (AMC 1996)*, vol. 1, Mar 1996, pp. 259–264.

[47] A. S. Hashim, B. Grămescu, and C. Niţu, "Pipe cracks detection methods–a review," in *International Conference of Mechatronics and Cyber-Mixmechatronics*. Springer, 2018, pp. 185–193.

[48] F. R. Hogan and J. R. Forbes, "Trajectory tracking, estimation, and control of a pendulum-driven spherical robot," *J. Guid. Control Dyn.*, pp. 1119–1125, 2015.

[49] E. Hughes, J. Hiley, K. Brown, and I. M. Smith, *Hughes Electrical & Electronic Technology*, 10^{th} ed. UK: Prentice Hall, 2008.

[50] K. Ilin, H. Moffatt, and V. Vladimirov, "Dynamics of a rolling robot," *Proc. Natl. Acad. Sci. U.S.A.*, vol. 114, no. 49, pp. 12 858–12 863, 2017.

[51] M. Ishikawa, R. Kitayoshi, and T. Sugie, "Volvot : A spherical mobile robot with eccentric twin rotors," in *IEEE Int. Conf. on Robot. and Biom. (ROBIO)*, Dec 2011, pp. 1462–1467.

[52] ——, "Volvot: A spherical mobile robot with eccentric twin rotors," in *Proc. IEEE Int. Conf. Robot. Biomimetics*, 2011, pp. 1462–1467.

[53] T. B. Ivanova, A. A. Kilin, and E. N. Pivovarova, "Controlled motion of a spherical robot with feedback. i," *J. Dyn. Control Syst.*, vol. 24, no. 3, pp. 497–510, 2018.

[54] A. H. Javadi A. and P. Mojabi, "Introducing glory: A novel strategy for an omnidirectional spherical rolling robot," *ASME J. Dyn. Syst.-T*, vol. 126, no. 3, pp. 678–683, 2004.

[55] J. Johnson, R. Senthilnathan, M. Negi, R. G. Patel, and A. Bhattacherjee, "A fuzzy logic-in-loop control for a novel reduced height ballbot prototype," *Procedia Comput. Sci.*, vol. 133, pp. 960–967, 2018.

[56] V. Jurdjevic, "The geometry of the plate-ball problem," *Arch. Ratio. Mech. Anal.*, vol. 124, no. 4, pp. 305–328, 1993.

[57] T. R. Kane, "Dynamics of nonholonomic systems," *ASME J. of Appl. Mech.*, vol. 28, no. 4, pp. 574–578, 1961.

[58] Y. L. Karavaev and A. A. Kilin, "The dynamics and control of a spherical robot with an internal omniwheel platform," *Regul. Chaotic Dyn.*, vol. 20, no. 2, pp. 134–152, 2015.

[59] E. Kayacan, E. Kayacan, H. Ramon, and W. Saeys, "Adaptive neuro-fuzzy control of a spherical rolling robot using sliding-mode-control-theory-based online learning algorithm," *IEEE Trans. Cybern.*, vol. 43, no. 1, pp. 170–179, 2013.

[60] E. Kayacan, Z. Y. Bayraktaroglu, and W. Saeys, "Modeling and control of a spherical rolling robot: a decoupled dynamics approach," *Robotica*, vol. 30, no. 4, pp. 671–680, 2012.

[61] A. A. Kilin, E. N. Pivovarova, and T. B. Ivanova, "Spherical robot of combined type: dynamics and control," *Regular and chaotic dynamics*, vol. 20, no. 6, pp. 716–728, 2015.

[62] B. Kiss, J. Lévine, and B. Lantos, "On motion planning for robotic manipulation with permanent rolling contacts," *Int. J. Robot. Res.*, vol. 21, no. 5-6, pp. 443–461, 2002.

[63] L. Cui and J. S. Dai, "A polynomial formulation of inverse kinematics of rolling contact," *ASME J. Mech. Robot.*, vol. 7, no. 2, pp. 041 003–041 009, 2015.

[64] T. Li and W. Liu, "Design and analysis of a wind-driven spherical robot with multiple shapes for environment exploration," *J. of Aerospace Eng.*, vol. 24, no. 1, pp. 135–139, 2010.

[65] T. Li, Z. Wang, and Z. Ji, "Dynamic modeling and simulation of the internal- and external-driven spherical robot," *J. of Aerospace Eng.*, vol. 25, no. 4, pp. 636–640, 2011.

[66] Z. Li and J. Canny, "Motion of two rigid bodies with rolling constraint," *IEEE Trans. Robot. Autom.*, vol. 6, no. 1, pp. 62–72, Feb 1990.

[67] K.-Y. Lian, L.-S. Wang, and L.-C. Fu, "Controllability of spacecraft systems in a central gravitational field," *IEEE Trans. Autom. Control*, vol. 39, no. 12, pp. 2426–2441, 1994.

[68] D. Liu, H. Sun, and Q. Jia, "Stabilization and path following of a spherical robot," in *Proc. IEEE Conf. Robot. Autom. and Mechatron.*, Sept 2008, pp. 676–682.

[69] Y. Liu and H. Yu, "A survey of underactuated mechanical systems," *IET Control Theory & Applications*, vol. 7, no. 7, pp. 921–935, 2013.

[70] C. Lobry, "Controllability of nonlinear systems on compact manifolds," *SIAM J. Contr.*, vol. 12, no. 1, pp. 1–4, 1974.

[71] S. Mahboubi, M. Seyyed Fakhrabadi, and A. Ghanbari, "Design and implementation of a novel spherical mobile robot," *J. Intell. Robot. Sys.*, vol. 71, no. 1, pp. 43–64, 2012.

[72] A. Marigo and A. Bicchi, "Rolling bodies with regular surface: Controllability theory and applications," *IEEE Trans. Autom. Control*, vol. 45, no. 9, pp. 1586–1599, 2000.

[73] F. L. Markley and D. Mortari, "Quaternion attitude estimation using vector observations." *Journal of the Astronautical Sciences*, vol. 48, no. 2, pp. 359–380, 2000.

[74] D. J. Montana, "The kinematics of contact and grasp," *Int. J. Robotics Res.*, vol. 7, no. 3, pp. 17–32, 1988.

[75] A. Morinaga, M. Svinin, and M. Yamamoto, "A motion planning strategy for a spherical rolling robot driven by two internal rotors," *IEEE Trans. Robot.*, vol. 30, no. 4, pp. 993–1002, 2014.

[76] ——, "A motion planning strategy for a spherical rolling robot driven by two internal rotors," *IEEE Trans. Robot.*, vol. 30, no. 4, pp. 993–1002, 2014.

[77] M. Mosallaei and K. Salahshoor, "Sensor fault detection using adaptive modified extended kalman filter based on data fusion technique," in *4th International Conference on Information and Automation for Sustainability*, 2008, pp. 513–518.

[78] R. Mukherjee and T. Das, "Feedback stabilization of a spherical mobile robot," in *Proc. IEEE/RSJ Int. Conf. on Intell. Robots Sys.*, vol. 3, 2002, pp. 2154–2162.

[79] R. Mukherjee, M. A. Minor, and J. T. Pukrushpan, "Motion planning for a spherical mobile robot: Revisiting the classical ball-plate problem," *Journal of Dynamic Systems, Measurement, and Control*, vol. 124, no. 4, pp. 502–511, 2002.

[80] V. Muralidharan and A. D. Mahindrakar, "Geometric controllability and stabilization of spherical robot dynamics," *IEEE Trans. Autom. Control*, vol. 60, no. 10, pp. 2762–2767, 2015.

[81] A. A. Nassiraei, Y. Kawamura, A. Ahrary, Y. Mikuriya, and K. Ishii, "Concept and design of a fully autonomous sewer pipe inspection mobile robot" kantaro"," in *Proceedings IEEE International Conference on Robotics and Automation*, 2007, pp. 136–143.

[82] A. M. Okamura, N. Smaby, and M. R. Cutkosky, "An overview of dexterous manipulation," in *Proc. IEEE Int. Conf. Robot. Autom.*, vol. 1, 2000, pp. 255–262.

[83] G. Oriolo and M. Vendittelli, "A framework for the stabilization of general nonholonomic systems with an application to the plate-ball mechanism," *IEEE Transactions on Robotics*, vol. 21, no. 2, pp. 162–175, 2005.

[84] G. Oriolo and M. Vendittelli, "A framework for the stabilization of general nonholonomic systems with an application to the plate-ball mechanism," *IEEE Trans. Robot.*, vol. 21, no. 2, pp. 162–175, April 2005.

[85] S. M. Persson and I. Sharf, "Invariant trapezoidal kalman filter for application to attitude estimation," *Journal of Guidance, Control, and Dynamics*, vol. 36, no. 3, pp. 721–733, 2013.

[86] V. Radhakrishnan, "Locomotion: Dealing with friction," *Proceedings of the National Academy of Sciences*, vol. 95, no. 10, pp. 5448–5455, 1998.

[87] D. Roetenberg, H. J. Luinge, C. T. Baten, and P. H. Veltink, "Compensation of magnetic disturbances improves inertial and magnetic sensing of human body segment orientation," *IEEE Trans. Neural Syst. Rehabil. Eng.*, vol. 13, no. 3, pp. 395–405, 2005.

[88] S.A. Tafrishi, Y. Bai, M. Svinin, E. Esmaeilzadeh, and M. Yamamoto, "Inverse dynamics-based motion control of a fluid-actuated rolling robot," *Russian Journal of Nonlinear Dynamics*, vol. 15, no. 4, pp. 611–622, 2019.

[89] M. Sampei, "Under-actuated systems: Nonlinear control showcase," in *International Conference on Advanced Engineering Theory and Applications*. Springer, 2017, pp. 3–14.

[90] H. M. Schepers, D. Roetenberg, and P. H. Veltink, "Ambulatory human motion tracking by fusion of inertial and magnetic sensing with adaptive actuation," *Medical & biological engineering & computing*, vol. 48, no. 1, p. 27, 2010.

[91] G. C. Schroll, "Design of a spherical vehicle with flywheel momentum storage for high torque capabilities," Master's thesis, Massachusetts Institute of Technology, Cambridge, MA, 2008.

[92] S. Seok, A. Wang, M. Y. M. Chuah, D. J. Hyun, J. Lee, D. M. Otten, J. H. Lang, and S. Kim, "Design principles for energy-efficient legged locomotion and implementation on the mit cheetah robot," *IEEE/ASME Transactions on Mechatronics*, vol. 20, no. 3, pp. 1117–1129, 2015.

[93] D. Serra, F. Ruggiero, A. Donaire, L. R. Buonocore, V. Lippiello, and B. Siciliano, "Control of nonprehensile planar rolling manipulation: A passivity-based approach," *IEEE Trans. Robot.*, vol. 35, no. 2, pp. 317–329, April 2019.

[94] L. F. Shampine and M. W. Reichelt, "The matlab ODE suite," *SIAM J. Scien. Comput.*, vol. 18, no. 1, pp. 1–22, 1997.

[95] T. Shimizu, S. Nakaura, and M. Sampei, "The control of a bipedal running robot based on output zeroing considered rotation of the ankle joint," in *Proceedings of the 45th IEEE Conference on Decision and Control*, 2006, pp. 6456–6461.

[96] A. H. Slocum, *Precision Machine Design*, 1^{st} ed. Society of Manufacturing, 1992.

[97] M. W. Spong, "Partial feedback linearization of underactuated mechanical systems," in *Proceedings of IEEE/RSJ International Conference on Intelligent Robots and Systems*, vol. 1, 1994, pp. 314–321.

[98] ——, "The swing up control problem for the acrobot," *IEEE control systems magazine*, vol. 15, no. 1, pp. 49–55, 1995.

[99] M. W. Spong and D. J. Block, "The pendubot: A mechatronic system for control research and education," in *Proceedings of 1995 34th IEEE Conference on Decision and Control*, vol. 1, 1995, pp. 555–556.

[100] D. S. Stilling and W. Szyszkowski, "Controlling angular oscillations through mass reconfiguration: a variable length pendulum case," *International Journal of Non-Linear Mechanics*, vol. 37, no. 1, pp. 89–99, 2002.

[101] R. L. Street, G. Z. Watters, and J. K. Vennard, *Elementary Fluid Mechanics*, 7^{th} ed. New York, USA: Wiley & sons, 1996.

[102] B. Sümer and M. Sitti, "Rolling and spinning friction characterization of fine particles using lateral force microscopy based contact pushing," *J. Adhes Sci. Technol.*, vol. 22, no. 5-6, pp. 481–506, 2008.

[103] M. Svinin and S. Hosoe, "Motion planning algorithms for a rolling sphere with limited contact area," *IEEE Trans. Robot.*, vol. 24, no. 3, pp. 612–625, 2008.

[104] M. Svinin, Y. Bai, and M. Yamamoto, "Dynamic model and motion planning for a pendulum-actuated spherical rolling robot," in *IEEE International Conference on Robotics and Automation*, 2015, pp. 656–661.

[105] M. Svinin, I. Goncharenko, Z.-W. Luo, and S. Hosoe, "Reaching movements in dynamic environments: How do we move flexible objects?" *IEEE Transactions on Robotics*, vol. 22, no. 4, pp. 724–739, 2006.

[106] M. Svinin and S. Hosoe, "Motion planning algorithms for a rolling sphere with limited contact area," *IEEE Trans. Robot.*, vol. 24, no. 3, pp. 612–625, 2008.

[107] S. A. Tafrishi, ""RollRoller" novel spherical mobile robot basic dynamical analysis and motion simulations," Master's thesis, University of Sheffield, Sheffield, UK, 2014.

[108] S. A. Tafrishi, Y. Bai, M. Svinin, E. Esmaeilzadeh, and M. Yamamoto, "Inverse dynamics-based motion control of a fluid-actuated rolling robot," *Russian Journal of Nonlinear Dynamics*, vol. 15, no. 4, pp. 611–622, 2019.

[109] S. A. Tafrishi, E. Esmaeilzadeh, M. Svinin, and M. Yamamoto, "A fluid-actuated driving mechanism for rolling robots," in *IEEE 4th International Conference on Advanced Robotics and Mechatronics (ICARM)*, 2019, pp. 256–261.

[110] S. A. Tafrishi, M. Svinin, E. Esmaeilzadeh, and M. Yamamoto, "Design, modeling, and motion analysis of a novel fluid actuated spherical rolling robot," *ASME Journal of Mechanism and Robotics*, vol. 11, no. 4, p. 041010, 2019.

[111] ——, "Design, modeling, and motion analysis of a novel fluid actuated spherical rolling robot," *Journal of Mechanisms and Robotics*, vol. 11, no. 4, p. 041010, 2019.

[112] ——, "A fluid-actuated driving mechanism for rolling robots," in *IEEE 4th International Conference on Advanced Robotics and Mechatronics (ICARM)*, vol. 1, 2019, pp. 3527–3533.

[113] S. A. Tafrishi, M. Svinin, and M. Yamamoto, "Singularity-free inverse dynamics for underactuated systems with a rotating mass," in *IEEE International Conference on Robotics and Automation (ICRA)*, 2020, pp. 3981–3987.

[114] K. Tapp, *Differential geometry of curves and surfaces*. New York: Springer, 2016.

[115] R. Tedrake, "Underactuated robotics: Learning, planning, and control for efficient and agile machines course notes for MIT 6.832," 2009.

[116] F. Tomik, S. Nudehi, L. L. Flynn, and R. Mukherjee, "Design, fabrication and control of spherobot: A spherical mobile robot," *J. of Intell. & Robot. Sys.*, vol. 67, no. 2, pp. 117–131, 2012.

[117] Trident Engineering. (2018) "GS61-series DC motor". Accessed November 19, 2018, www.tridenteng.co.uk.

[118] V. A. Tucker, "The energetic cost of moving about: Walking and running are extremely inefficient forms of locomotion. much greater efficiency is achieved by birds, fish and bicyclists," *Am. Sci.*, vol. 63, no. 4, pp. 413–419, 1975.

[119] A. Vretblad, *Fourier analysis and its applications*. Springer Science & Business Media, 2003, vol. 223.

[120] X. Wang, P. Cui, and H. Cui, "A note on poisson stability and controllability," *Nonlinear Dynamics*, vol. 66, no. 4, pp. 789–793, 2011.

[121] C. Wei-Hsi, C. Ching-Pei, Y. Wei-Shun, L. Chang-Hao, and L. Pei-Chun, "Design and implementation of an omnidirectional spherical robot omnicron," in *IEEE/ASME Int. Conf. Adv. Intell. Mechatron. (AIM)*, July 2012, pp. 719–724.

[122] J. Wittenburg, *Dynamics of systems of rigid bodies*. Springer-Verlag, 2013, vol. 33.

[123] A. Wolf, H. B. Brown, R. Casciola, A. Costa, M. Schwerin, E. Shamas, and H. Choset, "A mobile hyper redundant mechanism for search and rescue tasks," in *Proceedings IEEE/RSJ International Conference on Intelligent Robots and Systems*, vol. 3, 2003, pp. 2889–2895.

[124] D. F. Young, B. R. Munson, T. H. Okiishi, and W. W. Huebsch, *Brief Fluid: A Brief Introduction*, 5^{th} ed. USA: Wiley & sons, 2010.

[125] S. Yuan, L. Shao, C. L. Yako, A. Gruebele, and J. K. Salisbury, "Design and control of roller grasper v2 for in-hand manipulation," *arXiv preprint arXiv:2004.08499*, 2020.

[126] W. I. Zangwill, *Nonlinear programming: a unified approach*. Prentice-Hall Englewood Cliffs, NJ, 1969, vol. 196, no. 9.

Published Peer-Reviewed Papers

[1] S.A. Tafrishi, E. Esmaeilzadeh, M. Svinin, and M. Yamamoto, "A fluid-actuated driving mechanism for rolling robots," in *2019 IEEE 4th International Conference on Advanced Robotics and Mechatronics (ICARM)*, pp. 256–261, Toyonaka, Japan, 2019.

[2] S.A. Tafrishi, M. Svinin, E. Esmaeilzadeh, and M. Yamamoto. Design, modeling, and motion analysis of a novel fluid actuated spherical rolling robot. *ASME J. Mech. Robot.*, 11(4):041010, 2019.

[3] S.A. Tafrishi, Y. Bai, M. Svinin, E. Esmaeilzadeh, and M. Yamamoto. Inverse dynamics-based motion control of a fluid-actuated rolling robot. *Russian Journal of Nonlinear Dynamics*, 15(4):611–622, 2019.

[4] S.A. Tafrishi, M. Svinin, and M. Yamamoto, "Singularity-free inverse dynamics for underactuated systems with a rotating mass," in *2020 International Conference on Robotics and Automation (ICRA)*, pp. 256–261, Paris, France, 2020.